Felix Schmidt

Generalized Continua with Embedded Fibers and Dimension-Expanded Multi-scale Coupling

LNM Lehrstuhl für Numerische Mechanik

universi
UNIVERSITÄTSVERLAG SIEGEN

Felix Schmidt

Generalized Continua with Embedded Fibers and Dimension-Expanded Multi-scale Coupling

universi
UNIVERSITÄTSVERLAG SIEGEN

Vol. 2

Publication series of the Chair of Computational Mechanics

Editor: Prof. Dr. habil. Christian Hesch

Bibliografische Information der Deutschen Nationalbibliothek

Die Deutsche Nationalbibliothek verzeichnet diese Publikation in der Deutschen Nationalbibliografie; detaillierte Daten sind im Internet über http://dnb.dnb.de abrufbar

Impressum

Druck und Bindung:
UniPrint, Universität Siegen

Gedruckt auf alterungsbeständigem holz- und säurefreiem Papier

Siegen 2026: univers*i* – Universitätsverlag Siegen
www.uni-siegen.de/universi

ISBN 978-3-96182-240-9

doi.org/10.25819/ubsi/11013

Die Publikation erscheint unter der Creative Commons Lizenz CC-BY-SA

Generalized Continua with Embedded Fibers and Dimension-Expanded Multi-scale Coupling

DISSERTATION

zur Erlangung des Grades eines Doktors

der Ingenieurwissenschaften

vorgelegt von

M.Sc. Felix Schmidt

eingereicht bei der Naturwissenschaftlich-Technischen Fakultät

der Universität Siegen

Siegen 2026

Betreuer und erster Gutachter

Prof. Dr.-Ing. habil. Christian Hesch

Universität Siegen

Zweiter Gutachter

Prof. Dr.-Ing. habil. Fadi Aldakheel

Leibniz Universität Hannover

Tag der mündlichen Prüfung

11.06.2026

Abstract

This thesis addresses the modeling and simulation of microstructured and fiber-reinforced materials, for which classical first-gradient Cauchy continua fail to capture bending-dominated mechanisms, size effects, and non-local interactions, while fully resolved three-dimensional microstructural analyses are prohibitively expensive. Two complementary higher-order frameworks are developed, both formulated and discretized within an isogeometric analysis setting to exploit the required continuity of higher-order fields.

The first part focuses on higher-order continua induced by embedded slender reinforcements. A three-dimensional second-gradient material model is proposed in which families of fibers are represented by direction fields with associated stretch, shear, curvature and torsion measures. These measures are linked to energetically conjugate higher-order stresses and the resulting theory is implemented using spline-based C^1-continuous discretization. In a complementary discrete approach, geometrically exact Cosserat-type beams at finite strain are embedded in an overlapping three-dimensional Cauchy matrix. Kinematic coupling and consistent transfer of forces and moments are enforced through constraint fields that admit a systematic static condensation. Eliminating beam and coupling degrees of freedom yields an equivalent second-gradient continuum, which accurately reproduces the fully resolved beam-matrix response at significantly reduced computational cost.

The second part develops a continuous higher-order multi-scale formulation based on dimension expansion. A generalized macroscopic continuum is expanded with a microscopic fluctuation field via a Taylor expansion of the macroscopic deformation on the product domain and an energetically consistent averaging procedure. This leads to a higher-order macroscopic problem whose stresses are obtained from the microstructure, while microscopic fluctuation fields satisfy vanishing average conditions. A generalized solution scheme employing null-space reduction condenses micro-scale fluctuations at the RVE level, unifying monolithic and staggered coupling strategies. As a special case, the classical FE^2 method is recovered from the proposed framework by a deliberate choice of approximation space and a specific solution strategy. Numerical examples in one, two, and three dimensions demonstrate that the proposed frameworks robustly capture fiber-induced stiffness, curvature-driven size effects and non-local behavior, establishing a coherent and efficient toolbox for the analysis of microstructured materials.

Kurzfassung

Die vorliegende Arbeit befasst sich mit der Modellierung und Simulation mikrostrukturierter und faserverstärkter Materialien, für die klassische Erstgradienten-Kontinua (Cauchy) weder biegedominierte Mechanismen, noch Größeneffekte oder nichtlokale Wechselwirkungen adäquat erfassen können, während voll aufgelöste dreidimensionale Mikrostrukturanalysen rechnerisch kaum handhabbar sind. Es werden zwei komplementäre höhergradige Kontinuumsansätze entwickelt, die beide in ein isogeometrisches Analysegerüst eingebettet werden, um die für höhergradige Felder erforderliche Kontinuität bereitzustellen.

Im ersten Teil werden Kontinuumsmodelle für eingebettete schlanke Verstärkungen formuliert. Zunächst wird ein dreidimensionales Zweitgradienten-Materialmodell vorgeschlagen, in dem Faserfamilien durch Richtungsfelder beschrieben werden, denen Dehnungs-, Scher-, Krümmungs- und Torsionsmaße zugeordnet sind. Diese kinematischen Maße werden mit energetisch konjugierten höhergradigen Spannungen verknüpft und mittels spline-basierter, C^1-stetiger Diskretisierungen implementiert. Ergänzend wird ein diskreter Ansatz verfolgt, bei dem die geometrisch exakte Cosserat-Balkenformulierung im finiten Deformationsbereich in eine überlappende dreidimensionale Cauchy-Matrix eingebettet wird. Kinematische Kopplung sowie konsistente Übertragung von Kräften und Momenten werden durch Zwangsfelder sichergestellt, die eine systematische statische Kondensation ermöglichen. Durch Eliminierung von Freiheitsgraden der Balken und Kopplungen ergibt sich ein effektives Zweitgradienten-Kontinuum, das das vollständig aufgelöste Balken-Matrix-Verhalten bei deutlich reduzierten Rechenkosten präzise abbildet.

Im zweiten Teil wird eine kontinuierliche höhergradige Multiskalenformulierung auf Basis einer Dimensionserweiterung entwickelt. Ein generalisiertes makroskopisches Kontinuum wird über eine Taylor-Entwicklung der makroskopischen Deformation um Fluktuationen der Mikrostruktur auf den Produktraum von Makro- und Mikrodeformation erweitert. Basierend auf konsistenter energetischer Mittelung über das Mikrogebiet resultiert ein höherordentliches gekoppeltes Problem, bei dem makroskopische Spannungen sich aus der Mikrostruktur ableiten, während Fluktuationsfelder sowohl verschwindende Mittelwerte als auch das Gleichgewicht der Mikroskala erfüllen. Ein verallgemeinertes Lösungsverfahren auf Basis einer Nullraumreduktion ermöglicht die Kondensation mikroskopischer Fluktuationen auf RVE-Ebene und vereinheitlicht monolithische und gestaffelte Lösungsstrategien. Als Spezialfall mit bewusst gewähltem Ansatzraum sowie spezifischer Lösungsumsetzung geht so das klassische FE^2 als Spezialfall aus dem präsentierten Konzept hervor. Numerische Beispiele in ein-, zwei- und dreidimensionalen Einstellungen zeigen, dass die entwickelten Ansätze faserinduzierte Steifigkeit, krümmungsgetriebene Größeneffekte und nichtlokales Materialverhalten robust erfassen und so ein konsistentes und effizientes Werkzeug zur Analyse mikrostrukturierter Materialien bereitstellen.

Acknowledgements

I would like to express my sincere gratitude to my advisor Prof. Dr. Christian Hesch for the continuous guidance, trust, and intellectual freedom throughout this work. Your rigorous feedback, high standards and steady support shaped both the technical depth and the clarity of this dissertation, and I am grateful for the many discussions that helped sharpen the ideas beyond what I could have achieved on my own.

I also thank the members of my examination board, chairman Prof. Dr. Oliver Nelles, Prof. Dr. Kerstin Weinberg and co-referee Prof. Dr. Fadi Aldakheel for taking the time to review this thesis. I also gratefully acknowledge all other collaborators across the publications associated with this dissertation for their valuable contributions, insightful discussions, and continued support. I further acknowledge the opportunity to use the OMNI cluster at the University of Siegen, which enabled the large-scale simulations presented here, as well as the assistance and advice of the ZIMT HPC support team.

My appreciation extends to all researchers, including my current and former colleagues, Ashwin, Erhan, Stefan, Jonathan, Melanie and Maik, for the productive collaboration, the shared problem-solving and for creating an atmosphere in which I consistently felt part of a supportive community and of something genuinely meaningful. The working environment benefited greatly from your competence, openness and willingness to discuss everything and for sharing the small moments of humor along the way, from MATLAB quirks to C++ edge cases and the occasional numerical oddity. Special thanks go to Annika and Harald for their indispensable help in keeping day-to-day matters running smoothly, through organizational support and by offering an open ear when it was needed. I also thank the "canteen group" for the regular breaks that combined a healthy walk, lunch, honest conversations and humor that helped sustain focus and motivation over the long run.

I am equally grateful to my friends and family for their patience and encouragement throughout this demanding period. Thank you for understanding the phases when deadlines dominated and for providing stability, perspective and energy when it mattered most.

Above all, I want to thank Kirsten. Your support carried me through the difficult stretches of stress, doubt and long working hours. You were always patient and believed in me and I am deeply grateful to have you in my life. This dissertation would not exist in its present form without you.

Siegen, March 6, 2026 Felix Schmidt

Publications

This thesis is based on the following works, which were published up to completion of this thesis and prepared in collaboration with one or more co-authors.

[33] M. Dittmann et al. “A strain-gradient formulation for fiber reinforced polymers: hybrid phase-field model for porous-ductile fracture”. In: *Computational Mechanics* 67.6 (June 2021), pp. 1747–1768

[64] U. Khristenko et al. “Multidimensional coupling: A variationally consistent approach to fiber-reinforced materials”. In: *Computer Methods in Applied Mechanics and Engineering* 382 (Aug. 2021), p. 113869

[100] F. Schmidt et al. “Computational homogenization of higher-order continua”. In: *International Journal for Numerical Methods in Engineering* 123.11 (June 15, 2022), pp. 2499–2529

[99] F. Schmidt et al. “Numerical Homogenisation of Gradient Materials”. en. In: *Advanced Structured Materials*. Cham: Springer International Publishing, 2022, pp. 487–503

[57] C. Hesch et al. “Variational formulation and monolithic solution of computational homogenization methods”. In: *International Journal for Numerical Methods in Engineering* 125.20 (Oct. 30, 2024)

The author of this thesis contributed fundamental aspects with regard to theoretical outline, implementation, conducting the simulations and writing the articles.

Contents

List of Figures xiii

List of Tables xv

0 Notation and conventions 1
- 0.1 Sets and spaces . . . 1
- 0.2 Tensors . . . 4
- 0.3 Functions and function spaces . . . 8

1 Introduction 13
- 1.1 Motivation . . . 13
- 1.2 Higher-order continua and dimension-reduced coupling . . . 14
- 1.3 Multi-scale method . . . 15
- 1.4 Organization of the work . . . 17

2 Fundamentals of Isogeometric Analysis 19
- 2.1 Functional representation . . . 19
- 2.2 Geometric representation . . . 25
- 2.3 Parametric adjustments . . . 29
- 2.A Appendix A . . . 32

3 Second-order Continuum Mechanics 33
- 3.1 Configuration and kinematics . . . 34
- 3.2 Constitutive Framework and variational formulation . . . 37
- 3.3 Conservation Properties and Noether's Theorem . . . 42
- 3.4 Second-order boundary value problem . . . 51
- 3.5 Discretization and solution . . . 52
- 3.6 Mixed modes and constrained systems . . . 55
- 3.A Appendix A . . . 58

4 Continuous embedded fibers 61
- 4.1 Fiber kinematic . . . 61
- 4.2 Energetic response . . . 63
- 4.3 Numerical examples . . . 65

5 Dimension reduction: Discrete embedded fibers 73
- 5.1 Beam kinematic . . . 73
- 5.2 Energetic response . . . 75

5.3 Coupling constraints 78
5.4 Condensed system and second gradient model 83
5.5 Discrete multidimensional coupling model 88
5.6 Numerical investigation 92
5.A Appendix A 99

6 Dimension expansion: Continuous higher-order multi-scale method 103
6.1 Macroscopic boundary value problem 103
6.2 Microscopic continuum 105
6.3 Variational formulation 109
6.4 Discrete setting 113
6.5 Solution of the multi-scale problem 118
6.6 Numerical experiments 123
6.A Appendix A 144

7 Summary and outlook 147
7.1 Summary of the work 147
7.2 Outlook 150

Bibliography 151

List of Figures

2.1.1 1D basis functions. . . . 21
2.1.2 2D basis functions. . . . 22
2.1.3 Linear Lagrange basis functions. . . . 23
2.2.1 2D curve. . . . 26
2.2.2 2D surface. . . . 26

3.1.1 Generalized continuum: kinematics. . . . 36

4.1.1 Continuous fiber kinematic. . . . 62
4.3.1 Two-point bending test: setup. . . . 66
4.3.2 Two-point bending test: deflection. . . . 67
4.3.3 Two-point bending test: stresses. . . . 68
4.3.4 Clamped bending test: setup. . . . 68
4.3.5 Clamped bending test: deflection. . . . 69
4.3.6 Clamped bending test: stresses. . . . 70
4.3.7 Tensile test: setup. . . . 70
4.3.8 Tensile test: deflection. . . . 71
4.3.9 Tensile test: resistance. . . . 71
4.3.10 Tensile test: stresses. . . . 72

5.3.1 Coupled matrix-beam system. . . . 78
5.3.2 3D beam kinematic. . . . 79
5.6.1 Matrix-beam bending test: setup. . . . 92
5.6.2 Matrix-beam bending test: results. . . . 93
5.6.3 Matrix-beam bending test: convergence. . . . 94
5.6.4 Matrix-beam bending test: analysis. . . . 94
5.6.5 Matrix-beam torsion test: results. . . . 96
5.6.6 Matrix-beam torsion test: analysis. . . . 96
5.6.7 Matrix-beam shear test: results. . . . 97
5.6.8 Multiple beams: results. . . . 98

6.0.1 Continuous micro-scale expansion scheme. . . . 104
6.2.1 Micro-scale BVP: periodicity. . . . 107
6.6.1 First-order homogeneous RVE: setup. . . . 124
6.6.2 Second-order homogeneous RVE: results. . . . 127
6.6.3 Inhomogeneous second-order RVE: setup. . . . 129
6.6.4 Inhomogeneous second-order RVE: results. . . . 131
6.6.5 Inhomogeneous second-order RVE: fiber deformation. . . . 132

6.6.6 Inhomogeneous second-order RVE: 2D setup. 132
6.6.7 Unit cell comparison: results. 134
6.6.8 Unit cell comparison: homogenization. 135
6.6.9 Continuous 1D multi-scale test: setup. 135
6.6.10 Continuous 1D multi-scale test: accuracy. 137
6.6.11 Multi-scale test: Cook's Membrane. 138
6.6.12 2D multi-scale test: stress. 139
6.6.13 3D higher-order multi-scale: results. 142
6.A.1 First order homogeneous RVE: results. 145

List of Tables

2.3.1 Multi-grid algorithm. 31
2.A.1 2D surface: control points. 32

5.6.1 Matrix-beam bending test: accuracy. 95

6.4.1 Computational multi-scale algorithm. 119
6.6.1 First-order homogeneous RVE: accuracy. 126
6.6.2 Second-order homogeneous RVE: Material. 128
6.6.3 Second-order homogeneous RVE: higher-order contributions. 129
6.6.4 Second-order homogeneous RVE: higher-order contributions. 130
6.6.5 Continuous 2D multi-scale test: performance. 139
6.6.6 Continuous 2D multi-scale test: convergence. 140
6.6.7 3D higher-order multi-scale: performance. 143

0 Notation and conventions

0.1 Sets and spaces

0.1.1 Sets and set operations

First, we introduce some basic sets denoted by the common descriptors, with the empty set $\emptyset$, the set of integers $\mathbb{Z}$, the set of natural numbers $\mathbb{N}$ without and $\mathbb{N}_0$ with zero and the set of real numbers $\mathbb{R}$. Given a subset Ω of a topological space M, $\partial\Omega$ is its boundary, $\bar{\Omega}$ its closure and Ω° its interior. Moreover, the union of two sets is symbolized with $\cup$, whereas the intersection is denoted as $\cap$. Elements of a topological space are called points. If for the set M there exists a distance function between elements of a set $d\colon M \times M \to \mathbb{R}_0^+$, along with symmetry $d(x,y) = d(y,x)$ and triangle inequality $d(x,z) \leq d(x,y) + d(y,z)$ with $x, y, z \in M$, the function d is called metric and the ordered pair (M,d) is called metric space. A metric space is complete, if every Cauchy sequence in M converges to a limit, where in a Cauchy sequence $x_1, x_2, x_3, \cdots \in M$ for every positive real number $r \in \mathbb{R}^+$ a positive integer $N \in \mathbb{N}^+$ exists such that for all natural numbers $m, n > N$ follows $d(x_m, x_n) < r$. The product space is the Cartesian product of a family of spaces, where $M \coloneqq \prod_{i=1}^{d} M_i = M_1 \times M_2 \times \cdots \times M_d = \{(m_1, m_2, \ldots, m_d) | m_i \in M_i\}$ as the set of ordered pairs $(m_1, m_2, \ldots, m_d)$. For any multi-index $\boldsymbol{m} = (m_1, \ldots, m_d) \in \mathbb{N}_0^d$ we define its length by $|\boldsymbol{m}| \coloneqq m_1 + \cdots + m_d$ and its factorial by $\boldsymbol{m}! \coloneqq m_1! \ldots m_d!$. Given $\boldsymbol{m}, \boldsymbol{n} \in \mathbb{N}_0^d$ we write $\boldsymbol{m} \leq \boldsymbol{n}$ (resp. $\boldsymbol{m} < \boldsymbol{n}$) if $m_j \leq n_j$ (respectively $m_j < n_j$) for every $j = 1, \ldots, d$. Conducting the product of same sets with $M_i = M$, also called $d-$tuple or described as product of d copies of M, results in $M^d = \prod_{i=1}^{d} M$, where d is the dimension of M^d, denoted as $dim(M^d) = d$. An example is the real coordinate space $\mathbb{R}^n$, with $\mathbb{R}^2$ as the two-dimensional real coordinate plane and $\mathbb{R}^3$ the space of three-dimensional real coordinates.

A group is a special set which has an identity element and every element S is invertible. The identity element does not change any other element when an operation is applied. If an operation of two elements results in an identity element, the first is a left inverse of the second and the second the right inverse of the first element. Additionally it requires for its elements $S \times S \mapsto S$ and associativity. In associativity, the organization of operations, often implied by brackets, does not change the result if the sequence of operations is maintained, whereas with commutativity also changing the sequence does not change the result. If the group is a differential manifold, with multiplication and inverting being differentiable, it is called a Lie group.

0.1.2 Matrix space

For a field F, a matrix is a two-dimensional array whose entries are elements of F. Moreover, let $\mathbb{F}_{n,m} \coloneqq \{\boldsymbol{A} | \boldsymbol{A} \in \mathbb{R}^{m \times n}\}$ be the set of all $m \times n$ matrices with m entries in the first dimension and n entries in the second dimension. For any $\boldsymbol{A} \in \mathbb{F}_{n,m}$, the components are accessed by $[\boldsymbol{A}]_{ij} = A_{ij}$ with $1 \leq i \leq m, 1 \leq j \leq n$. The matrix product $\boldsymbol{C} = \boldsymbol{AB}$ of two matrices $\boldsymbol{A}^{m \times n}$ and $\boldsymbol{B}^{n \times o}$ is conducted using components by $[\boldsymbol{C}]_{ij} = [\boldsymbol{AB}]_{ij} = \sum_{k=1}^{n} A_{ik} B_{kj}$ and thus results in a $m \times o$ matrix and demands compatible sizes. Given arbitrary $p \times q$ matrix $\boldsymbol{B}$, its transpose is defined as $[\boldsymbol{B}^{\top}]_{ij} = [\boldsymbol{B}]_{ji}$. For a $m \times m$ matrix $\boldsymbol{A}$, referred to as a square matrix, we make use of the trace operator $\mathrm{tr}(\boldsymbol{A}) = A_{ii}$ and, if existent, define its inverse $\boldsymbol{A}^{-1}$ through the relationship $\boldsymbol{A}^{-1}\boldsymbol{A} = \boldsymbol{A}\boldsymbol{A}^{-1} = \boldsymbol{I}$. Here, we make use of the Einstein summation convention, denoting for repeated indices to be summarized over the range of that index, like $a_i b_i$ is conventionally short for $\sum_{i=1}^{d} a_i b_i = a_1 b_1 + a_2 b_2 + \cdots + a_d b_d$. Further in this context, $\boldsymbol{I}$ is the $m \times m$ identity matrix, defined as $[\boldsymbol{I}]_{ij} = \delta_{ij}$, where we introduced the Kronecker delta defined as

$$\delta_{ij} = \begin{cases} 1, & \text{if } i = j \\ 0, & \text{otherwise} \end{cases} . \tag{0.1}$$

The set of invertible $n \times n$ matrices over the field F along with matrix multiplication forms a general linear group of $\mathrm{GL}(n, F)$. For square matrices we can derive further properties. The determinant $\det(\boldsymbol{A})$ of matrix $\boldsymbol{A}$ is a scalar valued function, characterizing features in context of linear maps, see next paragraph. There exist various formulations for specific squared matrices (e.g. Lang [73]). For the 3×3 case a general form is given by

$$\begin{aligned} \det\left(\begin{bmatrix} A_{11} A_{12} A_{13} \\ A_{21} A_{22} A_{23} \\ A_{31} A_{32} A_{33} \end{bmatrix}\right) &= A_{11} A_{22} A_{33} + A_{12} A_{23} A_{31} + A_{13} A_{21} A_{32} \\ &\quad - A_{13} A_{22} A_{31} - A_{12} A_{21} A_{33} - A_{11} A_{23} A_{32} \,. \end{aligned} \tag{0.2}$$

Here, we introduce the Levi-Civita symbol

$$\varepsilon_{ijk} = \begin{cases} 1, & \text{if even permutation,} \\ -1, & \text{if odd permutation,} \\ 0, & \text{otherwise} \end{cases} \tag{0.3}$$

for which immediately follows the set of identities

$$\begin{aligned} \varepsilon_{ijk} &= \varepsilon_{kij} = -\varepsilon_{jik} = -\varepsilon_{ikj} = -\varepsilon_{kji} \\ \varepsilon_{ijk}\, \varepsilon_{kln} &= \delta_{il}\delta_{jn} - \delta_{in}\delta_{jl} \\ \varepsilon_{ijk}\, \varepsilon_{ijn} &= 2\delta_{kn} \\ \varepsilon_{ijk}\, \varepsilon_{ijk} &= 6 \,. \end{aligned} \tag{0.4}$$

Applied to the determinant we get

$$\det(\boldsymbol{A}) = \varepsilon_{ijk} A_{1i}\, A_{2j}\, A_{3k} = \frac{1}{6} \varepsilon_{ijk}\, \varepsilon_{pqr} A_{ip}\, A_{jq}\, A_{kr} \,. \tag{0.5}$$

If the matrix $\boldsymbol{A}$ is invertible, $\det(\boldsymbol{A}) \neq 0$ and thus $\boldsymbol{A}$ non-singular. Moreover, the matrix is called orthogonal, if $\boldsymbol{A}^\top = \boldsymbol{A}^{-1}$. Further, any $d \times d$ matrix $\boldsymbol{B} \in \mathrm{Sym}_d$ is called symmetric, if $\boldsymbol{B}^\top = \boldsymbol{B}$ with the space of symmetric matrices Sym_d. Skew-symmetry is given, if for $\boldsymbol{B} \in \mathrm{Skew}_d$ holds $\boldsymbol{B}^\top = -\boldsymbol{B}$ with the space of skew-symmetric matrices Skew_d. A given $d \times d$ matrix $\boldsymbol{C}$ can then be decomposed into skew and symmetric parts using

$$\boldsymbol{C} = \underbrace{\frac{1}{2}\left(\boldsymbol{C} - \boldsymbol{C}^\top\right)}_{\in \mathrm{Skew}_d} + \underbrace{\frac{1}{2}\left(\boldsymbol{C} + \boldsymbol{C}^\top\right)}_{\in \mathrm{Sym}_d} . \tag{0.6}$$

Additionally, for double concatenation of two matrices $\boldsymbol{A} \in \mathrm{Sym}_d$ and $\boldsymbol{B} \in \mathrm{Skew}_d$ follows $\boldsymbol{A} : \boldsymbol{B} = \boldsymbol{A}^\top : \boldsymbol{B}^\top = -\boldsymbol{A} : \boldsymbol{B} = 0$.

0.1.3 Vector spaces

Given field R, the non-empty set V is a vector space, also called linear space, over R, if therein certain conditions apply for addition of elements of V, called vectors, and the multiplication with elements of R, called scalars. These conditions include, among others, associativity and commutativity. Relating elements of one vector space to another $V \mapsto X$ is called a map. A structure preserving map from one structure to another is called a morphism. Here, the structures are vector spaces V_1 and V_2, thus if the properties of vector addition and scalar multiplication are preserved, the map is a linear transformation and called vector space homomorphism. If the linear map $V_1 \mapsto V_2$ is bijective, i.e. has a one to one relationship between both spaces and additionally is invertible, the mapping is called an isomorphism. If additionally the structure is mapped onto itself, the mapping is called an automorphism. Multi-linear maps are linear in all its arguments, e.g. a bilinear map $V \times W \mapsto X$ for vector spaces V, W, X is linear in both arguments V and W. For example, a $m \times n$ matrix in $\mathbb{R}$ resembles the linear map $\mathbb{R}^n \mapsto \mathbb{R}^m$, mapping vectors in $\mathbb{R}^n$ to vectors in $\mathbb{R}^m$. Moreover, for diffeomorphisms additionally the mapping itself and its inverse are continuously differentiable. For a vector space V, its dual space V^* is the set of all linear maps $\varphi \colon V \to R$ marked with an asterisk superscript. A vector $\boldsymbol{w} \in \mathbb{R}^n$ is called zero-vector, if $w_i = 0, \forall i \in 1, \ldots, n$ and writing as $\boldsymbol{w} = \boldsymbol{0}$.

A complete normed vector space V over field K, e.g. $K = \mathbb{R}$, where the norm $\|(\cdot)\|$ is a map of $V \mapsto \mathbb{R}_0^+$, is called a Banach space. The norm satisfies certain conditions for, i.e. non-negativity $\forall x \in V, \|x\| \geq 0$, positive definiteness that $\|x\| = 0$ only if $\boldsymbol{x} = \boldsymbol{0}$, absolute homogeneity $\|a\boldsymbol{x}\| = |a|\|\boldsymbol{x}\|$ and the triangle inequality $\|\boldsymbol{x}\| + \|\boldsymbol{y}\| \geq \|\boldsymbol{x} + \boldsymbol{y}\|$, where $x, y \in V$ and $a \in K$. Using the p-norm $\|\boldsymbol{x}\|_p := (\sum_{i=1}^n \mid x_i \mid^p)^{1/p}$ for finite-dimensional spaces, where $p \in \mathbb{R}, p \geq 0$, we denote the class of L^p spaces, also called Lebesgue spaces.

If a vector space over field R has an inner product of the form $\langle (\cdot), (\cdot) \rangle \colon V \times V \to R$, along with symmetry, linearity properties and positive definiteness, the vector space is called inner product space. A prominent example for inner product spaces are Hilbert spaces $\mathcal{H}$, where the inner product induces a norm as distance function and is thus a complete metric space and a Banach space. One of its members is the Euclidean vector space, which is

a finite-dimensional inner product space over the real numbers $\mathbb{R}$. The dot product for a $\mathbb{R}^n$ Euclidean space is an inner product and bilinear map, denoting $\langle \boldsymbol{u}, \boldsymbol{v} \rangle = \sum_{i=1}^{n} u_i v_i$, where $\boldsymbol{u}, \boldsymbol{v} \in \mathbb{R}^n$, which is further used to define the norm of a vector $\boldsymbol{u} \in \mathbb{R}^n$ in the form $\|\boldsymbol{u}\| \coloneqq \sqrt{\langle \boldsymbol{u}, \boldsymbol{u} \rangle} = \sqrt{\sum_{i=1}^{n} u_i^2}$, which is equivalent to the L^2-norm.

0.2 Tensors

0.2.1 Basis

In order to define objects consisting of multiple vector spaces, so called tensors, we establish the basis of a vector space. The subset B of vector space V over a field R is a basis of V, if B is a linearly independent subset of V and spans V, i.e. the span of B as the set of all linear combinations $\mathrm{span}(B) = \{a_1 \boldsymbol{w}_1 + a_2 \boldsymbol{w}_2 + \cdots + a_n \boldsymbol{w}_n \mid a_1, \ldots, a_n \in R \ , \ \boldsymbol{w}_1, \ldots, \boldsymbol{w}_n \in V\}$. It can be used to express every vector $\boldsymbol{f} \in V$ in the form $\boldsymbol{f} = \sum_{i=1}^{n} a_i \boldsymbol{w}_i$. Therein, $a_i \in R$ are scalar coefficients and $\boldsymbol{w}_i \in B$ basis vectors, thus also writing B^w. The number of basis vectors is the dimension of the vector space, thus for a vector space K^n over field K follows $\dim(K^n) = n$ due to the construction using the cartesian product. The basis $\{e_i\} \in \mathbb{R}^3$ is called orthonormal, if it holds $\boldsymbol{e}_i \cdot \boldsymbol{e}_j = \delta_{ij}$, with $i, j = 1, 2, 3$.

With given basis B and a dual set B^* existing in the dual space V^* it holds

$$\boldsymbol{v}^i \cdot \boldsymbol{v}_j = \delta^i{}_j \,, \quad \text{with} \quad \boldsymbol{v}^i \in B^* \,, \quad \boldsymbol{v}_j \in B \,, \tag{0.7}$$

implying the same index set for both basis sets. If additionally B^* spans V^*, i.e. the span of B^* the dual set B^* is called a dual basis. When working with both types of bases along with corresponding coefficients, we distinguish between these by positioning the indices. Assuming the vector space $\mathbb{R}^n$ with basis E and dual basis E^*, we can describe a vector $\boldsymbol{x} \in \mathbb{R}^n$ in E

$$\boldsymbol{x} = \sum_{i=1}^{n} x^i \boldsymbol{e}_i \,, \quad \text{with} \quad x^i \in \mathbb{R} \,, \quad \boldsymbol{e}_i \in E \tag{0.8}$$

as well as a covector $\boldsymbol{x}^\flat$ in E^*

$$\boldsymbol{x}^\flat = \sum_{i=1}^{n} x_i \boldsymbol{e}^i \,, \quad \text{with} \quad x_i \in \mathbb{R} \,, \quad \boldsymbol{e}^i \in E^* \,. \tag{0.9}$$

For both bases, we define their corresponding metric using the inner product $\boldsymbol{g}_{ij} = \boldsymbol{e}_i \cdot \boldsymbol{e}_j$ (covariant metric components) and $\boldsymbol{g}^{ij} = \boldsymbol{e}^i \cdot \boldsymbol{e}^j$ (contravariant metric components). Given $\boldsymbol{v}^i \cdot \boldsymbol{v}_j = g(\boldsymbol{v}^i, \boldsymbol{v}_j) = \delta^i{}_j$ makes $(\boldsymbol{v}^i)$ the reciprocal basis to $(\boldsymbol{v}^i)$ with corresponding coordinates $x_i = \boldsymbol{g}_{ij} x^j$. Using further $\boldsymbol{g}^{ik} \boldsymbol{g}_{kj} = \delta_{ij}$, it follows $\boldsymbol{x} = x^i \boldsymbol{e}_i = \boldsymbol{g}^{ki} x_i \boldsymbol{g}_{jk} \boldsymbol{e}^j = x_i \boldsymbol{e}^i$. Note, that for an orthonormal basis, i.e. $\boldsymbol{e}_i \cdot \boldsymbol{e}_j = \delta_{ij}$ follows $\boldsymbol{e}^i = \boldsymbol{e}_i$.

For a vector $\boldsymbol{u} = u^i \boldsymbol{e}_i$, the coefficient u^i is contravariant to the corresponding basis vector $\{\boldsymbol{e}_i\} \in \mathbb{R}^3$, marking the vector as tangent vector. Using the dual basis $\{e^i\} \in \mathbb{R}^3$, the cotangent vector $\boldsymbol{v} = v_i \boldsymbol{e}^i$ is composed of the covariant coefficient v_i.

0.2.2 Tensor product space

Pairing the elements of two vector spaces, $\boldsymbol{u} \in U$ and $\boldsymbol{v} \in V$, over a field R to a new vector space $U \otimes V$ via the bilinear map $U \times V \mapsto U \otimes V$ creates the new vector space $U \otimes V$, called tensor product space, where the symbol $\otimes$ denotes the tensor product and $\boldsymbol{u} \otimes \boldsymbol{v}$ its elements. If $\{\boldsymbol{u}_i\} \in U$ and $\{\boldsymbol{v}_j\} \in V$ form respective bases B^u and B^v, their tensor product forms the basis for elements of the tensor product space $\boldsymbol{C} \in U \otimes V$. Taking $U = \mathbb{R}^m$ and $V = \mathbb{R}^n$, the corresponding tensor product space is denoted as $U \otimes V = \mathbb{R}^{m \times n}$. Using the span property, we write

$$\boldsymbol{C} = \left(\sum_{i=1}^{m} u^i \boldsymbol{u}_i\right) \otimes \left(\sum_{j=1}^{n} v^j \boldsymbol{v}_j\right) = \sum_{i=1}^{m}\sum_{j=1}^{n} \left[u^i v^j\right]\ \boldsymbol{u}_i \otimes \boldsymbol{v}_j = \left[u^i v^j\right]\ \boldsymbol{u}_i \otimes \boldsymbol{v}_j = C^{ij}\ \boldsymbol{u}_i \otimes \boldsymbol{v}_j\ , \tag{0.10}$$

with coefficient array C^{ij}. Note, that the index order of the coefficients implies the order of the basis tensor product.

With given finite set of p copies of vector space V and q copies of the dual vector space $V*$, the tensor product $V \otimes V \otimes \cdots \otimes V^* \otimes V^*$ is a vector space with the bilinear map

$$\underbrace{V \times \cdots \times V}_{p\text{-times}} \times \overbrace{V^* \times \cdots \times V^*}^{q\text{-times}} \mapsto V \otimes \cdots \otimes V \otimes V^* \otimes \cdots \otimes V^*$$
$$= \left\{(\boldsymbol{v}_1 \otimes \cdots \otimes \boldsymbol{v}_p \otimes \boldsymbol{v}^1 \otimes \cdots \otimes \boldsymbol{v}^q \,|\, \boldsymbol{v}_i \in V\ ,\ \boldsymbol{v}^j \in V^*\right\}\ . \tag{0.11}$$

Its elements $\boldsymbol{T}$ are called tensors of type (p, q) and of order $n = p + q$. Using the basis representation $\boldsymbol{v_1} = v^1\boldsymbol{e}_1\ ,\ \boldsymbol{v_2} = v^2\boldsymbol{e}_2\ ,\ \ldots$ and $\boldsymbol{v^1} = v_1\boldsymbol{v}^1\ ,\ \boldsymbol{v}^2 = v_2\boldsymbol{e}^3\ ,\ \ldots$, we write

$$\boldsymbol{T} = v^i\boldsymbol{e}_i \otimes v^j\boldsymbol{e}_j \otimes \cdots \otimes v_k\boldsymbol{e}^k \otimes v_l\boldsymbol{e}^l \otimes \cdots = T^{ij\ldots}{}_{kl\ldots}\ \boldsymbol{e}_i \otimes \boldsymbol{e}_j \otimes \cdots \otimes \boldsymbol{e}^k \otimes \boldsymbol{e}^l \otimes \cdots\ . \tag{0.12}$$

The term *dyadics* or *dyads* in this work refers to tensors obtained by the tensor product. When combining standard and dual bases, the resulting tensor is called mixed variant.

Given a standard basis, any linear map can be expressed by a matrix. For two linear maps $f\colon V \to W$ and $g\colon X \to Y$ for vector spaces V, W, X, Y, with $f(\boldsymbol{v}) = \boldsymbol{w} = \boldsymbol{A}\boldsymbol{v}$ and $g(\boldsymbol{x}) = \boldsymbol{y} = \boldsymbol{B}\boldsymbol{x}$, the Kronecker product denoted by $\otimes$ gives the matrix of the tensor product. Therefore, tensors can be interpreted as an extension of the matrix concept towards infinite order, such that a tensor is a multidimensional array, whose components are the coefficients that are associated with a basis. Here, the dimension of the array corresponds to the order of the tensor. Regarding elements of tensors and matrices, we use the same notation, thus addressing the entries of the coefficient matrix. From first order up to higher order, tensors are generally marked in bold letters or symbols, e.g. $\boldsymbol{A}$, third order tensors in bold Fraktur letters, e.g. $\mathfrak{A}$, whereas their respective components are marked as the plain symbol with the index subscript or superscript. Alternatively we use square brackets around the tensor and put the index as subscript to it, e.g. $\left[\mathfrak{A}\right]_{ijk}$.

The definition of tensors gives rise to the application of the transpose in terms of reordering the tensor product, i.e. for a tensor $\boldsymbol{C}$ represented as the tensor product of $\boldsymbol{a} = u^i \boldsymbol{u}_i$ and $\boldsymbol{b} = v^j \boldsymbol{v}_j$ follows

$$\boldsymbol{C} = (\boldsymbol{b} \otimes \boldsymbol{a})^\top = \boldsymbol{a} \otimes \boldsymbol{b}\,, \tag{0.13}$$

or alternatively using the coefficient matrix $C_{ij} = u_i v_i$ and basis vectors

$$\boldsymbol{C} = \left(C^{ji} \boldsymbol{v}_j \otimes \boldsymbol{u}_i\right)^\top = C^{ij} \boldsymbol{u}_i \otimes \boldsymbol{v}_j. \tag{0.14}$$

In contrast to second order tensors, the transposition for tensors of order $n > 2$ requires further information about rearranged order in terms of the indices representing the respective basis to be shifted. Therefore we define the transpose $(\cdot)^{\top\alpha\beta}$, where $\alpha\beta \in \{1, \ldots, n | \alpha \neq \beta\}$, e.g.

$$\left[\boldsymbol{C}\right]_{ij} = \left[\left[\boldsymbol{C}\right]_{ji}\right]^{\top 12}, \quad \left[\boldsymbol{\mathfrak{C}}\right]_{ijk} = \left[\left[\boldsymbol{\mathfrak{C}}\right]_{jik}\right]^{\top 12}, \quad \left[\boldsymbol{\mathcal{C}}\right]_{ijkl} = \left[\left[\boldsymbol{\mathcal{C}}\right]_{ilkj}\right]^{\top 24}. \tag{0.15}$$

0.2.3 Basic tensor operations

For the scalar product in terms of the dot product of two vectors $[\boldsymbol{a} \cdot \boldsymbol{b}] = a_i\, b_i$, the dot product of a vector $\boldsymbol{f}$ and a second order tensors $\boldsymbol{G} = \boldsymbol{a} \otimes \boldsymbol{b}$, as well as the double dot product of two second order tensors $\boldsymbol{G}$ and $\boldsymbol{H} = \boldsymbol{c} \otimes \boldsymbol{d}$ hold

$$\begin{aligned} \boldsymbol{f} \cdot \boldsymbol{G} &= \boldsymbol{f} \cdot (\boldsymbol{a} \otimes \boldsymbol{b}) \\ &= (\boldsymbol{f} \cdot \boldsymbol{a}) \boldsymbol{b} \end{aligned} \tag{0.16}$$

and

$$\begin{aligned} \boldsymbol{F} : \boldsymbol{G} &= (\boldsymbol{a} \otimes \boldsymbol{b}) : (\boldsymbol{c} \otimes \boldsymbol{d}) \\ &= \boldsymbol{c} \cdot (\boldsymbol{a} \otimes \boldsymbol{b}) \cdot \boldsymbol{d} \end{aligned} \tag{0.17}$$

Formally, for a given basis we write for the dot product of two vectors and the double dot product of two second order tensors and the triple dot product of two third order tensors, we write

$$[\boldsymbol{a} \cdot \boldsymbol{b}] = a_i\, b_i \quad \text{and} \quad [\boldsymbol{A} : \boldsymbol{B}] = A_{ij}\, B_{ij} \quad \text{and} \quad [\boldsymbol{A} \vdots \boldsymbol{B}] = A_{ijk}\, B_{ijk}\,, \tag{0.18}$$

respectively.

Derived from the Euclidean norm, $\|a\| = \sqrt{a \cdot a}$, we expand the norm notation towards higher order tensors in the form $\|A\| = \sqrt{A : A}$ for second order tensors and $\|\mathfrak{A}\| = \sqrt{\mathfrak{A} \vdots \mathfrak{A}}$ for third order tensors. Moreover, we use the standard notation for multiplication of tensors in the form

$$\left[\boldsymbol{A}\boldsymbol{b}\right]_i = A_{ij}\, b_j\,, \quad \left[\boldsymbol{A}\boldsymbol{B}\right]_{ij} = A_{ik}\, B_{kj}\,, \quad \left[\boldsymbol{\mathfrak{A}} : \boldsymbol{B}\right]_i = A_{ijk}\, B_{jk} \quad \text{and} \quad \left[\boldsymbol{\mathfrak{A}}\boldsymbol{b}\right]_{ij} = A_{ijk}\, b_k. \tag{0.19}$$

Moreover, we introduce the cross product for two vectors $\boldsymbol{a} \in \mathbb{R}^3$ and $\boldsymbol{b} \in \mathbb{R}^3$ in the form $\left[\boldsymbol{c}\right]_i = \left[\boldsymbol{a} \times \boldsymbol{b}\right]_i = \varepsilon_{ijk}\, a_j b_k$. Furthermore, the scalar valued triple product for $\boldsymbol{a}, \boldsymbol{b}, \boldsymbol{c} \in \mathbb{R}^n$ is defined as

$$\varepsilon_{ijk}\, a_i\, b_j\, c_k = \boldsymbol{a} \cdot (\boldsymbol{b} \times \boldsymbol{c}) = \boldsymbol{b} \cdot (\boldsymbol{c} \times \boldsymbol{a}) = \boldsymbol{c} \cdot (\boldsymbol{a} \times \boldsymbol{b})\,. \tag{0.20}$$

Following Bonet et al. [19] and Bonet et al. [18], the cross product formalism is extended to various combinations of first order tensors $\boldsymbol{v}, \boldsymbol{w} \in \mathbb{R}^n$ to second order tensors $\boldsymbol{A}, \boldsymbol{B} \in \mathbb{R}^{n\times n}$, e.g.

$$\Big[\boldsymbol{v}\times\boldsymbol{A}\Big]_{ij} = \varepsilon_{ikl}\, v_k A_{lj}\,, \quad \Big[\boldsymbol{A}\times\boldsymbol{v}\Big]_{ij} = \varepsilon_{jkl}\, A_{ik} v_l \quad \text{and} \quad \Big[\boldsymbol{A} \mathbin{\overset{\times}{\times}} \boldsymbol{B}\Big]_{ij} = \varepsilon_{ikl}\, \varepsilon_{jmn}\, A_{km} B_{ln}\,. \tag{0.21}$$

The three-dimensional vector cross product for can be written using a matrix representation of the first vector $\boldsymbol{a} \times \boldsymbol{b} = [\boldsymbol{a}]_\times \boldsymbol{b}$ with the notation for the spin of a vector

$$\operatorname{spin}(\boldsymbol{a}) = [\boldsymbol{a}]_\times = \begin{bmatrix} 0 & -a_3 & a_2 \\ a_3 & 0 & -a_1 \\ -a_2 & a_1 & 0 \end{bmatrix}, \quad \text{where} \quad \Big[[\boldsymbol{a}]_\times\Big]_{ij} = -\varepsilon_{ijk}\, a_k\,. \tag{0.22}$$

Regarding a second order tensor $\boldsymbol{B}$ we define the axial vector

$$\operatorname{axl}(\boldsymbol{B}) = \frac{1}{2}\begin{bmatrix} B_{32} - B_{23} \\ B_{13} - B_{31} \\ B_{21} - B_{12} \end{bmatrix}, \quad \text{where} \quad \Big[\operatorname{axl}(\boldsymbol{B})\Big]_i = -\frac{1}{2}\varepsilon_{ijk}\Big[B\Big]_{jk}\,, \tag{0.23}$$

such that

$$\operatorname{axl}\Big([\boldsymbol{a}]_\times\Big) = \boldsymbol{a}. \tag{0.24}$$

The spin of a three-dimensional vector is skew-symmetric $[\boldsymbol{a}]_\times \in \mathfrak{so}(3)$ with the vector space of skew-symmetric tensors

$$\mathfrak{so}(3) = \{\boldsymbol{A} \in \mathbb{R}^{3\times 3} \,|\, \boldsymbol{A} + \boldsymbol{A}^\top = \boldsymbol{0}\}\,, \tag{0.25}$$

whose exponential map $\exp\colon \mathfrak{so}(3) \to \mathrm{SO}(3)$ as formal power series with $\exp(\boldsymbol{A}) = \boldsymbol{I} + \sum_{n=1}^{\inf} \boldsymbol{A}^n/n!$ is an element of the special orthogonal group $\mathrm{SO}(3)$, where

$$\mathrm{SO}(3) = \{\boldsymbol{R} \in \mathrm{GL}(3,\mathbb{R}) \,|\, \boldsymbol{R}^\top \boldsymbol{R} = \boldsymbol{R}\,\boldsymbol{R}^\top = \boldsymbol{I},\, \det(\boldsymbol{R}) = 1\}\,, \tag{0.26}$$

where $\boldsymbol{R}$ is a rotation matrix over the three-dimensional Euclidean space.

The eigensystem $E_\lambda := \{\boldsymbol{v} \neq \boldsymbol{0} \mid \boldsymbol{A}\boldsymbol{v} = \lambda\boldsymbol{v}\} \in \mathbb{R}$ is the set of all eigenvectors for the $n \times n$ square matrix and linear operator $\boldsymbol{A}$ on $\mathbb{R}$. Moreover, the set of eigenvectors $\boldsymbol{v} \cup \boldsymbol{0}$ to the same eigenvalue λ is called the corresponding eigenspace. In characteristics, the vector $\boldsymbol{v}$ is stretched but not rotated by $\boldsymbol{A}$ with λ being the stretch-factor. They can be obtained by solving the eigenvalue problem $p(\lambda) = \det(\boldsymbol{A} - \lambda\boldsymbol{I}) = 0$ and subsequently for eigenvalues λ_i obtain their eigenvectors $\boldsymbol{v}_i$ by solving $(\boldsymbol{A} - \lambda_i\boldsymbol{I})\boldsymbol{v}_i = \boldsymbol{0}$. For a $d \times d$ symmetric matrix $\boldsymbol{U}$, the eigenvalue-eigenvector problem of form $\boldsymbol{U}\boldsymbol{Q} = \operatorname{diag}(\lambda_i)\boldsymbol{Q}$, where $\boldsymbol{Q} = (\boldsymbol{n}_i, \ldots, \boldsymbol{n}_d)$ and $\{\boldsymbol{n}_i, \ldots, \boldsymbol{n}_d\}$ forms an orthonormal basis, leads to the spectral decomposition $\boldsymbol{U} = \lambda_i \boldsymbol{n}_i \otimes \boldsymbol{n}_i$.

0.3 Functions and function spaces

0.3.1 Functions

For a function $f\colon X \to Y$, we denote the image of a subset $A \subset X$ under f as $f(A) \coloneqq \{f(x) \mid x \in A\}$, the pre-image of subset $B \subset Y$ under f by $f^{-1}(B) \coloneqq \{x \in X \mid f(x) \in B\}$, the support of f by $\operatorname{supp}(f) \coloneqq \{x \in X \mid f(x) \neq 0\}$, and the restriction of f to A by $f|_A$. As shortened notation for the image of an element $a \in X$ we define $[f(x)]\!]_a \coloneqq f(a)$ and $[f(x)]\!]_a^b \coloneqq f(b) - f(a)$ as the difference of images $b \in X$ and a. The latter is used but not limited to a function $f(s), s \in \{a, b\}$, where $[\![f(s)]\!]_a^b$ marks the difference of its upper to lower bound. A function $f\colon \mathbb{R}^m \supset X \to Y \subset \mathbb{R}$ for the metric spaces X, Y has Lipschitz property, i.e. is *Lipschitz continuous*, if there exists a positive real constant $L > 0$ such that $d(f(x_1), f(x_2)) \leq L\, d(x_1, x_2)\,, \forall\, x_1, x_2 \in X$, which effectively bounds its first derivative. We further describe the limiting behavior of function $f(x)$ using the *Bachmann-Landau notation* $\mathcal{O}(x^2)$ for characterizing its growth.

Given Banach spaces X, Y, and Z, the single-argument maps $g\colon X \to Y$ and $f\colon Y \to Z$ are composed by using the circle operator $f \circ g\colon X \to Z$, $(f \circ g)(x) \coloneqq f(g(x))$, where first g, then f is evaluated. For product spaces, i.e. where $X = \mathrm{L}^2(\Omega)$, $Y = \mathcal{H}^1(\Omega)$ and $Z = \mathbb{R}$, and functions $g\colon X \to Y$ and $f\colon X \times Y \to Z$, the composite mapping $F \coloneqq f \circ (\mathrm{id}, g)$ is written as $F(x) = f(x, g(x))$, where the product map $(\mathrm{id}, g)\colon X \longrightarrow X \times Y$, $x \to (x, g(x))$ with the identity id on X expanding the function input for f.

The function $\mathcal{F}\colon \mathbb{R}^d \to \mathbb{R} \cup \{+\infty\}$ is *coercive*, if $\mathcal{F}(\boldsymbol{u}) \to \infty$ as $\|\boldsymbol{u}\| \to \infty$. Furthermore, $\mathcal{F}$ is *convex*, if for every pair of points $X, Y \in \mathbb{R}$ and every scalar $a \in [0, 1]$ holds $\mathcal{F}((1-a)X + aY) \leq (1-a)\mathcal{F}(X) + \mathcal{F}(Y)$, i.e. the function value of every point between X and Y is smaller or equal to the linear interpolation between these points. For twice differentiable functions this implies its Hessian is positive semi-definite. For *polyconvexity* of function $\mathcal{F}(\boldsymbol{w})$, there must exist a convex function for the set with all minors of $\boldsymbol{w}$.

0.3.2 Differentiation

For a single-argument function $g\colon \mathbb{R} \to \mathbb{R}$, we define its derivative using Leibniz's notation as

$$\frac{\mathrm{d}}{\mathrm{d}x} g(x) = \frac{\mathrm{d}g(x)}{\mathrm{d}x} = \lim_{\varepsilon \to 0} \frac{g(x+\varepsilon) - g(x)}{\varepsilon}. \tag{0.27}$$

For the multi-argument function $f\colon \mathbb{R}^d \to \mathbb{R}$, we use $\partial_i f$ as derivative along the i^{th} coordinate direction $\boldsymbol{e}_i$, where

$$\partial_i f(x) = \frac{\partial f(\boldsymbol{x})}{\partial x_i} = \lim_{\varepsilon \to 0} \frac{f(\boldsymbol{x} + \varepsilon \boldsymbol{e}_i) - f(\boldsymbol{x})}{\varepsilon}\,. \tag{0.28}$$

Generally, for an arbitrary direction $h \in \mathbb{R}^n$, the Gateaux derivative is

$$\mathrm{D}_G f(x)[h] \coloneqq \lim_{\varepsilon \to 0} \frac{f(x + \varepsilon h) - f(x)}{\varepsilon}, \tag{0.29}$$

provided the limit exists, and thus each partial derivative is a Gateaux derivative in direction $h = \boldsymbol{e}_i$. The function f is further Fréchet differentiable at x, if mapping $h \mapsto \mathrm{D}_G f(x)[h]$ is linear and bounded, such that the Fréchet derivative

$$\mathrm{D}f(x)\colon \mathbb{R}^n \to \mathbb{R}, \qquad \mathrm{D}f(x)[h] = \sum_{i=1}^{n} \partial_i f(x)\, h_i, \tag{0.30}$$

is the continuous linear operator whose action coincides with the directional derivative. For the composed function $F(x) = f(x, g(x))$ as by previous definition and under the assumption of both F and g being differentiable in their arguments, then F is Fréchet differentiable. Using the chain rule it follows

$$\mathrm{D}F(x)[h] = \mathrm{D}_1 f\Big(x, g(x)\Big)[h] \;+\; \mathrm{D}_2 f\Big(x, g(x)\Big)\Big[\mathrm{D}g(x)[h]\Big] \tag{0.31}$$

for every perturbation $h \in X$ and the partial derivatives

$$\mathrm{D}_1 f(x,y)\colon X \to Z \quad \text{and} \quad \mathrm{D}_2 f(x,y)\colon Y \to Z\,. \tag{0.32}$$

Arbitrary derivatives of order $m \in \mathbb{N}_0$ are denoted as $\partial_i^m f := \partial_i(\partial_i(\cdots(\partial_i f)))$ for the m-times differentiation, where $\partial_i^0 := 1$, i.e. the identity. With multi-index $\boldsymbol{m}$, we set $\partial^{\boldsymbol{m}} := \partial_1^{\alpha_1}, \ldots, \partial_d^{\alpha_d}$. Further we use the conventional symbols $\nabla(\cdot)$, $\nabla \otimes \nabla(\cdot)$, $\Delta(\cdot)$ and $\nabla\cdot\,(\cdot)$ for the gradient, Hessian, divergence, and Laplacian, respectively. For $g\colon U \to \mathbb{R}$, $f\colon U \to \mathbb{R}^m$ and $H\colon U \to \mathbb{R}^{m\times n}$, where $U \subset \mathbb{R}^n$, we get

$$\begin{gathered}\nabla g = (\partial_1 g, \ldots, \partial_n g)\,, \quad \nabla\cdot f = \partial_1 f_1 + \cdots + \partial_n f_n\,, \quad \Delta g = \nabla\cdot\nabla g = \partial_1^2 g + \cdots + \partial_n^2 g\,,\\ \nabla \otimes \nabla g = \begin{pmatrix} \partial_1\partial_1 g & \ldots & \partial_1\partial_n g \\ \vdots & \ddots & \vdots \\ \partial_n\partial_1 g & \ldots & \partial_n\partial_n g \end{pmatrix} \quad \text{and} \quad \nabla\cdot H = \begin{pmatrix} \sum_{j=1}^n \partial_j H_{1j} \\ \vdots \\ \sum_{j=1}^n \partial_j H_{mj} \end{pmatrix}.\end{gathered} \tag{0.33}$$

Thus the gradient of a vector field equals its Jacobian matrix, whereas the divergence of a tensor field is obtained by taking the divergence of each row. Using symbols, we can write the Fréchet derivative in coordinate form $Df(x) = \Big(\partial_1 f(x), \ldots, \partial_n f(x)\Big) = \nabla f(x)$, so that $Df(x)[h] = \nabla f(x)\cdot h$.

If no further indication on operators such as ∇ or Δ is given, they act on all variables. If they are applied to a specific set of Euclidean coordinates $\boldsymbol{X} \in \mathbb{R}^n$ with unit vectors $\{\boldsymbol{e_1}, \ldots, \boldsymbol{e_n}\}$ and coefficients $X_1, \ldots, X_n$, we attach a subscript and get

$$\nabla_{\mathrm{X}} g = \partial_{X_1} g\, \boldsymbol{e}_1 + \cdots + \partial_{X_n} g\, \boldsymbol{e}_n = (\partial_{X_1} g, \ldots, \partial_{X_n} g) \tag{0.34}$$

for a scalar field $g\colon U \times I \to \mathbb{R}$. Subsequently regarding Euclidean coordinates, explicitly writing basis vectors is omitted and made clear from the context unless stated otherwise. In index notation we then define for scalar field $a \in \mathbb{R}$, vector field $\boldsymbol{a} \in \mathbb{R}^n$, second order tensor $\boldsymbol{A} \in \mathbb{R}^{n\times n}$ and third order tensor $\mathfrak{A} \in \mathbb{R}^{n\times n\times n}$

$$\Big[\nabla_{\mathrm{X}} a\Big]_i = \partial_{X_i} a\,, \quad \Big[\nabla_{\mathrm{X}}\, \boldsymbol{a}\Big]_{ij} = \partial_{X_j}\Big[\boldsymbol{a}\Big]_i \quad \text{and} \quad \Big[\nabla_{\mathrm{X}}\, \boldsymbol{A}\Big]_{ijk} = \partial_{X_k}\Big[\boldsymbol{A}\Big]_{ij}\,. \tag{0.35}$$

For the divergence we state

$$[\nabla_{\mathrm{x}} \cdot \boldsymbol{a}] = \partial_{X_i}\Big[\boldsymbol{a}\Big]_i, \quad \Big[\nabla_{\mathrm{x}} \cdot \boldsymbol{A}\Big]_i = \partial_{X_j}\Big[\boldsymbol{A}\Big]_{ij} \quad \text{and} \quad \Big[\nabla_{\mathrm{x}} \cdot \mathfrak{A}\Big]_{ij} = \partial_{X_k}\Big[\mathfrak{A}\Big]_{ijk}, \tag{0.36}$$

with analogous notation for $\nabla_{\mathrm{x}} \otimes \nabla_{\mathrm{x}}(\cdot)$ and $\Delta_{\mathrm{x}}(\cdot)$. Since the nature of the dimensional expansion of the gradient is obvious, we abbreviate $\nabla^2_{\mathrm{x}}(\cdot) \coloneqq \nabla_{\mathrm{x}} \otimes \nabla_{\mathrm{x}}(\cdot)$. Note that, according to Schwarz's theorem, a symmetry arises when performing second derivatives, e.g. $\Big[\nabla^2_{\mathrm{x}} \boldsymbol{a}\Big]_{iJK} = \partial_{X_J}\partial_{X_K}\Big[\boldsymbol{a}\Big]_i = \partial_{X_K}\partial_{X_J}\Big[\boldsymbol{a}\Big]_i$.

Regarding differentiability, we define continuity classes

$$\begin{aligned} \mathrm{C}^k(U,V) \coloneqq \Big\{ & f = (f_1,\dots,f_m)^{\top} \colon U \to V \,\Big| \\ & \forall i \in \{1,\dots,m\}\ \forall \boldsymbol{b} \in \mathbb{N}_0^n \left(|\boldsymbol{b}| \le k\right) \colon \exists\, \partial^{\boldsymbol{b}} f_i \text{ with } \partial^{\boldsymbol{b}} f_i \in \mathrm{C}^0(U) \Big\} \end{aligned} \tag{0.37}$$

for $k \in \mathbb{N}_0 \cup \{-1, \infty\}$, $U \subset \mathbb{R}^n$ and $V \subset \mathbb{R}^m$, where $\mathrm{C}^{k-1}(U,V) \supsetneq \mathrm{C}^k(U,V)$ for $k \in \mathbb{N}$. As special cases, $\mathrm{C}^0(U,V)$ comprises continuous functions, $\mathrm{C}^\infty(U,V)$ are infinitely differentiable functions, also called smooth. In analysis, the term regularity may also refer to continuity.

0.3.3 Function spaces

Let $\Omega \subset \mathbb{R}^3$ be a physical bounded Lipschitz domain with volume element $\mathrm{d}V$ as Lebesgue measure $\mathrm{L3}(\cdot)$. The Lebesgue space of square-integrable scalar functions is

$$\mathrm{L}^2(\Omega) \coloneqq \Big\{ f \colon \Omega \to \mathbb{R} \;\Big|\; \int_\Omega |f(x)|^2 \,\mathrm{d}V < \infty \Big\}, \tag{0.38}$$

which forms a separable Hilbert space when equipped with the inner product $\langle f, g\rangle_\Omega \coloneqq \int_\Omega f \cdot g \,\mathrm{d}V$, and is accompanied by its norm $\|f\|_{\mathrm{L}^2(\Omega)} \coloneqq \sqrt{\langle f, f\rangle_\Omega}$. As extension to vector- and tensor-valued fields with $m \in \mathbb{N}$, we abbreviate $\mathrm{L}^2(\Omega)^m \coloneqq \mathrm{L}^2\Big(\Omega; \mathbb{R}^m\Big)$, where for given tensor fields $A, B \colon \Omega \to \mathbb{R}^{m\times n}$, we define the L^2 inner product by the double contraction

$$\langle A, B\rangle_\Omega \coloneqq \int_\Omega A \colon B \,\mathrm{d}V, \qquad A \colon B \coloneqq \mathrm{tr}\Big(A^{\top} B\Big) \tag{0.39}$$

and the corresponding norm $\|A\|_{\mathrm{L}^2(\Omega)} \coloneqq \sqrt{\langle A, A\rangle_\Omega}$. Taking additionally function derivatives into account, we arrive at Sobolev spaces of square integrable functions ($\mathrm{p} = 2$). For $k \in \mathbb{N}_0$, we write

$$\mathcal{H}^k(\Omega) \coloneqq \Big\{ f \in \mathrm{L}^2(\Omega) \;\Big|\; \partial^{\boldsymbol{b}} f \in \mathrm{L}^2(\Omega) \;\; \forall\, |\boldsymbol{b}| \le k \Big\}, \tag{0.40}$$

where $\partial^{\boldsymbol{b}}$ denotes the (weak) partial derivative of multi-index $\boldsymbol{b}$. Vector and tensor Sobolev spaces are written $\mathcal{H}^k(\Omega)^m$ and $\mathcal{H}^k\Big(\Omega; \mathbb{R}^{m\times n}\Big)$, respectively. If we consider the boundary

$\partial\Omega$ of domain Ω, the Trace space $\mathcal{H}^{1/2}(\partial\Omega)$ accommodates essential boundary data using the Trace Theorem with a trace operator $T\colon \mathcal{H}^1(\Omega) \to \mathcal{H}^{1/2}(\partial\Omega)$, which is the unique bounded linear extension of the restriction map on smooth functions. In particular, for $u \in \mathrm{C}^\infty(\overline{\Omega})$ is given by $Tu \coloneqq u|_{\partial\Omega}$. We further introduce its square norm

$$\|f\|_{\mathcal{H}^k(\Omega),2} \coloneqq \sqrt{\sum_{|\boldsymbol{b}|\leq k} \|\partial^{\boldsymbol{b}} f\|_{\mathrm{L}^2}^2} \,. \tag{0.41}$$

1 Introduction

1.1 Motivation

In the past decades, lightweight structures and advanced composite materials have become indispensable in many high-performance engineering applications, ranging from aerospace and automotive components, wind turbine blades, biomedical devices or civil infrastructure. Their outstanding stiffness- and strength-to-weight ratios are achieved by tailoring the underlying microstructure, for example through aligned fibers, layered laminates or engineered geometries. As a consequence, the effective structural response is no longer governed solely by the macroscopic geometry and loading, but is strongly influenced by the material architecture at multiple length scales, which must be accounted for in structural analysis and design.

A characteristic feature of many such materials is the presence of significant scale differentiation between the macroscopic structural dimensions and the characteristic size of the microstructural components. When the microstructure exhibits strong anisotropy or size effects, classical Cauchy continua, which only involve first gradients of the displacement field, may be insufficient as they cannot represent bending stiffness of embedded fibers, interface layers with finite thickness, long-range interactions induced by periodic architectures or a general material response of engineered structures ("meta-materials") in a physically transparent way. In such settings, the geometry and topology of the microstructure give rise to apparent non-local interactions and generalized boundary conditions that must be reflected by the underlying continuum model.

Resolving the microstructure explicitly in a fully three-dimensional setting appears to be a straightforward solution approach. However, such a brute-force resolution quickly leads to exorbitant computational costs, especially when the microstructure is complex or when the macroscopic component is large in contrast to the micro-scale. Moreover, in many engineering contexts we are not primarily interested in the detailed micro-scale stress state but in homogenized or effective properties, in robust and efficient design procedures and in reliable macroscopic models that yet retain the essential influence of the microstructure.

These observations motivate two complementary lines of development. First, generalized or higher-order continua enrich the macroscopic kinematics by additional fields or gradients and introduce intrinsic length scales into the constitutive response. In this way they capture size effects as well as fiber-induced bending and torsion in an effective manner without explicitly resolving the microstructure. Second, computational multi-scale schemes couple macroscopic and microscopic boundary value problems in a variationally consistent

fashion. Methods such as FE^2 and IGA^2 attach representative volume elements (RVEs) to macroscopic integration points and determine effective stresses and tangent moduli by solving micro-scale boundary value problems but fail to provide profound physical interpretation and rely on inaccurate numerical assumptions. Each route has distinct advantages and limitations in terms of accuracy, interpretability and computational cost. For both approaches, we aim at their combination, extension and generalization within this thesis, while reducing their weaknesses. Specifically, we pursue the following objectives:

- to formulate a continuous second-gradient continuum model that captures bending and torsion of embedded fibers in a three-dimensional matrix by means of higher-order kinematics and energetically conjugate higher-order stresses,
- to establish a variationally consistent coupling between generalized (reduced) continuum models and surrounding three-dimensional Cauchy continua, including suitable interface conditions and numerical discretizations, and
- to develop and implement a continuous higher-order multi-scale method that embeds a generalized continuum description at the macro-scale and extracts its effective material response from a microstructure in a variationally consistent, monolithic and computationally efficient manner.

The guiding principle throughout this thesis is the use of higher-order continua as an effective macro-scale representation of complex microstructural mechanics. Since higher-order theories involve additional derivatives of the kinematic fields and require enhanced smoothness of the approximation spaces, isogeometric analysis (IGA) based on spline functions is employed as the primary discretization technology. Its inherent C^1 or higher continuity throughout the internal body domain provides the regularity needed for second-gradient formulations and leads to numerically robust and accurate simulations.

1.2 Higher-order continua and dimension-reduced coupling

Generalized continua extend the classical Cauchy framework by either enriching the set of kinematic variables, like micro-rotations in Cosserat or micromorphic theories, or by including higher gradients of the primary fields, leading to strain-gradient or higher-order models (cf. Mindlin [85, 86], Toupin [116, 117], Altenbach et al. [3], Eringen [36], Germain [45], and Maugin and Metrikine [81] and Bertram and Forest [13] among others). From a phenomenological point of view, such theories allow to represent internal length scales explicitly in the constitutive law and to derive additional boundary conditions on higher-order tractions. From a computational point of view, they enable the incorporation of size effects within a continuum formulation without resolving all geometric details of the microstructure.

In the present work, higher-order continua are employed in two conceptually different but closely related ways. First, a second-gradient continuum material model is formulated

for fiber-reinforced composites. Here, the body is described by the usual deformation map and its first and second gradients. The fiber families are represented as embedded directions with associated stretch, shear, curvature and torsion measures. These kinematic quantities are linked to the second gradient of the motion in such a way that the bending and twisting behavior of rod-like constituents can be captured within a three-dimensional continuum, see also the works of Asmanoglo and Menzel [5, 6], dell'Isola et al. [31], Giorgio [46], Soldatos [110], Spencer and Soldatos [112], and Steigmann [113]. The resulting stored energy density comprises classical first-gradient contributions as well as additional terms depending on curvature-like measures, giving rise to higher-order stresses and size-dependent effects.

Second, higher-order continua appear naturally when embedding and consistently coupling dimension reduced structural elements into a surrounding matrix. In particular, slender short fibers are modeled as Cosserat-type beams embedded in an overlapping 3D continuum domain, building on well-established geometrically exact beam formulations [16, 17, 95, 96, 106, 108] and immersed/embedded approaches in dell'Isola et al. [29], Duong et al. [35], Hesch et al. [55, 56], Schulte et al. [103], and Steinbrecher et al. [114]. Based on a kinematic coupling of beam centerline deformation to the matrix as well as transferring forces and moments, the influence of beam bending and torsion reappears as higher-order contributions to the stress response with corresponding hyper-stresses representing bending and torsional moments of the embedded structures.

Within this thesis, both approaches for higher-order continua are explored, serving as a unifying framework for representing fiber-induced size effects. They are obtained either directly by postulating a second-gradient material law with embedded fiber directions or indirectly by condensing explicitly modeled beam-matrix systems. In both cases, the resulting formulations give rise to second-gradient theories with internal length scales and non-classical boundary conditions, naturally benefiting from the use of IGA which provides required smoothness on the discrete level.

1.3 Multi-scale method

While higher-order continua provide efficient phenomenological models for size effects and curvature-driven responses, they intentionally suppress the explicit resolution of the microstructure. In many situations this is sufficient and even desirable. However, in a broad range of applications one is interested not only in the effective macroscopic response but also in the underlying microstructural deformation mechanisms, in the calibration of constitutive parameters from a known microstructure or in the virtual design of engineered materials. In such cases, a purely single-scale continuum description is too restrictive and a systematic coupling between macroscopic fields and microscopic RVEs is required.

In this work, this coupling is not introduced via a classical point-wise FE^2 association (cf. Schröder [101], Matouš et al. [80]) between macroscopic integration points and RVEs, nor is it enforced primarily through the Hill-Mandel macro-homogeneity condition (cf. Geers

et al. [44], Hashin and Shtrikman [52], Hill [58, 59], Mori and Tanaka [88], and Willis [120]). Instead, the starting point is a *domain expansion* in which the macroscopic configuration Ω_0 is combined with a microscopic reference cell $\tilde{\Omega}_0$ to form the product domain $\Omega_0 \times \tilde{\Omega}_0$, such that the motion depends on both the macroscopic position $\boldsymbol{X}$ and the microscopic coordinate $\tilde{\boldsymbol{X}}$. The central idea is to decompose this motion into a macroscopic part and a purely fluctuating microscopic part and to derive the macroscopic equations by energetic averaging over the micro-domain.

More precisely, the kinematics are expanded in the macroscopic coordinate by means of a Taylor series up to second order, thus enabling the connection to the established fiber-reinforced second-order continua. The deformation on the product domain is written as a sum of a polynomial ansatz in $\boldsymbol{X}$ and a micro-fluctuation field that depends on both $\boldsymbol{X}$ and $\tilde{\boldsymbol{X}}$. The macroscopic coefficients of the Taylor expansion represent the generalized deformation measures, while the fluctuation field accounts for the fine-scale variations induced by the heterogeneous microstructure. A key assumption is that the fluctuation has vanishing average over the micro-cell, such that the macroscopic deformation is recovered as the cell average of the total motion. This separation ensures that the macroscopic and microscopic contributions are uniquely identified and that higher-order macroscopic gradients arise in a natural and systematic way from the Taylor expansion.

The continuous higher-order multi-scale framework is derived by integrating the microscopic stored energy density over the product domain $\Omega_0 \times \tilde{\Omega}_0$. Taking variations with respect to the macroscopic motion and the micro-fluctuation field and subsequently averaging over the micro domain leads to a coupled variational problem for both scales. In this construction, the macroscopic balance equations and higher-order stress measures emerge directly from the averaged microscopic energy and the kinematic expansion. The resulting formulation is consistent with energetic averaging principles and can be related to the classical Hill-Mandel condition.

The result of this procedure is a *continuous higher-order multi-scale framework* posed on the product domain. The macroscopic problem appears as a second-gradient continuum with associated first- and second-order stresses with generalized boundary conditions. The microscopic problem, defined on $\tilde{\Omega}_0$, governs the fluctuation field for each macroscopic position. Both are coupled through the Taylor coefficients of the macroscopic deformation and through the requirement of vanishing average fluctuations. In this sense, the multi-scale method provides a microstructurally grounded derivation of higher-order continuum behavior, where curvature-dependent macroscopic response and hyperstresses are identified as condensed measures of the microstructural deformation stored in the expansion coefficients.

For the numerical realization, the coupled problem is again discretized using IGA. On the microscopic domain, standard isogeometric bases are used for the fluctuation field. Different combinations of approximation spaces are considered, including variants in which continuous functions are used in the macroscopic coordinate and localized, Dirac-type ansatz functions are introduced in the microscopic coordinate to concentrate the micro response. This allows for a systematic study of how the choice of macro and micro approximation affects the quality of the resulting higher-order continuum response and to

recast the classical FE^2 framework and corresponding higher-order extensions, e.g. Feyel and Chaboche [41], Kouznetsova et al. [67], Miehe et al. [84], and Smit et al. [109].

Beyond the continuous higher-order multi-scale model itself, the efficiency of its numerical realization is crucial. Therefore, we propose a generalized solution scheme that further enhances the efficiency and robustness of the continuous multi-scale formulation. In contrast to classical nested FE^2-type strategies, the present approach does not enforce micro-scale equilibrium to be fully satisfied within each macro-scale Newton iteration. Instead, the macro and micro unknowns enter a unified global residual and the linearized coupled system is treated in a way that allows for controlled deviations from exact micro equilibrium during the outer iterations. The null-space reduction and the associated condensed operators are constructed such that these deviations are resolved simultaneously as the global Newton process converges. This leads to a more flexible algorithmic structure as the micro problem does not need to be iterated to full equilibrium at every macro step, significantly reducing the number of expensive micro evaluations and allowing for alternative linear and nonlinear solvers without violating the underlying variational structure. As a consequence, the generalized solution scheme combines the robustness of a monolithic formulation (cf. Lange et al. [74] among others) with the computational advantages typically associated with staggered methods, while avoiding the rigid assumption of exact micro equilibrium at each macro iteration.

1.4 Organization of the work

The thesis is structured to progress from numerical and theoretical foundations to specialized higher-order models and their application within a continuous multi-scale framework.

In chapter 2, the fundamentals of isogeometric analysis and finite element discretization are recalled. After introducing B-spline and NURBS basis functions and multi-patch geometries, emphasis is placed on aspects that are crucial for higher-order formulations, such as the construction of globally smooth approximation spaces and a knot-insertion based multi-grid algorithm.

Chapter 3 provides the continuum-mechanical background. The kinematics of bodies with higher-order gradients of the motion are developed, together with the associated balance laws, hyper-stresses and boundary conditions. These concepts form the theoretical basis for the higher-order material models and the multi-scale method developed later.

In chapter 4, a continuous second-gradient material model for fiber-reinforced composites is proposed and analyzed. Fiber families embedded in a matrix material are described by direction fields and associated first order stretch and shear as well as second-order curvature and torsion. The formulation, its isogeometric discretization, and the associated boundary conditions are discussed in detail. Numerical examples for fiber-reinforced specimens demonstrate the model's ability to capture fiber bending and torsion effects at the structural scale.

Chapter 5 focuses on a complementary approach in which the fibers are represented as geometrically exact Cosserat beams embedded into a three-dimensional matrix. After introducing the beam formulation, a consistent coupling is established maintaining kinematic constraints and the transfer of forces and moments consistently between beam and matrix in an overlapping domain. By means of static condensation, a reduced model is obtained that can be interpreted as a second-gradient continuum along the beam centerlines. The discrete formulation, including the use of quaternions for the parameterization of rotations and the isogeometric approximation of all fields, is discussed in detail. Numerical investigations illustrate the behavior of the coupled beam-matrix system and the quality of the reduced model.

In chapter 6, the continuous higher-order multi-scale method is formulated. Starting from the generalized macroscopic continuum, a coupled macro-micro problem is formulated on the product domain $\Omega_0 \times \tilde{\Omega}_0$. The variational structure, boundary conditions and the enforcement of both energetic consistency and kinematic averaging conditions are addressed. Several discrete variants of the macro-micro approximation spaces are considered, including Dirac-based ansatz functions at the macro level. A null-space reduction scheme is introduced to solve the resulting algebraic system efficiently. The performance and accuracy of the approach are examined in a series of numerical experiments ranging from one-dimensional benchmarks to three-dimensional higher-order problems.

Finally, chapter 7 summarizes the main findings of the thesis and provides an outlook on possible extensions and future research directions. In particular, the potential of the proposed frameworks for nonlinear constitutive behavior, damage or failure and more complex microstructures is discussed.

2 Fundamentals of Isogeometric Analysis

Solving real-world mechanical problems relies on geometrical and physical modeling. The numerical approach to solving these problems implies the use of computers. Here, we focus on a variety of numerical methods enabling us to transfer complex mathematical and physical relations into simple computational tasks. Numerical modeling therefore requires in the first step representing geometries and fields of interests as functions and in the next step a discretization. The isogeometric concept (**I**so**g**eometric **A**nalysis - *IGA*) aims to directly link the geometric modeling used in Computer Aided Design (*CAD*) for the functional representation and discretization used in the computational analysis (Computer Aided Engineering *CAE*). The terminology was prominently brought to wide readership by Cottrell, Hughes and Bazilevs in their 2009 book (Cottrell et al. [26]). We also refer to the fundamental works of Piegl and Tiller [92] among others. In this chapter we provide a brief introduction into geometric design with focus on basic concept of B-Splines and the implications of high-order continuity to the continuum model approach presented in chapter 3.

2.1 Functional representation

In general, functions are used to describe a set of coordinates $\boldsymbol{X} = X_1, \dots X_d$ in the d-dimensional space with $d \in \{1, 2, 3\}$. By smooth continuation of in one, two or three independent directions, the set of coordinates becomes a domain $\Omega \subset \mathbb{R}^d$, as line, surface or volume, respectively. One way of explicitly formulating the geometry is by employing a functional representation making one coordinate a function of all other coordinates, e.g. $X_3 = f(X_1, X_2) = X_1^2 + 2X_2$. Hence this approach is limited as the function can take only a single value and cannot represent some basic shapes like the hull of a sphere. Implicit formulations create a root finding problem $f(\boldsymbol{X}) = \boldsymbol{0}$ which omits this limitation but requires additional step of solving. Therefore, formulations are best suited, where geometric coordinates are explicit functions of an independent set of parameters. For example taking a point in space and following its position in time creates a time-parameterized curve in space.

2.1.1 B-Splines

A Spline itself is a function of piecewise defined polynomials. Univariate B-splines, meaning Basis-Splines within a single direction and minimal overlap, lay the foundation for multivariate splines, e.g. for surfaces and volumes, and further enhancements like Non-Uniform-Rational-B-Splines (*NURBS*).

Univariate B-Splines

We define a univariate B-Spline of degree p as the set of $\mathfrak{k}$ basis functions in the parametric space by the non-decreasing sequence* $\boldsymbol{\Xi} = [\xi_1, \xi_2, \ldots, \xi_{\mathfrak{k}+p+1}]$, where $\xi_i \in \mathbb{R}$ is called the i^{th} knot and the set $\boldsymbol{\Xi}$ is denoted as knot vector and additionally uniform, if all knots are equally spaced. Further, we define the breakpoint vector $\tilde{\boldsymbol{\Xi}} = \left[\tilde{\xi}_1, \ldots, \tilde{\xi}_{\tilde{n}}\right]$ as the set of $\tilde{n}$ unique (non-repeating) knots. The $\mathfrak{k}$ basis functions can be constructed by defining zero-degree piecewise constants with

$$\widehat{\mathcal{N}}_{i,0}(\xi) = \begin{cases} 1 & \text{if} \quad \xi_i \leq \xi < \xi_{i+1} \\ 0 & \text{otherwise} \end{cases} \tag{2.1}$$

as step function and the recursive application of the Cox-de Boor formula De Boor [27]

$$\widehat{\mathcal{N}}_{i,p}(\xi) = \frac{\xi - \xi_i}{\xi_{i+p} - \xi_i} \widehat{\mathcal{N}}_{i,p-1}(\xi) + \frac{\xi_{i+p+1} - \xi}{\xi_{i+p+1} - \xi_{i+1}} \widehat{\mathcal{N}}_{i+1,p-1}(\xi)\,. \tag{2.2}$$

Throughout for repeating knots we define $\frac{0}{0} \coloneqq 0$. The set of all $\mathfrak{k}$ basis functions $\left\{\widehat{\mathcal{N}}_{1,p}\,,\ \ldots\ ,\ \widehat{\mathcal{N}}_{\mathfrak{k},p}\right\}$ eventually forms the spline basis in the parametric domain $\hat{\Omega} \coloneqq [\xi_{p+1}\,,\ \xi_{\mathfrak{k}+1})$.

Remark 2.1.1 – Closed spline space. In order for the curve to be also defined at the right boundary $\xi_{\mathfrak{k}+1}$, eq. (2.1) needs to be adapted towards

$$\widehat{\mathcal{N}}_{i,0}(\xi) = \begin{cases} 1 & \text{if} \quad \xi_i \leq \xi < \xi_{i+1} \\ 1 & \text{if} \quad \xi = \xi_{i+1} = \tilde{\xi}_{\tilde{n}} \quad \wedge \quad \xi_i = \tilde{\xi}_{\tilde{n}-1} \\ 0 & \text{otherwise}\,, \end{cases} \tag{2.3}$$

yielding domain $\hat{\Omega} \coloneqq [\xi_{p+1}\,,\ \xi_{\mathfrak{k}+1}]$.

Given knot vector and polynomial degree, continuity of the spline basis is determined. As per definition, $\widehat{\mathcal{N}}_{i,p}$ is a C^∞-polynomial between adjacent breakpoints $(\tilde{\xi}_j, \tilde{\xi}_{j+1})$ for $j = 1\,,\ \ldots \tilde{n} - 1$, whereas at each breakpoint $\tilde{\xi}_j$ the multiplicity of that point, i.e. the number of repetitions r_j for $\tilde{\xi}_j$ in $\boldsymbol{\Xi}$, reduces the continuity C^{p-r_j}. Open knot vectors have exactly $r = p + 1$ repetitions of the first and last knot, leading to C^{-1}-continuity

*We use one-based indexing and begin with the index 1 as first entry in the vector.

on both ends and discontinuing ("cutting off") the spline. In figure 2.1.1, a B-Spline with varying continuity over the breakpoints as well as the corresponding basis functions are shown. As can be seen, the breakpoints form a mesh, such that $\hat{\Omega} = \bigcup_{\mathrm{e}=1}^{\tilde{n}-1} \hat{\Omega}^{\mathrm{e}}$ with elements $\hat{\Omega}^{\mathrm{e}} = [\tilde{\xi}_{\mathrm{e}}, \tilde{\xi}_{\mathrm{e}+1})$. It is worth noting that each element may have a different number of basis-functions with active support, i.e. with function value greater than zero.

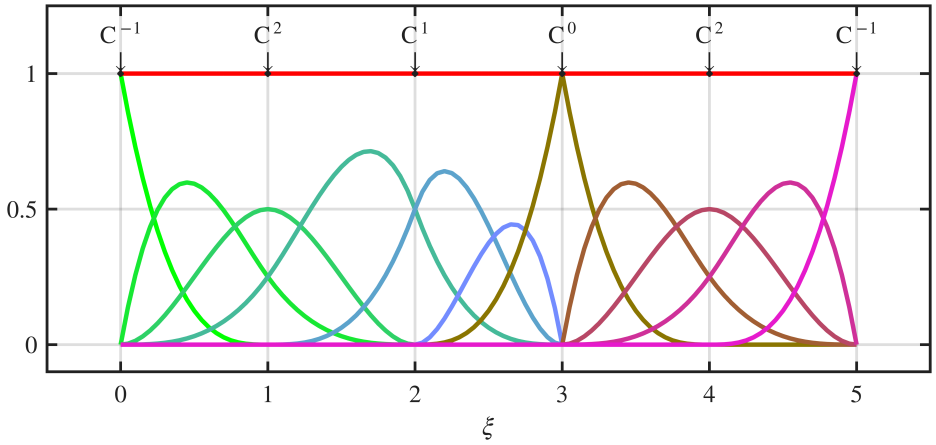


Figure 2.1.1 – 1D basis functions. Cubic basis functions for the knot vector $\Xi = [0, 0, 0, 0, 1, 2, 2, 3, 3, 3, 4, 5, 5, 5, 5]$ with given continuity at breakpoints building the mesh.

Multivariate B-Splines

For creating a multivariate domain $\hat{\Omega}$, we apply the tensor product of d univariate domains $\hat{\Omega} = \hat{\Omega}^{[1]} \times \hat{\Omega}^{[2]} \times \cdots \times \hat{\Omega}^{[d]}$ with associated knot vectors

$$\boldsymbol{\Xi}^{[\alpha]} = \left[\xi_1^{[\alpha]}, \xi_2^{[\alpha]}, \ldots, \xi_{\mathfrak{k}^{[\alpha]}+p^{[\alpha]}+1}^{[\alpha]}\right], \tag{2.4}$$

where $\alpha = 1, \ldots, d$. Here, we use Greek letters for indexing parametric dimensions and identify variables per dimension writing $(\cdot)^{[\alpha]}$. The multivariate functions follow by executing the tensor product of the univariate B-Splines $\widehat{\mathcal{N}}_{i^{[\alpha]},p^{[\alpha]}}^{[\alpha]}$ yielding

$$\widehat{\mathcal{B}}_{A,\boldsymbol{p}}(\boldsymbol{\xi}) = \widehat{\mathcal{B}}_{\boldsymbol{i},\boldsymbol{p}}(\boldsymbol{\xi}) = \prod_{\alpha=1}^{d} \widehat{\mathcal{N}}_{i^{[\alpha]},p^{[\alpha]}}^{[\alpha]}\left(\xi^{[\alpha]}\right), \tag{2.5}$$

where we use the multi-index $\boldsymbol{i} = \left(i^{[1]}, \ldots, i^{[d]}\right) \in \mathbb{N}^{[d]} \,|\, 1 \leq i^{[d]} \leq \mathfrak{k}^{[\alpha]} \;\forall\, \alpha = 1, \ldots, d$ with corresponding index space where $\boldsymbol{i} \in \boldsymbol{\Lambda}$, degree vector $\boldsymbol{p} = \left(p^{[1]}, \ldots, p^{[d]}\right)$ and parametric coordinates $\boldsymbol{\xi} = \left(\xi^{[1]}, \ldots, \xi^{[d]}\right)$. In figure 2.1.2, a two-dimensional domain with corresponding basis functions is shown. For global indexing the in total $\mathfrak{k} = \prod_{\alpha=1}^{d} \mathfrak{k}^{[\alpha]}$

functions, a natural scheme of the form

$$A := A(\boldsymbol{i}) = i^{[1]} + \sum_{\beta=2}^{d} \left(i^{[\beta]} - 1\right) \prod_{\gamma=1}^{\beta-1} \mathfrak{k}^{\gamma}\,, \quad A \in \Lambda := \{1, \ldots, \mathfrak{k}\}\,. \tag{2.6}$$

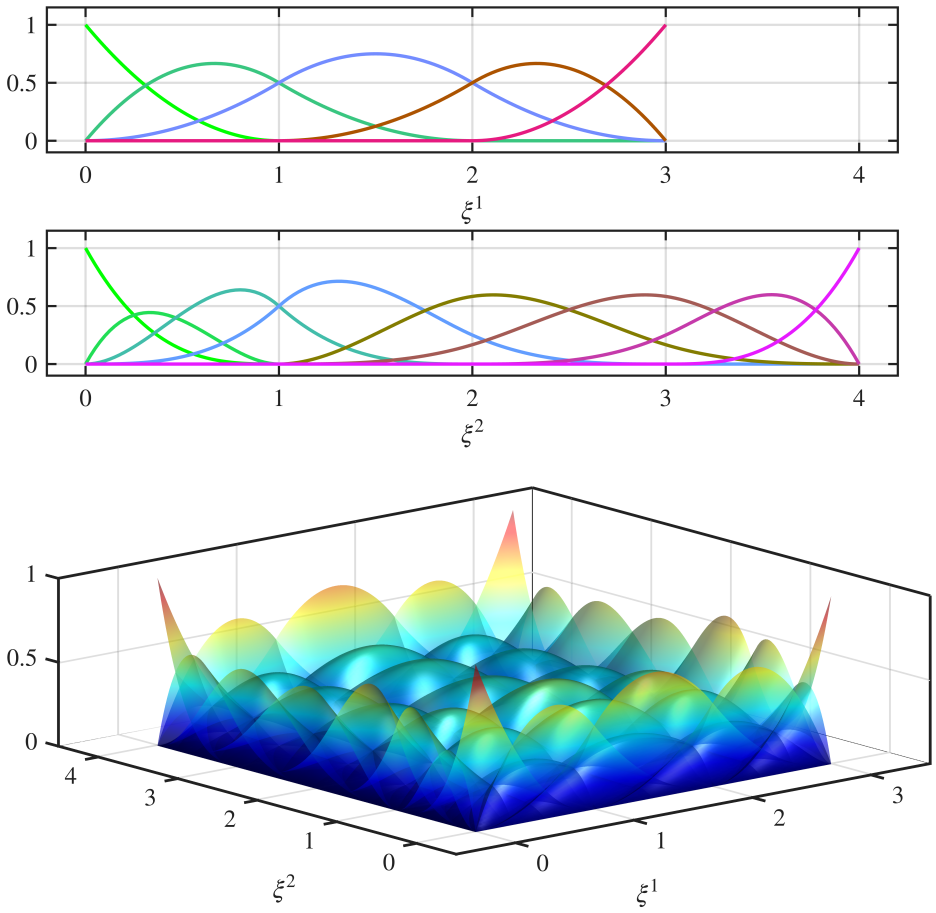


Figure 2.1.2 – 2D basis functions. Bivariate basis functions of degree $\boldsymbol{p} = (2, 3)$ for the knot vectors $\boldsymbol{\Xi}^{[1]} = [0, 0, 0, 1, 2, 3, 3, 3]$ and $\boldsymbol{\Xi}^{[2]} = [0, 0, 0, 0, 1, 1, 2, 3, 4, 4, 4, 4]$. Top: Univariate basis functions. Bottom: Multivariate basis functions

Now we take the breakpoint vectors $\tilde{\boldsymbol{\Xi}}^{[\alpha]}$, to describe the domain and the associated mesh

$$\hat{\Omega} := \prod_{\alpha=1}^{d} \left[\tilde{\xi}^{[\alpha]}_{p^{[\alpha]}+1}, \tilde{\xi}^{[\alpha]}_{\mathfrak{k}^{[\alpha]}+1}\right] \quad \text{and} \quad \hat{\Omega} = \bigcup_{\boldsymbol{e}} \hat{\Omega}^{\boldsymbol{e}}\,, \quad \hat{\Omega}^{\boldsymbol{e}} = \prod_{\alpha=1}^{d} \left[\tilde{\xi}^{[\alpha]}_{e^{[\alpha]}}, \tilde{\xi}^{[\alpha]}_{e^{[\alpha]}+1}\right), \tag{2.7}$$

where $\boldsymbol{e} = \left(e^{[1]}, \ldots, e^{[d]}\right), 1 \le e^{[\alpha]} \le \tilde{n}^{[\alpha]} - 1\,.$

For a breakpoint $\tilde{\xi}^{[\alpha]}_{j^{[\alpha]}}$, its multiplicity $r^{[\alpha]}_{j^{[\alpha]}}$ determines the continuity $\mathrm{C}^{c^{[\alpha]}}$ with $c^{[\alpha]} = p^{[\alpha]} - r^{[\alpha]}_{j^{[\alpha]}}$ on the resulting hyperplane. Furthermore, the tensor product leaves properties

of B-Splines intact, such as the *non-negativity* $\widehat{\mathcal{B}}_{\boldsymbol{i},\boldsymbol{p}}(\boldsymbol{\xi}) \geq 0$ and the *partition of unity* $\sum_{\boldsymbol{i}\in\boldsymbol{\Lambda}} \widehat{\mathcal{B}}_{\boldsymbol{i},\boldsymbol{p}}(\boldsymbol{\xi}) = 1$, respectively for all $\boldsymbol{\xi} \in \hat{\Omega}$. In this work, we solely make use of open knot vectors with non-repeating inner knots, such that additionally the *compact support* is given by $\operatorname{supp}\left(\widehat{\mathcal{B}}_{\boldsymbol{i},\boldsymbol{p}}\right) = \prod_{\alpha=1}^{d}[\xi^{[\alpha]}_{i^{[\alpha]}+1}, \xi^{[\alpha]}_{i^{[\alpha]}+p^{[\alpha]}+1})$, resulting in a fixed number of active functions within the parametric domain. In the context of function continuity, we introduce the convention, that a C^t multivariate B-Spline is at least t-continuous on the inside in any dimension, i.e. $\widehat{\mathcal{B}}_{\boldsymbol{i},\boldsymbol{p}}(\boldsymbol{\xi}) \in \mathrm{C}^{\boldsymbol{t}}$ for all $\boldsymbol{\xi} \in \prod_{\alpha=1}^{d}\left(\tilde{\xi}^{[\alpha]}_{1^{[\alpha]}}, \tilde{\xi}^{[\alpha]}_{\tilde{n}^{[\alpha]}}\right)$, where $\boldsymbol{t} = \left(t^{[\alpha]}\right)$ and $t^{[1]} = \cdots = t^{[d]} = t$. For open knot vectors without repetitions on the inside then follows $p^{[\alpha]} = t + 1 \quad \forall \alpha \in \{1, \ldots, d\}$.

Remark 2.1.2 – Lagrangian Elements. An open, uniform B-Spline basis of degree $p = 0$ resembles a constant function, thus multivariate B-Splines of degree $p^{[1]} = \cdots = p^{[d]} = 0$ are equal to constant shape functions of dimension d. For the linear case, i.e. $p^{[1]} = \cdots = p^{[d]} = 1$, each set $\left\{\widehat{\mathcal{N}}^{[\alpha]}_{i^{[\alpha]},p^{[\alpha]}}\right\}$ creates the typical hat functions of Lagrangian one-dimensional linear shape functions, see figure 2.1.3, such that the univariate B-Spline of $d = 1$ is equal to a mesh of Lagrangian linear line elements, the multivariate B-Spline of $d = 2$ is equal to a mesh of linear Lagrangian 4-node planar elements, for $d = 3$ equality is given with the linear Lagrangian 8-node volume element and so on, see Cottrell et al. [26] among others.

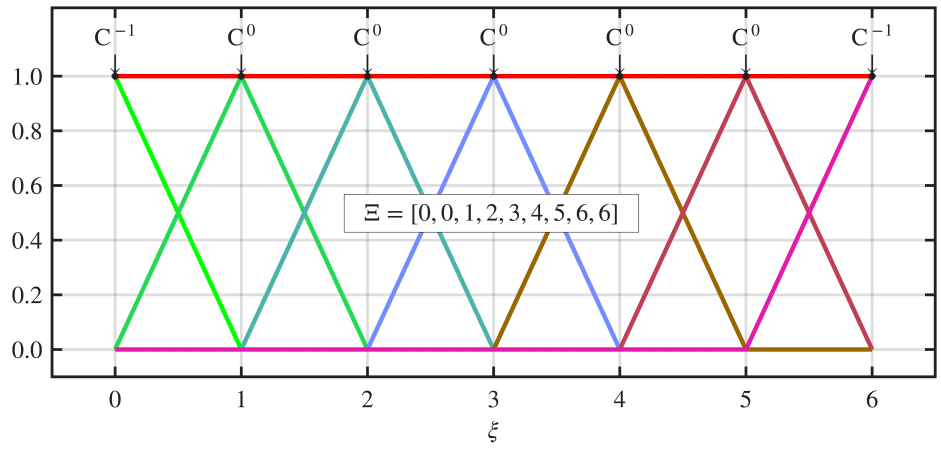


Figure 2.1.3 – Linear Lagrange basis functions. Linear univariate B-Splines representing a one-dimensional Lagrangian mesh.

NURBS

For the sake of completeness, *Non-Uniform-Rational-B-Splines* are an expansion of B-Splines towards a broader spectrum of shapes. They are constructed by multiplying

basis-functions with their associated weights $w^A > 0$ and normalizing them in order to have partition of unity

$$\widehat{\mathcal{R}}_{A,\boldsymbol{p}}(\boldsymbol{\xi}) = \frac{w^A \, \widehat{\mathcal{B}}_{A,\boldsymbol{p}}}{W(\boldsymbol{\xi})} \,, \tag{2.8}$$

with the weighing function $W(\boldsymbol{\xi}) = \sum_B w^B \, \widehat{\mathcal{B}}_{B,\boldsymbol{p}}$, for which both the repeated index does not indicate summation. The division of two piecewise polynomials results in a piecewise rational function, where numerator and denominator are of same degree. Continuity and other properties remain unchanged and thus are determined by the underlying knot vectors.

2.1.2 Derivatives of B-Splines

As will be seen in the following chapters, we are in need of derivatives for basis-functions. Taking the univariate B-Spline basis as in eq. (2.2), calculating its first derivative by

$$\frac{\mathrm{d}}{\mathrm{d}\xi}\widehat{\mathcal{N}}_{i,p}(\xi) = \frac{p}{\xi_{i+p} - \xi_i} \, \widehat{\mathcal{N}}_{i,p-1}(\xi) - \frac{p}{\xi_{i+p+1} - \xi_{i+1}} \, \widehat{\mathcal{N}}_{i+1,p-1}(\xi) \tag{2.9}$$

leads using the chain rule to the m^{th} order derivative

$$\frac{\mathrm{d}^{(m)}}{\mathrm{d}\xi^{(m)}}\widehat{\mathcal{N}}_{i,p}(\xi) = \frac{p}{\xi_{i+p} - \xi_i} \frac{\mathrm{d}^{(m-1)}}{\mathrm{d}\xi^{(m-1)}}\widehat{\mathcal{N}}_{i,p-1}(\xi) - \frac{p}{\xi_{i+p+1} - \xi_{i+1}} \frac{\mathrm{d}^{(m-1)}}{\mathrm{d}\xi^{(m-1)}}\widehat{\mathcal{N}}_{i+1,p-1}(\xi) \,, \tag{2.10}$$

see e.g. Piegl and Tiller [92] among others. Applying the tensor product for multivariate B-Splines of dimension d, calculating partial derivatives yields

$$\partial^{\boldsymbol{m}} \widehat{\mathcal{B}}_{A,\boldsymbol{p}}(\boldsymbol{\xi}) = \prod_{\alpha=1}^{d} \frac{\mathrm{d}^{\left(m^{[\alpha]}\right)}}{\mathrm{d}\xi^{[\alpha]\left(m^{[\alpha]}\right)}} \widehat{\mathcal{N}}^{[\alpha]}_{i^{[\alpha]},p^{[\alpha]}}\left(\xi^{[\alpha]}\right) , \tag{2.11}$$

where $\partial^{\boldsymbol{m}} \coloneqq \left(\partial^{m^{[1]}}_{[1]}, \ldots, \partial^{m^{[d]}}_{[d]}\right)$ and $\boldsymbol{m} \in \mathbb{N}^d_0$. For the expansion towards NURBS, the product/quotient rule yields

$$\partial^{\boldsymbol{n}} \widehat{\mathcal{R}}_{\boldsymbol{j},\boldsymbol{p}}(\boldsymbol{\xi}) = \frac{1}{W(\boldsymbol{\xi})} \left(w_{\boldsymbol{j}} \partial^{\boldsymbol{n}} \widehat{\mathcal{N}}_{\boldsymbol{j},\boldsymbol{p}} - \sum_{\boldsymbol{1} \leq \boldsymbol{k} \leq \boldsymbol{n}} \binom{\boldsymbol{n}}{\boldsymbol{k}} \partial^{\boldsymbol{n}-\boldsymbol{k}} \, \widehat{\mathcal{R}}_{\boldsymbol{j},\boldsymbol{p}}(\boldsymbol{\xi}) \, \partial^{\boldsymbol{k}} \, W(\boldsymbol{\xi}) \right) , \tag{2.12}$$

with the binomial coefficient

$$\binom{\boldsymbol{n}}{\boldsymbol{k}} = \frac{\boldsymbol{n}!}{\boldsymbol{k}! \, (\boldsymbol{n} - \boldsymbol{k})!} = \binom{n^{[1]}}{k^{[1]}} \cdots \binom{n^{[d]}}{k^{[d]}} , \quad \boldsymbol{n}, \boldsymbol{k} \in \mathbb{N}^d_0 \,. \tag{2.13}$$

2.2 Geometric representation

In the following we use the introduced Splines to represent geometrical shapes. Their parametric dimension $d_{\widehat{\Omega}}$ determines the kind of body they can describe, e.g. for spatial dimensions, $d_{\widehat{\Omega}} = 1$ results in a curve, $d_{\widehat{\Omega}} = 2$ is a surface and $d_{\widehat{\Omega}} = 3$ is a volume body. By extension towards a space-time framework, which is beyond the scope of this work, one parametric dimension is reserved for time, such that e.g. $d_{\widehat{\Omega}} = 2$ becomes a curve in time. Since the kind of shape does not necessarily determines the physical space it can occupy, we denote the physical dimension as $d_\Omega \in \{2, 3\}$. This becomes clear considering a curve, which can be in a $d_\Omega = 2$ or $d_\Omega = 3$ dimensional physical space, such that here $d_{\widehat{\Omega}} \leq d_\Omega \leq 3$.

2.2.1 Spline-based geometry

Taking the $\boldsymbol{p}$ degree basis functions $\widehat{\mathcal{R}}_{A,\boldsymbol{p}}$, a geometry $\boldsymbol{\mathcal{G}}_{\boldsymbol{p}}$ is defined as linear combination with associated vector-valued control points $\boldsymbol{P}^A$ in the form

$$\boldsymbol{\mathcal{G}}_{\boldsymbol{p}}(\boldsymbol{\xi}) = \sum_{A \in \Lambda} \boldsymbol{P}^A \, \widehat{\mathcal{R}}_{A,\boldsymbol{p}}(\boldsymbol{\xi}) \,, \quad \boldsymbol{\xi} \in \widehat{\Omega} \,. \tag{2.14}$$

Going back to the definition of NURBS in eq. (2.8), the connection of control points to weights becomes clearer

$$\boldsymbol{\mathcal{G}}_{\boldsymbol{p}}(\boldsymbol{\xi}) = \sum_{A \in \Lambda} \boldsymbol{P}^A \, w^A \, \frac{\widehat{\mathcal{B}}_{A,\boldsymbol{p}}(\boldsymbol{\xi})}{W(\boldsymbol{\xi})} \,. \tag{2.15}$$

The weight determines how much a control point "pulls" the geometry towards it, enabling to generate diverse geometries which can be controlled regarding desired continuity. Overall, B-Splines can be seen as a subset or special case of NURBS, obtained by setting all weights w^A to be equal. In combination with the resulting capabilities of replicating Lagrange basis functions up to degree one (see remark 2.1.2), we will use the NURBS notation $\widehat{\mathcal{R}}_{A,\boldsymbol{p}}$ for any kind of basis-function in the following sections.

Example: curve

In the following we will show some examples on each a B-Spline curve and a surface geometry, whereas for complex NURBS-geometries we refer to literature, see again Cottrell et al. [26] and Piegl and Tiller [92] among others. The curve in figure 2.2.1 is evaluated using the B-Spline basis shown in figure 2.1.1. Additionally, the associated control points are plotted and thin separator lines show the images of parametric element borders. Firstly, the non-interpolatory character becomes obvious since the inner control points do not coincide with the spline curve. Secondly close to control point $\boldsymbol{P}^7$ it can be seen, that the curve has an edge transitioning from the third to fourth element at breakpoint $\tilde{\xi}_4$ due to the low continuity C^0.

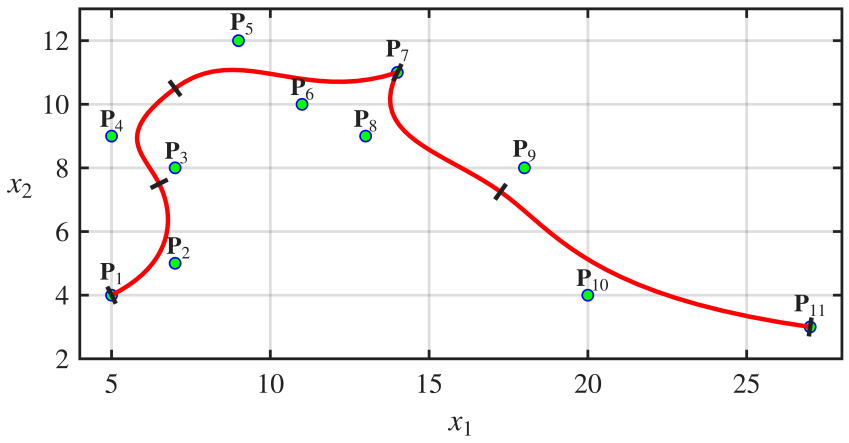


Figure 2.2.1 – 2D curve. Curve in $d_\Omega = 2$-dimensional space with control points $\boldsymbol{P}^1(5,4)$, $\boldsymbol{P}^2(7,5)$, $\boldsymbol{P}^3(7,8)$, $\boldsymbol{P}^4(5,9)$, $\boldsymbol{P}^5(9,12)$, $\boldsymbol{P}^6(11,10)$, $\boldsymbol{P}^7(14,11)$, $\boldsymbol{P}^8(13,9)$, $\boldsymbol{P}^9(18,8)$, $\boldsymbol{P}^10(20,4)$ and $\boldsymbol{P}^11(27,3)$.

Example: surface

The second example in figure 2.2.2 shows a complex surface in $d_\Omega = 3$-dimensional space created with the basis shown in figure 2.1.2.

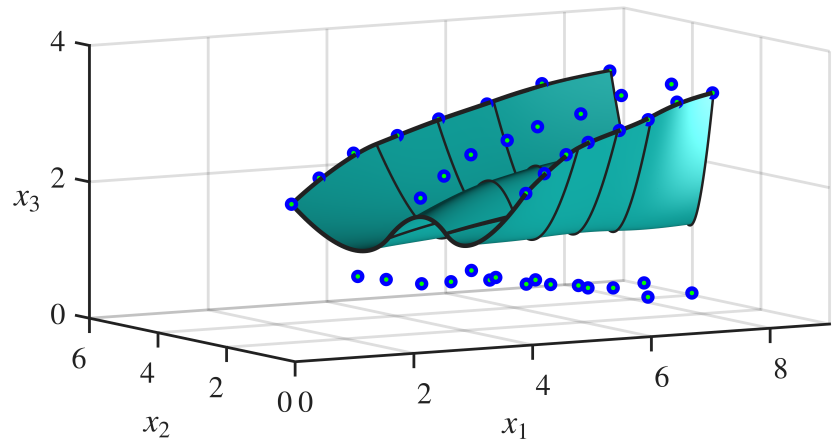


Figure 2.2.2 – 2D surface. Surface in $d_\Omega = 3$-dimensional space with control points as listed in table 2.A.1 (see section 2.A.1).

2.2.2 Spatial discretization

For the spatial discretization of a given (approximated) geometric domain Ω_0 with position vector $\boldsymbol{X}$, we assume the existence of a geometrical mapping $\boldsymbol{\mathcal{G}_p} : \widehat{\Omega} \to \Omega_0$ from parametric

to physical space such that

$$\boldsymbol{X}(\boldsymbol{\xi}) = \boldsymbol{\mathcal{G}}_{\boldsymbol{p}}(\boldsymbol{\xi}) = \sum_{A \in \Lambda} \boldsymbol{P}^A \, \widehat{\mathcal{R}}_{A,\boldsymbol{p}}(\boldsymbol{\xi}). \tag{2.16}$$

Further we also assume local existence of the inverse mapping $(\boldsymbol{\mathcal{G}}_{\boldsymbol{p}})^{-1}$. Concerning the map we introduce the Jacobian

$$\widehat{\mathbf{J}}(\boldsymbol{\xi}) = \frac{\partial \boldsymbol{X}(\boldsymbol{\xi})}{\partial \boldsymbol{\xi}} = \sum_{A \in \Lambda} \boldsymbol{P}^A \otimes \frac{\partial \widehat{\mathcal{R}}_{A,\boldsymbol{p}}}{\partial \boldsymbol{\xi}} \in \mathbb{R}^{d_\Omega \times d} \tag{2.17}$$

For a solid we have $d_\Omega = d$, thus $\widehat{\mathbf{J}}$ is square and invertible with $\widehat{\mathbf{J}}^{-1}(\boldsymbol{\xi}) = \frac{\partial \boldsymbol{\xi}}{\partial \boldsymbol{X}}$. Moreover we make use of its determinant $\widehat{j} = \det\left(\widehat{\mathbf{J}}\right)$ for integral transformation.

Derivatives

Regarding derivatives as gradients with respect to $\boldsymbol{X}$, we apply the chain rule yielding for the first and second gradient

$$\nabla_{\mathrm{X}} \widehat{\mathcal{R}}_{A,\boldsymbol{p}}(\boldsymbol{\xi}) = \frac{\partial \widehat{\mathcal{R}}_{A,\boldsymbol{p}}}{\partial \boldsymbol{\xi}} \, \widehat{\mathbf{J}}^{-1} \tag{2.18}$$

and

$$\nabla^2_{\mathrm{X}} \widehat{\mathcal{R}}_{A,\boldsymbol{p}}(\boldsymbol{\xi}) = \widehat{\mathbf{J}}^{-\top} \frac{\partial^2 \widehat{\mathcal{R}}_{A,\boldsymbol{p}}}{\partial \boldsymbol{\xi}^2} \, \widehat{\mathbf{J}}^{-1} + \left(\frac{\partial \widehat{\mathcal{R}}_{A,\boldsymbol{p}}}{\partial \boldsymbol{\xi}} \right)^{\top} : \nabla_{\mathrm{X}} \left(\widehat{\mathbf{J}}^{-1} \right), \tag{2.19}$$

respectively. Derivatives of the Jacobian are obtained by applying the chain-rule on its inverse

$$\nabla_{\mathrm{X}} \left(\widehat{\mathbf{J}}^{-1} \right) = -\widehat{\mathbf{J}}^{-1} \left(\frac{\partial \widehat{\mathbf{J}}}{\partial \boldsymbol{\xi}} \cdot \widehat{\mathbf{J}}^{-1} \right) \widehat{\mathbf{J}}^{-1} \tag{2.20}$$

Evaluation on reference element

Next, we introduce a fixed parent domain $\bar{\Omega} \coloneqq \prod_{\alpha=1}^{d} [-1, 1]$ with associated coordinates $\boldsymbol{\eta} = \left(\eta^{[1]}, \ldots, \eta^{[d]} \right)$ and create a link per element to the parameter coordinate $\boldsymbol{\xi}$ with the affine transformation

$$\boldsymbol{\xi} = \bar{\mathcal{G}}^e(\boldsymbol{\eta}) = \frac{1}{2} \begin{bmatrix} \eta^{[1]} \left(\tilde{\xi}^{[1]}_{e^{[1]}+1} - \tilde{\xi}^{[1]}_{e^{[1]}} \right) + \left(\tilde{\xi}^{[1]}_{e^{[1]}+1} + \tilde{\xi}^{[1]}_{e^{[1]}} \right) \\ \vdots \\ \eta^{[d]} \left(\tilde{\xi}^{[d]}_{e^{[d]}+1} - \tilde{\xi}^{[d]}_{e^{[d]}} \right) + \left(\tilde{\xi}^{[d]}_{e^{[d]}+1} + \tilde{\xi}^{[d]}_{e^{[d]}} \right) \end{bmatrix} \tag{2.21}$$

The Jacobian of this map is diagonal, such that we write

$$\bar{j}^e = \det\left(\frac{\partial \bar{\mathcal{G}}^e}{\partial \boldsymbol{\eta}} \right) = \left(\frac{1}{2} \right)^d \prod_{\alpha=1}^{d} \tilde{\xi}^{[\alpha]}_{e^{[\alpha]}+1} - \tilde{\xi}^{[\alpha]}_{e^{[\alpha]}} \, . \tag{2.22}$$

Gaussian quadrature

Using a natural scheme of the form $\mathrm{E} := \mathrm{E}(\boldsymbol{e})$ (cf. eq. (2.6)) for the in total $\mathfrak{E} = \prod_{\alpha=1}^{d}\left(\tilde{n}^{[\alpha]}-1\right)$ elements, we conduct element-wise integration of function $f(\boldsymbol{X})$ over the geometric domain

$$\int_{\Omega_0}\{f(\boldsymbol{X})\}\mathrm{d}V = \sum_{\mathrm{E}=1}^{\mathfrak{E}}\int_{\Omega_0^{\mathrm{E}}}\{f(\boldsymbol{X})\}\mathrm{d}V\,. \tag{2.23}$$

For each element contribution we then compose the parameter space transformation and element-wise mapping to the reference $\boldsymbol{\mathcal{G}}_{\boldsymbol{p}}\circ\bar{\mathcal{G}}^{\mathrm{E}}$ by using the mesh associating parametric with physical elements $\Omega_0^{\mathrm{E}} = \boldsymbol{X}\left(\widehat{\Omega}^{\mathrm{E}}\right)$ yielding

$$\int_{\Omega_0^{\mathrm{E}}}\{f(\boldsymbol{X})\}\mathrm{d}V = \int_{\widehat{\Omega}^{\mathrm{E}}}\left\{f(\boldsymbol{X}(\boldsymbol{\xi}))\widehat{j}\right\}\mathrm{d}\boldsymbol{\xi} = \int_{\bar{\Omega}}\left\{f(\boldsymbol{X}(\boldsymbol{\xi}(\boldsymbol{\eta})))\widehat{j}\,\bar{j}^{\mathrm{E}}\right\}\mathrm{d}\boldsymbol{\eta} \tag{2.24}$$

Quadrature is then performed on the reference domain $\bar{\Omega}$ with per-direction Gauss points $\left\{\eta_{\mathrm{g}}^{[\alpha]},\mathrm{w}_{\mathrm{g}}^{[\alpha]}\right\}$, $\mathrm{g}=1,\dots,n_{\mathrm{gp}}^{[\alpha]}$ and apply the tensor product. Therein $\eta_{\mathrm{g}}^{[\alpha]}$ is the Gauss point position, $\mathrm{w}_{\mathrm{g}}^{[\alpha]}$ its associated weight. For exact integration of polynomials we require for the number of Gauss points $n_{\mathrm{gp}}^{[\alpha]} \geq p^{[\alpha]}+1$. Using again a natural numbering scheme (cf. eq. (2.6)) for the $n_{\mathrm{gp}} = \prod_{\alpha=1}^{d} n_{\mathrm{gp}}^{[\alpha]}$ Gauss points with $\mathrm{G} := \mathrm{G}(\mathbf{g})$. The total weight follows from the tensor product by $\mathrm{w}_{\mathrm{G}} = \prod_{\alpha=1}^{d}\mathrm{w}_{\mathrm{g}}^{[\alpha]}$. Evaluation at the quadrature points is then done by conducting the compositions, e.g. $\boldsymbol{X}_{\mathrm{G}} = \boldsymbol{X}(\boldsymbol{\xi}(\boldsymbol{\eta}_{\mathrm{G}}))$, $\widehat{j}_{\mathrm{G}} = \widehat{j}(\boldsymbol{\xi}(\boldsymbol{\eta}_{\mathrm{G}}))$ and for the Spline basis $\left[\widehat{\mathcal{R}}_{A,\boldsymbol{p}}\right]\Big|_{\mathrm{G}} = \widehat{\mathcal{R}}_{A,\boldsymbol{p}}(\boldsymbol{\xi}_{\mathrm{G}})$. Thus, the integral eq. (2.24) is transformed into

$$\int_{\bar{\Omega}^{\mathrm{E}}}\left\{f(\boldsymbol{X}(\boldsymbol{\xi}(\boldsymbol{\eta})))\widehat{j}\,\bar{j}^{\mathrm{E}}\right\}\mathrm{d}\boldsymbol{\eta} \approx \sum_{\mathrm{G}=1}^{n_{\mathrm{gp}}} f(\boldsymbol{X}_{\mathrm{G}})\widehat{j}_{\mathrm{G}}\,\bar{j}^{\mathrm{E}}\mathrm{w}_{\mathrm{G}}. \tag{2.25}$$

Note again that, for the right choice of Gauss points, the quadrature of non-rational functions, i.e. in this context standard B-Splines, becomes exact.

Remark 2.2.1 – Further Integral evaluation. Besides the standard element-based Gaussian quadrature other integral evaluations may be considered, e.g. using Dirac Delta distributions. Citing Reali and Hughes [94],

> [a Dirac Delta distribution] can be formally constructed as the limit of a sequence of smooth functions with compact support converging to a distribution and satisfying the so-called shifting property, i.e.
>
> $$\int_{\Omega} f(\boldsymbol{X})\delta(\boldsymbol{X}-\boldsymbol{X}_i)\mathrm{d}V = f(\boldsymbol{X}_i), \tag{2.26}$$
>
> for every function f continuous at $\boldsymbol{X}_i \in \Omega$.

We refer to McRobie and Lasenby [82] and Weeger et al. [119] for isogeometric collocation methods.

2.3 Parametric adjustments

In the following, we briefly show a small selection of techniques used to adjust the B-Spline/NURBS basis in order to refine, enrich or elevate/decrease their degree without compromising geometric accuracy of the resulting geometry. These techniques become important considering simple shapes in the reference configuration whose deformation is expected to be more complex and especially considering continuity requirements. Since the tensor product structure allows us to treat each parametric direction independently, we focus on $d_{\widehat{\Omega}} = 1$ dimensional curves.

2.3.1 Degree elevation

In general, a p^{th} degree polynomial $\boldsymbol{G}_p$ curve is equal to a $(p+1)^{\text{th}}$ degree polynomial $\boldsymbol{G}_{p+1}$, if we embed $\boldsymbol{G}_p$ in a higher dimensional space. Practically this can be achieved by setting $\boldsymbol{G}_{p+1}(\xi) = \boldsymbol{G}_p(\xi) + \boldsymbol{0} \cdot (\xi)^{p+1}$. Taking the knot vector $\boldsymbol{\Xi} = [\xi_1, \xi_2, \ldots, \xi_{\mathfrak{k}+p+1}]$ and the associated NURBS geometry $\boldsymbol{\mathcal{G}}_p(\xi) = \sum_i^{\mathfrak{k}} \boldsymbol{P}_w^i \frac{\widehat{\mathcal{N}}_{i,p}(\xi)}{W(\xi)}$, there exists knot vector $\bar{\boldsymbol{\Xi}} = \left[\bar{\xi}_1, \bar{\xi}_2, \ldots, \bar{\xi}_{\bar{\mathfrak{k}}+\bar{p}+1}\right]$, with $\bar{p} = p+1$ and control points $\bar{\boldsymbol{P}}_w^i$, such that

$$\begin{aligned} \boldsymbol{\mathcal{G}}_p(\xi) &= \boldsymbol{\mathcal{G}}_{\bar{p}}(\xi) \\ \sum_i^{\mathfrak{k}} \boldsymbol{P}_w^i \frac{\widehat{\mathcal{N}}_{i,p}(\xi)}{W(\xi)} &= \sum_j^{\bar{\mathfrak{k}}} \bar{\boldsymbol{P}}_w^j \frac{\widehat{\mathcal{N}}_{j,\bar{p}}(\xi)}{\bar{W}(\xi)} \end{aligned} \tag{2.27}$$

Hence *degree elevation* is the process of finding $\bar{\boldsymbol{\Xi}}$ and $\bar{\boldsymbol{P}}_j^w$ which fulfill this condition. For preservation of geometry, the overall continuity has to remain the same. Since this is determined for each breakpoint by the order and its multiplicity, the latter also has to be raised by one

$$\bar{\boldsymbol{\Xi}} = \left[\underbrace{\xi_1, \ldots, \xi_1}_{r_1+1}, \underbrace{\xi_2, \ldots, \xi_2}_{r_2+1}, \ldots, \underbrace{\xi_{\tilde{\mathfrak{k}}}, \ldots, \xi_{\tilde{\mathfrak{k}}}}_{r_{\tilde{\mathfrak{k}}}+1} \right], \tag{2.28}$$

with $\tilde{\mathfrak{k}}$ additional knots leading to $\bar{\mathfrak{k}} = \mathfrak{k} + \tilde{\mathfrak{k}} - 1$ new basis functions respective control points. For the latter, there exist a variety of determination approaches, see e.g. Lai et al. [72] and Piegl and Tiller [92] among others. The simplest one is to build a set of linear equations using eq. (2.27) and solve for $\bar{\boldsymbol{P}}_w^j$ as pair of control point position and corresponding weight. Degree elevation is widely denoted as *p-refinement*.

2.3.2 Knot insertion

To enrich the function basis, we use *knot-insertion* to place a new knot $\bar{\xi} \in [\xi_j, \xi_{j+1})$ into the existing knot vector $\boldsymbol{\Xi}$ to obtain $\bar{\boldsymbol{\Xi}} = \left[\xi_1, \xi_2, \ldots, \xi_j, \bar{\xi}, \xi_{j+1}, , \ldots, \xi_{(\mathfrak{k}+1)+p+1}\right]$ with now $\mathfrak{k}+1$ new basis functions. If the knot value is already present, its multiplicity is increased

and thus continuity for that knot reduced. Otherwise, i.e. inserting a new unique knot $\bar{\xi} = \tilde{\bar{\xi}} \in \left(\tilde{\xi}_j, \tilde{\xi}_{j+1}\right)$, we now have $\tilde{\mathfrak{k}} + 1$ knots building the mesh and effectively split element j into two. Analogous to Lagrangian meshes, this method is also called *h-refinement*. Here, only the vector space basis is changed whereas the geometry and parameter space remain intact. The new set of control points to the $\mathfrak{k} + 1$ new basis functions is again obtained by solving a set of linear equations

$$\sum_{i}^{\mathfrak{k}} \boldsymbol{P}_w^i \frac{\widehat{\mathcal{N}}_{i,p}(\xi)}{W(\xi)} = \sum_{j}^{\mathfrak{k}+1} \bar{\boldsymbol{P}}_w^j \frac{\widehat{\mathcal{N}}_{j,p}(\xi)}{\bar{W}(\xi)} \,. \tag{2.29}$$

Utilizing linear independence and local support, inserting $\bar{\xi} \in [\xi_j, \tilde{\xi}_{j+1})$ breaks down to

$$\bar{\boldsymbol{P}}_i^w = \alpha_i \boldsymbol{P}_w^i + (1 - \alpha_i) \boldsymbol{P}_w^{i-1} \,, \tag{2.30}$$

where

$$\alpha_i = \begin{cases} 1 & i \leq j - p \\ \frac{\bar{\xi} - \xi_j}{\xi_{j+p} - \xi_j} & j - p + 1 \leq i \leq j \\ 0 & i \geq j + 1 \end{cases} . \tag{2.31}$$

Note, that the linear equation eq. (2.30) for the insertion of knot ξ_j can be written as a matrix-vector operation $\boldsymbol{M}^j = \boldsymbol{T}^{j,j-1} \boldsymbol{M}^{j-1}$ with $\boldsymbol{T}^{j,j-1} \in \mathbb{R}^{(\mathfrak{k}_j) \times \mathfrak{k}_{j-1}}$ containing the coefficients α_i, furthermore $\mathfrak{k}_{j-1}$ as number of control points before and $\mathfrak{k}_j = \mathfrak{k}_{j-1} + 1$ as number of control points after insertion. Moreover, we define $\boldsymbol{M}^{j-1} = \{\boldsymbol{P}_w^i\}^\top$ and $\boldsymbol{M}^j = \left\{\bar{\boldsymbol{P}}_w^i\right\}^\top$ as vectorized sets of old and new control points, respectively. For the set of $j = 1, \ldots, t$ knots to be sequentially inserted in a refinement process, the operation becomes

$$\begin{aligned} \boldsymbol{M}^t &= \boldsymbol{T}^{t,t-1} \boldsymbol{M}^{t-1} \\ &= \boldsymbol{T}^{t,t-1} \cdots \boldsymbol{T}^{2,1} \boldsymbol{T}^{1,0} \boldsymbol{M}^0 \\ &= \mathbb{T}^{1,0} \boldsymbol{M}^0 \,, \end{aligned} \tag{2.32}$$

where $\boldsymbol{T}^{1,0}$ inserts additional knot ξ_1 and so forth.

Finally, we associate the initial set of control points $\boldsymbol{M}^0$ with its mesh denoted as $\mathcal{M}^0$ and the resulting mesh as $\mathcal{M}^1$ with control points $\boldsymbol{M}^t$, generated by the *prolongation matrix* $\mathbb{T}^{1,0}$ and write

$$\mathcal{M}^1 = \mathbb{T}^{1,0} \circ \mathcal{M}^0 \,. \tag{2.33}$$

Knot insertion based multi-grid method

For a fast and efficient solution of any given discrete boundary value problem, we construct a series of nested meshes characterized by a linear dependency of the coarse shape functions from those of the fine scale. This can be easily obtained in the context of B-splines and NURBS, if the fine scale is constructed by a knot insertion method (see e.g. Hughes et al. [61] and Piegl and Tiller [92]). This technique provides all necessary topological information for the prolongation matrix $\mathbf{T}^{\text{pro}}$. Hence, a simple solution scheme detailed in algorithm 2.3.1 can be applied.

1: Construct a coarse scale mesh $\mathcal{M}^0$
2: **for** $i = 0 : n - 1$ **do** ▷ $n \coloneqq$ degrees of fineness
3: Refine mesh $\mathcal{M}^i$ using a knot-insertion to obtain the finer mesh $\mathcal{M}^{i+1}$
4: Construct prolongation matrix $\mathbb{T}^{i+1,i}$
5: **end for**
6: **for** $i = 0 : n - 1$ **do**
7: Solve a given boundary value problem on $\mathcal{M}^i$
8: Prolongate the solution $\mathcal{M}^{i+1} = \mathbb{T}^{i+1,i} \circ \mathcal{M}^i$
9: **end for**

Algorithm 2.3.1 – **Multi-grid algorithm.** Fast solving scheme using nested meshes

2.3.3 Hierarchical refinement and multi-patch geometries

There exist a variety of methods to further either enhance existing geometric description or to expand capabilities toward more complex geometries. We prominently point to hierarchical refinement, the process of subdividing targeted elements to locally increase accuracy as presented in Dittmann [32] and references therein. Regarding complex shapes, a widely used approach is to break down the geometry into easier to describe *patches* and subsequently re-combine these simple shapes, e.g. by employing mortar methods as described thoroughly in Schuß [104].

2.A Appendix A

2.A.1 Control points of Spline Surface

Point	x_1	x_2	x_3
$\boldsymbol{P}^1$	4.0	0.2	2.2
$\boldsymbol{P}^2$	3.2	0.4	1.1
$\boldsymbol{P}^3$	2.4	0.5	2.2
$\boldsymbol{P}^4$	1.4	0.6	1.1
$\boldsymbol{P}^5$	0.4	0.8	2.2
$\boldsymbol{P}^6$	4.6	0.7	2.4
$\boldsymbol{P}^7$	3.9	0.9	0.9
$\boldsymbol{P}^8$	3.2	1.2	2.4
$\boldsymbol{P}^9$	2.4	1.5	0.9
$\boldsymbol{P}^{10}$	1.5	1.9	2.4
$\boldsymbol{P}^{11}$	5.2	1.1	2.6
$\boldsymbol{P}^{12}$	4.7	1.4	0.7
$\boldsymbol{P}^{13}$	4.0	1.8	2.6
$\boldsymbol{P}^{14}$	3.4	2.2	0.7
$\boldsymbol{P}^{15}$	2.6	2.8	2.6
$\boldsymbol{P}^{16}$	5.8	1.5	2.7
$\boldsymbol{P}^{17}$	5.4	1.9	0.6
$\boldsymbol{P}^{18}$	4.9	2.3	2.7
$\boldsymbol{P}^{19}$	4.3	2.9	0.6
$\boldsymbol{P}^{20}$	3.8	3.6	2.7

Point	x_1	x_2	x_3
$\boldsymbol{P}^{21}$	6.5	1.8	2.8
$\boldsymbol{P}^{22}$	6.1	2.3	0.5
$\boldsymbol{P}^{23}$	5.7	2.8	2.8
$\boldsymbol{P}^{24}$	5.3	3.5	0.5
$\boldsymbol{P}^{25}$	4.9	4.3	2.8
$\boldsymbol{P}^{26}$	7.1	2.0	2.9
$\boldsymbol{P}^{27}$	6.8	2.5	0.4
$\boldsymbol{P}^{28}$	6.6	3.1	2.9
$\boldsymbol{P}^{29}$	6.3	3.9	0.4
$\boldsymbol{P}^{30}$	6.0	4.8	2.9
$\boldsymbol{P}^{31}$	7.7	2.2	3.1
$\boldsymbol{P}^{32}$	7.5	2.7	0.2
$\boldsymbol{P}^{33}$	7.4	3.3	3.1
$\boldsymbol{P}^{34}$	7.3	4.1	0.2
$\boldsymbol{P}^{35}$	7.1	5.1	3.1
$\boldsymbol{P}^{36}$	8.3	2.2	3.2
$\boldsymbol{P}^{37}$	8.3	2.8	0.2
$\boldsymbol{P}^{38}$	8.3	3.4	3.2
$\boldsymbol{P}^{39}$	8.3	4.2	0.2
$\boldsymbol{P}^{40}$	8.3	5.2	3.2

Table 2.A.1 – 2D surface: control points. Nodal data for B-Spline surface in figure 2.2.2.

3 Second-order Continuum Mechanics

In this chapter, we briefly cover the basics of generalized continuum mechanics in order to understand the mechanical problems introduced in the following chapters and start with a short historical context without any claim to completeness and refer to comprehensive literature on that topic, e.g. Altenbach and Eremeyev [2] and Altenbach et al. [3], Bertram [12], dell'Isola et al. [30], Forest and Trinh [42], and Maugin and Metrikine [81].

Historical background

Following Isaac Newton work in the late 17th century, among others, classical mechanics rests on Leonhard Euler's balances of linear and angular momentum (Euler [38] - 1757, translation Frisch [43]) in the mid 18th century, linking measurable kinematics to forces and torques or momenta with additions by Joseph-Louis Lagrange (Lagrange et al. [71] - 1788) and Pierre-Simon Laplace (Laplace et al. [75] - 1798). With introduction of a stress tensor and traction vector by Augustin-Louis Cauchy (Cauchy [21] - 1823), the Euler-Cauchy stress principle led to the Cauchy-continuum approach. Therein, curvature of surfaces was neglected and the overall stress/force relation assumed to be the reaction of first order changes of motion. The limitations are reached when considering size effects, motivating the inclusion of internal length scales or micro deformation, e.g. polar media with micro-rotations or torques (Cosserat and Cosserat [25] - 1909) and micromorphic extensions (Eringen [36] - 1999) which introduce further degrees of freedom. Keeping the initial set, another path is to include higher gradients of the motion.

Gabrio Piola (Piola [93] - 1848, translation Dell'Isola [28]) introduced higher gradients via a variational *virtual power* approach, expanding intermolecular forces into a series, such that derivatives of any order enter the stress law and anticipated *hyperstresses* ensuring Euclidean frame invariance. Similar ideas were given by Cauchy (Cauchy [22] - 1851) from balance laws for infinitesimal deformations. Ernst Hellinger (Hellinger [54] - 1907) systematically applied the Principle of virtual work to gradient materials, already noting higher boundary conditions and line forces. The following years, second-order hyperelastic material laws began to surface along with the higher order invariants or energy terms. Morton E. Gurtin (Gurtin [49] - 1965) examined the material and energetic theories in context of thermodynamic principles and concluded the necessity of present hyperstresses. Richard A. Toupin (Toupin [116] - 1962, Toupin [117] - 1964) and Raymond D. Mindlin (Mindlin [86] - 1965), finally delivered the fundamental small-strain, linear hyperelastic gradient theory up to third order.

3.1 Configuration and kinematics

We start with a short summary of continuum mechanics in which objects completely fill their occupying space, are assumed to be deformable and their respective properties such as material characteristics are distributed continuously. We consider the body $\mathcal{B} \subset \mathbb{R}^d$, $d \in \{1, 2, 3\}$, moving in the Euclidean space. For the geometrical description we use a Cartesian orthonormal basis with fixed origin $\mathcal{O}$. The body's geometrical region at time t in the time interval $I = [0, \tau] \subset \mathbb{R}_{\geq 0}$ is the Lipschitz bounded domain $\Omega_t \subset \mathbb{R}^d$, $t \in I$, called configuration, with boundary $\partial\Omega_t$ and outward unit normal $\boldsymbol{n}_t$. We attach a characteristic length scale ξ to the body, enabling the discussion on scale dependency. We define the initial configuration Ω_0 at $t = 0$ to be the reference configuration, which is load-, deformation- and stress-free. Configurations for $t > 0$ are referred to as actual or current. The movement is assumed to be smooth with respect to temporal changes. At any configuration, we assume each material point P of the body can be described using a position vector $\boldsymbol{x}_t \in \mathbb{R}^d$. For simplification, we define $\boldsymbol{X} \coloneqq \boldsymbol{x}_0$ for the reference position and further mark other quantities in the reference configuration with capital letters, i.e. $\boldsymbol{N} \coloneqq \boldsymbol{n}_0$ and $V \coloneqq V_0$. Since all configurations apart from the initial one require $t > 0$, the index regarding the point in time is omitted, i.e. $\boldsymbol{x} \coloneqq \boldsymbol{x}_t$ for the current position and $\Omega \coloneqq \Omega_t$ as current configuration. In *Lagrangian* (also called *material*) description of quantities or relations is with respect to the reference configuration, whereas the actual configuration is used in the *Eulerian* (also called *spatial*) description.

3.1.1 Kinematics

The motion $\boldsymbol{\varphi} : \Omega_0 \times I \to \mathbb{R}^d$ of the aforementioned body is defined to be the mapping $(\boldsymbol{X}, t) \mapsto \boldsymbol{\varphi}(\boldsymbol{X}, t) = \boldsymbol{x}$ and assumed to be a C^∞-diffeomorphism and to be globally injective. Due to the assumption of a smooth motion in time, the regularity requirement is strengthened to C^∞, although suitable finite continuity may be sufficient. Hence for all one-to-one mappings $\boldsymbol{\varphi}((\cdot), t) \in C^\infty(\Omega_0 \times I) : \Omega_0 \to \Omega$ for a given time t there exists an inverse one-to-one mapping $\boldsymbol{\varphi}^{-1}((\cdot), t) \in C^\infty(\Omega) : \Omega \to \Omega_0$, where $\boldsymbol{\varphi}^{-1}(\boldsymbol{x}, t) = \boldsymbol{X}$. Regarding time differentiation, we introduce $\dot{\boldsymbol{\varphi}} \coloneqq {}^{\partial\boldsymbol{\varphi}}/_{\partial t}$ and $\ddot{\boldsymbol{\varphi}} \coloneqq {}^{\partial^2\boldsymbol{\varphi}}/_{\partial t^2}$ as velocity and acceleration, respectively. The material deformation gradient is defined by

$$\boldsymbol{F} : \Omega_0 \to \mathbb{R}^{d\times d}, \quad \boldsymbol{F} = \nabla_{\!\mathrm{X}}\, \boldsymbol{x} = \nabla_{\!\mathrm{X}}\, \boldsymbol{\varphi} \tag{3.1}$$

which maps infinitesimal vectors $\mathrm{d}\boldsymbol{X}$ at the material point $\boldsymbol{X}$ in the reference configuration Ω_0 to the infinitesimal vector $\mathrm{d}\boldsymbol{x}$ at $\boldsymbol{x}$ in the deformed configuration Ω. Applying the chain rule on the composition $\boldsymbol{\varphi}^{-1}(\boldsymbol{\varphi}(\boldsymbol{X}, t), t) = \boldsymbol{X}$ leads to $(\nabla_{\!\mathrm{X}}\, \boldsymbol{\varphi}(\boldsymbol{X}, t))^{-1} = \nabla_{\!\mathrm{X}}\, \boldsymbol{\varphi}^{-1}((\boldsymbol{x}, t), t)$, yielding $\mathrm{d}\boldsymbol{x} = \boldsymbol{F}\mathrm{d}\boldsymbol{X}$ and $\mathrm{d}\boldsymbol{X} = \boldsymbol{F}^{-1}\mathrm{d}\boldsymbol{x}$. By taking the determinant of the deformation gradient $J(\boldsymbol{x}, t) \coloneqq \det(\boldsymbol{F})$ we get the volume transformation $\mathrm{d}V_t = J\mathrm{d}V$, where from the inverse mapping follows $J \neq 0$. We further demand $J > 0$, thus the deformation is orientation preserving and thereby ruling out interpenetration making the deformation mapping locally bijective.

By taking two linearly independent vectors $\boldsymbol{X}^{(1)}, \boldsymbol{X}^{(2)}$ at the boundary $\partial\Omega_0$ and outward reference normal vector $\boldsymbol{N}$, we can construct a three-edge parallelepiped with the infinitesimal area element $\mathrm{d}A$ via the cross product $\mathrm{d}\boldsymbol{X}^{(1)} \times \mathrm{d}\boldsymbol{X}^{(2)} = \boldsymbol{N}\mathrm{d}A$. When mapping the edges with the deformation gradient, we arrive at the well-known Nanson's formula $\boldsymbol{n}\mathrm{d}a = \mathrm{cof}(\boldsymbol{F})\boldsymbol{N}\mathrm{d}A$, where $\boldsymbol{H}$ is the co-factor or adjoint tensor given by

$$\boldsymbol{H} \coloneqq \mathrm{cof}(\boldsymbol{F}) = J\boldsymbol{F}^{-\top} = \frac{1}{2}(\boldsymbol{F} \bar{\times} \boldsymbol{F}). \tag{3.2}$$

Here, we used the formulation using the tensor-cross-product (see section 0.2). Using the cofactor, the Jacobian determinant can also be computed using

$$J = \det(\boldsymbol{F}) = \frac{1}{6}\boldsymbol{F} : (\boldsymbol{F} \bar{\times} \boldsymbol{F}). \tag{3.3}$$

A graphical representation of the different kinematical values is given in figure 3.1.1, see Betsch et al. [14] for further details.

The first order deformation gradient can be represented by

$$\boldsymbol{F} = \sum_i^d \lambda_i \, \boldsymbol{a}_i \otimes \boldsymbol{A}_i \,, \tag{3.4}$$

with eigenvalues (*principal stretches*) λ_i and principal directions $\boldsymbol{a}_i$ in the actual and $\boldsymbol{A}_i$ in the referential configuration. We then can express the additional first order kinematical set as follows

$$J = \prod_i^d \lambda_i \quad \text{and} \quad \boldsymbol{H} = \sum_i^d \lambda_j\lambda_k \, \boldsymbol{a}_i \otimes \boldsymbol{A}_i \,, \tag{3.5}$$

where $\{i, j, k\}$ is a permutation of $\{1, 2, 3\}$ for the case $d = 3$.

Remark 3.1.1 – Principal stretches. The deformation gradient $\boldsymbol{F}$ can be decomposed using left and right principal directions, $\boldsymbol{n}_i$ and $\boldsymbol{N}_i$, respectively, using

$$\boldsymbol{F}^\top \boldsymbol{a}_i = \lambda_i \, \boldsymbol{A}_i \quad \text{and} \quad \boldsymbol{F}\boldsymbol{A}_i = \lambda_i \, \boldsymbol{a}_i \,. \tag{3.6}$$

This can be linked to the computational detour of the polar composition $\boldsymbol{F} = \boldsymbol{R}\boldsymbol{U}$ with rotation matrix $\boldsymbol{R}$ and stretch tensor $\boldsymbol{U}$. Applying the eigenvalue decomposition on the stretches $\boldsymbol{U} = \sum_i^d \lambda_i \, \boldsymbol{A}_i \otimes \boldsymbol{A}_i$ and reinserting into the deformation gradient yields

$$\boldsymbol{F} = \boldsymbol{R}\sum_i^d \lambda_i \boldsymbol{A}_i \otimes \boldsymbol{A}_i = \sum_i^d \lambda_i (\boldsymbol{R}\boldsymbol{A}_i) \otimes \boldsymbol{A}_i = \sum_i^d \lambda_i \, \boldsymbol{a}_i \otimes \boldsymbol{A}_i \,, \tag{3.7}$$

with the eigenvectors $\boldsymbol{a}_i = \boldsymbol{R}\boldsymbol{A}_i$ rotated from the reference into the current position. Note, that $\boldsymbol{a}_i$ and $\boldsymbol{A}_i$ can be obtained by utilizing

$$\boldsymbol{b} = \boldsymbol{F}\boldsymbol{F}^\top = \boldsymbol{R}\boldsymbol{U}\boldsymbol{U}^\top\boldsymbol{R}^\top = \boldsymbol{R}\boldsymbol{U}^2\boldsymbol{R}^\top = \sum_i^d \lambda_i^2 \, \boldsymbol{a}_i \otimes \boldsymbol{a}_i \tag{3.8}$$

and

$$\boldsymbol{C} = \boldsymbol{F}^\top\boldsymbol{F} = \boldsymbol{U}^\top\boldsymbol{R}^\top\boldsymbol{R}\boldsymbol{U} = \boldsymbol{U}^2 = \sum_i^d \lambda_i^2 \, \boldsymbol{A}_i \otimes \boldsymbol{A}_i \,. \tag{3.9}$$

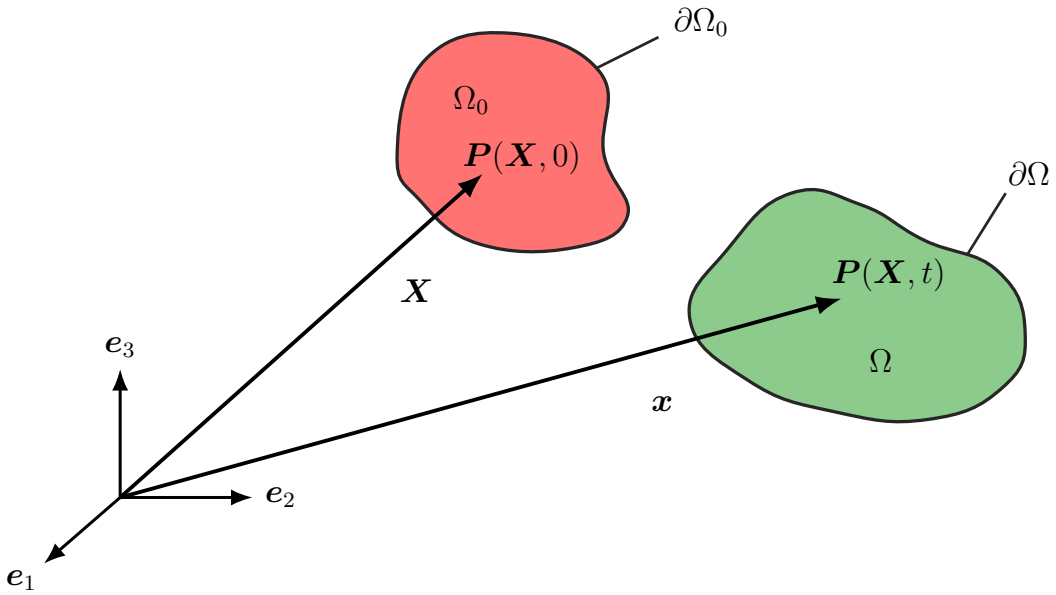


Figure 3.1.1 – Generalized continuum: kinematics. Graphical representation of kinematics at different configurations.

3.1.2 Second-order continuum

Extending from the classical so called *Cauchy continuum* in which deformation measures relating to the first gradient play a role, we extend the kinematical description towards higher gradients. Note, that upon dividing the boundary surface into a collection of patches we may introduce $\partial^2\Omega_0$ as set of curves on the boundary, cf. among others Javili et al. [62]. Therein also a discussion on the normal $\hat{\boldsymbol{N}}$, tangential to $\partial\Omega_0$ can be found. Regarding differentiability, we require sufficiently smooth fields in a neighborhood of the surface. Along $\partial^2\Omega_0$, we identify $\mathrm{d}S$ as the infinitesimal line element along the edges of these subsets of $\partial\Omega_0$.

The second-order deformation measure $\mathfrak{F}\colon \Omega_0 \to \mathbb{R}^{d\times d\times d}$ is then given by the second gradient of the mapping $\varphi(X)$ as

$$\mathfrak{F} := \nabla_{\mathrm{X}} \boldsymbol{F} = \nabla^2_{\mathrm{X}} \boldsymbol{\varphi}\,, \tag{3.10}$$

with symmetry on the last two indices $\mathfrak{F}^{\top 32} = \mathfrak{F}^{\top 23}$. We note that $\mathfrak{F}$ is proportional to the reciprocal length scale $\mathfrak{F} \propto \xi^{-1}$, whereas the first order deformation gradient is dimensionless. In general, we identify for the n^{th} order deformation gradient $\nabla^n_{\mathrm{X}} \propto \xi^{1-n}$. The presence and the material reaction to higher gradients (> 1) leads to the term of a *generalized continuum.*

3.2 Constitutive Framework and variational formulation

For the body we assume the existence of a suitable energy potential Ψ, also called the Helmholtz free energy density function, to account for the material response to deformation, see Agiasofitou and Lazar [1], Javili et al. [62], and Mindlin [87]. Here, Ψ depends on the first- and second-order deformation gradient and we define

$$\Psi := \Psi(\boldsymbol{X}, \boldsymbol{F}, \mathfrak{F}) = \Psi\Big(\boldsymbol{X}, \nabla_{\mathrm{x}}\boldsymbol{\varphi}, \nabla^2_{\mathrm{x}}\boldsymbol{\varphi}\Big) \colon \Omega_0 \to \mathbb{R}. \tag{3.11}$$

In contrast to classical or first order materials, where the dependency solely lies on the first gradient $\nabla_{\mathrm{x}}\boldsymbol{\varphi}$, this formulation allows to capture size effects, surface and edge phenomena as can be seen in the following paragraphs, and the mechanics of materials with microstructure Eringen [36], Mindlin [85], and Toupin [116].

Remark 3.2.1 – Higher order material laws. Note, that only a few examples of higher-order strain energy formulations exist in the literature. We refer, among others, to dell'Isola et al. [31], where a Piola homogenization procedure was employed to derive an appropriate formulation. We will show the specific construction of this type of gradient material formulation based on a continuum approach for fiber reinforced composites in chapter 4 as well as a natural result of a discrete fiber insertion in the context of the multidimensional beam coupling in chapter 5.

Integration over the body gives the internal stored energy $\Pi^{\mathrm{int}} \colon \Omega_0 \to \mathbb{R}$, where

$$\Pi^{\mathrm{int}} := \Pi^{\mathrm{int}}\Big(\boldsymbol{X}, \nabla_{\mathrm{x}}\boldsymbol{\varphi}, \nabla^2_{\mathrm{x}}\boldsymbol{\varphi}\Big) = \int_{\Omega_0} \Big\{ \Psi\Big(\boldsymbol{X}, \nabla_{\mathrm{x}}\boldsymbol{\varphi}, \nabla^2_{\mathrm{x}}\boldsymbol{\varphi}\Big) \Big\} \mathrm{d}V \,. \tag{3.12}$$

Further, we introduce the scalar mass density ρ_0 of the reference configuration, such that the kinetic energy $\Pi^{\mathrm{kin}} \colon \Omega_0 \to \mathbb{R}$ is given by

$$\Pi^{\mathrm{kin}} := \Pi^{\mathrm{kin}}(\dot{\boldsymbol{\varphi}}) = \int_{\Omega_0} \Big\{ \frac{1}{2} \rho_0 \|\dot{\boldsymbol{\varphi}}\|^2 \Big\} \mathrm{d}V \,, \tag{3.13}$$

with the time derivative of the map $\dot{\boldsymbol{\varphi}}$. Finally, external work due to forces is collected in

$$\Pi^{\mathrm{ext}} := \Pi^{\mathrm{ext}}\Big(\boldsymbol{X}, \nabla_{\mathrm{x}}\boldsymbol{\varphi}, \nabla^2_{\mathrm{x}}\boldsymbol{\varphi}\Big) \colon \Omega_0 \to \mathbb{R} \,, \tag{3.14}$$

such that the Lagrangian function is the energy difference between these three energies

$$\mathfrak{L}\Big(\boldsymbol{X}, \nabla_{\mathrm{x}}\boldsymbol{\varphi}, \nabla^2_{\mathrm{x}}\boldsymbol{\varphi}, \dot{\boldsymbol{\varphi}}\Big) = \int_{\Omega_0} \Big\{ \mathcal{L}\Big(\boldsymbol{X}, \nabla_{\mathrm{x}}\boldsymbol{\varphi}, \nabla^2_{\mathrm{x}}\boldsymbol{\varphi}, \dot{\boldsymbol{\varphi}}\Big) \Big\} \mathrm{d}V = \Pi^{\mathrm{kin}} - \Pi^{\mathrm{int}} + \Pi^{\mathrm{ext}} \,, \tag{3.15}$$

conform to the classical formulation $\mathfrak{L} = T - V$, with kinematic energy $T := \Pi^{\mathrm{kin}}$ and potential energy $V := \Pi^{\mathrm{int}} - \Pi^{\mathrm{ext}}$.

3.2.1 Hamilton's principle and variational calculus

In order to derive balance equations as well as to identify boundary conditions and external contributions, we apply the principle of stationary action. It postulates for the evolution of the system between two specified states $t_1, t_2 \in I$, that the action functional $\mathcal{A}$ as the time integral over the Lagrangian is stationary with respect to admissible variations. For stationarity, the variation $\delta\mathcal{A}$ must be zero and is then given by

$$\begin{aligned}\delta\mathcal{A}\left[\boldsymbol{\varphi}\right] &= \delta \int_{t_1}^{t_2} \Big\{ \mathfrak{L}\Big(\boldsymbol{X}, \nabla_{\mathrm{x}}\boldsymbol{\varphi}, \nabla_{\mathrm{x}}^2\boldsymbol{\varphi}, \dot{\boldsymbol{\varphi}}\Big) \Big\} \mathrm{d}t \\ &= \int_{t_1}^{t_2} \Big\{ \delta\Pi^{\mathrm{kin}}(\dot{\boldsymbol{\varphi}}) - \delta\Pi^{\mathrm{int}}\Big(\boldsymbol{X}, \nabla_{\mathrm{x}}\boldsymbol{\varphi}, \nabla_{\mathrm{x}}^2\boldsymbol{\varphi}\Big) + \delta\Pi^{\mathrm{ext}}\Big(\boldsymbol{X}, \nabla_{\mathrm{x}}\boldsymbol{\varphi}, \nabla_{\mathrm{x}}^2\boldsymbol{\varphi}\Big) \Big\} \mathrm{d}t = 0\,.\end{aligned} \tag{3.16}$$

Remark 3.2.2 – Second variation. Note that for sufficiency of the minimization problem eq. (3.16), the second-order *Legendre-Clebsch condition* has to be fulfilled, see also eq. (3.117).

For the variations, we separate the boundary $\partial\Omega_0$ using

$$\partial\Omega_0 = \partial\Omega_0^{\varphi} \cup \partial\Omega_0^{T}\,, \quad \text{where} \quad \partial\Omega_0^{\varphi} \cap \partial\Omega_0^{T} = \emptyset\,, \tag{3.17}$$

to provide first order essential (Dirichlet) and natural (Neumann) conditions on $\partial\Omega_0^{\varphi}$ and $\partial\Omega_0^{T}$, respectively. For the second-order boundary, we correspondingly introduce

$$\partial\Omega_0 = \partial\Omega_0^{\nabla\varphi} \cup \partial\Omega_0^{M}\,, \quad \text{where} \quad \partial\Omega_0^{\nabla\varphi} \cap \partial\Omega_0^{M} = \emptyset\,. \tag{3.18}$$

Then, we define the variational function of the motion $\delta\boldsymbol{\varphi}$ with the space of admissible variation functions

$$\mathcal{V}_{\delta\boldsymbol{\varphi}} = \Big\{ \delta\boldsymbol{\varphi} \in \mathcal{H}^2(\Omega_0) \mid \delta\boldsymbol{\varphi} = \boldsymbol{0} \text{ on } \partial\Omega_0^{\varphi} \times I\,, \quad \nabla_{\mathrm{x}}\delta\boldsymbol{\varphi}\boldsymbol{N} = \boldsymbol{0} \text{ on } \partial\Omega_0^{\nabla\varphi} \times I \Big\} \tag{3.19}$$

and additionally require $\delta\boldsymbol{\varphi}(\boldsymbol{X}, t_1) = \delta\boldsymbol{\varphi}(\boldsymbol{X}, t_2) = \boldsymbol{0}$ as well as $\nabla_{\mathrm{x}}\delta\boldsymbol{\varphi}(t_1) = \nabla_{\mathrm{x}}\delta\boldsymbol{\varphi}(t_2) = \boldsymbol{0}$ making the variations vanish for known values of $\boldsymbol{\varphi}$, also denoted as essential or Dirichlet boundaries. Varying with respect to the arguments and applying integration by parts on the temporal derivative yields

$$\begin{aligned}\int_{t_1}^{t_2} \Big\{ \delta\Pi^{\mathrm{kin}} \Big\} \mathrm{d}t &= \int_{t_1}^{t_2} \Bigg\{ \delta \int_{\Omega_0} \Big\{ \frac{1}{2}\rho_0 \|\dot{\boldsymbol{\varphi}}\|^2 \Big\} \mathrm{d}V \Bigg\} \mathrm{d}t \\ &= \int_{t_1}^{t_2} \Bigg\{ \int_{\Omega_0} \Big\{ \rho_0 \dot{\boldsymbol{\varphi}} \cdot \delta\dot{\boldsymbol{\varphi}} \Big\} \mathrm{d}V \Bigg\} \mathrm{d}t \\ &= \left[\rho_0 \dot{\boldsymbol{\varphi}} \cdot \delta\boldsymbol{\varphi}\right]_{t_1}^{t_2} - \int_{t_1}^{t_2} \Bigg\{ \int_{\Omega_0} \{ \rho_0 \ddot{\boldsymbol{\varphi}} \cdot \delta\boldsymbol{\varphi} \} \mathrm{d}V \Bigg\} \mathrm{d}t \\ &= -\int_{t_1}^{t_2} \Bigg\{ \int_{\Omega_0} \{ \delta\boldsymbol{\varphi} \cdot (\rho_0 \ddot{\boldsymbol{\varphi}}) \} \mathrm{d}V \Bigg\} \mathrm{d}t\,,\end{aligned} \tag{3.20}$$

where $\int_{\Omega_0}\{\rho_0\ddot{\boldsymbol{\varphi}}\}\mathrm{d}V$ gives the time derivative of the linear momentum for constant ρ_0. Regarding the internal energy, variation with respect to the deformation map leads to

$$\begin{aligned}\delta\Pi^{\mathrm{int}} &= \delta\int_{\Omega_0}\Big\{\Psi\Big(\boldsymbol{X},\nabla_{\mathrm{x}}\boldsymbol{\varphi},\nabla_{\mathrm{x}}^2\boldsymbol{\varphi}\Big)\Big\}\mathrm{d}V\\ &= \int_{\Omega_0}\left\{\frac{\partial\Psi}{\partial\nabla_{\mathrm{x}}\boldsymbol{\varphi}}:\nabla_{\mathrm{x}}\delta\boldsymbol{\varphi}+\frac{\partial\Psi}{\partial\nabla_{\mathrm{x}}^2\boldsymbol{\varphi}}:\nabla_{\mathrm{x}}^2\delta\boldsymbol{\varphi}\right\}\mathrm{d}V\\ &= \int_{\Omega_0}\Big\{\boldsymbol{P}:\nabla_{\mathrm{x}}\delta\boldsymbol{\varphi}+\boldsymbol{\mathfrak{P}}:\nabla_{\mathrm{x}}^2\delta\boldsymbol{\varphi}\Big\}\mathrm{d}V\,.\end{aligned}\tag{3.21}$$

Therein we identify the first order stress tensor, also known as First Piola-Kirchhoff stress tensor, and the second-order (hyper-) stress tensor defined as

$$\boldsymbol{P}\coloneqq\frac{\partial\Psi}{\partial\nabla_{\mathrm{x}}\boldsymbol{\varphi}}=\frac{\partial\Psi}{\partial\boldsymbol{F}}\quad\text{and}\quad\boldsymbol{\mathfrak{P}}\coloneqq\frac{\partial\Psi}{\partial\nabla_{\mathrm{x}}^2\boldsymbol{\varphi}}=\frac{\partial\Psi}{\partial\boldsymbol{\mathfrak{F}}}\,,\tag{3.22}$$

respectively. In the following, we restrict Ψ not to be directly depending on the position field, hence $\frac{\partial\Psi}{\partial\boldsymbol{\varphi}}=\boldsymbol{0}$. In order to derive boundary conditions relating to terms in $\delta\Pi^{\mathrm{ext}}$, we conduct integration by parts twice resulting in

$$\begin{aligned}\delta\Pi^{\mathrm{int}} &= \int_{\Omega_0}\{-\delta\boldsymbol{\varphi}\cdot(\nabla_{\mathrm{x}}\cdot\boldsymbol{P})+\nabla_{\mathrm{x}}\cdot(\delta\boldsymbol{\varphi}\cdot\boldsymbol{P})-\nabla_{\mathrm{x}}\cdot\boldsymbol{\mathfrak{P}}:\nabla_{\mathrm{x}}\delta\boldsymbol{\varphi}+\nabla_{\mathrm{x}}\cdot(\nabla_{\mathrm{x}}\delta\boldsymbol{\varphi}:\boldsymbol{\mathfrak{P}})\}\mathrm{d}V\\ &= \int_{\Omega_0}\{\delta\boldsymbol{\varphi}\cdot(\nabla_{\mathrm{x}}\cdot(\nabla_{\mathrm{x}}\cdot\boldsymbol{\mathfrak{P}}-\boldsymbol{P}))+\nabla_{\mathrm{x}}\cdot(\delta\boldsymbol{\varphi}\cdot(\boldsymbol{P}-\nabla_{\mathrm{x}}\cdot\boldsymbol{\mathfrak{P}}))+\nabla_{\mathrm{x}}\cdot(\nabla_{\mathrm{x}}\delta\boldsymbol{\varphi}:\boldsymbol{\mathfrak{P}})\}\mathrm{d}V.\end{aligned}\tag{3.23}$$

Remark 3.2.3 – Divergence theorem. The first order divergence theorem applied to smooth first, second and third order tensor fields $\boldsymbol{a}\in\mathbb{R}^d$, $\boldsymbol{B}\in\mathbb{R}^{d\times d}$ and $\boldsymbol{\mathcal{C}}\in\mathbb{R}^{d\times d\times d}$ reads

$$\int_{\Omega_0}\{\nabla_{\mathrm{x}}\cdot(\boldsymbol{a}\cdot\boldsymbol{B})\}\mathrm{d}V=\int_{\partial\Omega_0}\{\boldsymbol{a}\cdot\boldsymbol{B}\cdot\boldsymbol{N}\}\mathrm{d}A\,,\quad\int_{\Omega_0}\{\nabla_{\mathrm{x}}\cdot(\boldsymbol{B}:\boldsymbol{\mathcal{C}})\}\mathrm{d}V=\int_{\partial\Omega_0}\{\boldsymbol{B}:\boldsymbol{\mathcal{C}}\cdot\boldsymbol{N}\}\mathrm{d}A\tag{3.24}$$

The higher-order divergence theorem (see Gurtin [50], Mindlin [85], and Toupin [116]) furthermore states

$$\int_{\Omega_0}\{\nabla_{\mathrm{x}}\cdot\nabla_{\mathrm{x}}\cdot\boldsymbol{\mathcal{C}}\}\mathrm{d}V=\int_{\partial\Omega_0}\{\nabla_{\mathrm{x}}\cdot\boldsymbol{\mathcal{C}}\cdot\boldsymbol{N}\}\mathrm{d}A-\int_{\partial\Omega_0}\{\boldsymbol{\mathcal{C}}:\nabla_{\mathrm{x}}\boldsymbol{N}\}\mathrm{d}A+\int_{\partial^2\Omega_0}\Big\{\boldsymbol{\mathcal{C}}:\Big(\hat{\boldsymbol{N}}\otimes\boldsymbol{N}\Big)\Big\}\mathrm{d}S\,.\tag{3.25}$$

Further we make use of the divergence theorem (cf. remark 3.2.3) on the second and third term of eq. (3.23), yielding

$$\delta\Pi^{\text{int}} = \int_{\Omega_0} \{\delta\boldsymbol{\varphi} \cdot (\nabla_{\text{x}} \cdot (\nabla_{\text{x}} \cdot \boldsymbol{\mathfrak{P}} - \boldsymbol{P}))\} \mathrm{d}V + \int_{\partial\Omega_0} \{\delta\boldsymbol{\varphi} \cdot ((\boldsymbol{P} - \nabla_{\text{x}} \cdot \boldsymbol{\mathfrak{P}})\, \boldsymbol{N}) + \nabla_{\text{x}} \delta\boldsymbol{\varphi} : (\boldsymbol{\mathfrak{P}}\, \boldsymbol{N})\} \mathrm{d}A. \quad (3.26)$$

For the separation of higher order boundary contributions, we introduce the orthogonal decomposition $\nabla_{\text{x}\perp} \cdot (\cdot) = \nabla_{\text{x}}(\cdot) : (\boldsymbol{N} \otimes \boldsymbol{N})$ and $\nabla_{\text{x}\parallel} \cdot (\cdot) = \nabla_{\text{x}}(\cdot) : (\boldsymbol{I} - \boldsymbol{N} \otimes \boldsymbol{N})$, such that for the last term follows

$$\begin{aligned} \nabla_{\text{x}} \delta\boldsymbol{\varphi} : (\boldsymbol{\mathfrak{P}}\, \boldsymbol{N}) &= \nabla_{\text{x}} \cdot (\delta\boldsymbol{\varphi}\, \boldsymbol{\mathfrak{P}}\, \boldsymbol{N}) - \delta\boldsymbol{\varphi} \cdot \nabla_{\text{x}} \cdot (\boldsymbol{\mathfrak{P}}\, \boldsymbol{N}) \\ &= \nabla_{\text{x}\perp} \cdot (\delta\boldsymbol{\varphi}\, \boldsymbol{\mathfrak{P}}\, \boldsymbol{N}) + \nabla_{\text{x}\parallel} \cdot (\delta\boldsymbol{\varphi}\, \boldsymbol{\mathfrak{P}}\, \boldsymbol{N}) \\ &\quad - \delta\boldsymbol{\varphi} \cdot \nabla_{\text{x}\perp} \cdot (\boldsymbol{\mathfrak{P}}\, \boldsymbol{N}) - \delta\boldsymbol{\varphi} \cdot \nabla_{\text{x}\parallel} \cdot (\boldsymbol{\mathfrak{P}}\, \boldsymbol{N}). \end{aligned} \quad (3.27)$$

Applying the product rule for the orthogonal component

$$\delta\boldsymbol{\varphi} \cdot \nabla_{\text{x}\perp} \cdot (\boldsymbol{\mathfrak{P}}\, \boldsymbol{N}) = \nabla_{\text{x}\perp} \cdot (\delta\boldsymbol{\varphi}\, \boldsymbol{\mathfrak{P}}\, \boldsymbol{N}) - \nabla_{\text{x}\perp} \delta\boldsymbol{\varphi} : (\boldsymbol{\mathfrak{P}}\, \boldsymbol{N}) \quad (3.28)$$

and the divergence theorem on the parallel component

$$\int_{\partial\Omega_0} \left\{\nabla_{\text{x}\parallel} \cdot (\delta\boldsymbol{\varphi}\, \boldsymbol{\mathfrak{P}}\, \boldsymbol{N})\right\} \mathrm{d}A = \int_{\partial^2\Omega_0} \left\{(\delta\boldsymbol{\varphi}\, \boldsymbol{\mathfrak{P}}\, \boldsymbol{N}) \cdot \hat{\boldsymbol{N}}\right\} \mathrm{d}S - \int_{\partial\Omega_0} \{K\, (\delta\boldsymbol{\varphi}\, \boldsymbol{\mathfrak{P}}\, \boldsymbol{N}) \cdot \boldsymbol{N}\} \mathrm{d}A, \quad (3.29)$$

we obtain for the last term in eq. (3.26)

$$\begin{aligned} &\int_{\partial\Omega_0} \{\nabla_{\text{x}} \delta\boldsymbol{\varphi} : (\boldsymbol{\mathfrak{P}}\, \boldsymbol{N})\} \mathrm{d}A \\ &\qquad = -\int_{\partial\Omega_0} \left\{\delta\boldsymbol{\varphi} \cdot \left(K\, (\boldsymbol{\mathfrak{P}}\, \boldsymbol{N})\boldsymbol{N} + \nabla_{\text{x}\parallel} \cdot (\boldsymbol{\mathfrak{P}}\, \boldsymbol{N})\right) - \nabla_{\text{x}\perp} \delta\boldsymbol{\varphi} : (\boldsymbol{\mathfrak{P}}\, \boldsymbol{N})\right\} \mathrm{d}A \\ &\qquad\qquad + \int_{\partial^2\Omega_0} \left\{\delta\boldsymbol{\varphi} \cdot \left(\boldsymbol{\mathfrak{P}} : \left(\hat{\boldsymbol{N}} \otimes \boldsymbol{N}\right)\right)\right\} \mathrm{d}S. \end{aligned} \quad (3.30)$$

with the curvature of the surface $K \coloneqq -\nabla_{\text{x}\parallel} \cdot \boldsymbol{N}$.

Remark 3.2.4 – Higher order boundaries. We remark here that, depending on the exact formulation of the energy density or with derived higher order gradient models like Grioli-Koiter-Mindlin-Toupin indeterminate couple stress model, surface conditions involving $\text{curl}(\boldsymbol{u}) = \nabla \times \boldsymbol{u}$ may arise. We refer to Madeo et al. [77] and again Javili et al. [62] among others on a discussion of (independent) geometric and traction boundaries.

Combining all of the above, the virtual internal energy reads

$$\begin{aligned}\delta\Pi^{\text{int}} = &\int_{\Omega_0}\{\delta\boldsymbol{\varphi}\cdot(-\nabla_{\text{X}}\cdot(\boldsymbol{P}-\nabla_{\text{X}}\cdot\mathfrak{P}))\}\mathrm{d}V\\ &+\int_{\partial\Omega_0}\Big\{\delta\boldsymbol{\varphi}\cdot\Big((\boldsymbol{P}-\nabla_{\text{X}}\cdot\mathfrak{P})\,\boldsymbol{N}-K\,(\mathfrak{P}\,\boldsymbol{N})\boldsymbol{N}-\nabla_{\text{X}\parallel}\cdot(\mathfrak{P}\,\boldsymbol{N})\Big)\Big\}\mathrm{d}A\\ &+\int_{\partial\Omega_0}\{\nabla_{\text{X}\perp}\delta\boldsymbol{\varphi}:(\mathfrak{P}\,\boldsymbol{N})\}\mathrm{d}A+\int_{\partial^2\Omega_0}\Big\{\delta\boldsymbol{\varphi}\cdot\Big(\mathfrak{P}:\Big(\hat{\boldsymbol{N}}\otimes\boldsymbol{N}\Big)\Big)\Big\}\mathrm{d}S. \end{aligned}\tag{3.31}$$

Inspecting the surface and line terms, we can derive a set of natural boundary conditions constituting external contributions along with volumetric body forces. Hence, we have

$$\delta\Pi^{\text{ext}} = \int_{\Omega_0}\Big\{\delta\boldsymbol{\varphi}\cdot\overline{\boldsymbol{B}}\Big\}\mathrm{d}V+\int_{\partial\Omega_0^T}\Big\{\delta\boldsymbol{\varphi}\cdot\overline{\boldsymbol{T}}\Big\}\mathrm{d}A+\int_{\partial\Omega_0^M}\Big\{\nabla_{\text{X}\perp}\delta\boldsymbol{\varphi}:\overline{\boldsymbol{M}}\Big\}\mathrm{d}A+\int_{\partial^2\Omega_0^L}\Big\{\delta\boldsymbol{\varphi}\cdot\ \overline{\boldsymbol{L}}\Big\}\mathrm{d}S \tag{3.32}$$

with the common body force per unit volume $\overline{\boldsymbol{B}}$, the traction forces $\overline{\boldsymbol{T}}$ on $\partial\Omega_0^T$ and the hyper-stress traction force $\overline{\boldsymbol{M}}$ on $\partial\Omega_0^M$. For completeness, we included the line forces $\overline{\boldsymbol{L}}$ on boundary $\partial^2\Omega_0^N$. In general we mark external contributions with an overline $\overline{(\cdot)}$. Insertion of the virtual energy contributions eq. (3.20), eq. (3.21) and eq. (3.32) into the action functional eq. (3.16) finally yields

$$\begin{aligned}\delta\mathcal{A}\,[\boldsymbol{\varphi}] = \int_{t_1}^{t_2}\Bigg\{&\int_{\Omega_0}\{-\delta\boldsymbol{\varphi}\cdot(\rho_0\ddot{\boldsymbol{\varphi}})\}\mathrm{d}V-\int_{\Omega_0}\Big\{\boldsymbol{P}:\nabla_{\text{X}}\delta\boldsymbol{\varphi}+\mathfrak{P}\vdots\nabla_{\text{X}}^2\delta\boldsymbol{\varphi}\Big\}\mathrm{d}V\\ &+\int_{\Omega_0}\Big\{\delta\boldsymbol{\varphi}\cdot\overline{\boldsymbol{B}}\Big\}\mathrm{d}V+\int_{\partial\Omega_0^T}\Big\{\delta\boldsymbol{\varphi}\cdot\overline{\boldsymbol{T}}\Big\}\mathrm{d}A+\int_{\partial\Omega_0^M}\Big\{\nabla_{\text{X}\perp}\delta\boldsymbol{\varphi}:\overline{\boldsymbol{M}}\Big\}\mathrm{d}A+\int_{\partial^2\Omega_0^L}\Big\{\delta\boldsymbol{\varphi}\cdot\ \overline{\boldsymbol{L}}\Big\}\mathrm{d}S\Bigg\}\mathrm{d}t\,.\end{aligned}\tag{3.33}$$

By comparison with eq. (3.31), we obtain for arbitrariness of variations $\delta\boldsymbol{\varphi}$ in time and space the corresponding strong form of the as law of motion (*Euler-Lagrange equation*)

$$\rho_0\ddot{\boldsymbol{\varphi}} = \nabla_{\text{X}}\cdot(\boldsymbol{P}-\nabla_{\text{X}}\cdot\mathfrak{P})+\overline{\boldsymbol{B}}\,, \tag{3.34}$$

with the set of Neumann boundaries

$$\begin{aligned}(\boldsymbol{P}-\nabla_{\text{X}}\cdot\mathfrak{P})\,\boldsymbol{N}-K\,(\mathfrak{P}\,\boldsymbol{N})\boldsymbol{N}-\nabla_{\text{X}\parallel}\cdot(\mathfrak{P}\,\boldsymbol{N}) &= \overline{\boldsymbol{T}}(\boldsymbol{X},t) \quad \text{on} \quad \partial\Omega_0^T\times I\\ \mathfrak{P}\,\boldsymbol{N} &= \overline{\boldsymbol{M}}(\boldsymbol{X},t) \quad \text{on} \quad \partial\Omega_0^M\times I\\ \mathfrak{P}:\Big(\hat{\boldsymbol{N}}\otimes\boldsymbol{N}\Big) &= \overline{\boldsymbol{L}}(\boldsymbol{X},t) \quad \text{on} \quad \partial^2\Omega_0^N\times I\,,\end{aligned}\tag{3.35}$$

Dirichlet conditions

$$\begin{aligned}\boldsymbol{\varphi}(\boldsymbol{X},t) &= \overline{\boldsymbol{\varphi}} \quad \text{on} \quad \partial\Omega_0^{\varphi}\times I\\ \nabla_{\text{X}}\boldsymbol{\varphi}\boldsymbol{N} &= \overline{\nabla_{\text{X}}\boldsymbol{\varphi}\boldsymbol{N}} \quad \text{on} \quad \partial\Omega_0^{\nabla\varphi}\times I\end{aligned}\tag{3.36}$$

and initial configuration

$$\boldsymbol{\varphi}(\boldsymbol{X},0)=\boldsymbol{X}\,,\quad \dot{\boldsymbol{\varphi}}(\boldsymbol{X},0)=\overline{\boldsymbol{v}_0}\quad\text{and}\quad\ddot{\boldsymbol{\varphi}}(\boldsymbol{X},0)=\overline{\boldsymbol{a}_0}\,. \tag{3.37}$$

3.3 Conservation Properties and Noether's Theorem

Noether´s theorem focuses on symmetry aspects of a physical system. Therefore following Marsden and Hughes [78], we take a general vector field $\boldsymbol{\eta} \in \mathcal{Q}$ with associated C^1-continuous flow $\boldsymbol{q}'_\varepsilon$ by

$$\left[\frac{\mathrm{d}\boldsymbol{q}'_\varepsilon(\boldsymbol{q},\varepsilon)}{\mathrm{d}\varepsilon}\right]\Bigg|_{\varepsilon=0} = \boldsymbol{\eta}(\boldsymbol{q})\,. \tag{3.38}$$

If it holds for a function $\boldsymbol{\mathcal{F}}$

$$\boldsymbol{\mathcal{F}}(\boldsymbol{q},\nabla\boldsymbol{q}) = \boldsymbol{\mathcal{F}}\left(\boldsymbol{q}'_\varepsilon, \frac{\partial\boldsymbol{q}'_\varepsilon}{\partial\boldsymbol{q}}\cdot(\nabla\boldsymbol{q})\right), \tag{3.39}$$

then $\boldsymbol{\mathcal{F}}$ is symmetric (*invariant*) under the flow $\boldsymbol{q}'_\varepsilon$. We identify $\mathcal{Q} = \mathbb{R}^3\times I$ with $\boldsymbol{q} = \{\boldsymbol{\varphi}, t\}$ and inspect symmetries in space ($\boldsymbol{\varphi}$) and time (t) separately, giving

$$\left[\frac{\mathrm{d}\boldsymbol{\varphi}'_\varepsilon}{\mathrm{d}\varepsilon}\right]\Bigg|_{\varepsilon=0} = \boldsymbol{\varsigma} \quad \text{and} \quad \left[\frac{\mathrm{d}t'_\varepsilon}{\mathrm{d}\varepsilon}\right]\Bigg|_{\varepsilon=0} = \zeta\,. \tag{3.40}$$

Therefore we take the action functional eq. (3.33) $\boldsymbol{\mathcal{F}} = \mathcal{A}[\boldsymbol{\varphi}] = \int_{t_1}^{t_2}\{\mathfrak{L}\}$, and assume invariance under transformations (*perturbations*) in space and time, resulting in conservation laws of the motion. As introduced in the variational principle (see section 3.A.1), we identify the perturbed variables $\boldsymbol{q}'_\varepsilon(\boldsymbol{q},\varepsilon) = \mathcal{G}_\varepsilon\circ\boldsymbol{q}$ with the infinitesimal scalar parameter ε and the generator function $\mathcal{G}_\varepsilon(\boldsymbol{q})$.

3.3.1 Balance of Linear Momentum

We set $t'_\varepsilon = t$ and the arbitrary translational flow $\boldsymbol{\varphi}'_\varepsilon = \boldsymbol{\varphi}+\varepsilon\boldsymbol{\varsigma}$ in space with a constant vector $\boldsymbol{\varsigma}$, thereby giving constant variations with vanishing gradients $\nabla_{\mathrm{X}}\boldsymbol{\varsigma} = \boldsymbol{0}$ and $\nabla^2_{\mathrm{X}}\boldsymbol{\varsigma} = \boldsymbol{0}$. Acting as rigid body movement or a shift in the coordinate system, the reference configuration is influenced by the same flow $\boldsymbol{X}'_\varepsilon = \boldsymbol{X}+\varepsilon\boldsymbol{\varsigma}$. Inserting $\delta\boldsymbol{\varphi} = \boldsymbol{\varsigma}$ in eq. (3.33) and accounting for the shift of the reference configurations yields

$$\begin{aligned}\delta\mathcal{A}[\boldsymbol{\varphi}] = \left[\frac{\mathrm{d}\mathfrak{L}(\boldsymbol{\varphi}'_\varepsilon)}{\mathrm{d}\varepsilon}\right]\Bigg|_{\varepsilon=0} = \int_{t_1}^{t_2}\Bigg\{\int_{\Omega_0}\{-\boldsymbol{\varsigma}\cdot(\rho_0\ddot{\boldsymbol{\varphi}})\}\mathrm{d}V - \overbrace{\int_{\Omega_0}\left\{\boldsymbol{P}:\nabla_{\mathrm{X}}\boldsymbol{\varsigma} + \boldsymbol{\mathfrak{P}}:\nabla^2_{\mathrm{X}}\boldsymbol{\varsigma}\right\}\mathrm{d}V}^{=0}\\ + \int_{\Omega_0}\left\{\boldsymbol{\varsigma}\cdot\overline{\boldsymbol{B}}\right\}\mathrm{d}V + \int_{\partial\Omega_0^T}\left\{\boldsymbol{\varsigma}\cdot\overline{\boldsymbol{T}}\right\}\mathrm{d}A + \underbrace{\int_{\partial\Omega_0^M}\left\{\nabla_{\mathrm{X}\perp}\boldsymbol{\varsigma}:\overline{\boldsymbol{M}}\right\}\mathrm{d}A}_{=0} + \int_{\partial^2\Omega_0^L}\left\{\boldsymbol{\varsigma}\cdot\ \overline{\boldsymbol{L}}\right\}\mathrm{d}S\Bigg\}\mathrm{d}t = 0\,,\end{aligned} \tag{3.41}$$

leaving external and inertia terms. For arbitrary variations in space and time we obtain the balance of linear momentum (*Euler's first law of motion*)

$$\begin{aligned}\frac{\mathrm{d}}{\mathrm{d}t}\boldsymbol{p} &= \frac{\mathrm{d}}{\mathrm{d}t}\int\limits_{\Omega_0}\{\rho_0\dot{\boldsymbol{\varphi}}\}\mathrm{d}V \\ &= \int\limits_{\Omega_0}\{\rho_0\ddot{\boldsymbol{\varphi}}\}\mathrm{d}V \\ &= \int\limits_{\Omega_0}\left\{\overline{\boldsymbol{B}}\right\}\mathrm{d}V + \int\limits_{\partial\Omega_0^T}\left\{\overline{\boldsymbol{T}}\right\}\mathrm{d}A + \int\limits_{\partial^2\Omega_0^L}\left\{\overline{\boldsymbol{L}}\right\}\mathrm{d}S\,,\end{aligned} \tag{3.42}$$

where the temporal change of the linear momentum $\boldsymbol{p}$ is the result of the acting external forces.

3.3.2 Balance of Angular Momentum

For rotational invariance, leaving $t'_\varepsilon = t$, we take a rotation matrix $\boldsymbol{Q}_\varepsilon \in \mathrm{SO}(3)$ acting on the deformation map $\boldsymbol{\varphi}'_\varepsilon = \boldsymbol{Q}_\varepsilon(t)\boldsymbol{\varphi}$. The rotation as Lie algebra can be expressed using the exponential map $\boldsymbol{Q}_\varepsilon(t) = \exp(\varepsilon\hat{\boldsymbol{\varsigma}}(t))$, where $\hat{\boldsymbol{\varsigma}}(t) \in \mathfrak{so}(3)$ is a skew-symmetric matrix. Hence, we simply take $\delta\boldsymbol{\varphi} = \hat{\boldsymbol{\varsigma}}\boldsymbol{\varphi} = \boldsymbol{\varsigma}\times\boldsymbol{\varphi}$, with the axial (pseudo-)vector $\boldsymbol{\varsigma}$ (i.e. $[\boldsymbol{\varsigma}]_\times = \hat{\boldsymbol{\varsigma}}$). Analogously it follows $\hat{\boldsymbol{\varsigma}}(t_1) = \hat{\boldsymbol{\varsigma}}(t_2) = \boldsymbol{0}$, respectively $\boldsymbol{\varsigma}(t_1) = \boldsymbol{\varsigma}(t_2) = \boldsymbol{0}$, For the time derivative part, we get for the kinetic energy eq. (3.13)

$$\begin{aligned}\int\limits_{t_1}^{t_2}\left\{\delta\Pi^{\mathrm{kin}}\right\}\mathrm{d}t &= \int\limits_{t_1}^{t_2}\left\{\delta\int\limits_{\Omega_0}\left\{\frac{1}{2}\rho_0\|\dot{\boldsymbol{\varphi}}\|^2\right\}\mathrm{d}V\right\}\mathrm{d}t \\ &= \int\limits_{t_1}^{t_2}\left\{\int\limits_{\Omega_0}\left\{\rho_0\ddot{\boldsymbol{\varphi}}\cdot\frac{\partial}{\partial t}(\boldsymbol{\varsigma}\times\boldsymbol{\varphi})\right\}\mathrm{d}V\right\}\mathrm{d}t \\ &= \int\limits_{t_1}^{t_2}\left\{\dot{\boldsymbol{\varsigma}}\cdot\int\limits_{\Omega_0}\{\boldsymbol{\varphi}\times(\rho_0\dot{\boldsymbol{\varphi}})\}\mathrm{d}V + \boldsymbol{\varsigma}\cdot\int\limits_{\Omega_0}\{\dot{\boldsymbol{\varphi}}\times(\rho_0\dot{\boldsymbol{\varphi}})\}\mathrm{d}V\right\}\mathrm{d}t \\ &= \left[\boldsymbol{\varsigma}\cdot\int\limits_{\Omega_0}\{\boldsymbol{\varphi}\times(\rho_0\dot{\boldsymbol{\varphi}})\}\mathrm{d}V\right]\Bigg|_{t_1}^{t_2} - \int\limits_{t_1}^{t_2}\left\{\boldsymbol{\varsigma}\cdot\frac{\mathrm{d}}{\mathrm{d}}t\int\limits_{\Omega_0}\{\boldsymbol{\varphi}\times(\rho_0\dot{\boldsymbol{\varphi}})\}\mathrm{d}V\right\}\mathrm{d}t \\ &= -\int\limits_{t_1}^{t_2}\left\{\boldsymbol{\varsigma}\cdot\frac{\mathrm{d}}{\mathrm{d}t}\boldsymbol{J}\right\}\mathrm{d}t\,.\end{aligned} \tag{3.43}$$

The remaining term contains the angular momentum $\boldsymbol{J} = \int_{\Omega_0}\{\boldsymbol{\varphi} \times (\rho_0 \dot{\boldsymbol{\varphi}})\}\mathrm{d}V$ or more precisely its time derivative, for which we can equivalently write

$$\begin{aligned}\frac{\mathrm{d}}{\mathrm{d}t}\boldsymbol{J} &= \frac{\mathrm{d}}{\mathrm{d}t}\int_{\Omega_0}\{\boldsymbol{\varphi} \times (\rho_0 \dot{\boldsymbol{\varphi}})\}\mathrm{d}V \\ &= \int_{\Omega_0}\left\{\rho_0 \underbrace{\dot{\boldsymbol{\varphi}} \times \dot{\boldsymbol{\varphi}}}_{=0} + \boldsymbol{\varphi} \times (\rho_0 \ddot{\boldsymbol{\varphi}})\right\}\mathrm{d}V \\ &= \int_{\Omega_0}\{\boldsymbol{\varphi} \times (\rho_0 \ddot{\boldsymbol{\varphi}})\}\mathrm{d}V\,.\end{aligned} \tag{3.44}$$

Inserting the variations and the above into eq. (3.16) with further utilizing the triple product then gives

$$\begin{aligned}\delta\mathcal{A}[\boldsymbol{\varphi}] = \int_{t_1}^{t_2}\Bigg\{ &-\boldsymbol{\varsigma} \cdot \frac{\mathrm{d}}{\mathrm{d}t}\boldsymbol{J} - \delta\Pi^{\mathrm{int}} + \boldsymbol{\varsigma} \cdot \int_{\Omega_0}\Big\{\boldsymbol{\varphi} \times \overline{\boldsymbol{B}}\Big\}\mathrm{d}V \\ &+ \boldsymbol{\varsigma} \cdot \int_{\partial\Omega_0^T}\Big\{\boldsymbol{\varphi} \times \overline{\boldsymbol{T}}\Big\}\mathrm{d}A + \boldsymbol{\varsigma} \cdot \int_{\partial\Omega_0^M}\Big\{\Big(\boldsymbol{FN} \times \overline{\boldsymbol{MN}}\Big)\Big\}\mathrm{d}A + \boldsymbol{\varsigma} \cdot \int_{\partial^2\Omega_0^L}\Big\{\boldsymbol{\varphi} \times \overline{\boldsymbol{L}}\Big\}\mathrm{d}S\Bigg\}\mathrm{d}t = 0\,,\end{aligned} \tag{3.45}$$

where for the external hyper-stress traction force $\overline{\boldsymbol{MN}}$ (see section 3.A.2) following transformation is used

$$\begin{aligned}\nabla_{\mathrm{X}\perp}(\boldsymbol{\varsigma} \times \boldsymbol{\varphi}) : \overline{\boldsymbol{M}} &= \nabla_{\mathrm{X}N}(\boldsymbol{\varsigma} \times \boldsymbol{\varphi}) \cdot \overline{\boldsymbol{MN}} \\ &= (\boldsymbol{\varsigma} \times \nabla_{\mathrm{X}}\boldsymbol{\varphi}\boldsymbol{N}) \cdot \overline{\boldsymbol{MN}} \\ &= \boldsymbol{\varsigma} \cdot \Big(\boldsymbol{FN} \times \overline{\boldsymbol{MN}}\Big)\,.\end{aligned} \tag{3.46}$$

Moreover, internal contributions read

$$\begin{aligned}\delta\Pi^{\mathrm{int}} &= \int_{\Omega_0}\Big\{\boldsymbol{P} : \nabla_{\mathrm{X}}(\hat{\boldsymbol{\varsigma}}\boldsymbol{\varphi}) + \boldsymbol{\mathfrak{P}} \vdots \nabla_{\mathrm{X}}^2(\hat{\boldsymbol{\varsigma}}\boldsymbol{\varphi})\Big\}\mathrm{d}V \\ &= \int_{\Omega_0}\left\{\hat{\boldsymbol{\varsigma}}^{\top} : \left(\underbrace{\boldsymbol{P} \cdot \nabla_{\mathrm{X}}\boldsymbol{\varphi} + \boldsymbol{\mathfrak{P}} : \nabla_{\mathrm{X}}^2}_{:=\boldsymbol{A}}\right)\right\}\mathrm{d}V\,.\end{aligned} \tag{3.47}$$

For suitability of the energy formulation we demand a rigid body motion or a change of the observer not to influence the energy. Consequently following this *frame-indifference* (or *material objectivity*), $\delta\Pi^{\mathrm{int}}$ has to vanish. Since $\hat{\boldsymbol{\varsigma}}$ is a skew-symmetric matrix, double contraction with a matrix leaves only skew parts. Therefore we require in a strong sense the skew part of the integral to vanish $\frac{1}{2}(\boldsymbol{A} - \boldsymbol{A}^{\top}) = \boldsymbol{0}$, i.e. $\boldsymbol{A} - \boldsymbol{A}^{\top} = \boldsymbol{0}$ in order to eliminate internal energy contributions

$$\boldsymbol{P} \cdot \nabla_{\mathrm{X}}\boldsymbol{\varphi} + \boldsymbol{\mathfrak{P}} : \nabla_{\mathrm{X}}^2\boldsymbol{\varphi} = \Big(\boldsymbol{P} \cdot \nabla_{\mathrm{X}}\boldsymbol{\varphi} + \boldsymbol{\mathfrak{P}} : \nabla_{\mathrm{X}}^2\boldsymbol{\varphi}\Big)^{\top}. \tag{3.48}$$

If higher order contributions vanish, the condition is equal to the well known first order Cauchy symmetry eq. $(3.49)_1$. Therefore, we independently require the following symmetry conditions, for which an alternative form is given in section 3.A.3,

$$\boldsymbol{P}\cdot\nabla_{\mathrm{x}}\boldsymbol{\varphi}=(\boldsymbol{P}\cdot\nabla_{\mathrm{x}}\boldsymbol{\varphi})^{\top}\quad\text{and}\quad\boldsymbol{\mathfrak{P}}:\nabla_{\mathrm{x}}^{2}\boldsymbol{\varphi}=\Big(\boldsymbol{\mathfrak{P}}:\nabla_{\mathrm{x}}^{2}\boldsymbol{\varphi}\Big)^{\top}. \tag{3.49}$$

Utilizing the material stress symmetry and rearranging in terms of the rotational variation gives for the action functional eq. (3.45) now

$$\begin{aligned}\delta\mathcal{A}[\boldsymbol{\varphi}]=\int_{t_1}^{t_2}\Bigg\{&-\boldsymbol{\varsigma}\cdot\frac{\mathrm{d}}{\mathrm{d}t}\boldsymbol{J}+\boldsymbol{\varsigma}\cdot\int_{\Omega_0}\Big\{\boldsymbol{\varphi}\times\overline{\boldsymbol{B}}\Big\}\mathrm{d}V\\&+\boldsymbol{\varsigma}\cdot\int_{\partial\Omega_0^T}\Big\{\boldsymbol{\varphi}\times\overline{\boldsymbol{T}}\Big\}\mathrm{d}A+\boldsymbol{\varsigma}\cdot\int_{\partial\Omega_0^M}\Big\{\Big(\boldsymbol{FN}\times\overline{\boldsymbol{MN}}\Big)\Big\}\mathrm{d}A+\boldsymbol{\varsigma}\cdot\int_{\partial^2\Omega_0^L}\Big\{\boldsymbol{\varphi}\times\overline{\boldsymbol{L}}\Big\}\mathrm{d}S\Bigg\}\mathrm{d}t=0\,.\end{aligned} \tag{3.50}$$

Arbitrariness of variations leads to the balance of angular momentum

$$\frac{\mathrm{d}}{\mathrm{d}t}\boldsymbol{J}=\int_{\Omega_0}\Big\{\boldsymbol{\varphi}\times\overline{\boldsymbol{B}}\Big\}\mathrm{d}V+\int_{\partial\Omega_0^T}\Big\{\boldsymbol{\varphi}\times\overline{\boldsymbol{T}}\Big\}\mathrm{d}A+\int_{\partial\Omega_0^M}\Big\{\Big(\boldsymbol{FN}\times\overline{\boldsymbol{MN}}\Big)\Big\}\mathrm{d}A+\int_{\partial^2\Omega_0^L}\Big\{\boldsymbol{\varphi}\times\overline{\boldsymbol{L}}\Big\}\mathrm{d}S \tag{3.51}$$

stating that the change in angular momentum is equal to the applied external torque.

3.3.3 First Law of Thermodynamics

The first law of thermodynamics asserts, that the total energy is conserved in a thermodynamics system. Hence, during the motion of a material domain, its change of energy is equal to the power supplied by external contributions. Utilizing again the action functional eq. (3.33) and setting $t'_{\varepsilon}=t+\varepsilon$, where $\zeta=1$. For the field variation we get $\delta\boldsymbol{\varphi}=\boldsymbol{\varphi}(\boldsymbol{X},t+\varepsilon)-\boldsymbol{\varphi}(\boldsymbol{X},t)=\varepsilon\dot{\boldsymbol{\varphi}}$ for small ε. Inserting into the action functional and factoring out arbitrary constant ε yields

$$\begin{aligned}\delta\mathcal{A}[\boldsymbol{\varphi}]=\int_{t_1}^{t_2}\Bigg\{&\int_{\Omega_0}\{-\dot{\boldsymbol{\varphi}}\cdot(\rho_0\ddot{\boldsymbol{\varphi}})\}\mathrm{d}V\\&-\int_{\Omega_0}\Big\{\boldsymbol{P}:\nabla_{\mathrm{x}}\dot{\boldsymbol{\varphi}}+\boldsymbol{\mathfrak{P}}:\nabla_{\mathrm{x}}^{2}\dot{\boldsymbol{\varphi}}\Big\}\mathrm{d}V+\int_{\Omega_0}\Big\{\dot{\boldsymbol{\varphi}}\cdot\overline{\boldsymbol{B}}\Big\}\mathrm{d}V\\&+\int_{\partial\Omega_0^T}\Big\{\dot{\boldsymbol{\varphi}}\cdot\overline{\boldsymbol{T}}\Big\}\mathrm{d}A+\int_{\partial\Omega_0^M}\Big\{\nabla_{\mathrm{x}\perp}\dot{\boldsymbol{\varphi}}:\overline{\boldsymbol{M}}\Big\}\mathrm{d}A+\int_{\partial^2\Omega_0^L}\Big\{\dot{\boldsymbol{\varphi}}\cdot\ \overline{\boldsymbol{L}}\Big\}\mathrm{d}S\Bigg\}\mathrm{d}t=0\,.\end{aligned} \tag{3.52}$$

The first contribution restores the rate of the kinetic energy by integration by parts

$$\int_{\Omega_0}\{\dot{\boldsymbol{\varphi}}\cdot(\rho_0\ddot{\boldsymbol{\varphi}})\}\mathrm{d}V=\frac{\mathrm{d}}{\mathrm{d}t}\int_{\Omega_0}\Big\{\frac{1}{2}\rho_0\dot{\boldsymbol{\varphi}}\cdot\dot{\boldsymbol{\varphi}}\Big\}\mathrm{d}V\,. \tag{3.53}$$

Regarding internal contributions, we introduce the term *stress power*, where from the defined internal energy eq. (3.11) we get

$$\int_{\Omega_0}\Big\{\boldsymbol{P} : \nabla_{\mathrm{x}}\dot{\boldsymbol{\varphi}} + \boldsymbol{\mathfrak{P}} \vdots \nabla_{\mathrm{x}}^2\dot{\boldsymbol{\varphi}}\Big\}\mathrm{d}V = \frac{\mathrm{d}}{\mathrm{d}t}\int_{\Omega_0}\{\Psi\}\mathrm{d}V + \mathcal{D}^{\mathrm{int}}\,, \tag{3.54}$$

introducing an internal dissipation function $\mathcal{D}^{\mathrm{int}}$ collecting non-reversible energy, e.g. emerging from plasticity, viscoelasticity or fracture. Linking dissipation with heat generation and the second law of thermodynamics, we require $\mathcal{D}^{\mathrm{int}} \geq 0$. For non-dissipative processes, i.e. pure elastic deformations, follows $\mathcal{D}^{\mathrm{int}} = 0$.

Rearranging and utilizing the fundamental lemma of calculus for arbitrary intervals finally yields the balance of energy (more precisely *power balance*)

$$\begin{aligned}&\frac{\mathrm{d}}{\mathrm{d}t}\int_{\Omega_0}\Big\{\frac{1}{2}\rho_0\dot{\boldsymbol{\varphi}}\cdot\dot{\boldsymbol{\varphi}} + \Psi\Big\}\mathrm{d}V + \mathcal{D}^{\mathrm{int}}\\ &\qquad= \int_{\Omega_0}\Big\{\dot{\boldsymbol{\varphi}}\cdot\overline{\boldsymbol{B}}\Big\}\mathrm{d}V + \int_{\partial\Omega_0^T}\Big\{\dot{\boldsymbol{\varphi}}\cdot\overline{\boldsymbol{T}}\Big\}\mathrm{d}A + \int_{\partial\Omega_0^M}\Big\{\nabla_{\mathrm{x}\perp}\dot{\boldsymbol{\varphi}} : \overline{\boldsymbol{M}}\Big\}\mathrm{d}A + \int_{\partial^2\Omega_0^L}\Big\{\dot{\boldsymbol{\varphi}}\cdot\ \overline{\boldsymbol{L}}\Big\}\mathrm{d}S\,.\end{aligned} \tag{3.55}$$

Remark 3.3.1 – Second Law of Thermodynamics. We require the system to follow the Clausius-Duhem inequality in order to obey the second law of thermodynamics

$$\mathcal{D}^{\eta} \coloneqq \frac{\mathrm{d}}{\mathrm{d}t}\int_{\Omega_0}\{\eta\}\mathrm{d}V \geq \int_{\Omega_0}\Big\{\frac{1}{\theta}R\Big\}\mathrm{d}V - \int_{\partial\Omega_0}\Big\{\frac{1}{\theta}\boldsymbol{Q}\cdot\boldsymbol{N}\Big\}\mathrm{d}A\,, \tag{3.56}$$

with the current temperature θ, the specific entropy η, heat source R and heat flux $\boldsymbol{Q}$. Since the formulations throughout this work do not include thermal processes, leaving the domain purely isothermal ($\theta = \theta_0$) without a potential heat flux on the boundary ($\boldsymbol{Q} = \boldsymbol{0}$) or heat sources ($R = 0$). The second law of thermodynamics then breaks down to $\mathcal{D}^{\eta} \geq 0$, which is immediately fulfilled if we state $\eta = 0$, restricting to purely non-thermal processes.

3.3.4 Choice of Helmholtz energy density

As established in the discussion of the balance of angular momentum (cf. section 3.3.2) and, implicitly, of the balance of linear momentum (cf. section 3.3.1), material objectivity requires invariance of the stored energy under superposed rigid body motions. In particular, for $\widehat{\boldsymbol{\varphi}} = \boldsymbol{Q}\boldsymbol{\varphi} + \boldsymbol{c}$, with $\boldsymbol{Q} \in \mathrm{SO}(3)$ and $\boldsymbol{c} \in \mathbb{R}^3$, objectivity demands $\Psi(\boldsymbol{F}, \mathfrak{F}) = \Psi\Big(\widehat{\boldsymbol{F}}, \widehat{\mathfrak{F}}\Big)$. With the induced transformations of the kinematic arguments

$$\begin{aligned}\widehat{\boldsymbol{F}} &= \nabla_{\mathrm{x}}(\boldsymbol{Q}\boldsymbol{\varphi} + \boldsymbol{c}) = \boldsymbol{Q}\boldsymbol{F} \quad \text{and}\\ \widehat{\mathfrak{F}} &= \nabla_{\mathrm{x}}^2(\boldsymbol{Q}\boldsymbol{\varphi} + \boldsymbol{c}) = \boldsymbol{Q}\mathfrak{F}\,,\end{aligned} \tag{3.57}$$

translational invariance is satisfied trivially, while rotational invariance imposes the nontrivial constraint

$$\Psi(\boldsymbol{Q}\boldsymbol{F}, \boldsymbol{Q}\mathfrak{F}) = \Psi(\boldsymbol{F}, \mathfrak{F})\,. \tag{3.58}$$

This requirement restricts the admissible functional forms of Ψ and, consequently, the stress measures derived from it. This can easily be achieved by introducing a set of strain and strain gradient measures

$$\boldsymbol{C} \coloneqq \boldsymbol{F}^{\top}\boldsymbol{F} \quad \text{and} \quad \boldsymbol{\mathcal{K}} \coloneqq \boldsymbol{F}^{\top}\mathfrak{F}\,, \tag{3.59}$$

where $\boldsymbol{C}$ is the right Cauchy-Green deformation tensor and $\boldsymbol{\mathcal{K}}$ a higher order strain measure, cf. Asmanoglo and Menzel [5] and Marsden and Hughes [78]. Conducting the rotation on these measures yields

$$\widehat{\boldsymbol{C}} = \widehat{\boldsymbol{F}}^{\top}\widehat{\boldsymbol{F}} = (\boldsymbol{Q}\boldsymbol{F})^{\top}\boldsymbol{Q}\boldsymbol{F} = \boldsymbol{F}^{\top}\boldsymbol{Q}^{\top}\boldsymbol{Q}\boldsymbol{F} = \boldsymbol{F}^{\top}\boldsymbol{F} = \boldsymbol{C} \tag{3.60}$$

and

$$\widehat{\boldsymbol{\mathcal{K}}} = \widehat{\boldsymbol{F}}^{\top}\widehat{\mathfrak{F}} = (\boldsymbol{Q}\boldsymbol{F})^{\top}\boldsymbol{Q}\mathfrak{F} = \boldsymbol{F}^{\top}\boldsymbol{Q}^{\top}\boldsymbol{Q}\mathfrak{F} = \boldsymbol{F}^{\top}\mathfrak{F} = \boldsymbol{\mathcal{K}}\,, \tag{3.61}$$

which hence are invariant (*objective*). Note that alternative second-order strain measures may also be objective, e.g. among others $\boldsymbol{K} = \boldsymbol{F}^{-1}\mathfrak{F}$ as used in Bertram [12] or simply $\mathfrak{K} = \mathfrak{F}\cdot\mathfrak{F}$. Following the chain rule, variation on $\widehat{\Psi}(\boldsymbol{C}, \boldsymbol{\mathcal{K}})$ with respect to the new strain measures leads to

$$\begin{aligned}
\delta\Psi &= \frac{\partial\Psi}{\partial\boldsymbol{F}} : \nabla_{\mathrm{X}}\delta\boldsymbol{\varphi} + \frac{\partial\Psi}{\partial\mathfrak{F}} \vdots \nabla^2_{\mathrm{X}}\delta\boldsymbol{\varphi} \\
&= \frac{\partial\Psi}{\partial\boldsymbol{C}} : \frac{\partial\boldsymbol{C}}{\partial\boldsymbol{F}} : \nabla_{\mathrm{X}}\delta\boldsymbol{\varphi} + \frac{\partial\Psi}{\partial\boldsymbol{\mathcal{K}}} \vdots \frac{\partial\boldsymbol{\mathcal{K}}}{\partial\boldsymbol{F}} : \nabla_{\mathrm{X}}\delta\boldsymbol{\varphi} + \frac{\partial\Psi}{\partial\boldsymbol{\mathcal{K}}} \vdots \frac{\partial\boldsymbol{\mathcal{K}}}{\partial\mathfrak{F}} \vdots \nabla^2_{\mathrm{X}}\delta\boldsymbol{\varphi} \\
&= \frac{\partial\Psi}{\partial\boldsymbol{C}} : \left(\boldsymbol{F}^{\top}\nabla_{\mathrm{X}}\delta\boldsymbol{\varphi} + (\nabla_{\mathrm{X}}\delta\boldsymbol{\varphi})^{\top}\boldsymbol{F}\right) + \frac{\partial\Psi}{\partial\boldsymbol{\mathcal{K}}} \vdots (\nabla_{\mathrm{X}}\delta\boldsymbol{\varphi})^{\top}\mathfrak{F} + \frac{\partial\Psi}{\partial\boldsymbol{\mathcal{K}}} \vdots \boldsymbol{F}^{\top}\nabla^2_{\mathrm{X}}\delta\boldsymbol{\varphi} \\
&= \underbrace{\left(\boldsymbol{F}\, 2\frac{\partial\Psi}{\partial\boldsymbol{C}} + \mathfrak{F} : \frac{\partial\Psi}{\partial\boldsymbol{\mathcal{K}}}\right)}_{=\boldsymbol{P}} : \nabla_{\mathrm{X}}\delta\boldsymbol{\varphi} + \underbrace{\boldsymbol{F}\frac{\partial\Psi}{\partial\boldsymbol{\mathcal{K}}}}_{=\mathfrak{P}} \vdots \nabla^2_{\mathrm{X}}\delta\boldsymbol{\varphi}\,.
\end{aligned} \tag{3.62}$$

Therein, we can identify the well-known symmetric Second Piola-Kirchhoff Stress tensor $\boldsymbol{S} \coloneqq 2\frac{\partial\Psi}{\partial\boldsymbol{C}}$ and the hyper-stress tensor $\mathcal{M} = \frac{\partial\Psi}{\partial\boldsymbol{\mathcal{K}}}$. Inserted in the condition for angular momentum eq. (3.49), we achieve symmetry

$$\begin{aligned}
&(\boldsymbol{F}\boldsymbol{S} + \mathcal{M} : \mathfrak{F})\boldsymbol{F}^{\top} + \boldsymbol{F}\mathcal{M} : \mathfrak{F} \\
&= \boldsymbol{F}\boldsymbol{S}\boldsymbol{F}^{\top} + \mathfrak{F} : \mathcal{M}\cdot\boldsymbol{F} + \boldsymbol{F}\mathcal{M} : \mathfrak{F} \\
&= \boldsymbol{S} : \boldsymbol{F}\otimes\boldsymbol{F}^{\top} + \mathcal{M} \vdots \left(\mathfrak{F}\otimes\boldsymbol{F}^{\top} + \boldsymbol{F}^{\top}\otimes\mathfrak{F}\right) \in \mathrm{Sym}\,.
\end{aligned} \tag{3.63}$$

Remark 3.3.2 – Index notation for angular momentum symmetry. Contraction is done on corresponding indices, thus the last line in index notation reads

$$[\boldsymbol{S}]_{AB}[\boldsymbol{F}]_{iA}[\boldsymbol{F}]_{jB} + [\mathcal{M}]_{ABC}\Big([\mathfrak{F}]_{iBC}[\boldsymbol{F}]_{jA} + [\boldsymbol{F}]_{iB}[\mathfrak{F}]_{jAC}\Big) \tag{3.64}$$

with symmetries $[\boldsymbol{S}]_{AB} = [\boldsymbol{S}]_{BA}$, $[\mathcal{M}]_{ABC} = [\mathcal{M}]_{ACB}$ and $[\mathfrak{F}]_{iBC} = [\mathfrak{F}]_{iCB}$.

Another way of ensuring frame-indifference is the use of *invariants*, that are constructed especially in this regard as they define an invariant as any scalar valued function $f : \mathbb{R}^{d\times d} \to \mathbb{R}$, which fulfills $f(\boldsymbol{A}) = f(\boldsymbol{Q}\boldsymbol{A}\boldsymbol{Q}^{\top})$. For first order components there are three *principal* invariants of right Cauchy Green tensor eq. (3.59) $_a$ which can directly be expressed using the kinematical set in eq. (3.1) to eq. (3.3)

$$\begin{aligned} \mathrm{I}_{\boldsymbol{C}} &= \mathrm{tr}(\boldsymbol{C}) = \mathrm{tr}\Big(\boldsymbol{F}^{\top}\boldsymbol{F}\Big) = \boldsymbol{F} : \boldsymbol{F} \\ \mathrm{II}_{\boldsymbol{C}} &= \frac{1}{2}\Big((\mathrm{tr}(\boldsymbol{C}))^2 - \mathrm{tr}\Big(\boldsymbol{C}^2\Big)\Big) = \boldsymbol{H} : \boldsymbol{H} \\ \mathrm{III}_{\boldsymbol{C}} &= \det(\boldsymbol{C}) = J^2\,, \end{aligned} \tag{3.65}$$

see e.g. Bonet et al. [18]. Suggestions for invariants of second-order deformation tensors have also been made, e.g. by Soldatos [110], but depend strongly on the intended use scenario and are quite extensive to be generalized.

In order to find a solution, we then require the existence of minimizers implying (poly-)convexity and coercivity as shown in Ball et al. [10] (see also Healey and Krömer [53] among others). From a physical point of view, orientation is preserved by demanding $\Psi \to \infty$ as $J = \det(\boldsymbol{F}) \to 0^+$, thereby requiring infinite energy in order to compress the Ω_0 to zero volume. Additionally self-penetration or self-contact must be prohibited, leading to injectivity (cf. Ciarlet and Nečas [24], Healey and Krömer [53], and Palmer and Healey [91]), which is beyond the scope of this work. For the investigation of further requirements on the energy density, we conduct a split into a pure first order part and an additional second-order part $\Psi(\boldsymbol{F}, \mathfrak{F}) \coloneqq \Psi_1(\boldsymbol{F}) + \Psi_2(\boldsymbol{F}, \mathfrak{F})$, allowing us to find criteria for each part. As stated in Ball et al. [10], for energies of order $N = 2$ with present second-order contributions no further convexity assumptions have to be made. For a vanishing higher order contribution, leaving $\Psi = \Psi_1$ of grade $N = 1$, we then must apply the usual criteria of polyconvexity, e.g. established in Ball [9], see also Hartmann and Neff [51].

For the initial state, we further demand the material formulation has to fulfill

$$[\![\Psi]\!]_{\boldsymbol{\varphi}_0} = 0\,, \quad [\![\boldsymbol{P}]\!]_{\boldsymbol{\varphi}_0} = \left[\frac{\partial \Psi}{\partial \boldsymbol{F}}\right]\Bigg|_{\boldsymbol{\varphi}_0} = \boldsymbol{0} \quad \text{and} \quad [\![\mathfrak{P}]\!]_{\boldsymbol{\varphi}_0} = \left[\frac{\partial \Psi}{\partial \mathfrak{F}}\right]\Bigg|_{\boldsymbol{\varphi}_0} = \boldsymbol{0}\,, \tag{3.66}$$

where

$$[\![\boldsymbol{F}]\!]_{\boldsymbol{\varphi}_0} = \nabla_{\mathrm{X}} \boldsymbol{\varphi}_0 = \boldsymbol{I} \quad \text{and} \quad [\![\mathfrak{F}]\!]_{\boldsymbol{\varphi}_0} = \nabla^2_{\mathrm{X}} \boldsymbol{\varphi}_0 = \boldsymbol{0}\,, \tag{3.67}$$

such that the body is energy- and stress-free at the deformation-less reference configuration $\boldsymbol{\varphi}_0$.

Remark 3.3.3 – Material properties. It should be pointed out, that a wide range of supplementary criteria from a material behavioral point of view exist, such as isomorphy or isotropy among others. Nonetheless we do not further restrict the energy formulations used throughout this work.

Examples for material models

In the following we introduce certain first grade material models for the three-dimensional case ($d = 3$), which are used in this work and refer to Hartmann and Neff [51] among others for investigation towards polyconvexity. Note that two-dimensional versions can be obtained simply by restricting the kinematic in the third direction, such that $x_3 = X_3 =$ constant. As an example, take the first order deformation gradient

$$\nabla_{\mathrm{X}} \boldsymbol{\varphi} = \begin{bmatrix} & & 0 \\ & \boldsymbol{F}_{2\mathrm{D}} & 0 \\ & & \\ 0 & 0 & 1 \end{bmatrix}, \tag{3.68}$$

where $\boldsymbol{F}_{2\mathrm{D}} : \Omega_0 \to \mathbb{R}^{2\times 2}$. For $\mathfrak{F}$ all second partial derivatives related to the third direction become zero.

Many material formulations have variations related to the treatment of volumetric changes where *incompressible* models demand $J = 1$, whereas without restriction we use the term *compressible*. The latter can easily be achieved by adding terms to account for volumetric changes. To offer flexibility in formulating the models, the determinant is used to separate incompressible (*isochoric*) and volumetric parts

$$\bar{\boldsymbol{F}} := J^{-\frac{1}{3}} \boldsymbol{F}, \tag{3.69}$$

where $\det\left(\bar{\boldsymbol{F}}\right) = 1$, see Sansour [98] among others.

Mooney-Rivlin

First, we give the well-known *Mooney-Rivlin* constitutive model

$$\Psi_{\mathrm{MR}}(\boldsymbol{F}, \boldsymbol{H}, J) := \alpha\,(\boldsymbol{F} : \boldsymbol{F} - 3) + \beta\,(\boldsymbol{H} : \boldsymbol{H} - 3) + f(J), \tag{3.70}$$

where $f(J) = -2\,(\alpha + 2\,\beta)\ln(J) + \gamma/2\,(J-1)^2$ with non-negative material parameters α, β, γ. In particular, Ψ_{MR} is (poly-)convex with respect to its 19 variables, i.e. the components of $\boldsymbol{F}$, $\boldsymbol{H}$ and J, by calculating the Hessian of Ψ_{MR}, see Bonet et al. [18].

Ogden

Additionally we introduce a polyconvex, compressible *Ogden* material model that is formulated using the eigenvalues λ_a of $\boldsymbol{F}$, where the volumetric-isochoric split eq. (3.69) is applied reading

$$\bar{\lambda}_a = J^{-\frac{1}{3}} \lambda_a, \tag{3.71}$$

see eq. (3.4) for the eigenvalue decomposition of the deformation gradient. The material description then states

$$\Psi_{\mathrm{OD}}(\lambda_a) := \Psi_{\mathrm{OD}}^{\mathrm{iso}}\left(\bar{\lambda}_a\right) + \Psi_{\mathrm{OD}}^{\mathrm{vol}}(J(\lambda_a)), \tag{3.72}$$

where

$$\Psi_{\mathrm{OD}}^{\mathrm{iso}} \coloneqq \sum_{a=1}^{3} \sum_{b} \frac{\mu_b}{\alpha_b} \left((\bar{\lambda}_a)^{\alpha_b} - 1 \right) \tag{3.73}$$

and

$$\Psi_{\mathrm{OD}}^{\mathrm{vol}} \coloneqq \frac{\kappa}{\beta^2} \left(\beta \ln(J) + (J)^{-\beta} - 1 \right) . \tag{3.74}$$

The parameters μ_b and α_b with $b \in \mathbb{N}$ are related to shear, whereas parameters κ and β contribute to the bulk modulus. For the special case of $b = 1$ and $\alpha = 2$, one may recover a type of Neo-Hooke energy, cf. Holzapfel [60], as shown in eq. (3.76).

Neo-Hooke

The *Neo-Hooke* model is rooted in standard material testing. It is related to the Mooney-Rivlin model but trades in polyconvexity for simplicity as it omits contributions of the co-factor $\boldsymbol{H}$, i.e. setting $\beta = 0$ in eq. (3.70)

$$\Psi_{\mathrm{NH}}(\boldsymbol{F}, J) \coloneqq \alpha \, (\boldsymbol{F} : \boldsymbol{F} - 3) + f(J), \tag{3.75}$$

where $f(J) = -2\,\alpha \, \ln(J) + \gamma/2 \, (J-1)^2$ with $\alpha, \gamma > 0$. In this context, alternative parameters $\{\mu, \lambda\}$, called *material moduli* are used, where $\mu = 2\,\alpha$ and $\lambda = \gamma/2$, see also remark 3.3.4. Note that alternative formulations exist using the volumetric-isochoric split eq. (3.69), e.g.

$$\bar{\Psi}_{\mathrm{NH}}(\boldsymbol{F}, J) \coloneqq \frac{\mu}{2} \left(J^{-\frac{2}{3}} \boldsymbol{F} : \boldsymbol{F} - 3 \right) + \frac{\kappa}{2} (J-1)^2 - \mu \ln(J) \, , \tag{3.76}$$

where $\frac{\mu}{2} \sim \alpha$ and $\kappa \sim \gamma$.

Saint-Venant Kirchhoff

Taking the Green-Lagrange deformation tensor $\boldsymbol{C}$ in eq. (3.9), we can derive the Green-Lagrange strain tensor $\boldsymbol{E} = \frac{1}{2}(\boldsymbol{C} - \boldsymbol{I})$ and formulate *Saint-Venant Kirchhoff* material model

$$\Psi_{\mathrm{SVK}}(\boldsymbol{F}) \coloneqq \frac{\lambda}{2} (\mathrm{tr}(\boldsymbol{E}))^2 + \mu \, \mathrm{tr}\left(\boldsymbol{E}^2 \right) , \tag{3.77}$$

which is not polyconvex and not coercive, since $\lim_{J \to 0^+} \Psi_{\mathrm{SVK}} = 0$. It is related to the previously introduced Neo-Hookean model eq. (3.76) and can be obtained by inserting $\boldsymbol{C} = 2\boldsymbol{E} + \boldsymbol{I}$ with expansion of J, omitting $\mathcal{O}(\boldsymbol{E}^3)$-terms.

Remark 3.3.4 – Lamé-Parameter. We can relate the so called *Lamé parameters* λ and μ (also known as Lamé's first and second parameters) to other material constants in linear elasticity. The second Lamé parameter μ corresponds directly to the *shear modulus* G, characterizing a material's resistance to shear deformation, whereas the

first Lamé parameter λ is related to the *Young's modulus* E and G. Alternatively the *Poisson's ratio* ν is used. The relations are given as

$$\lambda = \frac{G(E-2\,G)}{3G-E} = \frac{E\nu}{(1+\nu)(1-2\nu)} \quad \text{and} \quad \mu = G = \frac{E}{2(1+\nu)}\,. \tag{3.78}$$

3.4 Second-order boundary value problem

Although a complete dynamic framework incorporating time derivatives and inertial contributions has been established for completeness, the remainder of this work is restricted to the static case. Hence in the following inertia effects and dissipation are neglected. The strong and weak form of the given static problem is summarized. For brevity, the time-interval notation was omitted.

Static equilibrium

$$\nabla_{\mathrm{x}} \cdot (\boldsymbol{P} - \nabla_{\mathrm{x}} \cdot \mathfrak{P}) + \overline{\boldsymbol{B}} = 0 \tag{3.79}$$

Weak form

$$\begin{aligned}&\int_{\Omega_0} \Big\{ \boldsymbol{P} : \nabla_{\mathrm{x}} \delta\boldsymbol{\varphi} + \mathfrak{P} \vdots \nabla_{\mathrm{x}}^2 \delta\boldsymbol{\varphi} \Big\} \mathrm{d}V \\ &\quad = \int_{\Omega_0} \Big\{ \delta\boldsymbol{\varphi} \cdot \overline{\boldsymbol{B}} \Big\} \mathrm{d}V + \int_{\partial\Omega_0^T} \Big\{ \delta\boldsymbol{\varphi} \cdot \overline{\boldsymbol{T}} \Big\} \mathrm{d}A + \int_{\partial\Omega_0^M} \Big\{ \nabla_{\mathrm{x}\perp} \delta\boldsymbol{\varphi} : \overline{\boldsymbol{M}} \Big\} \mathrm{d}A + \int_{\partial^2\Omega_0^L} \Big\{ \delta\boldsymbol{\varphi} \cdot \ \overline{\boldsymbol{L}} \Big\} \mathrm{d}S\end{aligned} \tag{3.80}$$

Trial functions

$$\mathcal{V}_{\delta\boldsymbol{\varphi}} = \Big\{ \delta\boldsymbol{\varphi} \in \mathcal{H}^2(\Omega_0) \mid \delta\boldsymbol{\varphi} = \boldsymbol{0} \text{ on } \partial\Omega_0^{\varphi}, \quad \nabla_{\mathrm{x}} \delta\boldsymbol{\varphi} \boldsymbol{N} = \boldsymbol{0} \text{ on } \partial\Omega_0^{\nabla\varphi} \Big\} \tag{3.81}$$

Kinematic

$$\boldsymbol{F} = \nabla_{\mathrm{x}} \boldsymbol{\varphi}\,, \quad \mathfrak{F} = \nabla_{\mathrm{x}}^2 \boldsymbol{\varphi} \tag{3.82}$$

Constitutive Stress relations

$$\boldsymbol{P} = \frac{\partial \Psi}{\partial \boldsymbol{F}}\,, \quad \mathfrak{P} = \frac{\partial \Psi}{\partial \mathfrak{F}} \tag{3.83}$$

Neumann conditions

$$\begin{aligned}(\boldsymbol{P} - \nabla_{\mathrm{x}} \cdot \mathfrak{P})\,\boldsymbol{N} - K\,(\mathfrak{P}\,\boldsymbol{N})\boldsymbol{N} - \nabla_{\mathrm{x}\parallel} \cdot (\mathfrak{P}\,\boldsymbol{N}) = \overline{\boldsymbol{T}} \text{ on } \partial\Omega_0^T\,,& \\ \mathfrak{P}\,\boldsymbol{N} = \overline{\boldsymbol{M}} \text{ on } \partial\Omega_0^M \quad \text{and} \quad \mathfrak{P} : \Big(\hat{\boldsymbol{N}} \otimes \boldsymbol{N}\Big) = \overline{\boldsymbol{L}} \text{ on } \partial^2\Omega_0^N&\end{aligned} \tag{3.84}$$

Dirichlet conditions

$$\boldsymbol{\varphi} = \overline{\boldsymbol{\varphi}} \text{ on } \partial\Omega_0^{\varphi} \quad \text{and} \quad \nabla_{\mathrm{x}} \boldsymbol{\varphi} \boldsymbol{N} = \overline{\nabla_{\mathrm{x}} \boldsymbol{\varphi} \boldsymbol{N}} \text{ on } \partial\Omega_0^{\nabla\varphi} \tag{3.85}$$

3.5 Discretization and solution

Concerning the spatial discretization, the domain Ω_0 is approximated using the (NUR-)B-Spline framework established in chapter 2. Discretization and subsequently integral evaluation is then conducted following the steps elaborated in section 2.2.2. For brevity, the approximation using a geometrical mapping to parameter space is implied by writing $\mathcal{R}^A \coloneqq \widehat{\mathcal{R}}_{A,\boldsymbol{p}}(\boldsymbol{\xi})$ with the order $\boldsymbol{p}$ either given in context or arbitrary. With required regularity, e.g. $p^{[\alpha]} \geq 2$ we write $\mathcal{R}^B_{\geq 2} \coloneqq \widehat{\mathcal{R}}_{B,\boldsymbol{p}}(\boldsymbol{\xi})$.

3.5.1 Approximation of geometry and fields

Hence, we approximate the domain $\Omega_0 \approx \Omega_0^{\mathrm{h}}$ and write for the position vector

$$\boldsymbol{X}^{\mathrm{h}} = \sum_{A \in \Lambda} \boldsymbol{q}_A \, \mathcal{R}^A \,, \tag{3.86}$$

with control-points $\boldsymbol{q}_A \in \mathbb{R}^d$. The overset $(\cdot)^{\mathrm{h}}$ denotes variables obtained directly by discretization or functions of approximated arguments. Alongside domain, motion $\boldsymbol{\varphi}$ and its variation $\delta\boldsymbol{\varphi}$ must be discretized as well. Employing the *isoparametric concept*, we use the same shape-functions

$$\boldsymbol{\varphi} \approx \boldsymbol{\varphi}^{\mathrm{h}} = \sum_{A \in \Lambda} \boldsymbol{\varphi}_A \, \mathcal{R}^A \,, \quad \boldsymbol{\varphi}^{\mathrm{h}} \in \mathcal{V}_{\boldsymbol{\varphi}}^{\mathrm{h}} \tag{3.87}$$

and

$$\delta\boldsymbol{\varphi} \approx \delta\boldsymbol{\varphi}^{\mathrm{h}} = \sum_{A \in \Lambda} \delta\boldsymbol{\varphi}_A \, \mathcal{R}^A \,, \quad \delta\boldsymbol{\varphi}^{\mathrm{h}} \in \mathcal{V}_{\delta\boldsymbol{\varphi}}^{\mathrm{h}} \tag{3.88}$$

with solution and test space

$$\begin{aligned} \mathcal{V}_{\boldsymbol{\varphi}}^{\mathrm{h}} &\coloneqq \left\{ \boldsymbol{\varphi}^{\mathrm{h}} \in \mathcal{H}^2\left(\Omega_0^{\mathrm{h}}\right) \mid \boldsymbol{\varphi}^{\mathrm{h}} = \overline{\boldsymbol{\varphi}}^{\mathrm{h}} \text{ on } \partial\Omega_0^{\varphi,\mathrm{h}}, \quad \nabla_{\mathrm{X}} \boldsymbol{\varphi}^{\mathrm{h}} \boldsymbol{N}^{\mathrm{h}} = \overline{\nabla_{\mathrm{X}} \boldsymbol{\varphi} \boldsymbol{N}}^{\mathrm{h}} \text{ on } \partial\Omega_0^{\nabla\varphi,\mathrm{h}} \right\} \quad \text{and} \\ \mathcal{V}_{\delta\boldsymbol{\varphi}}^{\mathrm{h}} &\coloneqq \left\{ \delta\boldsymbol{\varphi}^{\mathrm{h}} \in \mathcal{H}^2\left(\Omega_0^{\mathrm{h}}\right) \mid \delta\boldsymbol{\varphi}^{\mathrm{h}} = \boldsymbol{0} \text{ on } \partial\Omega_0^{\varphi,\mathrm{h}}, \quad \nabla_{\mathrm{X}} \delta\boldsymbol{\varphi}^{\mathrm{h}} \boldsymbol{N}^{\mathrm{h}} = \boldsymbol{0} \text{ on } \partial\Omega_0^{\nabla\varphi,\mathrm{h}} \right\}, \end{aligned} \tag{3.89}$$

respectively, fulfilling the Dirichlet conditions. Further, $\boldsymbol{\varphi}_A, \delta\boldsymbol{\varphi}_A \in \mathbb{R}^d$ and with each $\boldsymbol{\varphi}_A$ resembling d degrees of freedom. Due to the use of open knot vectors, the boundary constraints, i.e. $\delta\boldsymbol{\varphi} = \boldsymbol{0}$ on $\partial\Omega_0^{\varphi}$ and $\nabla_{\mathrm{X}} \delta\boldsymbol{\varphi} \boldsymbol{N} = \boldsymbol{0}$ on $\partial\Omega_0^{\nabla\varphi}$, have to be fulfilled by restricting values for control-points $\delta\boldsymbol{q}_B$ related to these bounds. Note, that $\Omega_0^{\mathrm{h}} = \boldsymbol{\varphi}_0^{\mathrm{h}}$ at reference configuration, thus $\boldsymbol{q}_A = \boldsymbol{\varphi}_{A,0}$. The approximation of other introduced fields and respective variations follows the same pattern.

Regarding the weak form in eq. (3.80), we define $R_{\boldsymbol{\varphi}}(\boldsymbol{\varphi}, \delta\boldsymbol{\varphi}) : \mathcal{V}_{\delta\boldsymbol{\varphi}} \to \mathcal{V}^*_{\delta\boldsymbol{\varphi}}$,

$$R_{\boldsymbol{\varphi}}(\boldsymbol{\varphi}; \delta\boldsymbol{\varphi}) \coloneqq \delta\mathcal{A}\left[\boldsymbol{\varphi}\right] = \delta\Pi^{\mathrm{int}} - \delta\Pi^{\mathrm{ext}} = 0 \qquad \forall\, \delta\boldsymbol{\varphi} \in \mathcal{V}_{\delta\boldsymbol{\varphi}} \,. \tag{3.90}$$

Inserting approximations we get for the internal part

$$\begin{aligned}\delta\Pi^{\mathrm{int,h}} &= \int_{\Omega_0^{\mathrm{h}}} \Big\{ \boldsymbol{P}^{\mathrm{h}} : \nabla_{\mathrm{X}} \left(\delta\boldsymbol{\varphi}_A \mathcal{R}^A \right) + \boldsymbol{\mathfrak{P}}^{\mathrm{h}} \vdots \nabla_{\mathrm{X}}^2 \left(\delta\boldsymbol{\varphi}_A \mathcal{R}^A \right) \Big\} \mathrm{d}V \\ &= \delta\boldsymbol{\varphi}_A \cdot \int_{\Omega_0^{\mathrm{h}}} \Big\{ \boldsymbol{P}^{\mathrm{h}} \cdot \nabla_{\mathrm{X}} \mathcal{R}^A + \boldsymbol{\mathfrak{P}}^{\mathrm{h}} : \nabla_{\mathrm{X}}^2 \mathcal{R}^A \Big\} \mathrm{d}V \end{aligned} \tag{3.91}$$

and external contributions with omitted line forces accordingly

$$\delta\Pi^{\mathrm{ext,h}} = \delta\boldsymbol{\varphi}_A \cdot \left(\int_{\Omega_0^{\mathrm{h}}} \Big\{ \mathcal{R}^A \, \overline{\boldsymbol{B}}^{\mathrm{h}} \Big\} \mathrm{d}V + \int_{\partial\Omega_0^{T,\mathrm{h}}} \Big\{ \mathcal{R}^A \cdot \overline{\boldsymbol{T}}^{\mathrm{h}} \Big\} \mathrm{d}A + \int_{\partial\Omega_0^{M,\mathrm{h}}} \Big\{ \nabla_{\mathrm{X}\perp} \mathcal{R}^A \cdot \overline{\boldsymbol{M}}^{\mathrm{h}} \Big\} \mathrm{d}A \right). \tag{3.92}$$

Putting together yields the discrete system $\delta\boldsymbol{\varphi}_A \cdot \boldsymbol{R}_{\boldsymbol{\varphi}}^A(\boldsymbol{\varphi}^{\mathrm{h}}, \mathcal{R}^A) = 0$ with

$$\begin{aligned}\boldsymbol{R}_{\boldsymbol{\varphi}}^A(\boldsymbol{\varphi}^{\mathrm{h}}, \mathcal{R}^A) \coloneqq & \int_{\Omega_0^{\mathrm{h}}} \Big\{ \boldsymbol{P}^{\mathrm{h}} \cdot \nabla_{\mathrm{X}} \mathcal{R}^A + \boldsymbol{\mathfrak{P}}^{\mathrm{h}} : \nabla_{\mathrm{X}}^2 \mathcal{R}^A \Big\} \mathrm{d}V \\ & - \left(\int_{\Omega_0^{\mathrm{h}}} \Big\{ \mathcal{R}^A \, \overline{\boldsymbol{B}}^{\mathrm{h}} \Big\} \mathrm{d}V + \int_{\partial\Omega_0^{T,\mathrm{h}}} \Big\{ \mathcal{R}^A \, \overline{\boldsymbol{T}}^{\mathrm{h}} \Big\} \mathrm{d}A + \int_{\partial\Omega_0^{M,\mathrm{h}}} \Big\{ \nabla_{\mathrm{X}\perp} \mathcal{R}^A \cdot \overline{\boldsymbol{M}}^{\mathrm{h}} \Big\} \mathrm{d}A \right), \end{aligned} \tag{3.93}$$

accompanied by discrete conditions eq. (3.82). For arbitrary values $\delta\boldsymbol{\varphi}_A$ we obtain the vector-valued equation $\boldsymbol{R}_{\boldsymbol{\varphi}} = \boldsymbol{0}$, where the nodal dependency A is omitted.

Remark 3.5.1 – Regularity. Due to the incorporation of second-order contributions, the variational problem requires approximation functions which are globally at least C^1-continuous, satisfying $\boldsymbol{\varphi}^{\mathrm{h}}, \delta\boldsymbol{\varphi}^{\mathrm{h}} \in \mathcal{H}^2\big(\Omega_0^{\mathrm{h}}\big)$. To meet this continuity requirement, apply (NUR-)B-Splines $\mathcal{R}_{\geq 2}^A$. For non-existent second-order involvement, we require $\boldsymbol{\varphi}^{\mathrm{h}}, \delta\boldsymbol{\varphi}^{\mathrm{h}} \in \mathcal{H}^1\big(\Omega_0^{\mathrm{h}}\big)$ and use $\mathcal{R}_{\geq 1}^A$.

3.5.2 Consistent Linearization and Newton-Raphson

Solving above system requires finding a solution $\boldsymbol{\varphi} \in \mathcal{V}_{\boldsymbol{\varphi}}$ (called *root*) fulfilling eq. (3.93) and associated boundary conditions. Because the balance in general reveals a nonlinear behavior, we introduce $R_{\boldsymbol{\varphi}}(\boldsymbol{\varphi}, \delta\boldsymbol{\varphi})$ as residual operator and root finding methods have to be applied. Throughout this work we use the Newton-Raphson method, for which we linearize $R_{\boldsymbol{\varphi}}$ at a given point $\boldsymbol{\varphi}^{(k)}$ using Taylor expansion up to first order and solve for the linearized system employing a classical linear solver. This root is then used to linearize at $\boldsymbol{\varphi}^{(k+1)}$ and repeat solving until a convergence criterion is fulfilled. In this work, we make use of the norm of the residual, i.e. we assume the solved state if $\|\boldsymbol{R}_{\boldsymbol{\varphi}}\| < \varepsilon$ for a

small value $\varepsilon \in \mathbb{R}_{>0}$. For linearization we take the Fréchet derivative in direction $\Delta\boldsymbol{\varphi}$ such that we seek an increment $\Delta\boldsymbol{\varphi}^{(k)} = \boldsymbol{\varphi}^{(k+1)} - \boldsymbol{\varphi}^{(k)}$ linearized system, satisfying

$$R_{\boldsymbol{\varphi}}(\boldsymbol{\varphi}^{(k)}, \delta\boldsymbol{\varphi}) + \mathrm{D}_{\boldsymbol{\varphi}} R_{\boldsymbol{\varphi}}(\boldsymbol{\varphi}^{(k)}, \delta\boldsymbol{\varphi}) \cdot \Delta\boldsymbol{\varphi}^{(k)} = 0 \qquad \forall\, \delta\boldsymbol{\varphi} \in \mathcal{V}_{\delta\boldsymbol{\varphi}}\,. \tag{3.94}$$

Introducing the tangent

$$K_{\boldsymbol{\varphi}\boldsymbol{\varphi}}(\boldsymbol{\varphi}^{(k)}, \delta\boldsymbol{\varphi}) \coloneqq \mathrm{D}_{\boldsymbol{\varphi}} R_{\boldsymbol{\varphi}}(\boldsymbol{\varphi}^{(k)}, \delta\boldsymbol{\varphi}) = \left[\mathrm{D}_{\boldsymbol{\varphi}} R_{\boldsymbol{\varphi}}(\boldsymbol{\varphi}, \delta\boldsymbol{\varphi})\right]\!\!\rceil_{\boldsymbol{\varphi}=\boldsymbol{\varphi}^{(k)}}\,, \tag{3.95}$$

the Newton step then requires finding $\Delta\boldsymbol{\varphi}^{(k)} \in \mathcal{V}_{\boldsymbol{\varphi}}$ satisfying

$$K_{\boldsymbol{\varphi}\boldsymbol{\varphi}}(\boldsymbol{\varphi}^{(k)}, \delta\boldsymbol{\varphi})\; \Delta\boldsymbol{\varphi}^{(k)} = -R_{\boldsymbol{\varphi}}(\boldsymbol{\varphi}^{(k)}, \delta\boldsymbol{\varphi}) \quad \forall\, \delta\boldsymbol{\varphi} \in \mathcal{V}_{\delta\boldsymbol{\varphi}}. \tag{3.96}$$

After solving eq. (3.96), the update $\boldsymbol{\varphi}^{(k+1)} = \boldsymbol{\varphi}^{(k)} + \Delta\boldsymbol{\varphi}^{(k)}$ is conducted and the steps repeat until reaching convergence criterion. For the discretized system with residual vector $\boldsymbol{R}_{\boldsymbol{\varphi}}^{(k)} = \left[\boldsymbol{R}_{\boldsymbol{\varphi}}^{A}(\boldsymbol{\varphi}^{\mathrm{h},(k)}, \mathcal{R}^{A})\right]$, linearization is done with respect to discrete values $\boldsymbol{\varphi}_B$, giving the tangent matrix

$$\boldsymbol{K}_{\boldsymbol{\varphi}\boldsymbol{\varphi}}^{(k)} \coloneqq \left[\mathrm{D}_{\boldsymbol{\varphi}_B}\left[\boldsymbol{R}_{\boldsymbol{\varphi}}^{A}(\boldsymbol{\varphi}^{\mathrm{h},(k)}, \mathcal{R}^{A})\right]\right]\!\!\rceil_{\boldsymbol{\varphi}_B=\boldsymbol{\varphi}_B^{(k)}} = \left[\boldsymbol{K}_{\boldsymbol{\varphi}\boldsymbol{\varphi}}^{AB,(k)}(\boldsymbol{\varphi}^{\mathrm{h},(k)}, \mathcal{R}^{A}, \mathcal{R}^{B})\right] \tag{3.97}$$

yielding

$$\boldsymbol{K}_{\boldsymbol{\varphi}\boldsymbol{\varphi}}^{AB,(k)}\; \Delta\boldsymbol{\varphi}_B^{(k)} = -\boldsymbol{R}_{\boldsymbol{\varphi}}^{A,(k)} \tag{3.98}$$

where $\Delta\boldsymbol{\varphi}_B^{(k)} = \boldsymbol{\varphi}_B^{(k+1)} - \boldsymbol{\varphi}_B^{(k)}$ with discrete degrees of freedom $\boldsymbol{\varphi}_B$. In general, the Newton iteration counter (k) and the control-point indices are omitted, such that the system to be solved in every Newton step is written as $\boldsymbol{K}_{\boldsymbol{\varphi}\boldsymbol{\varphi}}\,\Delta\boldsymbol{\varphi} = -\boldsymbol{R}_{\boldsymbol{\varphi}}$.

The convergence of this method is locally quadratic and thus depends on the start-value for $k = 0$, which in practice is a known solution of a similar problem. Hence, an incremental load-application scheme, where external contributions or a prescribed displacement are gradually increased, can provide good starting conditions. This can be interpreted as a homotopy, where an auxiliary parameter $t \in [0, 1]$ is introduced in the function $H(\boldsymbol{\varphi}, t) \coloneqq \delta\Pi^{\mathrm{int}}(\boldsymbol{\varphi}, \overline{\boldsymbol{\varphi}}(t)) - t\,\delta\Pi^{\mathrm{ext}}(\boldsymbol{\varphi}, \overline{\boldsymbol{\varphi}}(t))$, scaling external contributions and essential boundary conditions via $\overline{\boldsymbol{\varphi}}(t) \coloneqq (1-t)\boldsymbol{\varphi}^{*} + t\,\overline{\boldsymbol{\varphi}}$. Hence H transitions from the trivial problem $H(\boldsymbol{\varphi}, t=0) = \delta\Pi^{\mathrm{int}}(\boldsymbol{\varphi}, \overline{\boldsymbol{\varphi}}(0)) = 0$ with easily accessible or known solution $\boldsymbol{\varphi}^{*}$ (e.g. $\boldsymbol{\varphi}^{*} = \boldsymbol{\varphi}_0$) to the fully loaded problem $H(\boldsymbol{\varphi}, t=1) = \delta\Pi^{\mathrm{int}}(\boldsymbol{\varphi}, \overline{\boldsymbol{\varphi}}) - \delta\Pi^{\mathrm{ext}}(\boldsymbol{\varphi}, \overline{\boldsymbol{\varphi}}) = R_{\boldsymbol{\varphi}} = 0$ with the desired solution. Note, that further improvements such as predictor updates may be applied. Besides homotopy, other methods/algorithms or enhancements on Newton's method can further accelerate root finding, like line-search and damped Newton methods (cf. Bonet and Wood [20] and Schuß et al. [105] among many others).

3.5.3 Multi-field systems and block structure

On the basis of the dual-field problem

$$\{\boldsymbol{\varphi}^{*}, \boldsymbol{w}^{*}\} = \arg\left\{\inf_{\boldsymbol{\varphi}\in\mathcal{V}_{\boldsymbol{\varphi}}}\; \inf_{\boldsymbol{w}\in\mathcal{V}_{\boldsymbol{w}}}\; \mathfrak{L}^{*}(\boldsymbol{\varphi}, \boldsymbol{w})\right\}, \tag{3.99}$$

with residuals

$$R_{\boldsymbol{\varphi}}(\boldsymbol{\varphi}, \boldsymbol{w}, \delta\boldsymbol{\varphi}) \coloneqq \delta_{\boldsymbol{\varphi}}\mathfrak{L}(\boldsymbol{\varphi}, \boldsymbol{w}) \quad \text{and} \quad R_{\boldsymbol{w}}(\boldsymbol{\varphi}, \boldsymbol{w}, \delta\boldsymbol{w}) \coloneqq \delta_{\boldsymbol{w}}\mathfrak{L}(\boldsymbol{\varphi}, \boldsymbol{w}) \,, \tag{3.100}$$

we now derive the steps for the Newton solution algorithm, representative of any multi-field problem including constrained systems.

At a given state $(\boldsymbol{\varphi}^{(k)}, \boldsymbol{w}^{(k)})$ within iterations, the directional derivatives in the increments $(\Delta\boldsymbol{\varphi}, \Delta\boldsymbol{w})$ read

$$\begin{aligned} R_{\boldsymbol{\varphi}} + \mathrm{D}_{\boldsymbol{\varphi}} R_{\boldsymbol{\varphi}} \cdot \Delta\boldsymbol{\varphi} + \mathrm{D}_{\boldsymbol{w}} R_{\boldsymbol{\varphi}} \cdot \Delta\boldsymbol{w} = 0, \\ R_{\boldsymbol{w}} + \mathrm{D}_{\boldsymbol{\varphi}} R_{\boldsymbol{w}} \cdot \Delta\boldsymbol{\varphi} + \mathrm{D}_{\boldsymbol{w}} R_{\boldsymbol{w}} \cdot \Delta\boldsymbol{w} = 0, \end{aligned} \tag{3.101}$$

for all $(\delta\boldsymbol{\varphi}, \delta\boldsymbol{w}) \in \mathcal{V}_{\boldsymbol{\varphi}} \times \mathcal{V}_{\boldsymbol{w}}$. Defining the tangent blocks

$$\begin{aligned} K_{\boldsymbol{\varphi}\boldsymbol{\varphi}} &\coloneqq [\![\mathrm{D}_{\boldsymbol{\varphi}}\delta_{\boldsymbol{\varphi}}\mathfrak{L}]\!]_{(\boldsymbol{\varphi}^{(k)}, \boldsymbol{w}^{(k)})} \,, & K_{\boldsymbol{\varphi}\boldsymbol{w}} &\coloneqq [\![\mathrm{D}_{\boldsymbol{w}}\delta_{\boldsymbol{\varphi}}\mathfrak{L}]\!]_{(\boldsymbol{\varphi}^{(k)}, \boldsymbol{w}^{(k)})} \,, \\ K_{\boldsymbol{w}\boldsymbol{\varphi}} &\coloneqq [\![\mathrm{D}_{\boldsymbol{\varphi}}\delta_{\boldsymbol{w}}\mathfrak{L}]\!]_{(\boldsymbol{\varphi}^{(k)}, \boldsymbol{w}^{(k)})} \quad \text{and} & K_{\boldsymbol{w}\boldsymbol{w}} &\coloneqq [\![\mathrm{D}_{\boldsymbol{w}}\delta_{\boldsymbol{w}}\mathfrak{L}]\!]_{(\boldsymbol{\varphi}^{(k)}, \boldsymbol{w}^{(k)})} \,, \end{aligned} \tag{3.102}$$

the discrete Newton step reads

$$\begin{bmatrix} \boldsymbol{K}_{\boldsymbol{\varphi}\boldsymbol{\varphi}} & \boldsymbol{K}_{\boldsymbol{\varphi}\boldsymbol{w}} \\ \boldsymbol{K}_{\boldsymbol{w}\boldsymbol{\varphi}} & \boldsymbol{K}_{\boldsymbol{w}\boldsymbol{w}} \end{bmatrix} \begin{bmatrix} \Delta\boldsymbol{\varphi} \\ \Delta\boldsymbol{w} \end{bmatrix} = - \begin{bmatrix} \boldsymbol{R}_{\boldsymbol{\varphi}} \\ \boldsymbol{R}_{\boldsymbol{w}} \end{bmatrix} . \tag{3.103}$$

We further point out that in choosing the same space of ansatz-functions for variation and solution, a system obtained by an underlying variational potential $G(\boldsymbol{a}, \boldsymbol{b})$ becomes symmetric, since variation with respect to field $\boldsymbol{a}$ reads $\delta_{\boldsymbol{a}}G = \delta\boldsymbol{a} \cdot \mathrm{D}_{\boldsymbol{a}}G = \boldsymbol{a} \cdot \boldsymbol{R}_{\boldsymbol{a}}$ and hence the tangent $\mathrm{D}_{\boldsymbol{b}}\boldsymbol{R}_{\boldsymbol{a}}$ with respect to field $\boldsymbol{b}$ reads $\mathrm{D}_{\boldsymbol{b}}\mathrm{D}_{\boldsymbol{a}}G = \mathrm{D}_{\boldsymbol{b}}\mathrm{D}_{\boldsymbol{a}}G$ (cf. Schwarz's theorem).

3.6 Mixed modes and constrained systems

In the variational treatment in certain continuum mechanic frameworks presented in this work, we make use of mixed modes, in which additional fields, e.g. a derived kinematic or stress responses, are introduced and coupled in a single functional. Therefore, we use the terms *primary* and *secondary* for initial and additional fields, respectively. Coupling is usually done by formulating equality constraints and enforcing them using Lagrange multipliers. More generally, constrained systems (including but not limited to mixed modes) lead to optimization problems with m equality constraints formulated to fulfill $f_\alpha \colon \Omega_0 \to 0, \alpha = 1, \dots, m$ and n inequality constraints $g_\beta \colon \Omega_0 \to \mathbb{R}^-, \beta = 1, \dots, n$. Introducing Lagrange multiplier fields $\lambda_\alpha(\boldsymbol{\varphi}, \boldsymbol{F}, \mathfrak{F})$ and $\mu_\beta(\boldsymbol{\varphi}, \boldsymbol{F}, \mathfrak{F})$ for each constraint, transforms the imposed stationarity of the Lagrangian $\mathfrak{L}$ to the augmented Lagrangian $\mathfrak{L}^*$

$$\mathfrak{L}^*[\boldsymbol{\varphi}, \{\lambda_\alpha\}, \{\mu_\beta\}] \coloneqq \mathfrak{L} + \underbrace{\int_{\Omega_0} \{\lambda_\alpha f_\alpha\} \mathrm{d}V}_{\coloneqq \Phi_{\boldsymbol{\lambda}}} + \underbrace{\int_{\Omega_0} \{\mu_\beta g_\beta\} \mathrm{d}V}_{\coloneqq \Phi_{\boldsymbol{\mu}}} \tag{3.104}$$

such that the stationarity condition now reads

$$\delta_{\boldsymbol{\varphi}}\mathfrak{L}^* = 0\,, \quad \delta_{\boldsymbol{\lambda}}\mathfrak{L}^* = 0 \quad \text{and} \quad \delta_{\boldsymbol{\mu}}\mathfrak{L}^* = 0\,. \tag{3.105}$$

Taking the stationarity along with the primal and dual feasibility, $f_\alpha = 0\,,\ \lambda_\alpha \geq 0\,\forall\alpha$ and $g_\beta \leq 0\,,\ \mu_\beta \geq 0\,\forall\beta$, respectively, with complementary slackness $\mu_\beta\, g_\beta = 0$ comprise the well-known Karush-Kuhn-Tucker conditions.

Since non-equilibrium conditions are not considered in this work, the subsequent analysis is restricted to equilibrium conditions. The nonlinear weak form of a system with equality constraint $\boldsymbol{f}$ and multiplier field $\boldsymbol{\lambda} \in \mathcal{Q}$ then requires finding $(\boldsymbol{\varphi}, \boldsymbol{\lambda}) \in \mathcal{V}_{\boldsymbol{\varphi}} \times \mathcal{Q}$ such that

$$\begin{aligned} R_{\boldsymbol{\varphi}}(\boldsymbol{\varphi}, \boldsymbol{\lambda}, \delta\boldsymbol{\varphi}) &\coloneqq \delta_{\boldsymbol{\varphi}}\mathfrak{L}(\boldsymbol{\varphi}) + \delta_{\boldsymbol{\varphi}}\Phi_{\boldsymbol{\lambda}}(\boldsymbol{\varphi}, \boldsymbol{\lambda}) = 0 \quad \forall\, \delta\boldsymbol{\varphi} \in \mathcal{V}_{\delta\boldsymbol{\varphi}}, \\ R_{\boldsymbol{\lambda}}(\boldsymbol{\varphi}, \delta\boldsymbol{\lambda}) &\coloneqq \delta_{\boldsymbol{\lambda}}\Phi_{\boldsymbol{\lambda}}(\boldsymbol{\varphi}) = 0 \quad \forall\, \delta\boldsymbol{\lambda} \in \mathcal{Q}\,. \end{aligned} \tag{3.106}$$

The above given saddle point problem of finding the critical point can be directly stated via the inf-sup formalism

$$\{\boldsymbol{\varphi}^*, \boldsymbol{\lambda}^*\} = \arg\left\{ \inf_{\boldsymbol{\varphi}\in\mathcal{V}_{\boldsymbol{\varphi}}} \sup_{\boldsymbol{\lambda}\in\mathcal{Q}} \mathfrak{L}^*(\boldsymbol{\varphi}, \boldsymbol{\lambda}) \right\}, \tag{3.107}$$

where solution $\{\boldsymbol{\varphi}^*, \boldsymbol{\lambda}^*\} \in \mathcal{V}_{\boldsymbol{\varphi}} \times \mathcal{Q}$ is the argument obtained by minimizing $\mathfrak{L}^*$ among all possible fields $\boldsymbol{\varphi} \in \mathcal{V}_{\boldsymbol{\varphi}}$ and maximizing among all possible $\boldsymbol{\lambda} \in \mathcal{Q}$.

3.6.1 Inf-Sup (LBB) Condition for the Constrained System

For above system, linearization reads

$$\begin{aligned} A = K_{\boldsymbol{\varphi}\boldsymbol{\varphi}} &\coloneqq [\mathrm{D}_{\boldsymbol{\varphi}}(\delta_{\boldsymbol{\varphi}}\mathfrak{L} + \delta_{\boldsymbol{\varphi}}\Phi_{\boldsymbol{\lambda}})]\rrbracket_{(\boldsymbol{\varphi}^{(k)}, \boldsymbol{\lambda}^{(k)})}\,, & B = K_{\boldsymbol{\varphi}\boldsymbol{\lambda}} &\coloneqq [\mathrm{D}_{\boldsymbol{\lambda}}\delta_{\boldsymbol{\varphi}}\Phi_{\boldsymbol{\lambda}}]\rrbracket_{(\boldsymbol{\varphi}^{(k)}, \boldsymbol{\lambda}^{(k)})}\,, \\ C = K_{\boldsymbol{\lambda}\boldsymbol{\varphi}} &\coloneqq [\mathrm{D}_{\boldsymbol{\varphi}}\delta_{\boldsymbol{\lambda}}\Phi_{\boldsymbol{\lambda}}]\rrbracket_{(\boldsymbol{\varphi}^{(k)}, \boldsymbol{\lambda}^{(k)})}\,, \quad \text{and} & D = K_{\boldsymbol{\lambda}\boldsymbol{\lambda}} &\coloneqq [\mathrm{D}_{\boldsymbol{\lambda}}\delta_{\boldsymbol{\lambda}}\Phi_{\boldsymbol{\lambda}}]\rrbracket_{(\boldsymbol{\varphi}^{(k)}, \boldsymbol{\lambda}^{(k)})}\,, \end{aligned} \tag{3.108}$$

such that the discrete Newton step assumes the canonical saddle-point form

$$\begin{bmatrix} \boldsymbol{A} & \boldsymbol{B} \\ \boldsymbol{C} & \boldsymbol{0} \end{bmatrix} \begin{bmatrix} \Delta\boldsymbol{\varphi} \\ \Delta\boldsymbol{\lambda} \end{bmatrix} = - \begin{bmatrix} \boldsymbol{R}_{\boldsymbol{\varphi}} \\ \boldsymbol{R}_{\boldsymbol{\lambda}} \end{bmatrix}\,, \tag{3.109}$$

where $\boldsymbol{A}$ is the tangent of the primal operator, $\boldsymbol{B}$ contains the action of the multiplier and $\boldsymbol{C}$ is the linearized constraint. Note that due to the construction of $\Phi_{\boldsymbol{\lambda}}$, the linearized variation with respect to the multiplier field vanishes, i.e. $\boldsymbol{D} = \boldsymbol{0}$, and the system inherits the symmetry $\boldsymbol{B}^{\mathsf{T}} = \boldsymbol{C}$.

Regarding stability of Galerkin methods for multi-field saddle point problems we refer to the literature on that topic, e.g. Krischok and Linder [70] and Chapelle and Bathe [23] among others. In the discretized state, stability test in terms of second variation can be directly performed on the tangent matrix

$$\boldsymbol{H} = \begin{bmatrix} \boldsymbol{A} & \boldsymbol{C}^{\mathsf{T}} \\ \boldsymbol{C} & \boldsymbol{0} \end{bmatrix} \tag{3.110}$$

as the Hessian of $\mathfrak{L}^*$ that must satisfy the LBB (*Ladyzhenskaya - Babuška - Brezzi*) condition

$$0 < \beta^{\mathrm{h}} = \inf_{\delta\boldsymbol{\lambda}^{\mathrm{h}} \in \mathcal{Q}^{\mathrm{h}}} \sup_{\delta\boldsymbol{\varphi}^{\mathrm{h}} \in \mathcal{V}^{\mathrm{h}}_{\delta\boldsymbol{\varphi}}} \frac{-\det(\boldsymbol{H})}{\|\delta\boldsymbol{\varphi}^{\mathrm{h}}\|^2_{\mathcal{V}_{\delta\boldsymbol{\varphi}}} \, \|\delta\boldsymbol{\lambda}^{\mathrm{h}}\|^2_{\mathcal{Q}}} \tag{3.111}$$

with norms $\|(\cdot)\|$ for corresponding spaces (cf. section 0.3.3) and nonzero vectors $\delta\boldsymbol{\lambda}$, $\delta\boldsymbol{\varphi}$. Evaluating the determinant of the Hessian results in $\det(\boldsymbol{H}) = \boldsymbol{A}\boldsymbol{0} - \boldsymbol{C}^{\mathsf{T}}\boldsymbol{C}$, hence with definition of the bilinear form $b_{\boldsymbol{\varphi}^*}(\delta\boldsymbol{\varphi}^{\mathrm{h}}, \delta\boldsymbol{\lambda}^{\mathrm{h}}) = [\![\mathrm{D}_{\boldsymbol{\varphi}}\delta_{\boldsymbol{\lambda}}\Phi_{\boldsymbol{\lambda}}]\!]_{\boldsymbol{\varphi}^*}\,\delta\boldsymbol{\varphi}$, we can alternatively state

$$0 < \beta^{\mathrm{h}} = \inf_{\delta\boldsymbol{\lambda}^{\mathrm{h}} \in \mathcal{Q}^{\mathrm{h}}} \sup_{\delta\boldsymbol{\varphi}^{\mathrm{h}} \in \mathcal{V}^{\mathrm{h}}_{\delta\boldsymbol{\varphi}}} \frac{\left(b_{\boldsymbol{\varphi}^*}(\delta\boldsymbol{\varphi}, \delta\boldsymbol{\lambda})\right)^2}{\|\delta\boldsymbol{\varphi}^{\mathrm{h}}\|^2_{\mathcal{V}_{\delta\boldsymbol{\varphi}}} \, \|\delta\boldsymbol{\lambda}^{\mathrm{h}}\|^2_{\mathcal{Q}}} \,. \tag{3.112}$$

A uniform lower bound $\beta > 0$ guarantees that every admissible multiplier mode $\delta\boldsymbol{\lambda}^{\mathrm{h}}$ is controlled by some $\delta\boldsymbol{\varphi}^{\mathrm{h}}$ through the bilinear form and discrete $\beta^{\mathrm{h}} > 0$ gives criteria for compatible $\mathcal{V}^{\mathrm{h}}_{\delta\boldsymbol{\varphi}} \times \mathcal{Q}^{\mathrm{h}}$ pairings ensuring well-posed and non-oscillatory discrete saddle point problem. Hence, $\mathcal{Q}^{\mathrm{h}}$ has to be chosen not to over- or under-constrain the system, resulting in ill-conditioning of $\boldsymbol{H}$ or spurious oscillations.

Remark 3.6.1 – LBB. We point out, that one may write above equation using the positive square root of the function, yielding in a standard form

$$0 < \beta^{\mathrm{h}} = \inf_{\delta\boldsymbol{\lambda}^{\mathrm{h}} \in \mathcal{Q}^{\mathrm{h}}} \sup_{\delta\boldsymbol{\varphi}^{\mathrm{h}} \in \mathcal{V}^{\mathrm{h}}_{\delta\boldsymbol{\varphi}}} \frac{b_{\boldsymbol{\varphi}^*}(\delta\boldsymbol{\varphi}, \delta\boldsymbol{\lambda})}{\|\delta\boldsymbol{\varphi}^{\mathrm{h}}\|_{\mathcal{V}_{\delta\boldsymbol{\varphi}}} \, \|\delta\boldsymbol{\lambda}^{\mathrm{h}}\|_{\mathcal{Q}}} \,. \tag{3.113}$$

3.A Appendix A

3.A.1 First variation

The variation $\delta\mathcal{F}$ of a function $\mathcal{F} \coloneqq \mathcal{F}\Big(\boldsymbol{X},\, \boldsymbol{\varphi},\, \nabla_{\mathrm{x}}\boldsymbol{\varphi},\, \nabla^2_{\mathrm{x}}\boldsymbol{\varphi},\, \dot{\boldsymbol{\varphi}}\Big)$ is conducted following these steps:

I Consider a one-parameter variational transformation of the primary field $\boldsymbol{\varphi}'_\varepsilon(\boldsymbol{\varphi}, \varepsilon) = \mathcal{G}_\varepsilon \circ \boldsymbol{\varphi}$, with the infinitesimal scalar parameter ε and a generator function $\mathcal{G}_\varepsilon(\boldsymbol{\varphi})$, where $[\mathcal{G}_\varepsilon(\boldsymbol{\varphi}) \circ \boldsymbol{\varphi}]\!]_{\varepsilon=0} = \boldsymbol{\varphi}$. Note, that since the whole reference configuration is known, no variation is conducted on $\boldsymbol{X}$.

II Expand $\mathcal{F}'_\varepsilon \coloneqq \mathcal{F}\Big(\boldsymbol{\varphi}'_\varepsilon, \nabla_{\mathrm{x}}\boldsymbol{\varphi}'_\varepsilon, \nabla^2_{\mathrm{x}}\boldsymbol{\varphi}'_\varepsilon\Big)$ with a linear Taylor series around $\varepsilon = 0$

$$\mathcal{F}'_\varepsilon = \mathcal{F} + \frac{\partial \mathcal{F}}{\partial \boldsymbol{\varphi}} \cdot (\boldsymbol{\varphi}'_\varepsilon - \boldsymbol{\varphi}) + \frac{\partial \mathcal{F}}{\partial \nabla_{\mathrm{x}}\boldsymbol{\varphi}} : (\nabla_{\mathrm{x}}\boldsymbol{\varphi}'_\varepsilon - \nabla_{\mathrm{x}}\boldsymbol{\varphi}) + \frac{\partial \mathcal{F}}{\partial \nabla^2_{\mathrm{x}}\boldsymbol{\varphi}} \vdots \Big(\nabla^2_{\mathrm{x}}\boldsymbol{\varphi}'_\varepsilon - \nabla^2_{\mathrm{x}}\boldsymbol{\varphi}\Big) + \frac{\partial \mathcal{F}}{\partial \dot{\boldsymbol{\varphi}}} \cdot \Big(\dot{\boldsymbol{\varphi}}'_\varepsilon - \dot{\boldsymbol{\varphi}}\Big) + \mathcal{O}\Big(\varepsilon^2\Big)\,, \tag{3.114}$$

where

$$\left[\frac{\partial^n \mathcal{F}'_\varepsilon}{\partial\Big((\cdot)'_\varepsilon\Big)^n}\right]\Bigg|_{\varepsilon=0} = \frac{\partial^n \mathcal{F}}{\partial(\cdot)^n}\,, \quad n \in \mathbb{N}_0\,. \tag{3.115}$$

III Take the variation using

$$\delta\mathcal{F} = \lim_{\varepsilon\to 0} \frac{\mathcal{F}'_\varepsilon - \mathcal{F}}{\varepsilon} = \left[\frac{\mathrm{d}\mathcal{F}'_\varepsilon}{\mathrm{d}\varepsilon}\right]\Bigg|_{\varepsilon=0}\,. \tag{3.116}$$

Note that for sufficiency considerations this can be extended to second variation, as the second-order term ε^2 in eq. (3.114). For a solution $\{\boldsymbol{\varphi}^*\} = \arg\Big\{\inf_{\boldsymbol{\varphi}\in\mathcal{V}_{\boldsymbol{\varphi}}} \mathcal{F}\Big\}$, i.e. fulfilling necessary stationarity $\delta\mathcal{F} = 0$, the sufficient condition for a minimum lies in the second variation

$$\mathcal{F}(\boldsymbol{\varphi}^* + \delta\boldsymbol{\varphi}) - \mathcal{F}(\boldsymbol{\varphi}^*) = \mathcal{O}\Big(\varepsilon^2\Big) \geq 0 \quad \forall \delta\boldsymbol{\varphi} \in \mathcal{V}_{\delta\boldsymbol{\varphi}}. \tag{3.117}$$

Example: Set $\boldsymbol{\varphi}'_\varepsilon = \boldsymbol{\varphi} + \varepsilon\delta\boldsymbol{\varphi}$, leading to

$$\dot{\boldsymbol{\varphi}}'_\varepsilon = \dot{\boldsymbol{\varphi}} + \varepsilon\delta\dot{\boldsymbol{\varphi}}\,, \quad \nabla_{\mathrm{x}}\boldsymbol{\varphi}'_\varepsilon = \nabla_{\mathrm{x}}\boldsymbol{\varphi} + \varepsilon\nabla_{\mathrm{x}}\delta\boldsymbol{\varphi} \quad \text{and} \quad \nabla^2_{\mathrm{x}}\boldsymbol{\varphi}'_\varepsilon = \nabla^2_{\mathrm{x}}\boldsymbol{\varphi} + \varepsilon\nabla^2_{\mathrm{x}}\delta\boldsymbol{\varphi}\,. \tag{3.118}$$

Conducting the Taylor series

$$\mathcal{F}'_\varepsilon = \mathcal{F} + \varepsilon\frac{\partial \mathcal{F}}{\partial \boldsymbol{\varphi}} \cdot \delta\boldsymbol{\varphi} + \varepsilon\frac{\partial \mathcal{F}}{\partial \nabla_{\mathrm{x}}\boldsymbol{\varphi}} : \nabla_{\mathrm{x}}\delta\boldsymbol{\varphi} + \varepsilon\frac{\partial \mathcal{F}}{\partial \nabla^2_{\mathrm{x}}\boldsymbol{\varphi}} \vdots \nabla^2_{\mathrm{x}}\delta\boldsymbol{\varphi} + \varepsilon\frac{\partial \mathcal{F}}{\partial \dot{\boldsymbol{\varphi}}} \cdot \delta\dot{\boldsymbol{\varphi}} + O\Big(\varepsilon^2\Big)\,, \tag{3.119}$$

and inserting yields

$$\delta\mathcal{F} = \frac{\partial \mathcal{F}}{\partial \boldsymbol{\varphi}} \cdot \delta\boldsymbol{\varphi} + \frac{\partial \mathcal{F}}{\partial \nabla_{\mathrm{x}}\boldsymbol{\varphi}'_\varepsilon} : \nabla_{\mathrm{x}}\delta\boldsymbol{\varphi} + \frac{\partial \mathcal{F}}{\partial \nabla^2_{\mathrm{x}}\boldsymbol{\varphi}} \vdots \nabla^2_{\mathrm{x}}\delta\boldsymbol{\varphi}\,. \tag{3.120}$$

Unless stated otherwise, the variation is directly given by employing these steps.

3.A.2 Traction on hyper-surfaces

There exist equivalent formulations for the traction force $\overline{\boldsymbol{T}}$, e.g. used in Bertram and Forest [13], where

$$\begin{aligned}\overline{\boldsymbol{T}} &= (\boldsymbol{P} - \nabla_{\mathrm{x}} \cdot \boldsymbol{\mathfrak{P}})\,\boldsymbol{N} - K\,(\boldsymbol{\mathfrak{P}}\,\boldsymbol{N})\boldsymbol{N} - \nabla_{\mathrm{x}\parallel} \cdot (\boldsymbol{\mathfrak{P}}\,\boldsymbol{N}) \\ &= (\boldsymbol{P} - \nabla_{\mathrm{x}} \cdot \boldsymbol{\mathfrak{P}})\,\boldsymbol{N} - K\,\boldsymbol{\mathfrak{P}} : (\boldsymbol{N} \otimes \boldsymbol{N}) - \Big(\boldsymbol{N} \cdot \Big(\nabla_{\mathrm{x}\parallel} \cdot \boldsymbol{\mathfrak{P}}\Big) + \boldsymbol{\mathfrak{P}} : \Big(\nabla_{\mathrm{x}\parallel}\boldsymbol{N}\Big)\Big) \\ &= (\boldsymbol{P} - \nabla_{\mathrm{x}} \cdot \boldsymbol{\mathfrak{P}})\,\boldsymbol{N} - \Big(\nabla_{\mathrm{x}\parallel} \cdot \boldsymbol{\mathfrak{P}}\Big) \cdot \boldsymbol{N} + \boldsymbol{\mathfrak{P}} : \Big(\Big(\nabla_{\mathrm{x}\parallel} \cdot \boldsymbol{N}\Big)(\boldsymbol{N} \otimes \boldsymbol{N}) - \nabla_{\mathrm{x}\parallel}\boldsymbol{N}\Big) \\ &= (\boldsymbol{P} - \nabla_{\mathrm{x}} \cdot \boldsymbol{\mathfrak{P}})\,\boldsymbol{N} - \nabla_{\mathrm{x}\parallel} \cdot ((\boldsymbol{\mathfrak{P}} \cdot \boldsymbol{N})(\boldsymbol{I} - \boldsymbol{N} \otimes \boldsymbol{N}))\,.\end{aligned} \tag{3.121}$$

Introducing the normal gradient $\nabla_{\mathrm{x}N}(\cdot) = (\nabla_{\mathrm{x}}(\cdot))\boldsymbol{N}$ (see Javili et al. [62]), the third part of the internal virtual work eq. (3.31) containing the normal gradient alternatively reads

$$\nabla_{\mathrm{x}\perp}\delta\boldsymbol{\varphi} : (\boldsymbol{\mathfrak{P}}\boldsymbol{N}) = \nabla_{\mathrm{x}N}\delta\boldsymbol{\varphi} \cdot (\boldsymbol{\mathfrak{P}} : (\boldsymbol{N} \otimes \boldsymbol{N}))\,, \tag{3.122}$$

such that the external hyper-stress traction force can be set by $\boldsymbol{\mathfrak{P}} : (\boldsymbol{N} \otimes \boldsymbol{N}) = \overline{\boldsymbol{M}\boldsymbol{N}}$ on $\partial\Omega_0^M \times I$. We refer to Fedele [39] for the conversion into Eulerian description.

3.A.3 Higher order stress symmetry

With integration by parts for the higher order term and application of the divergence theorem we get

$$\begin{aligned}\delta\Pi^{\mathrm{int}} &= \int_{\Omega_0}\Big\{\boldsymbol{P} : \nabla_{\mathrm{x}}(\hat{\boldsymbol{\varsigma}}\boldsymbol{\varphi}) + \boldsymbol{\mathfrak{P}} : \nabla_{\mathrm{x}}^2(\hat{\boldsymbol{\varsigma}}\boldsymbol{\varphi})\Big\}\mathrm{d}V \\ &= \int_{\Omega_0}\Big\{\hat{\boldsymbol{\varsigma}}^{\top} : (\boldsymbol{P} \cdot \nabla_{\mathrm{x}}\boldsymbol{\varphi} - \nabla_{\mathrm{x}} \cdot \boldsymbol{\mathfrak{P}} : \nabla_{\mathrm{x}}\boldsymbol{\varphi})\Big\}\mathrm{d}V + \int_{\partial\Omega_0}\{(\nabla_{\mathrm{x}}(\hat{\boldsymbol{\varsigma}}\boldsymbol{\varphi}) : \boldsymbol{\mathfrak{P}})\boldsymbol{N}\}\mathrm{d}A \\ &= \int_{\Omega_0}\Bigg\{\hat{\boldsymbol{\varsigma}}^{\top} : \underbrace{(\boldsymbol{P} \cdot \nabla_{\mathrm{x}}\boldsymbol{\varphi} - \nabla_{\mathrm{x}} \cdot \boldsymbol{\mathfrak{P}} \cdot \nabla_{\mathrm{x}}\boldsymbol{\varphi})}_{:=\boldsymbol{B}}\Bigg\}\mathrm{d}V + \int_{\partial\Omega_0}\{(\boldsymbol{\varsigma} \times \nabla_{\mathrm{x}}\boldsymbol{\varphi}) : \boldsymbol{\mathfrak{P}}\boldsymbol{N}\}\mathrm{d}A\,,\end{aligned} \tag{3.123}$$

where the latter integral enters the momentum balance as part of the boundary conditions. Following the mentioned symmetry for $\boldsymbol{B}$, the condition now reads

$$(\boldsymbol{P} - \nabla_{\mathrm{x}} \cdot \boldsymbol{\mathfrak{P}}) \cdot \nabla_{\mathrm{x}}\boldsymbol{\varphi} = ((\boldsymbol{P} - \nabla_{\mathrm{x}} \cdot \boldsymbol{\mathfrak{P}}) \cdot \nabla_{\mathrm{x}}\boldsymbol{\varphi})^{\top}\,, \tag{3.124}$$

where again to account for vanishing higher order contributions, we may require $\boldsymbol{P} \cdot \nabla_{\mathrm{x}}\boldsymbol{\varphi} = (\boldsymbol{P} \cdot \nabla_{\mathrm{x}}\boldsymbol{\varphi})^{\top}$ and $(\nabla_{\mathrm{x}} \cdot \boldsymbol{\mathfrak{P}}) \cdot \nabla_{\mathrm{x}}\boldsymbol{\varphi} = ((\nabla_{\mathrm{x}} \cdot \boldsymbol{\mathfrak{P}}) \cdot \nabla_{\mathrm{x}}\boldsymbol{\varphi})^{\top}$.

4 Continuous embedded fibers

In the previous chapter, we developed a comprehensive framework for the general second-order continuum mechanics, where the kinematic description of a body is extended to include second higher-order gradients of the motion. This approach allows to account for size effects and non-local interactions due to micro-structure and curvature-driven phenomena that cannot be fully captured using a classical Cauchy continuum. The extended kinematical set provides instruments for material modeling, allowing withing a concise formulation to account for internal length scales and higher-order boundary conditions. A large field in this regard are composite material, where dissimilar structures are combined and at least one is subjected to bending, twisting or its response is dominated by curvature.

Increasing in area of application as well as manufacturing capabilities, a variety of fiber-reinforced composites, such as steel beam reinforced concrete or glass-/carbon fiber infused polymers directly fall into that category. Their characteristics lead to interpretation of a matrix material with embedded idealized one-dimensional structures for which experiments, e.g. in Schulte et al. [103] for woven fabrics in a polymer matrix, suggest significant bending and twisting resistance.

In this chapter we first propose a continuous second-gradient material model enabling to incorporate such effects. Therein the link from rod-like structures with curvature towards second-order deformation gradients is shown and explicit interpretation in terms of bending and twisting is provided. Subsequently, the model is inserted in the established framework, which eventually allows us to conduct simulations showing the capabilities of both framework and material model.

4.1 Fiber kinematic

Following preliminary works on fibers (e.g. Asmanoglo and Menzel [5, 6], Soldatos [110], and Spencer and Soldatos [112]), we consider a fabric of fibers embedded into a matrix material. We simplify the structure of fibers by assuming $f \in \mathbb{N}$ families of fiber directions

$$\boldsymbol{L}^\alpha : \Omega_0 \to \mathbb{R}^d\,, \quad \alpha = 1, \dots, f \tag{4.1}$$

with normalized lengths $\|\boldsymbol{L}^\alpha\| = 1$, $\bar{\boldsymbol{L}}^\alpha = \boldsymbol{L}^\alpha$ and initial straightness $\nabla_{\mathrm{X}} \boldsymbol{L}^\alpha = \boldsymbol{0}$. The surrounding body is subjected to the motion introduced in section 3.1.1 and depicted in

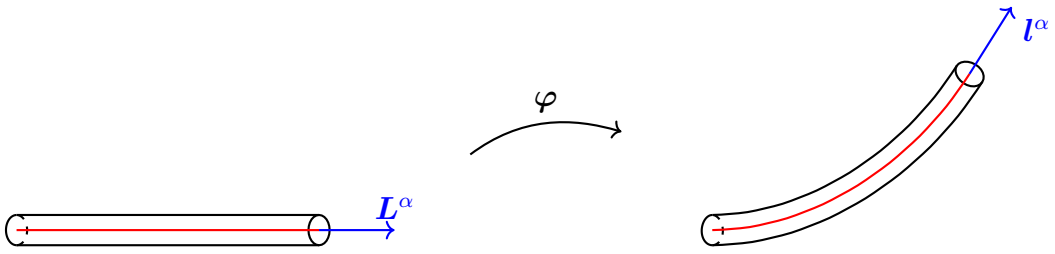


Figure 4.1.1 – Continuous fiber kinematic. Deformation of the continuous fiber embedded in a matrix.

figure 4.1.1. Therefore, its current direction $\boldsymbol{l}^\alpha : \Omega \to \mathbb{R}^d$ is determined by the deformation gradient $\boldsymbol{F}$, see eq. (3.1), yielding

$$\boldsymbol{l}^\alpha = \boldsymbol{F}\boldsymbol{L}^\alpha = \varepsilon^\alpha \bar{\boldsymbol{l}}^\alpha \,. \tag{4.2}$$

Here we further introduced the current normalized fiber direction $\bar{\boldsymbol{l}}^\alpha\Omega \to \mathbb{R}^d$, with $\|\bar{\boldsymbol{l}}^\alpha\| = 1$, as well as the fiber stretch $\varepsilon^\alpha : \Omega \to \mathbb{R}$, defined by

$$\varepsilon^\alpha = \|\boldsymbol{l}^\alpha\| = \|\boldsymbol{F}\boldsymbol{L}^\alpha\| = \sqrt{\boldsymbol{L}^\alpha \cdot \boldsymbol{F}^\top\boldsymbol{F} \cdot \boldsymbol{L}^\alpha} \,. \tag{4.3}$$

Incorporating the findings on pantographic structures, see dell'Isola et al. [31] among others, we additionally aim to describe the shear deformation between two initially not coinciding fiber directions $\boldsymbol{L}^\alpha \neq \boldsymbol{L}^\beta$. Thus, we introduce the shear measure $\phi^{\alpha\beta} : \Omega \to \mathbb{R}$ based on the change of angle $\gamma^{\alpha,\beta} = \sphericalangle\left(\bar{\boldsymbol{l}}^\alpha, \bar{\boldsymbol{l}}^\beta\right)$, calculated by

$$\begin{aligned} \phi^{\alpha\beta} &= \tan\left(\gamma^{\alpha,\beta} - \gamma_0^{\alpha,\beta}\right) \\ &= \tan\left(\operatorname{acos}\left(\bar{\boldsymbol{l}}^\alpha \cdot \bar{\boldsymbol{l}}^\beta\right) - \operatorname{acos}\left(\boldsymbol{L}^\alpha \cdot \boldsymbol{L}^\beta\right)\right) , \end{aligned} \tag{4.4}$$

where e.g. for initially orthogonal fiber directions we have $\gamma_0 = \frac{\pi}{2}$. Following the works of Asmanoglo and Menzel [5] and Spencer and Soldatos [112] among others, we take into account curvature and twisting effects in addition to dilation and shear. The true curvature $\boldsymbol{\kappa}^\alpha : \Omega \to \mathbb{R}^d$ is obtained in the current deformation by projecting the spatial gradient of the fiber direction onto itself

$$\boldsymbol{\kappa}^\alpha = \nabla_{\mathrm{x}}\bar{\boldsymbol{l}}^\alpha \cdot \bar{\boldsymbol{l}}^\alpha = \nabla_{\mathrm{X}}\bar{\boldsymbol{l}}^\alpha \boldsymbol{F}^{-1} \cdot \left(\frac{1}{\varepsilon^\alpha}\boldsymbol{F}\boldsymbol{L}^\alpha\right) = \frac{1}{\varepsilon^\alpha}\nabla_{\mathrm{X}}\bar{\boldsymbol{l}}^\alpha \cdot \boldsymbol{L}^\alpha \,. \tag{4.5}$$

With given kinematics, we employ an alternative expression by analyzing the material gradient of the deformed fiber vectors $\nabla_{\mathrm{X}}\boldsymbol{l}^\alpha$ projected onto the initial fiber direction $\nabla_{\mathrm{X}}\boldsymbol{l}^\alpha\,\boldsymbol{L}^\alpha$, giving

$$\nabla_{\mathrm{X}}\boldsymbol{l}^\alpha \cdot \boldsymbol{L}^\alpha = \nabla_{\mathrm{X}}(\boldsymbol{F}\boldsymbol{L}^\alpha) \cdot \boldsymbol{L}^\alpha = \nabla_{\mathrm{X}}\boldsymbol{F} : (\boldsymbol{L}^\alpha \otimes \boldsymbol{L}^\alpha) = \mathfrak{F} : (\boldsymbol{L}^\alpha \otimes \boldsymbol{L}^\alpha) \,, \tag{4.6}$$

where we identify the second gradient of motion $\mathfrak{F}$, see eq. (3.10). Inserting the split into current normed fiber direction and stretch reveals two separable contributions - one associated with the stretch rate and one related to the gradient of direction

$$\nabla_{\mathrm{X}}\boldsymbol{l}^\alpha \cdot \boldsymbol{L}^\alpha = \nabla_{\mathrm{X}}\left(\varepsilon^\alpha\bar{\boldsymbol{l}}^\alpha\right) \cdot \boldsymbol{L}^\alpha = (\nabla_{\mathrm{X}}\varepsilon^\alpha \cdot \boldsymbol{L}^\alpha)\,\bar{\boldsymbol{l}}^\alpha + \varepsilon^\alpha\,\nabla_{\mathrm{X}}\bar{\boldsymbol{l}}^\alpha \cdot \boldsymbol{L}^\alpha \,, \tag{4.7}$$

which after some calculations* reveals

$$\begin{aligned}\boldsymbol{\kappa}^\alpha &= \frac{1}{\varepsilon^\alpha}\nabla_{\mathrm{X}}\bar{\boldsymbol{l}}^\alpha \cdot \boldsymbol{L}^\alpha \\ &= \frac{1}{(\varepsilon^\alpha)^2}\nabla_{\mathrm{X}}\boldsymbol{l}^\alpha \cdot \boldsymbol{L}^\alpha - (\nabla_{\mathrm{X}}\varepsilon^\alpha \cdot \boldsymbol{L}^\alpha)\bar{\boldsymbol{l}}^\alpha \\ &= \frac{1}{\|\boldsymbol{F}\boldsymbol{L}^\alpha\|^2}\left(\boldsymbol{\mathfrak{F}} : (\boldsymbol{L}^\alpha \otimes \boldsymbol{L}^\alpha) - \frac{1}{\|\boldsymbol{F}\boldsymbol{L}^\alpha\|^2}\Big(\boldsymbol{L}^\alpha \cdot \boldsymbol{F}^\top\boldsymbol{\mathfrak{F}} : (\boldsymbol{L}^\alpha \otimes \boldsymbol{L}^\alpha)\Big)\boldsymbol{F}\boldsymbol{L}^\alpha\right).\end{aligned} \tag{4.8}$$

4.2 Energetic response

Based on the introduced kinematic, we build the constitutive framework for fiber reinforced composites. Introducing volume fractions $\zeta^{\mathrm{m}} \in \mathbb{R}_{>0}$ for the matrix material and correspondingly $\zeta^{\mathrm{f},\alpha} \in \mathbb{R}_{>0}$ for each fiber direction, where $\zeta^{\mathrm{m}} + \sum_{\alpha=1}^{f}\zeta^{\mathrm{f},\alpha} = 1$, we propose the stored energy density to take the form

$$\begin{aligned}\Psi(\boldsymbol{F},\boldsymbol{\mathfrak{F}}) &\coloneqq \zeta^{\mathrm{m}}\Psi^{\mathrm{m}}(\boldsymbol{F},\boldsymbol{\mathfrak{F}}) + \sum_{\alpha=1}^{f}\zeta^{\mathrm{f},\alpha}\Psi^{\mathrm{f},\alpha}(\boldsymbol{F},\boldsymbol{\mathfrak{F}}) + \sum_{\substack{\alpha,\beta\in\{1,\dots,f\}\\ \alpha<\beta}}\Big(\zeta^{\mathrm{f},\alpha}+\zeta^{\mathrm{f},\beta}\Big)\Psi^{\mathrm{f},\alpha\beta}(\boldsymbol{F},\boldsymbol{\mathfrak{F}}) \\ &= \zeta^{\mathrm{m}}\Psi^{\mathrm{m}}(\boldsymbol{F},\boldsymbol{H},J) + \sum_{\alpha=1}^{f}\zeta^{\mathrm{f},\alpha}\Psi^{\mathrm{f},\alpha}(\varepsilon^\alpha,\boldsymbol{\kappa}^\alpha) + \sum_{\substack{\alpha,\beta\in\{1,\dots,f\}\\ \alpha<\beta}}\Big(\zeta^{\mathrm{f},\alpha}+\zeta^{\mathrm{f},\beta}\Big)\Psi^{\mathrm{f},\alpha\beta}\Big(\phi^{\alpha\beta}\Big).\end{aligned} \tag{4.9}$$

Therein, the total Helmholtz energy is additively composed of the matrix contribution Ψ^{m} (cf. section 3.3.4), the individual fiber contributions $\Psi^{\mathrm{f},\alpha}$ accounting for stretching and curvature, and the coupling term $\Psi^{\mathrm{f},\alpha\beta}$ for shear interactions between distinct fiber directions. With the set of constitutive coefficients $a^\alpha, c^\alpha \in \mathbb{R}_{>0}$ per fiber and $b^{\alpha,\beta} > 0$ per fiber combination, we constitute

$$\Psi^{\mathrm{f},\alpha\beta}\Big(\phi^{\alpha\beta}\Big) \coloneqq \frac{1}{2}b^{\alpha,\beta}\Big(\phi^{\alpha\beta}\Big)^2 \tag{4.10}$$

and

$$\Psi^{\mathrm{f},\alpha}(\varepsilon^\alpha,\boldsymbol{\kappa}^\alpha) \coloneqq \frac{1}{2}a^\alpha(\varepsilon^\alpha-1)^2 + \frac{1}{2}c^\alpha\boldsymbol{\kappa}^\alpha\cdot\boldsymbol{\kappa}^\alpha\,. \tag{4.11}$$

For the curvature, we may extend the material description towards differentiating between directions of flexure

$$\Psi^{\mathrm{f},\alpha}(\varepsilon^\alpha,\boldsymbol{\kappa}^\alpha) \coloneqq \frac{1}{2}a^\alpha(\varepsilon^\alpha-1)^2 + \frac{1}{2}\boldsymbol{\kappa}^\alpha\cdot\boldsymbol{c}^\alpha\,\boldsymbol{\kappa}^\alpha\,, \tag{4.12}$$

with the fiber bending stiffness tensor $\boldsymbol{c}^\alpha \in \mathbb{R}^{d\times d}$ given in the current configuration.

*$\nabla_{\mathrm{X}}\varepsilon^\alpha = \nabla_{\mathrm{X}}\|\boldsymbol{F}\boldsymbol{L}^\alpha\| = \frac{\boldsymbol{F}\boldsymbol{L}^\alpha}{\|\boldsymbol{F}\boldsymbol{L}^\alpha\|}\cdot\boldsymbol{\mathfrak{F}}\cdot\boldsymbol{L}^\alpha = \frac{1}{\|\boldsymbol{F}\boldsymbol{L}^\alpha\|}\boldsymbol{L}^\alpha\cdot\boldsymbol{F}^\top\boldsymbol{\mathfrak{F}}\cdot\boldsymbol{L}^\alpha$.

Remark 4.2.1 – Referential parameter set. Given curvature $\boldsymbol{\kappa}^\alpha$, we can derive a referential representation by $\boldsymbol{\kappa}_0^\alpha : \Omega_0 \to \mathbb{R}^d$, $\boldsymbol{\kappa}_0^\alpha = \boldsymbol{F}^\top \cdot \boldsymbol{\kappa}^\alpha$, yielding an objective stress measure (cf. eq. $(3.59)_2$ and Spencer and Soldatos [112]). Inserting yields

$$\begin{aligned} \boldsymbol{\kappa}^\alpha \cdot \boldsymbol{c}^\alpha \, \boldsymbol{\kappa}^\alpha &= \left(\boldsymbol{F}^{-\top}\boldsymbol{\kappa}_0^\alpha\right) \cdot \boldsymbol{c}^\alpha \left(\boldsymbol{F}^{-\top}\boldsymbol{\kappa}_0^\alpha\right) \\ &= \boldsymbol{\kappa}_0^\alpha \cdot \underbrace{\left(\boldsymbol{F}^{-1}\boldsymbol{c}^\alpha \boldsymbol{F}^{-\top}\right)}_{:=\boldsymbol{C}^\alpha} \boldsymbol{\kappa}_0^\alpha \,, \end{aligned} \tag{4.13}$$

with the pull-back material tensor $\boldsymbol{C}^\alpha = \boldsymbol{F}^{-1}\boldsymbol{c}^\alpha\boldsymbol{F}^{-\top}$. Another referential curvature measure can be obtained by utilizing the rotation matrix of the polar decomposition with $\boldsymbol{K} : \Omega_0 \to \mathbb{R}^d$, $\boldsymbol{K} = \boldsymbol{R}^\top \cdot \boldsymbol{\kappa}^\alpha$, giving

$$\begin{aligned} \boldsymbol{\kappa}^\alpha \cdot \boldsymbol{c}^\alpha \, \boldsymbol{\kappa}^\alpha &= (\boldsymbol{R}\boldsymbol{K}^\alpha) \cdot \boldsymbol{c}^\alpha \, (\boldsymbol{R}\boldsymbol{K}^\alpha) \\ &= \boldsymbol{K}^\alpha \cdot \underbrace{\left(\boldsymbol{R}^\top \boldsymbol{c}^\alpha \boldsymbol{R}\right)}_{:=\mathbb{C}^\alpha} \boldsymbol{K} \,, \end{aligned} \tag{4.14}$$

with the rotation-pulled referential material tensor $\mathbb{C}^\alpha = \boldsymbol{R}^\top\boldsymbol{c}^\alpha\boldsymbol{R}$. Note that the latter only changes basis whereas the former rescales anisotropically due to the inclusion of stretch $\boldsymbol{c}^\alpha = \boldsymbol{U}^{-1}\mathbb{C}^\alpha\boldsymbol{U}^{-1}$.

If we consider the particular case of aforementioned woven fabric, we have two identical fibers in two distinct directions. The energy is then given as

$$\begin{aligned} \Psi(\boldsymbol{F}, \mathfrak{F}) = \zeta^{\mathrm{m}}\Psi^{\mathrm{m}}(\boldsymbol{F}, \boldsymbol{H}, J) \\ + \zeta^{\mathrm{f},1}\Psi^{\mathrm{f},1}\left(\varepsilon^1, \boldsymbol{\kappa}^1\right) + \zeta^{\mathrm{f},2}\Psi^{\mathrm{f},2}\left(\varepsilon^2, \boldsymbol{\kappa}^2\right) + \left(\zeta^{\mathrm{f},1} + \zeta^{\mathrm{f},2}\right)\Psi^{\mathrm{f},12}\left(\phi^{12}\right) \end{aligned} \tag{4.15}$$

Assuming uniform weaving, i.e. $\zeta^{\mathrm{f},1} = \zeta^{\mathrm{f},2} = \frac{1-\zeta^{\mathrm{m}}}{2}$ with identical material parameters $a^1 = a^2 = a$ and $\boldsymbol{c}^1 = \boldsymbol{c}^2 = \boldsymbol{c}$, allows for a simplified total fiber energy contribution

$$\begin{aligned} \Psi^{\mathrm{f}}\left(\varepsilon^1, \varepsilon^2, \boldsymbol{\kappa}^1, \boldsymbol{\kappa}^2, \phi^{12}\right) &:= \Psi^{\mathrm{f},1}\left(\varepsilon^1, \boldsymbol{\kappa}^1\right) + \Psi^{\mathrm{f},2}\left(\varepsilon^2, \boldsymbol{\kappa}^2\right) + \Psi^{\mathrm{f},12}\left(\phi^{12}\right) \\ &= \frac{1}{2}a\left(\left(\varepsilon^1 - 1\right)^2 + \left(\varepsilon^2 - 1\right)^2\right) + \frac{1}{2}\left(\boldsymbol{\kappa}^1 \cdot \boldsymbol{c}\,\boldsymbol{\kappa}^1 + \boldsymbol{\kappa}^2 \cdot \boldsymbol{c}\,\boldsymbol{\kappa}^2\right) + b\left(\phi^{12}\right)^2 \end{aligned} \tag{4.16}$$

yielding[†]

$$\Psi(\boldsymbol{F}, \mathfrak{F}) = \zeta^{\mathrm{m}}\Psi^{\mathrm{m}}(\boldsymbol{F}, \boldsymbol{H}, J) + \frac{1-\zeta^{\mathrm{m}}}{2}\Psi^{\mathrm{f}}\left(\varepsilon^1, \varepsilon^2, \boldsymbol{\kappa}^1, \boldsymbol{\kappa}^2, \phi^{12}\right), \tag{4.17}$$

cf. Dittmann et al. [33]. With these two fiber directions, one can construct the fiber bending stiffness tensor $\boldsymbol{c}$ for distinct in-plane and out-of-plane behavior, see also dell'Isola et al. [31], with the unit normal

$$\boldsymbol{n} = \frac{\bar{\boldsymbol{l}}^1 \times \bar{\boldsymbol{l}}^2}{\|\bar{\boldsymbol{l}}^1 \times \bar{\boldsymbol{l}}^2\|} \tag{4.18}$$

[†] $\left(\zeta^{\mathrm{f},1} + \zeta^{\mathrm{f},2}\right)\Psi^{\mathrm{f},12} = 2^{\,1-\zeta^{\mathrm{m}}/2}\Psi^{\mathrm{f},12} = {}^{(1-\zeta^{\mathrm{m}}/2)}\, b\left(\phi^{12}\right)^2$

to the plane span$\left(\bar{\boldsymbol{l}}^1, \bar{\boldsymbol{l}}^2\right)$, provided $\bar{\boldsymbol{l}}^1$ and $\bar{\boldsymbol{l}}^2$ are not collinear ($\bar{\boldsymbol{l}}^1 \neq \bar{\boldsymbol{l}}^2$). The orthogonal-tangential split yields

$$\boldsymbol{c} \coloneqq c_{\#}(\boldsymbol{I} - \boldsymbol{n} \otimes \boldsymbol{n}) + c_{\perp}(\boldsymbol{n} \otimes \boldsymbol{n}) \,, \tag{4.19}$$

with in-plane and out-of-plane stiffnesses $c_{\#}$ and $c_{\perp}$, respectively. See remark 4.2.2 for equivalent transformations of the isotropic and rotationally invariant split using fiber directions in the reference configuration and the deformation tensor. Revisiting the underlying beam theory, one can associate the tensional stiffness with the Young's modulus E_{f} in linear elasticity. Investigating a single fiber direction and conducting a bending test as shown in section 4.3.1, allows for interpretation of the bending parameters. Averaging the number of fibers per unit cross section - thus a measurement of areal density - constitutes $c = \nu_f E_{\mathrm{f}}\, I$, with the second moment of area I and the areal density ν_f. For a deeper analysis we refer to the works of Asmanoglo and Menzel [7] as well as Soldatos [111] and references therein.

Remark 4.2.2 – Orthogonal projection to fiber-plane. Using the initial fiber directions, the out-of-plane vector normal to the tangent space of the fibers can be expressed as

$$\boldsymbol{n} = \frac{(\boldsymbol{F}\boldsymbol{L}^1)\times(\boldsymbol{F}\boldsymbol{L}^2)}{\|(\boldsymbol{F}\boldsymbol{L}^1)\times(\boldsymbol{F}\boldsymbol{L}^2)\|} = \frac{\boldsymbol{H}(\boldsymbol{L}^1\times\boldsymbol{L}^2)}{\|\boldsymbol{H}(\boldsymbol{L}^1\times\boldsymbol{L}^2)\|} = \frac{\boldsymbol{F}^{-\top}\boldsymbol{N}}{\|\boldsymbol{F}^{-\top}\boldsymbol{N}\|} \,, \tag{4.20}$$

with the vector in reference configuration $\boldsymbol{N} = \frac{\boldsymbol{L}^1\times\boldsymbol{L}^2}{\|\boldsymbol{L}^1\times\boldsymbol{L}^2\|}$. The orthogonal-tangential split finally yields

$$\boldsymbol{n} \otimes \boldsymbol{n} = \frac{\boldsymbol{F}^{-\top}\boldsymbol{N} \otimes \boldsymbol{F}^{-\top}\boldsymbol{N}}{\boldsymbol{N} \cdot (\boldsymbol{F}^{\top}\boldsymbol{F})^{-1}\boldsymbol{N}} \,. \tag{4.21}$$

Given kinematics, traceable to the first- and second-order deformation gradients $\boldsymbol{F}$ and $\mathfrak{F}$, the proposed Helmholtz energy can be inserted into the second-order continuum framework, summarized in section 3.4, and discretized according to section 3.5.

4.3 Numerical examples

This section now investigates the characteristics and performance of the proposed energy formulation for continuous, endless fibers. Higher-order contributions of the fiber model are verified by two bending benchmark. Subsequently, a set of tensile tests illustrates the influence of different fiber orientations. Throughout, the matrix is modeled by a Mooney-Rivlin material, cf. eq. (3.70), with parameters $\alpha = 1000\,{}^{\mathrm{N}}/_{\mathrm{mm}^2}$, $\beta = 500\,{}^{\mathrm{N}}/_{\mathrm{mm}^2}$, and $\gamma = 1000\,{}^{\mathrm{N}}/_{\mathrm{mm}^2}$, and a matrix volume fraction of $\zeta^{\mathrm{m}} = 0.5$. All length scales are given in mm. First- and second-order stresses are given in ${}^{\mathrm{N}}/_{\mathrm{mm}^2}$ and ${}^{\mathrm{N\,mm}}/_{\mathrm{mm}^2}$, respectively. Unless stated otherwise, all tests use the same specimen, $(0, 100) \times (-5, 5) \times (-5, 5)$, discretized by $40 \times 4 \times 4$ tri-quadratic B-spline elements.

4.3.1 Two-point bending test

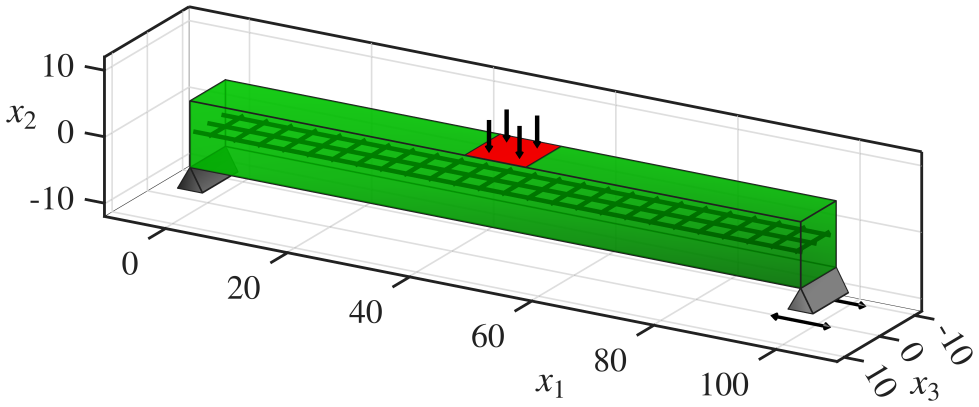


Figure 4.3.1 – Two-point bending test: setup. Problem setting with lines illustrating the two fiber family directions.

The first example verifies the higher-order response of the fiber material in a two-point bending setup. The left lower edge $\partial\Omega_0^{\varphi,l} = \{\boldsymbol{X} \in \mathbb{R}^3 \,|\, X_1 = 0,\ X_2 = -5,\ -5 < X_3 < 5\}$ is fixed in x_1, x_2 and x_3 direction, while the right edge $\partial\Omega_0^{\varphi,r} = \{\boldsymbol{X} \in \mathbb{R}^3 \,|\, X_1 = 100,\ X_2 = -5,\ -5 < X_3 < 5\}$ is fixed in x_2 and x_3, see figure 4.3.1. A surface traction is applied at the top center such that the remaining boundary $\partial\Omega_0^T = \partial\Omega_0 \backslash \left(\partial\Omega_0^{\varphi,l} \cup \partial\Omega_0^{\varphi,r}\right)$ is subjected to $\overline{\boldsymbol{T}}\colon\ \partial\Omega_0^T \to \mathbb{R}^3$,

$$\overline{\boldsymbol{T}}(\boldsymbol{X}) = \begin{cases} (0, -200, 0)^\top \,\mathrm{N/mm^2} & \text{if } 45 < X_1 < 55,\ X_2 = 5,\ -5 < X_3 < 5 \\ (0, 0, 0)^\top \,\mathrm{N/mm^2} & \text{otherwise.} \end{cases} \tag{4.22}$$

The load is applied incrementally in $n_l = 20$ steps, resulting in the scaled traction $\boldsymbol{T}_k = k\,\boldsymbol{T}/n_l$ in step k.

Two fiber families are considered with $\boldsymbol{L}^1 = (1, 0, 0)^\top$ and $\boldsymbol{L}^2 = (0, 0, 1)^\top$, such that the applied traction induces an out-of-plane bending of the fiber network. The test is performed for two fiber parameter settings. In both cases, $b = 0\,\mathrm{N/mm^2}$ and $c_\# = 0\,\mathrm{N}$ remain constant. First, the fiber response is purely tensile with $a = 50 \cdot 10^{+3}\,\mathrm{N/mm^2}$ and $c_\perp = 0\,\mathrm{N}$. Second, a pure bending response of the fibers is prescribed by setting $a = 0\,\mathrm{N/mm^2}$ and adjusting the bending stiffness to $c_\perp = {}^{1250}/_3 \cdot 10^{+3}\,\mathrm{N}$. This value is obtained by assuming a single layer of fibers spanning the whole thickness of the geometry, such that an equivalent bending stiffness associated with the extensional stiffness follows from $c_\perp = a\,{}^I/_A$, with the second moment of area $I = {}^1/_{12}\,W\,H^3$ and the area $A = W\,H$, yielding $c_\perp = {}^a/_{12}\,H^2$. Inserting $a = 50 \cdot 10^{+3}\,\mathrm{N/mm^2}$ and $H = 10\,\mathrm{mm}$ gives the above value. Consequently, if the thickness is sufficiently resolved for a slender geometry ($L >> H$, $L >> W$), the deformation response should be essentially identical for the pure-tension and pure-bending fiber settings. Figure 4.3.2 shows the x_2-deflection of the Point $\boldsymbol{P}_t = (50, 0, 0)^\top$ versus the applied load.

As expected, the two results are in close agreement. In particular, in this bending-dominated configuration the tensile/compressive behavior of the continuum fiber model

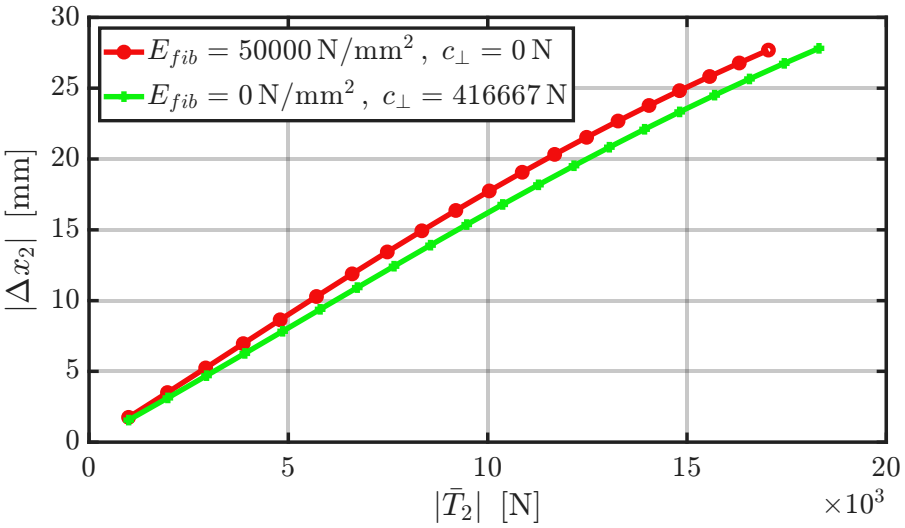


Figure 4.3.2 – Two-point bending test: deflection. Force-displacement curves for bending tests.

is already represented by the bending terms. This outcome is both important and well established as strain-gradient effects originate from a microstructure with an intrinsic length scale and if that microstructure is already resolved within a first-order continuum description, the corresponding second-order contributions should be omitted to avoid double counting.

Moreover, figure 4.3.3 compares the first- and second-order stresses for both settings. In the pure-tension case, no second-order stresses arise, whereas in the pure-bending case the fibers generate only second-order stresses and the first-order stress is carried by the matrix. The present benchmark can also be used to calibrate the in-plane bending parameter $c_\#$ by rotating the second fiber direction to align with the loading direction.

4.3.2 Clamped bending test

The second example targets the anisotropic bending stiffness tensor with distinct in-plane and out-of-plane parameters $c_\#$ and $c_\perp$. As shown in figure 4.3.4, the specimen is clamped on the left face, $\partial\Omega_0^{\varphi,l} = \{\boldsymbol{X} \in \mathbb{R}^3 \,|\, X_1 = 0,\ -5 < X_2 < 5,\ -5 < X_3 < 5\}$, fixing in x_1, x_2 and x_3. On the right face, a uniform traction is applied equally in x_2 and x_3 direction, i.e. on $\partial\Omega_0^T = \partial\Omega_0 \backslash \partial\Omega_0^{\varphi,l}$ we prescribe $\overline{\boldsymbol{T}}$: $\partial\Omega_0^T \to \mathbb{R}^3$,

$$\overline{\boldsymbol{T}}(\boldsymbol{X}) = \begin{cases} (0,-10,-10)^\top\,\mathrm{N/mm^2} & \text{if } X_1 = 100,\ -5 < X_2 < 5,\ -5 < X_3 < 5 \\ (0,0,0)^\top\,\mathrm{N/mm^2} & \text{otherwise}\,. \end{cases} \tag{4.23}$$

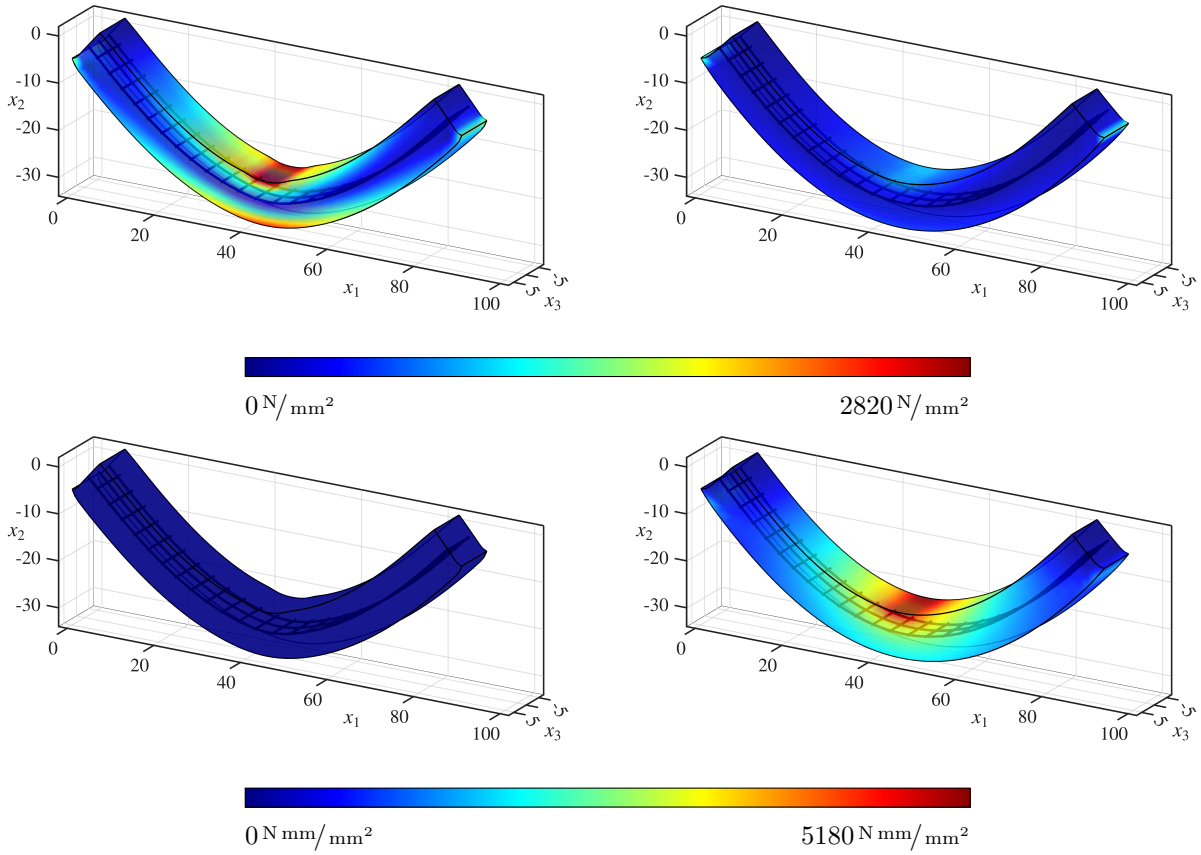


Figure 4.3.3 – Two-point bending test: stresses. Left to right: pure tensile and pure bending settings. Top to bottom: Normed first-order stress $\|\boldsymbol{P}\|$ and normed second-order stress $\|\mathfrak{P}\|$.

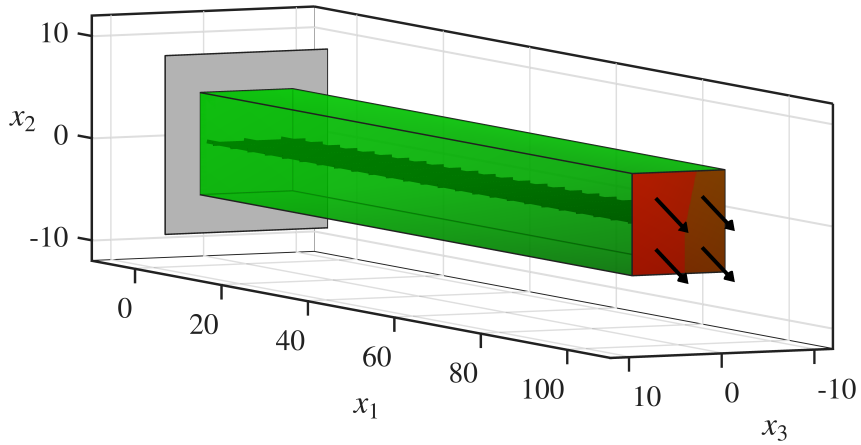


Figure 4.3.4 – Clamped bending test: setup. Problem setting with lines illustrating the two fiber family directions.

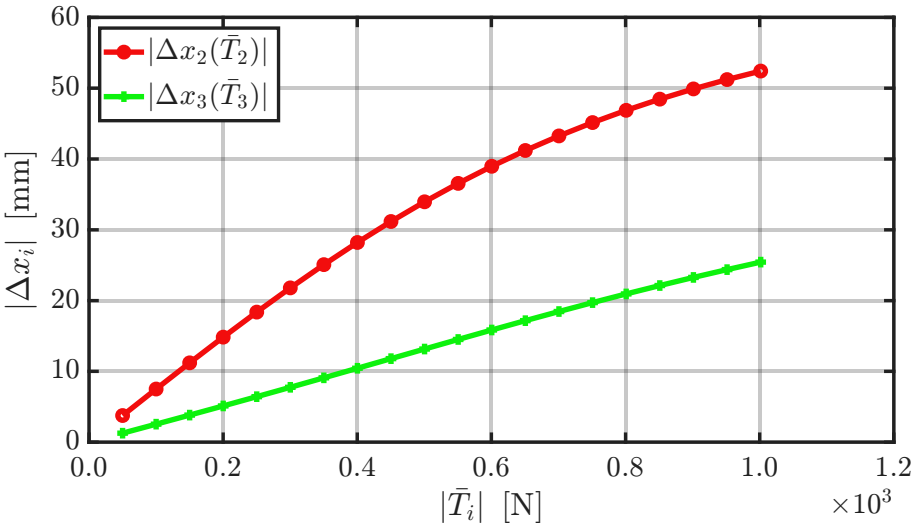


Figure 4.3.5 – Clamped bending test: deflection. Displacement curves for clamped bending test.

The fiber parameters are set to $a = 5 \cdot 10^{+3}\,\mathrm{N/mm^2}$, $b = 50\,\mathrm{N/mm^2}$, $c_\# = 600 \cdot 10^{+3}\,\mathrm{N}$ and $c_\perp = 6 \cdot 10^{+3}\,\mathrm{N}$. Since $c_\# \gg c_\perp$, the larger in-plane bending resistance should produce a smaller x_3 deflection compared to x_2. This behavior is confirmed in figure 4.3.5, which shows the displacement of $\boldsymbol{P}_c = (100, 0, 0)^\top$ in the x_2 and x_3 directions as a function of the applied load. The corresponding distributions of first- and second-order stresses are shown in figure 4.3.6.

4.3.3 Tensile test

Finally, a series of tensile tests is conducted to demonstrate the influence of the fiber orientations. The specimen is clamped on the left face, $\partial\Omega_0^{\varphi,l} = \{\boldsymbol{X} \in \mathbb{R}^3 \,|\, X_1 = 0,\ -5 < X_2 < 5,\ -5 < X_3 < 5\}$, and a uniform displacement in the X_1 direction is prescribed on the right face, $\partial\Omega_0^{\varphi,r} = \{\boldsymbol{X} \in \mathbb{R}^3 \,|\, X_1 = 100,\ -5 < X_2 < 5,\ -5 < X_3 < 5\}$, with

$$x_1(\boldsymbol{X}) = X_1 + 30 \qquad \forall \boldsymbol{X} \in \partial\Omega_0^{\varphi,r}\,, \tag{4.24}$$

while x_2 and x_3 remain unconstrained, cf. figure 4.3.7. The fiber parameters are set to $a = 150 \cdot 10^{+3}\,\mathrm{N/mm^2}$, $b = 15 \cdot 10^{+3}\,\mathrm{N/mm^2}$, $c_\# = 18 \cdot 10^{+3}\,\mathrm{N}$ and $c_\perp = 0.18 \cdot 10^{+3}\,\mathrm{N}$, allowing strong stress contributions from tensile, shear and bending deformation.

Figure 4.3.8 shows the deflection of $\boldsymbol{P}_c = (100, 0, 0)^\top$ for different fiber orientations. Here, $\Phi = \phi^{12}$ (cf. eq. (4.4)) denotes the angle between both fiber families, while γ_1 and γ_2 represent rotations around the X_1 and X_3 axis, respectively, such that

$$\boldsymbol{L}^1 = \boldsymbol{R}_1(\gamma_1)\,\boldsymbol{R}_3(\gamma_2)\,(1,0,0)^\top \quad \text{and} \quad \boldsymbol{L}^2 = \boldsymbol{R}_1(\gamma_1)\,\boldsymbol{R}_3(\gamma_2)\,\boldsymbol{R}_3(\phi^{12})\,(1,0,0)^\top, \tag{4.25}$$

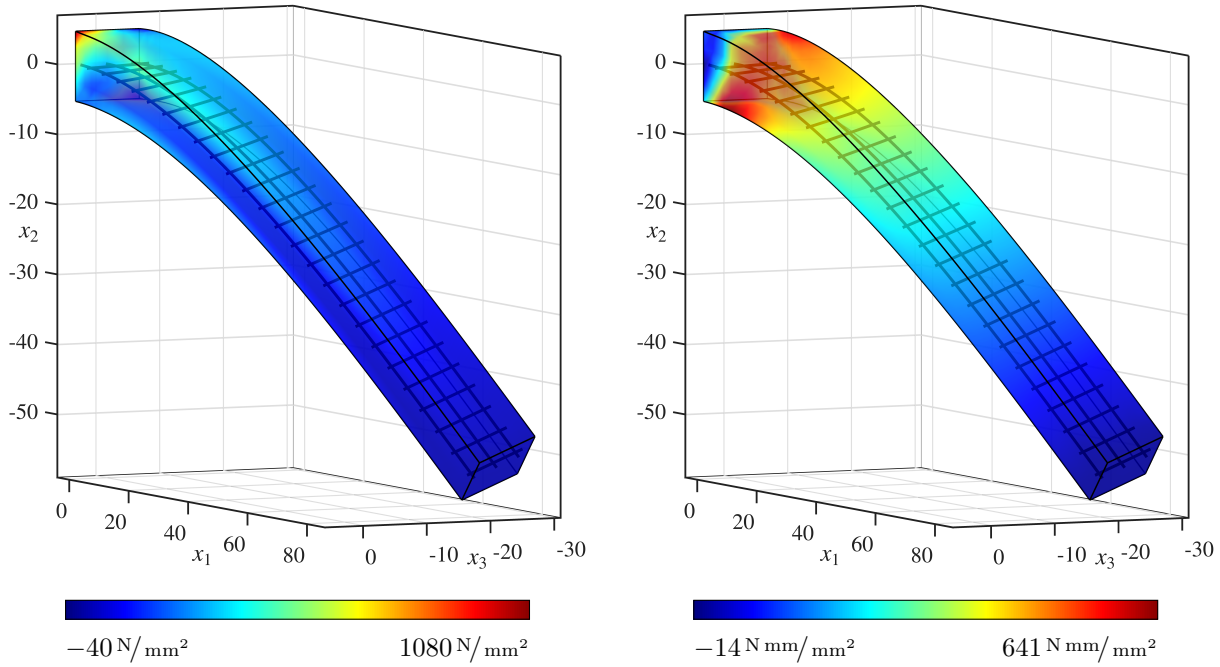


Figure 4.3.6 – **Clamped bending test: stresses.** Left to right: $\|\boldsymbol{P}\|$ and $\|\mathfrak{P}\|$.

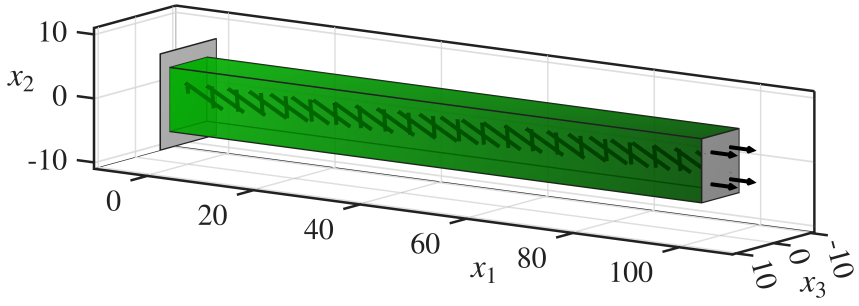


Figure 4.3.7 – **Tensile test: setup.** Problem setting with exemplary fiber family.

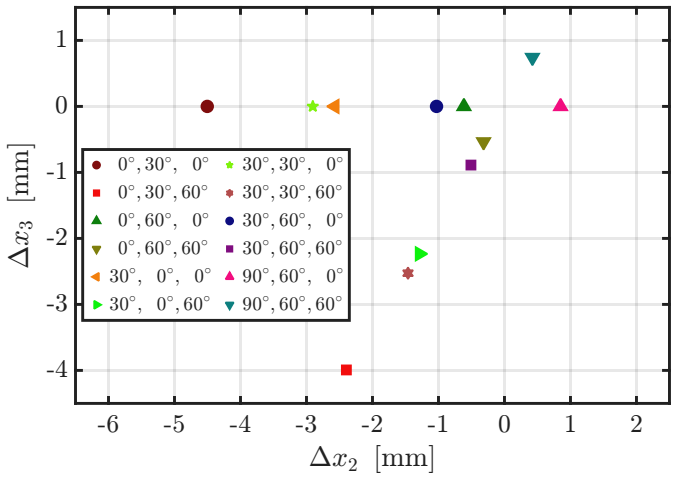


Figure 4.3.8 – Tensile test: deflection. Displacement in x_2 and x_3 direction.

using rotation matrices $\boldsymbol{R}_i(\theta) \coloneqq \exp\left(\theta\, [\boldsymbol{e}_i]_\times\right) \in \mathrm{SO}(3)$ (cf. eq. (0.25) to (0.26)). The results show that γ_1 primarily governs the axial (x_1) displacement, whereas γ_2 mainly affects the transverse (x_2) deflection.

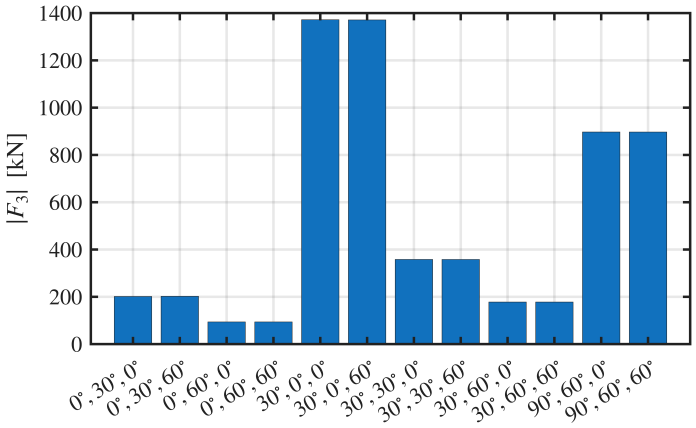


Figure 4.3.9 – Tensile test: resistance. Residual resistance force.

In addition, figure 4.3.9 shows the residual reaction associated with the moving Dirichlet constraint. For coinciding fiber directions, i.e. $\phi^{12} = 0$, the axial resistance is comparatively low since no shear resistance is activated. For configurations permitting shear deformation, the largest tensile resistance occurs when both fiber directions have a substantial component aligned with the loading direction, e.g. for $(30°, 0°, 0°)$ and $(30°, 0°, 60°)$, as sets $(\Phi, \gamma_1, \gamma_2)$. In contrast, varying γ_2 has little influence because it does not change the relative orientation of the fiber plane with respect to the imposed axial motion.

For completeness, figure 4.3.10 shows the first- and second-order stress for selected configurations.

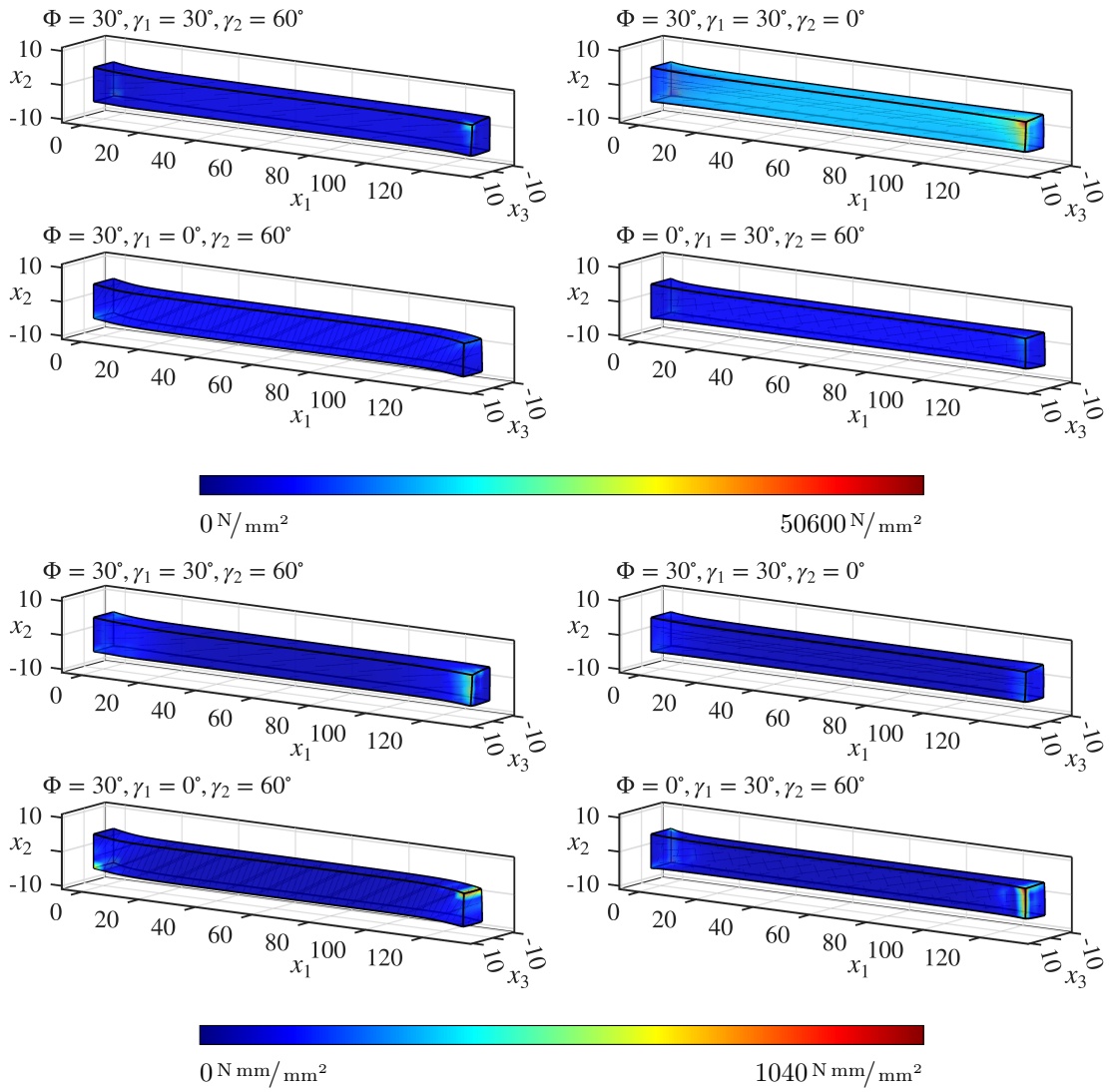


Figure 4.3.10 – **Tensile test: stresses.** Stress of selected configurations $((30°, 30°, 60°)$, $(30°, 30°, 0°)$, $(30°, 0°, 60°)$ and $(0°, 30°, 60°)$ arranged clockwise). Rows (top to bottom): $\|\boldsymbol{P}\|$ and $\|\mathfrak{P}\|$.

5 Dimension reduction: Discrete embedded fibers

The previously introduced continuous fiber material model manages to capture initially straight aligned oriented fiber bundles. It is suitable for woven fabrics as by design all fibers assumed to be endless within the body boundaries and evenly distributed, but fails for finite length, randomly spread and individually oriented single fibers found for example in short-fiber reinforced composites.

In this chapter, we thus derive a model for the embedding of one-dimensional arbitrary fibers into a suitable three-dimensional matrix material. As will be shown, a more complex but also more general second-gradient system arises. In contrast to the previous approach, we employ a discrete beam formulation and insert it into the matrix with yielding overlapping domains. We then identify coupling constraints allowing to transfer forces and moments from beam to matrix and in addition provide a reduced model.

Here we intend to embed fibers with a length-to-radius ratio of 40, common for e.g. fiber reinforced polymers, and reasonably restrict the three-dimensional continuum kinematics of a discrete fiber body along its axis direction to a beam-like kinematic. In particular, we use Cosserat beams as geometrically exact beams, introduced in Cosserat and Cosserat [25] and comprehensively elaborated in Rubin [97] among others.

5.1 Beam kinematic

As introduced in section 3.1, we consider a beam to be a three-dimensional body occupying the geometrical region $\breve{\Omega}_t \subset \mathbb{R}^3$. We denote its reference configuration as $\breve{\Omega}_0$ with boundary $\partial\breve{\Omega}_0$, where $\partial\breve{\Omega}_0 = \partial\breve{\Omega}_0^D \cup \partial\breve{\Omega}_0^N$ and $\partial\breve{\Omega}_0^D \cap \partial\breve{\Omega}_0^N = \emptyset$, see section 3.2.1 for details on essential (D) and natural (N) boundaries. For the position vector in that configuration we employ the following kinematical ansatz

$$\breve{\boldsymbol{X}}(\breve{\theta}^\alpha, \breve{\theta}^3) = \breve{\boldsymbol{\varphi}}_0(\breve{\theta}^3) + \breve{\theta}^\alpha \, \breve{\boldsymbol{D}}_\alpha(\breve{\theta}^3)\,, \tag{5.1}$$

where $\breve{\boldsymbol{\varphi}}_0(\breve{\theta}^3) = \breve{\theta}^3 \breve{\boldsymbol{D}}_3$ with $\breve{\theta}^3 \in [0,\, L]$ as parametrization along the center line of the beam with length L, see also figure 5.3.1. Following the parametrization, we denote the endpoints, where $\breve{\theta}^3 = 0$ and $\breve{\theta}^3 = L$, as $\partial\breve{\Omega}_0^{\breve{E}}$. Further, the orthonormal triad $\left\{\breve{\boldsymbol{D}}_1,\, \breve{\boldsymbol{D}}_2,\, \breve{\boldsymbol{D}}_3\right\}$ with convective coordinates $(\breve{\theta}^1, \breve{\theta}^2, \breve{\theta}^3) \in \breve{\Omega}_0$ is introduced, where $\breve{\boldsymbol{D}}_\alpha$ with $\alpha = 1, 2$ span the cross-section plane. Moreover $\breve{\boldsymbol{D}}_3$ functions as center direction line for the initially straight

assumed beam. Hence the orthonormal reference triad remains constant along the center line and thus $\breve{\boldsymbol{D}}'_\alpha = 0$, where $(\cdot)'$ represents the derivative with respect to $\breve{\theta}^3$. Note that in order to avoid confusion for commonly used symbols, the notation $\breve{(\cdot)}$ always indicates values corresponding to the beam.

Regarding its motion, the current position of the geometrically exact beam is then given by

$$\breve{\boldsymbol{x}}(\breve{\theta}^\alpha, \breve{\theta}^3) = \breve{\boldsymbol{\varphi}}(\breve{\theta}^3) + \breve{\theta}^\alpha \, \breve{\boldsymbol{d}}_\alpha(\breve{\theta}^3)\,, \tag{5.2}$$

where the orthonormal triad $\breve{\boldsymbol{d}}_\alpha$ is related to the reference triad via the rotation tensor $\breve{\boldsymbol{R}} \in \mathrm{SO}(3)$, i.e. $\breve{\boldsymbol{R}} = \breve{\boldsymbol{d}}_i \otimes \breve{\boldsymbol{D}}_i$, see eq. (0.26). From the coordinate-direction pairs $\left\{\breve{\theta}^\alpha, \breve{\boldsymbol{D}}_\alpha\right\}$ and $\left\{\breve{\theta}^3, \breve{\boldsymbol{D}}_3\right\}$, we can compute the deformation gradient following Auricchio et al. [8] by

$$\breve{\boldsymbol{F}} = \nabla_{\breve{\mathrm{X}}} \breve{\boldsymbol{x}} = \frac{\partial \breve{\boldsymbol{x}}}{\partial \breve{\theta}^\alpha} \otimes \breve{\boldsymbol{D}}_\alpha + \frac{\partial \breve{\boldsymbol{x}}}{\partial \breve{\theta}^3} \otimes \breve{\boldsymbol{D}}_3\,, \tag{5.3}$$

yielding

$$\breve{\boldsymbol{F}} = \breve{\boldsymbol{d}}_\alpha \otimes \breve{\boldsymbol{D}}_\alpha + \left(\breve{\boldsymbol{\varphi}}' + \breve{\theta}^\alpha \, \breve{\boldsymbol{d}}'_\alpha\right) \otimes \breve{\boldsymbol{D}}_3\,, \tag{5.4}$$

noting again $\breve{\boldsymbol{D}}'_\alpha = 0$ for the aforementioned case of a straight initial beam.

We further aim to introduce new strain and curvature measures (cf. Betsch and Steinmann [17], Eugster et al. [37]) by multiplying the deformation gradient with the identity $\breve{\boldsymbol{R}}\,\breve{\boldsymbol{R}}^\top = \breve{\boldsymbol{R}}^\top \breve{\boldsymbol{R}} = \boldsymbol{I}$ and substituting $\breve{\boldsymbol{d}}_\alpha \otimes \breve{\boldsymbol{D}}_\alpha = \breve{\boldsymbol{R}} - \breve{\boldsymbol{d}}_3 \otimes \breve{\boldsymbol{D}}_3$. Setting further $\breve{\boldsymbol{R}}^\top \breve{\boldsymbol{d}}'_\alpha = \breve{\boldsymbol{R}}^\top \breve{\boldsymbol{R}}' \, \breve{\boldsymbol{D}}_\alpha$ and $\breve{\boldsymbol{D}}_3 = \breve{\boldsymbol{R}}^\top \breve{\boldsymbol{d}}_3$, eq. (5.5) along with the spin-notation in eq. (0.22) yields

$$\begin{aligned}
\breve{\boldsymbol{F}} &= \breve{\boldsymbol{R}}\left(\breve{\boldsymbol{R}}^\top \breve{\boldsymbol{\varphi}}' \otimes \breve{\boldsymbol{D}}_3 + \breve{\boldsymbol{R}}^\top\left(\breve{\boldsymbol{R}} - \breve{\boldsymbol{d}}_3 \otimes \breve{\boldsymbol{D}}_3\right) + \breve{\theta}^\alpha \, \breve{\boldsymbol{R}}^\top \breve{\boldsymbol{R}}' \, \breve{\boldsymbol{D}}_\alpha \otimes \breve{\boldsymbol{D}}_3\right), \\
&= \breve{\boldsymbol{R}}\left(\underbrace{\left[\breve{\boldsymbol{R}}^\top \breve{\boldsymbol{\varphi}}' - \breve{\boldsymbol{D}}_3\right]}_{\coloneqq \breve{\boldsymbol{G}}} \otimes \breve{\boldsymbol{D}}_3 + \breve{\theta}^\alpha \, \underbrace{\breve{\boldsymbol{R}}^\top \breve{\boldsymbol{R}}'}_{\coloneqq \left[\breve{\boldsymbol{K}}\right]_\times} \breve{\boldsymbol{D}}_\alpha \otimes \breve{\boldsymbol{D}}_3 + \boldsymbol{I}\right) \\
&= \breve{\boldsymbol{R}}\left(\breve{\boldsymbol{G}} \otimes \breve{\boldsymbol{D}}_3 + \left[\breve{\boldsymbol{K}}\right]_\times \breve{\theta}^\alpha \, \breve{\boldsymbol{D}}_\alpha \otimes \breve{\boldsymbol{D}}_3 + \boldsymbol{I}\right),
\end{aligned} \tag{5.5}$$

with the axial-shear strain vector $\breve{\boldsymbol{G}} : \breve{\Omega}_0 \to \mathbb{R}^3$ and the torsional-bending strain vector $\breve{\boldsymbol{K}} : \breve{\Omega}_0 \to \mathbb{R}^3$ with

$$\breve{\boldsymbol{G}} = \breve{\boldsymbol{R}}^\top \breve{\boldsymbol{\varphi}}' - \breve{\boldsymbol{D}}_3 \quad \text{and} \quad \left[\breve{\boldsymbol{K}}\right]_\times = \breve{\boldsymbol{R}}^\top \breve{\boldsymbol{R}}'\,, \tag{5.6}$$

and their counterpart in the current configuration

$$\breve{\boldsymbol{g}} = \breve{\boldsymbol{R}}\,\breve{\boldsymbol{G}} \quad \text{and} \quad \breve{\boldsymbol{k}} = \breve{\boldsymbol{R}}\,\breve{\boldsymbol{K}}, \tag{5.7}$$

respectively. Recalling the polar decomposition in remark 3.1.1, we can identify the stretch tensor $\breve{\boldsymbol{U}}$ using

$$\breve{\boldsymbol{F}} = \breve{\boldsymbol{R}}\,\breve{\boldsymbol{U}}\,, \quad \breve{\boldsymbol{U}} = \boldsymbol{I} + \breve{\boldsymbol{B}} \otimes \breve{\boldsymbol{D}}_3, \quad \text{with} \quad \breve{\boldsymbol{B}} = \breve{\boldsymbol{G}} + (\breve{\boldsymbol{K}} \times \breve{\theta}^\alpha \, \breve{\boldsymbol{D}}_\alpha). \tag{5.8}$$

With regard to eq. (0.22) and eq. (0.26), the rotation tensor can be defined in terms of a vector $\breve{\boldsymbol{\phi}} \in \mathbb{R}^3$ with basis $\left\{\breve{\boldsymbol{d}}_1, \breve{\boldsymbol{d}}_2, \breve{\boldsymbol{d}}_3\right\}$ via the exponential map $\breve{\boldsymbol{R}}(\breve{\boldsymbol{\phi}}) = e^{\left[\breve{\phi}\right]_\times}$ for which a closed form expression is given by Rodrigues formula

$$\breve{\boldsymbol{R}}(\breve{\boldsymbol{\phi}}) = \boldsymbol{I} + \frac{\cos^2\left(\breve{\theta}\right)\|\breve{\boldsymbol{\phi}}\|}{\|\breve{\boldsymbol{\phi}}\|}\left[\breve{\boldsymbol{\phi}}\right]_\times + \frac{1}{2}\left(\frac{\sin\left(\|\breve{\boldsymbol{\phi}}\|/2\right)}{\|\breve{\boldsymbol{\phi}}\|/2}\right)^2\left(\left[\breve{\boldsymbol{\phi}}\right]_\times\right)^2, \tag{5.9}$$

which is used to derive the spatial variation of $\delta\breve{\boldsymbol{R}}$ using $\delta\breve{\boldsymbol{\phi}}$ via

$$\delta\breve{\boldsymbol{R}} = \left[\delta\breve{\boldsymbol{\phi}}\right]_\times \breve{\boldsymbol{R}}, \tag{5.10}$$

cf. Meier et al. [83]. For parametrization of the rotation tensor itself, we employ unit quaternions $\breve{\mathfrak{q}} \in \mathcal{S}^3 = \{(\breve{\mathfrak{q}}_0, \breve{\mathfrak{q}}) \mid \breve{\mathfrak{q}}_0 \in \mathbb{R},\ \breve{\mathfrak{q}} \in \mathbb{R}^3,\ \breve{\mathfrak{q}}_0^2 + \breve{\mathfrak{q}} \cdot \breve{\mathfrak{q}} = 1\}$ yielding with the Euler-Rodrigues formula (cf. Betsch and Siebert [15] and Marsden and Ratiu [79])

$$\begin{aligned}\breve{\boldsymbol{R}}(\breve{\mathfrak{q}}) &= (2\breve{\mathfrak{q}}_0^2 - 1)\,\boldsymbol{I} + 2\breve{\mathfrak{q}}_0[\breve{\mathfrak{q}}]_\times + 2\,\breve{\mathfrak{q}} \otimes \breve{\mathfrak{q}} \\ &= \begin{bmatrix} 1 - 2(\breve{\mathfrak{q}}_2^2 + \breve{\mathfrak{q}}_3^2) & 2(\breve{\mathfrak{q}}_1\breve{\mathfrak{q}}_2 - \breve{\mathfrak{q}}_0\breve{\mathfrak{q}}_3) & 2(\breve{\mathfrak{q}}_1\breve{\mathfrak{q}}_3 + \breve{\mathfrak{q}}_0\breve{\mathfrak{q}}_2) \\ 2(\breve{\mathfrak{q}}_1\breve{\mathfrak{q}}_2 + \breve{\mathfrak{q}}_0\breve{\mathfrak{q}}_3) & 1 - 2(\breve{\mathfrak{q}}_1^2 + \breve{\mathfrak{q}}_3^2) & 2(\breve{\mathfrak{q}}_2\breve{\mathfrak{q}}_3 - \breve{\mathfrak{q}}_0\breve{\mathfrak{q}}_1) \\ 2(\breve{\mathfrak{q}}_1\breve{\mathfrak{q}}_3 - \breve{\mathfrak{q}}_0\breve{\mathfrak{q}}_2) & 2(\breve{\mathfrak{q}}_2\breve{\mathfrak{q}}_3 + \breve{\mathfrak{q}}_0\breve{\mathfrak{q}}_1) & 1 - 2(\breve{\mathfrak{q}}_1^2 + \breve{\mathfrak{q}}_2^2) \end{bmatrix}. \end{aligned} \tag{5.11}$$

5.2 Energetic response

In Ortigosa et al. [89] it is shown that the introduced kinematical set eq. (5.8) can be used to express the cofactor $\boldsymbol{H}$ and the determinant J, such that Helmholtz-energy function can be rewritten as $\Psi(\boldsymbol{F}, \boldsymbol{H}, J) \equiv \breve{\Psi}(\breve{\boldsymbol{B}}(\breve{\boldsymbol{G}}, \breve{\boldsymbol{K}}))$. Hence, with given local cross-section $\breve{A}(\breve{\theta}^3)$, the Mooney-Rivlin material model as presented in eq. (3.70) now writes

$$\begin{aligned}\breve{\Psi}\left(\breve{\boldsymbol{B}}(\breve{\boldsymbol{G}}, \breve{\boldsymbol{K}})\right) = \int_{\breve{A}(\breve{\theta}^3)} \Big\{ \quad & \alpha\left(\breve{\boldsymbol{B}} \cdot \breve{\boldsymbol{B}} + 2\,\breve{\boldsymbol{B}} \cdot \breve{\boldsymbol{D}}_3 + 3\right) \\ & + \beta\left(2\,\breve{\boldsymbol{B}} \cdot \breve{\boldsymbol{B}} - \left(\breve{\boldsymbol{D}}_3 \times \breve{\boldsymbol{B}}\right) \cdot \left(\breve{\boldsymbol{D}}_3 \times \breve{\boldsymbol{B}}\right) + 4\,\breve{\boldsymbol{B}} \cdot \breve{\boldsymbol{D}}_3 + 3\right) \\ & + f\left(\breve{\boldsymbol{B}} \cdot \breve{\boldsymbol{D}}_3 + 1\right)\Big\}\,\mathrm{d}\breve{\theta}^1\,\mathrm{d}\breve{\theta}^2\,, \end{aligned} \tag{5.12}$$

with material parameters α, β and volumetric function $f(J)$, such that by using the centerline $\breve{\mathcal{C}}_0 = [0,\, L] \subset \mathbb{R}$ we can write the total internal energy as line integral

$$\breve{\Pi}^{\mathrm{int}} = \int_{\breve{\mathcal{C}}_0} \left\{\breve{\Psi}\left(\breve{\boldsymbol{B}}\left(\breve{\boldsymbol{G}}, \breve{\boldsymbol{K}}\right)\right)\right\} \mathrm{d}\breve{\theta}^3. \tag{5.13}$$

For a constant cross section $\breve{A}(\breve{\theta}^3) = \breve{E} = \text{const.}$ (with $\left(\breve{A}(\breve{\theta}^3)\right)' = 0$), the cross-sectional integral can be computed a priori. Following Steinbrecher et al. [114] and Weeger et al. [119], we write the energy directly in terms of $\breve{\boldsymbol{G}}$ and $\breve{\boldsymbol{K}}$ providing

$$\breve{\Psi}(\breve{\boldsymbol{G}}, \breve{\boldsymbol{K}}) \coloneqq \frac{1}{2}\,\breve{\boldsymbol{G}} \cdot \breve{\mathbb{K}}_1\,\breve{\boldsymbol{G}} + \frac{1}{2}\,\breve{\boldsymbol{K}} \cdot \breve{\mathbb{K}}_2\,\breve{\boldsymbol{K}}, \tag{5.14}$$

with diagonal 3×3 matrices $\breve{\mathbb{K}}_1$ and $\breve{\mathbb{K}}_2$ containing material constants and the cross-section geometrical parameters. For a simple model we set

$$\breve{\mathbb{K}}_1 = \operatorname{diag}\big(G\breve{A}_1,\, G\breve{A}_2,\, E\breve{A}\big) \quad \text{and} \quad \breve{\mathbb{K}}_2 = \operatorname{diag}\big(E\breve{I}_1,\, E\breve{I}_2,\, G\breve{I}_p\big) \tag{5.15}$$

using Young's modulus E, shear modulus G in combination with the cross-section area $\breve{A}$, effective shear areas $\breve{A}_1$, $\breve{A}_2$ and the planar second moments of area $\breve{I}_1$, $\breve{I}_2$ and the polar second moment of area $\breve{I}_p = \breve{I}_1 + \breve{I}_2$. For a circular cross-section with radius $\breve{r}$ we get $\breve{A}_1 = \breve{A}_2 = \breve{A} = \frac{\pi}{\breve{r}}^2$ and $\breve{I}_1 = \breve{I}_2 = \frac{\pi}{4}\breve{r}^4$. Hence we can clearly see relations to the fiber material law in eq. (4.14).

Dual to the strain vectors $\breve{\boldsymbol{G}}$ and $\breve{\boldsymbol{K}}$ we introduce two stress measures. That is the translational stress $\breve{\boldsymbol{S}} : \breve{\Omega}_0 \to \mathbb{R}^d$ and $\breve{\boldsymbol{s}} : \breve{\Omega} \to \mathbb{R}^d$ as well as the rotational hyper-stress $\breve{\boldsymbol{W}} : \breve{\Omega}_0 \to \mathbb{R}^d$ and $\breve{\boldsymbol{w}} : \breve{\Omega} \to \mathbb{R}^d$, in reference and current configuration respectively, reading

$$\breve{\boldsymbol{S}} = \frac{\partial \breve{\Psi}}{\partial \breve{\boldsymbol{G}}}, \quad \breve{\boldsymbol{s}} = \breve{\boldsymbol{R}}\,\breve{\boldsymbol{S}} \quad \text{and} \quad \breve{\boldsymbol{W}} = \frac{\partial \breve{\Psi}}{\partial \breve{\boldsymbol{K}}}, \quad \breve{\boldsymbol{w}} = \breve{\boldsymbol{R}}\,\breve{\boldsymbol{W}}\,. \tag{5.16}$$

5.2.1 Virtual work of the beam

Conducting the first variation (see section 3.A.1), the internal virtual work of the beam yields

$$\delta\breve{\Pi}^{\text{int}} = \int_{\breve{\mathcal{C}}_0} \Big\{ \breve{\boldsymbol{S}} \cdot \delta\breve{\boldsymbol{G}} + \breve{\boldsymbol{W}} \cdot \delta\breve{\boldsymbol{K}} \Big\}\, \mathrm{d}\breve{\theta}^3 \tag{5.17}$$

with variations of the beam strain measures

$$\delta\breve{\boldsymbol{G}} = \delta\Big(\breve{\boldsymbol{R}}^{\top}\breve{\boldsymbol{\varphi}}' - \breve{\boldsymbol{D}}_3\Big) = \delta\breve{\boldsymbol{R}}^{\top}\breve{\boldsymbol{\varphi}}' + \breve{\boldsymbol{R}}^{\top}\delta\breve{\boldsymbol{\varphi}}' = -\breve{\boldsymbol{R}}^{\top}\Big[\delta\breve{\boldsymbol{\phi}}\Big]_{\times}\breve{\boldsymbol{\varphi}}' + \breve{\boldsymbol{R}}^{\top}\delta\breve{\boldsymbol{\varphi}}' \tag{5.18}$$

and

$$\Big[\delta\breve{\boldsymbol{K}}\Big]_{\times} = \delta\Big(\breve{\boldsymbol{R}}^{\top}\breve{\boldsymbol{R}}'\Big) = -\breve{\boldsymbol{R}}^{\top}\Big[\delta\breve{\boldsymbol{\phi}}\Big]_{\times}\breve{\boldsymbol{R}}' + \breve{\boldsymbol{R}}^{\top}\Big(\Big[\delta\breve{\boldsymbol{\phi}}\Big]_{\times}\breve{\boldsymbol{R}}\Big)' = \breve{\boldsymbol{R}}^{\top}\Big[\delta\breve{\boldsymbol{\phi}}'\Big]_{\times}\breve{\boldsymbol{R}}\,, \tag{5.19}$$

such that the axial vector $\delta\breve{\boldsymbol{K}}$ is then given by

$$\delta\breve{\boldsymbol{K}} = \operatorname{axl}\Big(\Big[\delta\breve{\boldsymbol{K}}\Big]_{\times}\Big) = \breve{\boldsymbol{R}}^{\top}\delta\breve{\boldsymbol{\phi}}'\,, \tag{5.20}$$

see eq. (0.3) and eq. (0.22)) to eq. (0.24) for details on the Levi-Civita permutation ε_{ijk}, spin and axial vector.

Insertion into the internal virtual work eq. (5.17) results in

$$\begin{aligned}
\delta\breve{\Pi}^{\text{int}} &= \int_{\breve{\mathcal{C}}_0} \Big\{ \Big(\breve{\boldsymbol{R}}\,\breve{\boldsymbol{S}}\Big) \cdot \delta\breve{\boldsymbol{\varphi}}' - \Big(\breve{\boldsymbol{\varphi}}' \times \breve{\boldsymbol{R}}\,\breve{\boldsymbol{S}}\Big) \cdot \delta\breve{\boldsymbol{\phi}} + \Big(\breve{\boldsymbol{R}}\,\breve{\boldsymbol{W}}\Big) \cdot \delta\breve{\boldsymbol{\phi}}' \Big\}\, \mathrm{d}\breve{\theta}^3 \\
&= \int_{\breve{\mathcal{C}}_0} \Big\{ \breve{\boldsymbol{s}} \cdot \delta\breve{\boldsymbol{\varphi}}' - (\breve{\boldsymbol{\varphi}}' \times \breve{\boldsymbol{s}}) \cdot \delta\breve{\boldsymbol{\phi}} + \breve{\boldsymbol{w}} \cdot \delta\breve{\boldsymbol{\phi}}' \Big\}\, \mathrm{d}\breve{\theta}^3.
\end{aligned} \tag{5.21}$$

Constituting external distributed forces $\overset{\breve{}}{\overline{\boldsymbol{s}}}$ and moments $\overset{\breve{}}{\overline{\boldsymbol{w}}}$ along with endpoint contributions $\overset{\breve{}}{\overline{\boldsymbol{s}}}_{\breve{E}}$ and $\overset{\breve{}}{\overline{\boldsymbol{w}}}_{\breve{E}}$, we assume the existence of an external energy functional

$$\breve{\Pi}^{\text{ext}} = \int_{\breve{\mathcal{C}}_0} \left\{ \overset{\breve{}}{\overline{\boldsymbol{s}}} \cdot \breve{\boldsymbol{\varphi}} + \overset{\breve{}}{\overline{\boldsymbol{w}}} \cdot \breve{\boldsymbol{\phi}} \right\} \mathrm{d}\breve{\theta}^3 + \left[\!\!\left[\overset{\breve{}}{\overline{\boldsymbol{s}}}_{\breve{E}} \cdot \breve{\boldsymbol{\varphi}} + \overset{\breve{}}{\overline{\boldsymbol{w}}}_{\breve{E}} \cdot \breve{\boldsymbol{\phi}} \right]\!\!\right]_0^L, \tag{5.22}$$

hence we obtain after integration by parts the classical balance equations in the actual configuration, cf. Antman [4] - ch. 8,

$$\begin{aligned} -\int_{\breve{\mathcal{C}}_0} \left\{ \delta\breve{\boldsymbol{\varphi}} \cdot \left(\breve{\boldsymbol{s}}' + \overset{\breve{}}{\overline{\boldsymbol{s}}} \right) \right\} \mathrm{d}\breve{\theta}^3 = 0, \\ -\int_{\breve{\mathcal{C}}_0} \left\{ \delta\breve{\boldsymbol{\phi}} \cdot \left(\breve{\boldsymbol{w}}' + \breve{\boldsymbol{\varphi}}' \times \breve{\boldsymbol{s}} + \overset{\breve{}}{\overline{\boldsymbol{w}}} \right) \right\} \mathrm{d}\breve{\theta}^3 = 0, \end{aligned} \tag{5.23}$$

for all $(\delta\breve{\boldsymbol{\varphi}}, \delta\breve{\boldsymbol{\phi}}) \in \breve{\mathcal{V}}_{\delta\boldsymbol{\varphi}}$, where the functional trial space $\breve{\mathcal{V}}_{\delta\boldsymbol{\varphi}}$ consisting of suitable and kinematically admissible variations fulfilling boundary conditions $\breve{\boldsymbol{s}} = \overset{\breve{}}{\overline{\boldsymbol{s}}}_{\breve{E}}$ on $\partial\breve{\Omega}_0^{\breve{s},\breve{E}}$ and $\breve{\boldsymbol{w}} = \overset{\breve{}}{\overline{\boldsymbol{w}}}_{\breve{E}}$ on $\partial\breve{\Omega}_0^{\breve{w},\breve{E}}$.

5.2.2 Mixed finite element method

In order to gain flexibility towards avoiding shear locking, a mixed (or *Hu-Washizu type*, see section 3.6) method is employed by introducing independent fields equaling the deformation measures eq. (5.7), with the spatial axial-shear strain vector $\breve{\mathfrak{g}} \overset{!}{=} \breve{\boldsymbol{g}}$ and the torsional-bending strain vector $\breve{\mathfrak{k}} \overset{!}{=} \breve{\boldsymbol{k}}$. By examining how the corresponding Lagrange multipliers act, we denote them as resultant translational force and rotational stress, $\breve{\mathfrak{w}}$ and $\breve{\mathfrak{s}}$, respectively. Eventually, the augmented strain energy function is given as

$$\breve{\Psi}_{HW} = \breve{\Psi}\left(\breve{\boldsymbol{R}}^{\top}\breve{\mathfrak{g}}, \breve{\boldsymbol{R}}^{\top}\breve{\mathfrak{k}} \right) + \breve{\mathfrak{s}} \cdot (\breve{\boldsymbol{g}} - \breve{\mathfrak{g}}) + \breve{\mathfrak{w}} \cdot \left(\breve{\boldsymbol{k}} - \breve{\mathfrak{k}} \right), \tag{5.24}$$

such that first variation now yields

$$\begin{aligned} \int_{\breve{\mathcal{C}}_0} \Bigg\{ & - \delta\breve{\boldsymbol{\varphi}} \cdot \left(\breve{\mathfrak{s}}' + \overset{\breve{}}{\overline{\boldsymbol{s}}} \right) - \delta\breve{\boldsymbol{\phi}} \cdot \left(\breve{\mathfrak{w}}' + \breve{\boldsymbol{\varphi}}' \times \breve{\mathfrak{s}} + \overset{\breve{}}{\overline{\boldsymbol{w}}} \right) + \delta\breve{\mathfrak{g}} \cdot \left(\frac{\partial\breve{\Psi}(\breve{\boldsymbol{R}}^{\top}\breve{\mathfrak{g}}, \breve{\boldsymbol{R}}^{\top}\breve{\mathfrak{k}})}{\partial\breve{\mathfrak{g}}} - \breve{\mathfrak{s}} \right) \\ & + \delta\breve{\mathfrak{k}} \cdot \left(\frac{\partial\breve{\Psi}(\breve{\boldsymbol{R}}^{\top}\breve{\mathfrak{g}}, \breve{\boldsymbol{R}}^{\top}\breve{\mathfrak{k}})}{\partial\breve{\mathfrak{k}}} - \breve{\mathfrak{w}} \right) + \delta\breve{\mathfrak{s}} \cdot (\breve{\boldsymbol{g}} - \breve{\mathfrak{g}}) + \delta\breve{\mathfrak{w}} \cdot \left(\breve{\boldsymbol{k}} - \breve{\mathfrak{k}} \right) \Bigg\} \mathrm{d}\breve{\theta}^3 = 0. \end{aligned} \tag{5.25}$$

Assuming the kinematical augmentations to be fulfilled locally, the last two variations with respect to $\delta\breve{\mathfrak{s}}$ and $\delta\breve{\mathfrak{w}}$ in eq. (5.25) cancel out and we can rewrite the mixed formulation as

$$\begin{aligned} \int_{\breve{\mathcal{C}}_0} \Bigg\{ & - \delta\breve{\boldsymbol{\varphi}} \cdot \left(\breve{\mathfrak{s}}' + \overset{\breve{}}{\overline{\boldsymbol{s}}} \right) - \delta\breve{\boldsymbol{\phi}} \cdot \left(\breve{\mathfrak{w}}' + \breve{\boldsymbol{\varphi}}' \times \breve{\mathfrak{s}} + \overset{\breve{}}{\overline{\boldsymbol{w}}} \right) \\ & + \delta\breve{\mathfrak{g}} \cdot (\breve{\boldsymbol{s}} - \breve{\mathfrak{s}}) + \delta\breve{\mathfrak{k}} \cdot (\breve{\boldsymbol{w}} - \breve{\mathfrak{w}}) \Bigg\} \mathrm{d}\breve{\theta}^3 = 0, \end{aligned} \tag{5.26}$$

with stresses $\check{\boldsymbol{s}}, \check{\boldsymbol{w}}$ given in eq. (5.16).

5.3 Coupling constraints

Building upon the continuous description of fiber-reinforced polymers chapter 4, we now introduce a multidimensional coupling framework for the matrix-beam system for the embedding of a beam into a matrix as illustrated in figure 5.3.1.

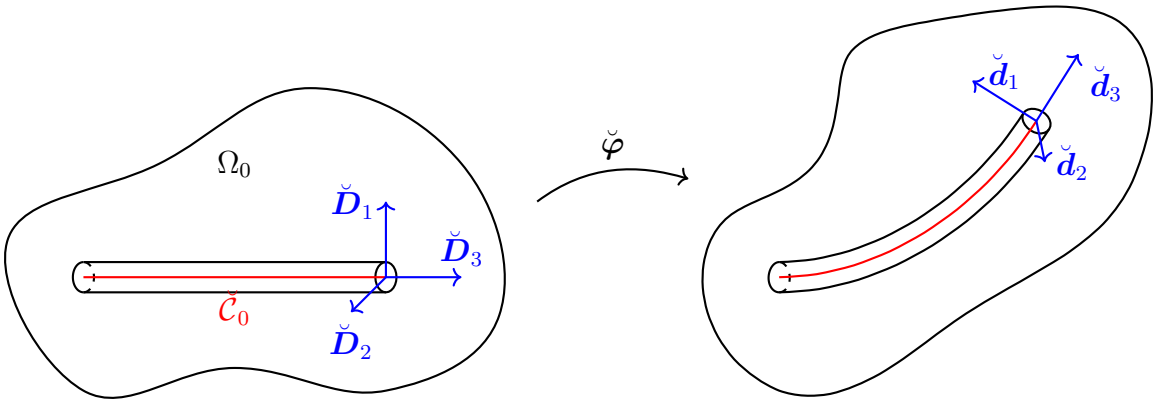


Figure 5.3.1 – Coupled matrix-beam system. Deformation of the coupled matrix-beam system.

Originating from a surface-to-volume interaction principle, we derive a surrogate model in which dedicated coupling constraints enable the consistent transfer of both force resultants and bending moments between beam and matrix. Construction of the coherent model relies on two main assumptions:

A1 Overlapping domains. The matrix continuum is extended into the beam domain. This overlap introduces additional stiffness, whose magnitude depends on the beam cross section and the stiffness ratio between matrix and beam.

A2 Coupling forces. We introduce coupling forces via Lagrange multipliers, which are defined such that, they reproduce the mean force, bending and torsional moments, as well as shear and dilatational components when applied to the beam cross-section.

Analyses of modeling errors induced by overlapping domains exist for various problems, e.g. diffusion in Köppl et al. [65] and for fluid-structure interaction in Liu et al. [76]. Generally, surplus matrix contributions can be systematically removed by adopting a continuum-degenerated beam formulation, which ensures compatibility of stress measures between beam and matrix. Nevertheless, the reduced kinematical representation of the beam cross-section remains inherent to the model.

These assumptions are particularly suitable for fiber-reinforced polymers, where fibers generally have a great stiffness contrast relative to the surrounding matrix and are small in

cross-section, mostly determined by their radius. Under such conditions, the influence of the overlapping region is negligible compared to the overall material response. This balance allows the surrogate model to retain accuracy while substantially reducing computational effort, making it a practical and efficient tool for simulating fiber-reinforced composites with arbitrary fiber directions and lengths.

5.3.1 Geometric coupling conditions

For the coupling we inspect the contact area between matrix and beam, i.e. mantle $\partial\breve{\Omega}_0^{\breve{C}}$ and end faces $\breve{A}(0) = \breve{A}(L) = \breve{E}$ as shown in figure 5.3.2, to identify the Lagrange Multipliers as coupling forces of the constraint. Their total work over the whole matrix/beam interface reads

$$\breve{\Pi}^{\text{con}}_{\partial\breve{\Omega}_0} = \int\limits_{\partial\breve{\Omega}_0} \{\breve{\boldsymbol{\mu}} \cdot (\boldsymbol{\varphi} - \breve{\boldsymbol{x}})\} \mathrm{d}A = \breve{\Pi}^{\text{con}}_{\breve{C}} + \breve{\Pi}^{\text{con}}_{\breve{E}}, \tag{5.27}$$

with

$$\breve{\Pi}^{\text{con}}_{\breve{C}} = \int\limits_{\breve{\mathcal{C}}_0} \left\{ \int_{\breve{C}(\breve{\theta}^3)} \{\breve{\boldsymbol{\mu}} \cdot (\boldsymbol{\varphi} - \breve{\boldsymbol{x}})\} \, \mathrm{d}\breve{C} \right\} \mathrm{d}\breve{\theta}^3, \qquad \breve{\Pi}^{\text{con}}_{\breve{E}} = \left[\!\!\left[\int_{\breve{A}(\breve{\theta}^3)} \{\breve{\boldsymbol{\mu}} \cdot (\boldsymbol{\varphi} - \breve{\boldsymbol{x}})\} \, \mathrm{d}\breve{A} \right]\!\!\right]_0^L. \tag{5.28}$$

Therein, $\breve{C}(\breve{\theta}^3)$ is the boundary of cross-section $\breve{A}(\breve{\theta}^3)$, each in terms of the arc length $\breve{\theta}^3$ and $\boldsymbol{\varphi}$ is the position vector of the matrix. For clarity, we introduce some notational conventions. Let $f(\boldsymbol{X}) : \Omega_0 \to \mathbb{R}^d$ be any function. Its restriction to the beam domain $\breve{\Omega}_0$ in convective coordinates is written as $f\big(\breve{\theta}^\alpha, \breve{\theta}^3\big) \coloneqq f\Big(\breve{\boldsymbol{X}}\big(\breve{\theta}^\alpha, \breve{\theta}^3\big)\Big)$. Furthermore, the trace $[f]\!]_{\breve{\mathcal{C}}_0}$ of f on the beam centerline $\breve{\mathcal{C}}_0$ is expressed as $f\big(\breve{\theta}^3\big) \coloneqq f\Big(\breve{\boldsymbol{\varphi}}_0\big(\breve{\theta}^3\big)\Big)$, $\breve{\theta}^3 \in \breve{\mathcal{C}}_0$.

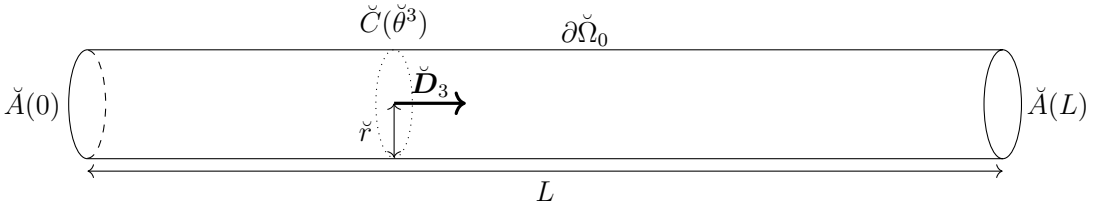


Figure 5.3.2 – 3D beam kinematic. 3D beam reference configuration.

5.3.2 Coupling forces

For a beam representing a fiber, we assume a circular cross-section, determined by the radius $\breve{r}$, such that area and the circumference result in $|\breve{E}| = \pi\,\breve{r}^2$ and $|\breve{C}| = 2\,\pi\,\breve{r}$, respectively. The Lagrange multiplier $\breve{\boldsymbol{\mu}}$, physically interpreted as the interface load, is then defined on the beam mantle $\partial\breve{\Omega}_0^{\breve{C}} = \Big\{(\breve{r}\,\cos\big(\breve{\beta}\big), \breve{r}\,\sin\big(\breve{\beta}\big), \breve{\theta}^3) \mid \breve{\theta}^3 \in [0, L], \breve{\beta} \in [0, 2\pi]\Big\}$, with angle $\breve{\beta} = \arctan\big(\breve{\theta}^2/\breve{\theta}^1\big)$ along the beam cross-section circumference.

We then decompose $\breve{\boldsymbol{\mu}} = \breve{\boldsymbol{\mu}}(\breve{\beta}, \breve{\theta}^3)$ in a Fourier series as periodic function of the angle and truncate after the first two terms

$$\breve{\boldsymbol{\mu}}(\breve{\beta}, \breve{\theta}^3) = \breve{\boldsymbol{\eta}}(\breve{\theta}^3) + \breve{\boldsymbol{\nu}}_1(\breve{\theta}^3)\,\cos\Big(\breve{\beta}\Big) + \breve{\boldsymbol{\nu}}_2(\breve{\theta}^3)\,\sin\Big(\breve{\beta}\Big), \tag{5.29}$$

identifying $\breve{\boldsymbol{\eta}}(\breve{\theta}^3) = \frac{1}{2\,\pi}\int_0^{2\pi}\Big\{\breve{\boldsymbol{\mu}}(\breve{\beta}, \breve{\theta}^3)\Big\}\mathrm{d}\breve{\beta}$ as mean cross-sectional load along $\breve{\boldsymbol{\nu}}_\alpha$, $\alpha \in \{1, 2\}$, as the first cosine/sine Fourier coefficients composing the load fluctuation

$$\breve{\boldsymbol{\nu}}(\breve{\beta}, \breve{\theta}^3) \coloneqq \breve{\boldsymbol{\Sigma}}(\breve{\theta}^3)\,\breve{\boldsymbol{N}}(\breve{\beta}) = \breve{\boldsymbol{\nu}}_1(\breve{\theta}^3)\,\cos\Big(\breve{\beta}\Big) + \breve{\boldsymbol{\nu}}_2(\breve{\theta}^3)\,\sin\Big(\breve{\beta}\Big). \tag{5.30}$$

Therein $\breve{\boldsymbol{\Sigma}} = \breve{\boldsymbol{\nu}}_\alpha \otimes \breve{\boldsymbol{D}}_\alpha$ denotes the interface stress tensor and $\breve{\boldsymbol{N}} = \breve{\boldsymbol{D}}_1\,\cos\Big(\breve{\beta}\Big) + \breve{\boldsymbol{D}}_2\,\sin\Big(\breve{\beta}\Big)$ is the unit outer normal on the interface in reference configuration. Note that for a circular circumference $\int_0^{2\pi}\Big\{\breve{\boldsymbol{\nu}}(\breve{\beta}, \breve{\theta}^3)\Big\}\mathrm{d}\breve{\beta} = 0$. The decomposition $\breve{\boldsymbol{\mu}}(\breve{\beta}, \breve{\theta}^3) = \breve{\boldsymbol{\eta}}(\breve{\theta}^3) + \breve{\boldsymbol{\Sigma}}\,\breve{\boldsymbol{N}}$ allows us to physically associate $\breve{\boldsymbol{\eta}}$ with the resulting cross-section forces for the position coupling of beam center-line to matrix, and $\breve{\boldsymbol{\nu}}$, respectively $\breve{\boldsymbol{\Sigma}}$, with the coupled stresses, shears and hydrostatic pressure responsible for transferring beam bending and torsion to the matrix.

Inspecting the coupling stress tensor $\breve{\boldsymbol{\Sigma}} = \breve{\boldsymbol{\nu}}_\alpha \otimes \breve{\boldsymbol{D}}_\alpha$, we recognize it has only six degrees of freedom due to nonexistent contributions in centerline direction. By introducing a map from the Cartesian coordinate system to the beam triad $\breve{\mathbb{T}} \coloneqq \breve{\boldsymbol{D}}_j \otimes \boldsymbol{e}_j$, we can further associate its entries

$$\breve{\boldsymbol{\Sigma}} = \breve{\boldsymbol{R}}\,\breve{\mathbb{T}}\begin{bmatrix} \breve{\varpi}_1 & \breve{\varpi}_3 - \breve{\vartheta}_3 & 0 \\ \breve{\varpi}_3 + \breve{\vartheta}_3 & \breve{\varpi}_2 & 0 \\ -2\,\breve{\vartheta}_2 & 2\,\breve{\vartheta}_1 & 0 \end{bmatrix}\breve{\mathbb{T}}^{\top}, \tag{5.31}$$

giving $\breve{\varpi}_1$, $\breve{\varpi}_2$, $\breve{\varpi}_3$ related to dilatation and shear of the cross-section, as well as $\breve{\vartheta}_1$ and $\breve{\vartheta}_2$ related to bending, and $\breve{\vartheta}_3$ associated to torsion. For separation of dilatation/shear $\breve{\boldsymbol{\varpi}} = \breve{\varpi}_j\,\breve{\boldsymbol{d}}_j$ from bending/torsion $\breve{\boldsymbol{\vartheta}} = \breve{\vartheta}_j\,\breve{\boldsymbol{d}}_j = \mathrm{axl}\Big(\breve{\boldsymbol{\Sigma}}\,\breve{\boldsymbol{R}}^{\top}\Big)$, we introduce the following split

$$\breve{\boldsymbol{\Sigma}} = \Big(\breve{\mathbb{P}}_\alpha\,\breve{\boldsymbol{\vartheta}} + \breve{\mathbb{Q}}_\alpha\,\breve{\boldsymbol{\varpi}}\Big) \otimes \breve{\boldsymbol{D}}_\alpha, \tag{5.32}$$

using the projections

$$\begin{aligned} \breve{\mathbb{P}}_1 &= \quad \breve{\boldsymbol{d}}_2 \otimes \breve{\boldsymbol{d}}_3 - 2\,\breve{\boldsymbol{d}}_3 \otimes \breve{\boldsymbol{d}}_2, & \breve{\mathbb{Q}}_1 &= \breve{\boldsymbol{d}}_1 \otimes \breve{\boldsymbol{d}}_1 + \breve{\boldsymbol{d}}_2 \otimes \breve{\boldsymbol{d}}_3, \\ \breve{\mathbb{P}}_2 &= -\breve{\boldsymbol{d}}_1 \otimes \breve{\boldsymbol{d}}_3 + 2\,\breve{\boldsymbol{d}}_3 \otimes \breve{\boldsymbol{d}}_1, & \breve{\mathbb{Q}}_2 &= \breve{\boldsymbol{d}}_2 \otimes \breve{\boldsymbol{d}}_2 + \breve{\boldsymbol{d}}_1 \otimes \breve{\boldsymbol{d}}_3. \end{aligned} \tag{5.33}$$

5.3.3 Centerline restriction

In order to simplify coupling of the whole domain in eq. (5.28) - eq. (5.27), we aim at a restriction to the beam centerline. Therefore we introduce the cross-sectional average deformation gradient using Green's Theorem

$$\boldsymbol{F}_c \coloneqq \frac{1}{|\breve{E}|}\int\limits_{\breve{C}(\breve{\theta}^3)} \Big\{\boldsymbol{\varphi} \otimes \breve{\boldsymbol{N}}\Big\}\,\mathrm{d}\breve{C} \tag{5.34}$$

and the decomposition of $\boldsymbol{\varphi}$ into circular mean

$$\boldsymbol{\varphi}_c \coloneqq \frac{1}{|\breve{C}|} \int\limits_{\breve{C}(\breve{\theta}^3)} \{\boldsymbol{\varphi}\} \, \mathrm{d}\breve{C} \tag{5.35}$$

along Fourier cosine and sine coefficients

$$\hat{\boldsymbol{\varphi}}_1 \coloneqq \frac{1}{|\breve{E}|} \int\limits_{\breve{C}(\breve{\theta}^3)} \left\{\boldsymbol{\varphi} \, \cos\left(\breve{\beta}\right)\right\} \mathrm{d}\breve{C} \quad \text{and} \quad \hat{\boldsymbol{\varphi}}_2 \coloneqq \frac{1}{|\breve{E}|} \int\limits_{\breve{C}(\breve{\theta}^3)} \left\{\boldsymbol{\varphi} \, \sin\left(\breve{\beta}\right)\right\} \mathrm{d}\breve{C}. \tag{5.36}$$

Subsequently, the energy contribution eq. $(5.28)_1$ as constrained coupling on the beam mantle $\partial\breve{\Omega}_0^{\breve{C}}$, is derived by substitution of eq. (5.29) and eq. (5.30), yielding

$$\begin{aligned} \breve{\Pi}_{\breve{C}}^{\mathrm{con}} &= \int\limits_{\breve{\mathcal{C}}_0} \left\{ \int_{\breve{C}(\breve{\theta}^3)} \{\breve{\boldsymbol{\mu}} \cdot (\boldsymbol{\varphi} - \breve{\boldsymbol{x}})\} \, \mathrm{d}\breve{C} \right\} \mathrm{d}\breve{\theta}^3 \\ &= \int\limits_{\breve{\mathcal{C}}_0} \left\{ \int_{\breve{C}(\breve{\theta}^3)} \left\{ \left(\breve{\boldsymbol{\eta}} + \breve{\boldsymbol{\Sigma}} \, \breve{\boldsymbol{N}}\right) \cdot \left(\boldsymbol{\varphi} - \left(\breve{\boldsymbol{\varphi}} + \breve{\boldsymbol{R}} \, \breve{\boldsymbol{N}} \, \breve{r}\right)\right) \right\} \mathrm{d}\breve{C} \right\} \mathrm{d}\breve{\theta}^3. \end{aligned} \tag{5.37}$$

Note that $\int_{\breve{C}(\breve{\theta}^3)} \left\{\breve{\boldsymbol{N}}\right\} \mathrm{d}\breve{C} = \boldsymbol{0}$ for the circular assumed beam. Thus, the integral part $\int_{\breve{C}(\breve{\theta}^3)} \left\{\breve{\boldsymbol{N}} \otimes \breve{\boldsymbol{N}}\right\} \mathrm{d}\breve{C}$ using $\breve{\boldsymbol{N}} = \breve{\boldsymbol{D}}_1 \cos\left(\breve{\beta}\right) + \breve{\boldsymbol{D}}_2 \sin\left(\breve{\beta}\right)$ can directly be evaluated

$$\begin{aligned} \int\limits_{\breve{C}(\breve{\theta}^3)} \left\{\breve{\boldsymbol{N}} \otimes \breve{\boldsymbol{N}}\right\} \mathrm{d}\breve{C} &= \breve{r} \int\limits_0^{2\pi} \left\{\breve{\boldsymbol{N}} \otimes \breve{\boldsymbol{N}}\right\} \mathrm{d}\breve{\beta} \\ &= \breve{r} \breve{\boldsymbol{D}}_1 \otimes \breve{\boldsymbol{D}}_1 \underbrace{\int\limits_0^{2\pi} \left\{\cos^2\left(\breve{\beta}\right)\right\} \mathrm{d}\breve{\beta}}_{=\pi} + \breve{r} \breve{\boldsymbol{D}}_2 \otimes \breve{\boldsymbol{D}}_2 \underbrace{\int\limits_0^{2\pi} \left\{\sin^2\left(\breve{\beta}\right)\right\} \mathrm{d}\breve{\beta}}_{=\pi} \\ &\quad + \breve{r} \left[\breve{\boldsymbol{D}}_1 \otimes \breve{\boldsymbol{D}}_2 + \breve{\boldsymbol{D}}_2 \otimes \breve{\boldsymbol{D}}_1\right] \underbrace{\int\limits_0^{2\pi} \left\{\sin\left(\breve{\beta}\right) \cos\left(\breve{\beta}\right)\right\} \mathrm{d}\breve{\beta}}_{=0} \\ &= \breve{r} \pi \, \breve{\boldsymbol{D}}_\alpha \otimes \breve{\boldsymbol{D}}_\alpha. \end{aligned} \tag{5.38}$$

Using the identity $\breve{\boldsymbol{\Sigma}} \, \breve{\boldsymbol{D}}_\alpha \otimes \breve{\boldsymbol{D}}_\alpha = \breve{\boldsymbol{\Sigma}}$, we write for eq. (5.37)

$$\begin{aligned} \breve{\Pi}_{\breve{C}}^{\mathrm{con}} &= \int\limits_{\breve{\mathcal{C}}_0} \left\{ \breve{\boldsymbol{\eta}} \cdot \int_{\breve{C}(\breve{\theta}^3)} \{(\boldsymbol{\varphi} - \breve{\boldsymbol{\varphi}})\} \, \mathrm{d}\breve{C} \right\} \mathrm{d}\breve{\theta}^3 + \int\limits_{\breve{\mathcal{C}}_0} \left\{ \breve{\boldsymbol{\Sigma}} : \int_{\breve{C}(\breve{\theta}^3)} \left\{ \left(\boldsymbol{\varphi} - \breve{\boldsymbol{R}} \, \breve{\boldsymbol{N}} \, \breve{r}\right) \otimes \breve{\boldsymbol{N}} \right\} \mathrm{d}\breve{C} \right\} \mathrm{d}\breve{\theta}^3 \\ &= \int\limits_{\breve{\mathcal{C}}_0} \left\{ \breve{\boldsymbol{\eta}} \cdot \left[\int_{\breve{C}(\breve{\theta}^3)} \{\boldsymbol{\varphi}\} \, \mathrm{d}\breve{C} - \breve{\boldsymbol{\varphi}} |\breve{C}| \right] \right\} \mathrm{d}\breve{\theta}^3 + \int\limits_{\breve{\mathcal{C}}_0} \left\{ \breve{\boldsymbol{\Sigma}} : \left[\int_{\breve{C}(\breve{\theta}^3)} \left\{\boldsymbol{\varphi} \otimes \breve{\boldsymbol{N}}\right\} \mathrm{d}\breve{C} - \pi \, \breve{r}^2 \, \breve{\boldsymbol{R}} \right] \right\} \mathrm{d}\breve{\theta}^3, \end{aligned} \tag{5.39}$$

hence it follows with insertion of eq. (5.34) and eq. (5.35)

$$\breve{\Pi}^{\mathrm{con}}_{\breve{C}} = \int_{\breve{\mathcal{C}}_0} \left\{ \breve{\boldsymbol{\eta}} \cdot (\boldsymbol{\varphi}_c - \breve{\boldsymbol{\varphi}}) \, |\breve{C}| \right\} \mathrm{d}\breve{\theta}^3 + \int_{\breve{\mathcal{C}}_0} \left\{ \breve{\boldsymbol{\Sigma}} : \left(\boldsymbol{F}_c - \breve{\boldsymbol{R}} \right) |\breve{E}| \right\} \mathrm{d}\breve{\theta}^3 \,. \tag{5.40}$$

Variation of the work associated to the kinematic constraints then yields for the circumference

$$\begin{aligned} \delta\breve{\Pi}^{\mathrm{con}}_{\breve{C}} = \int_{\breve{\mathcal{C}}_0} \Big\{ \Big[\delta\breve{\boldsymbol{\eta}} \cdot (\boldsymbol{\varphi}_c - \breve{\boldsymbol{\varphi}}) + \breve{\boldsymbol{\eta}} \cdot (\delta\boldsymbol{\varphi}_c - \delta\breve{\boldsymbol{\varphi}}) \Big] |\breve{C}| \Big\} \, \mathrm{d}\breve{\theta}^3 \\ + \int_{\breve{\mathcal{C}}_0} \left\{ \left(\breve{\boldsymbol{\Sigma}} : \left(\delta \boldsymbol{F}_c - \left[\delta\breve{\boldsymbol{\phi}} \right]_\times \breve{\boldsymbol{R}} \right) + \delta\breve{\boldsymbol{\Sigma}} : \left(\boldsymbol{F}_c - \breve{\boldsymbol{R}} \right) \right) |\breve{E}| \right\} \mathrm{d}\breve{\theta}^3, \end{aligned} \tag{5.41}$$

noting $\breve{\boldsymbol{\Sigma}} : \left(\left[\delta\breve{\boldsymbol{\phi}} \right]_\times \breve{\boldsymbol{R}} \right) = 2\, \breve{\boldsymbol{\vartheta}} \cdot \delta\breve{\boldsymbol{\phi}}$. Moreover, contributions of the faces read

$$\breve{\Pi}^{\mathrm{con}}_{\breve{E}} = \left[\!\!\left[\int_{\breve{A}(\breve{\theta}^3)} \{ \breve{\boldsymbol{\mu}} \cdot (\boldsymbol{\varphi} - \breve{\boldsymbol{x}}) \} \, \mathrm{d}\breve{A} \right]\!\!\right]_0^L = \left[\!\!\left[\breve{\boldsymbol{\mu}}_{\breve{E}} \cdot (\boldsymbol{\varphi}_{\breve{E}} - \breve{\boldsymbol{\varphi}}) |\breve{E}| + \mathcal{O}\left(\breve{r}^3 \right) \right]\!\!\right]_0^L, \tag{5.42}$$

where we denoted cross-sectional means

$$\breve{\boldsymbol{\mu}}_{\breve{E}} \coloneqq \frac{1}{|\breve{E}|} \int_{\breve{E}} \{ \breve{\boldsymbol{\mu}} \} \, \mathrm{d}\breve{A}, \quad \text{and} \quad \boldsymbol{\varphi}_{\breve{E}} \coloneqq \frac{1}{|\breve{E}|} \int_{\breve{E}} \{ \boldsymbol{\varphi} \} \, \mathrm{d}\breve{A} \,, \tag{5.43}$$

with $\int_{\breve{E}} \{(\cdot)\} \, \mathrm{d}\breve{A} = \left\{ \int_{\breve{A}(0)} \{(\cdot)\} \, \mathrm{d}\breve{A} \vee \int_{\breve{A}(L)} \{(\cdot)\} \, \mathrm{d}\breve{A} \right\}$. $\breve{A}(0) = \breve{A}(L) = \breve{E}$. Under the aforementioned assumption of a large length to radius ratio, the $\mathcal{O}(\breve{r}^3)$ term is negligible. The virtual work associated with the endpoint contributions then reads

$$\delta\breve{\Pi}^{\mathrm{con}}_{\breve{E}} = \left[\!\!\left[\delta\breve{\boldsymbol{\mu}}_{\breve{E}} \cdot (\boldsymbol{\varphi}_{\breve{E}} - \breve{\boldsymbol{\varphi}}) |\breve{E}| + \breve{\boldsymbol{\mu}}_{\breve{E}} \cdot (\delta\boldsymbol{\varphi}_{\breve{E}} - \delta\breve{\boldsymbol{\varphi}}) |\breve{E}| \right]\!\!\right]_0^L . \tag{5.44}$$

In the case of an embedded face, this takes form of an essential boundary condition $\breve{\boldsymbol{\varphi}} = \boldsymbol{\varphi}_{\breve{E}}$, imposed via Lagrange multiplier as addition to the external endpoint contributions in eq. (5.22) as $\breve{\mathfrak{s}} = \overline{\breve{\boldsymbol{s}}}_{\breve{E}} + \breve{\boldsymbol{\mu}}_{\breve{E}} |\breve{E}|$ on $\partial\breve{\Omega}_0^{\breve{\mathfrak{s}},\breve{E}}$. For a partially embedded beam, i.e. one or both faces are not in the matrix domain, the cross-sectional area is manually set to zero, thus canceling the corresponding contribution and leaving only Neumann boundary condition $\breve{\mathfrak{s}} = \overline{\breve{\mathfrak{s}}}_{\breve{E}}$ on $\partial\breve{\Omega}_0^{\breve{\mathfrak{s}},\breve{E}}$ instead. By accounting for higher-order terms $\mathcal{O}(\breve{r}^3)$ in eq. (5.42), additional Dirichlet boundary conditions for the beam directors may be prescribed.

5.3.4 Total coupled system

For the variational calculus (see section 3.2.1) of the Lagrangian for the coupled matrix-beam system, we collect all virtual work parts yielding

$$\delta\breve{\mathfrak{L}}\left(\boldsymbol{\varphi}, \breve{\boldsymbol{\varphi}}, \breve{\boldsymbol{R}}, \breve{\mathfrak{s}}, \breve{\mathfrak{w}}, \breve{\boldsymbol{\eta}}, \breve{\boldsymbol{\mu}}_{\breve{E}}, \breve{\boldsymbol{\vartheta}}, \breve{\boldsymbol{\varpi}} \right) = \delta\Pi^{\mathrm{int}} - \delta\Pi^{\mathrm{ext}} + \delta\breve{\Pi}^{\mathrm{int}} - \delta\breve{\Pi}^{\mathrm{ext}} + \delta\breve{\Pi}^{\mathrm{con}}_{\breve{C}} + \delta\breve{\Pi}^{\mathrm{con}}_{\breve{E}} = 0, \tag{5.45}$$

in terms of eq. (3.80) (only first gradient terms) and eq. (5.26) along with the virtual work of the coupling forces in eq. (5.41). Based on their variation, we can separate between matrix and beam including mixed-constitutive parts as well as coupling contributions. For parts associated to the matrix we obtain

$$\int_{\Omega_0}\Big\{\boldsymbol{P} : \nabla_{\!\mathrm{X}}\delta\boldsymbol{\varphi} - \overline{\boldsymbol{B}}\cdot\delta\boldsymbol{\varphi}\Big\}\mathrm{d}V - \int_{\partial\Omega_0^N}\Big\{\overline{\boldsymbol{T}}\cdot\delta\boldsymbol{\varphi}\Big\}\mathrm{d}A + \Big[\breve{\boldsymbol{\mu}}_{\breve{E}}\cdot\delta\boldsymbol{\varphi}_{\breve{E}}|\breve{E}|\Big]_0^L + \int_{\breve{\mathcal{C}}_0}\Big\{\breve{\boldsymbol{\eta}}\cdot\delta\boldsymbol{\varphi}_c|\breve{C}| + \breve{\boldsymbol{\Sigma}}(\breve{\boldsymbol{\vartheta}},\breve{\boldsymbol{\varpi}}) : \delta\boldsymbol{F}_c|\breve{E}|\Big\}\,\mathrm{d}\breve{\theta}^3 = 0, \quad (5.46)$$

with constitutive equations and boundary conditions eq. (3.83) and eq. (3.84) - eq. (3.85). For the beam we have the two balance equations

$$-\int_{\breve{\mathcal{C}}_0}\Big\{\Big(\breve{\mathfrak{s}}' + \overline{\breve{\mathfrak{s}}} + \breve{\boldsymbol{\eta}}|\breve{C}|\Big)\cdot\delta\breve{\boldsymbol{\varphi}}\Big\}\,\mathrm{d}\breve{\theta}^3 = 0, \quad (5.47)$$

$$-\int_{\breve{\mathcal{C}}_0}\Big\{\Big(\breve{\mathfrak{w}}' + \breve{\boldsymbol{\varphi}}'\times\breve{\mathfrak{s}} + \overline{\breve{\mathfrak{w}}} + 2\,\breve{\boldsymbol{\vartheta}}\,|\breve{E}|\Big)\cdot\delta\breve{\boldsymbol{\phi}}\Big\}\,\mathrm{d}\breve{\theta}^3 = 0, \quad (5.48)$$

accompanied by endpoint conditions

$$\Big[(\breve{\boldsymbol{\varphi}} - \boldsymbol{\varphi}_{\breve{E}})|\breve{E}|\Big]_{\partial\breve{\Omega}_0^{\breve{E}}} = 0\,, \quad \Big[\breve{\mathfrak{s}}\Big]_{\partial\breve{\Omega}_0^{\breve{E}}} = \overline{\breve{\boldsymbol{s}}}_{\breve{E}} + \breve{\boldsymbol{\mu}}_{\breve{E}}|\breve{E}| \quad \text{and} \quad \Big[\breve{\mathfrak{w}}\Big]_{\partial\breve{\Omega}_0^{\breve{E}}} = \overline{\breve{\boldsymbol{w}}}_{\breve{E}}\,, \quad (5.49)$$

where $|\breve{E}| = 0$ if the corresponding face is not embedded, supplemented by the mixed parts for the stresses eq. (5.16) as weak constitutive equations

$$\int_{\breve{\mathcal{C}}_0}\{\delta\breve{\mathfrak{g}}\cdot(\breve{\boldsymbol{s}} - \breve{\mathfrak{s}})\}\,\mathrm{d}\breve{\theta}^3 = 0, \quad (5.50)$$

$$\int_{\breve{\mathcal{C}}_0}\Big\{\delta\breve{\mathfrak{k}}\cdot(\breve{\boldsymbol{w}} - \breve{\mathfrak{w}})\Big\}\,\mathrm{d}\breve{\theta}^3 = 0\,. \quad (5.51)$$

Eventually, we have the coupling constraints

$$\int_{\breve{\mathcal{C}}_0}\Big\{\delta\breve{\boldsymbol{\eta}}\cdot(\boldsymbol{\varphi}_c - \breve{\boldsymbol{\varphi}})\,|\breve{C}|\Big\}\,\mathrm{d}\breve{\theta}^3 = 0, \quad (5.52)$$

$$\int_{\breve{\mathcal{C}}_0}\Big\{\delta\breve{\boldsymbol{\Sigma}} : \Big(\boldsymbol{F}_c - \breve{\boldsymbol{R}}\Big)|\breve{E}|\Big\}\,\mathrm{d}\breve{\theta}^3 = 0. \quad (5.53)$$

5.4 Condensed system and second gradient model

In the following we derive a condensed version of the whole system eq. (5.46) - eq. (5.53) in order to reduce the degrees of freedom to be calculated as well as to give a direct link between bending/torsion of the beam and higher order stress contributions. The

general goal is to directly include the coupling conditions and thus geometric dependencies preferably eliminating Lagrange multipliers. In a first step by utilizing the projections eq. (5.32) with eq. (5.33), we write $\delta\breve{\boldsymbol{\Sigma}} = \left(\breve{\mathbb{P}}_\alpha\,\delta\breve{\boldsymbol{\vartheta}} + \breve{\mathbb{Q}}_\alpha\,\delta\breve{\boldsymbol{\varpi}}\right) \otimes \breve{\boldsymbol{D}}_\alpha$, giving a two part representation of constraint eq. (5.53) as

$$\int_{\breve{\mathcal{C}}_0} \left\{ \left(\breve{\mathbb{P}}_\alpha^\top \left[\boldsymbol{F}_c\,\breve{\boldsymbol{D}}_\alpha - \breve{\boldsymbol{d}}_\alpha \right] \right) \cdot \delta\breve{\boldsymbol{\vartheta}} |\breve{E}| \right\} \mathrm{d}\breve{\theta}^3 = 0, \tag{5.54}$$

$$\int_{\breve{\mathcal{C}}_0} \left\{ \left(\breve{\mathbb{Q}}_\alpha^\top \left[\boldsymbol{F}_c\,\breve{\boldsymbol{D}}_\alpha - \breve{\boldsymbol{d}}_\alpha \right] \right) \cdot \delta\breve{\boldsymbol{\varpi}} |\breve{E}| \right\} \mathrm{d}\breve{\theta}^3 = 0, \tag{5.55}$$

effectively separating bending and torsion eq. (5.54) from dilatation and shear eq. (5.55). It is worth noting that $\breve{\mathbb{P}}_\alpha^\top \breve{\boldsymbol{d}}_\alpha = 0$ holds in eq. (5.54) due to the orthogonality of directors. Furthermore, the final condition turns out to be independent of the beam variables, constraining only the matrix stretches and shears, as will be demonstrated next.

5.4.1 Static condensation

To directly link matrix and beam position, we set $\delta\breve{\boldsymbol{\varphi}} = \delta\boldsymbol{\varphi}_c$ in eq. (5.47), enabling to combine with eq. (5.46) yielding

$$\begin{aligned} \int_{\Omega_0} \left\{ \boldsymbol{P} : \nabla_{\mathrm{X}} \delta\boldsymbol{\varphi} - \overline{\boldsymbol{B}} \cdot \delta\boldsymbol{\varphi} \right\} \mathrm{d}V - \int_{\partial\Omega_0^N} \left\{ \overline{\boldsymbol{T}} \cdot \delta\boldsymbol{\varphi} \right\} \mathrm{d}A \\ + \left[\breve{\boldsymbol{\mu}}_{\breve{E}} \cdot \delta\boldsymbol{\varphi}_{\breve{E}} |\breve{E}| \right]_0^L - \int_{\breve{\mathcal{C}}_0} \left\{ \left(\breve{\mathfrak{s}}' + \overline{\breve{\boldsymbol{s}}} \right) \cdot \delta\boldsymbol{\varphi}_c \right\} \mathrm{d}\breve{\theta}^3 + \int_{\breve{\mathcal{C}}_0} \left\{ \breve{\boldsymbol{\Sigma}} : \delta\boldsymbol{F}_c |\breve{E}| \right\} \mathrm{d}\breve{\theta}^3 = 0 \end{aligned} \tag{5.56}$$

and thus ultimately eliminating Lagrange multipliers $\breve{\boldsymbol{\eta}}$ for the interior, whereas endpoint constraints $\breve{\boldsymbol{\mu}}_{\breve{E}}$ remain. Further for resolving the second set of Lagrange multipliers $\breve{\boldsymbol{\Sigma}}$, the dependence of the rotation in terms of the cross-section alignment is employed. Therefore we take the constraint $\breve{\boldsymbol{\Sigma}} : \left(\delta\boldsymbol{F}_c - \left[\delta\breve{\boldsymbol{\phi}}\right]_\times \breve{\boldsymbol{R}} \right)$ of eq. (5.41), recall that $\breve{\boldsymbol{\Sigma}} : \left(\left[\delta\breve{\boldsymbol{\phi}}\right]_\times \breve{\boldsymbol{R}} \right) = 2\,\breve{\boldsymbol{\vartheta}} \cdot \delta\breve{\boldsymbol{\phi}}$ and insert the split eq. (5.32), note again the vanishing symmetric part of eq. (5.54), leaving

$$\begin{aligned} 0 &= \breve{\boldsymbol{\Sigma}} : \left(\delta\boldsymbol{F}_c - \delta\breve{\boldsymbol{R}} \right) \\ \Leftrightarrow \quad \breve{\boldsymbol{\Sigma}} : \delta\breve{\boldsymbol{R}} &= \breve{\boldsymbol{\Sigma}} : \delta\boldsymbol{F}_c \\ \Leftrightarrow \quad \breve{\boldsymbol{\Sigma}} : \left(\left[\delta\breve{\boldsymbol{\phi}}\right]_\times \breve{\boldsymbol{R}} \right) &= \breve{\boldsymbol{\Sigma}} : \delta\boldsymbol{F}_c \\ \Leftrightarrow \quad 2\,\breve{\boldsymbol{\vartheta}} \cdot \delta\breve{\boldsymbol{\phi}} &= \breve{\mathbb{P}}_\alpha\,\breve{\boldsymbol{\vartheta}} \otimes \breve{\boldsymbol{D}}_\alpha\,\delta\boldsymbol{F}_c \\ \Leftrightarrow \quad \delta\breve{\boldsymbol{\phi}} &= \frac{1}{2}\,\breve{\mathbb{P}}_\alpha^\top\,\delta\boldsymbol{F}_c\,\breve{\boldsymbol{D}}_\alpha. \end{aligned} \tag{5.57}$$

Insertion into eq. (5.48) along with eq. (5.105) yields

$$-\int_{\breve{\mathcal{C}}_0} \left\{ \left(\frac{1}{2}\,\breve{\mathbb{P}}_\alpha \left(\breve{\mathfrak{w}}' + \breve{\boldsymbol{\varphi}}' \times \breve{\mathfrak{s}} + \overline{\breve{\boldsymbol{w}}} \right) \otimes \breve{\boldsymbol{D}}_\alpha + \left(\breve{\boldsymbol{\Sigma}} - \breve{\mathbb{Q}}_\alpha \breve{\boldsymbol{\varpi}} \breve{\boldsymbol{D}}_\alpha \right) |\breve{E}| \right) : \delta\boldsymbol{F}_c \right\} \mathrm{d}\breve{\theta}^3 = 0. \tag{5.58}$$

Combining with eq. (5.56) we obtain for the balance equations of both matrix and beam

$$\int_{\Omega_0}\Big\{\boldsymbol{P} : \nabla_{\mathrm{X}}\delta\boldsymbol{\varphi} \;-\; \overline{\boldsymbol{B}}\cdot\delta\boldsymbol{\varphi}\Big\}\mathrm{d}V - \int_{\partial\Omega_0^N}\Big\{\overline{\boldsymbol{T}}\cdot\delta\boldsymbol{\varphi}\Big\}\mathrm{d}A + \Big[\!\Big[\breve{\boldsymbol{\mu}}_{\breve{E}}\cdot\delta\boldsymbol{\varphi}_{\breve{E}}\,|\breve{E}|\Big]\!\Big]_0^L$$
$$-\int_{\breve{\mathcal{C}}_0}\Big\{\Big(\frac{1}{2}\,\breve{\mathbb{P}}_\alpha\Big(\breve{\mathfrak{w}}\breve{\mathfrak{w}}' + \breve{\boldsymbol{\varphi}}'\times\breve{\mathfrak{s}} + \overline{\breve{\mathfrak{w}}}\Big)\otimes\breve{\boldsymbol{D}}_\alpha - \breve{\mathbb{Q}}_\alpha\overline{\breve{\boldsymbol{\varpi}}}\breve{\boldsymbol{D}}_\alpha|\breve{E}|\Big) : \delta\boldsymbol{F}_c + \Big(\breve{\mathfrak{s}}' + \overline{\breve{\mathfrak{s}}}\Big)\cdot\delta\boldsymbol{\varphi}_c\Big\}\,\mathrm{d}\breve{\theta}^3 = 0, \tag{5.59}$$

supplemented by coupling conditions

$$\int_{\breve{\mathcal{C}}_0}\Big\{\delta\breve{\boldsymbol{\eta}}\cdot(\boldsymbol{\varphi}_c - \breve{\boldsymbol{\varphi}})\,|\breve{C}|\Big\}\,\mathrm{d}\breve{\theta}^3 + \int_{\breve{\mathcal{C}}_0}\Big\{\breve{\mathbb{P}}_\alpha^\top\boldsymbol{F}_c\breve{\boldsymbol{D}}_\alpha\cdot\delta\breve{\boldsymbol{\vartheta}}|\breve{E}|\Big\}\,\mathrm{d}\breve{\theta}^3$$
$$+\int_{\breve{\mathcal{C}}_0}\Big\{\Big(\breve{\mathbb{Q}}_\alpha^\top\Big(\boldsymbol{F}_c - \breve{\boldsymbol{R}}\Big)\breve{\boldsymbol{D}}_\alpha\Big)\cdot\delta\overline{\breve{\boldsymbol{\varpi}}}|\breve{E}|\Big\}\,\mathrm{d}\breve{\theta}^3 = 0, \tag{5.60}$$

along the unchanged mixed constitutive parts

$$\int_{\breve{\mathcal{C}}_0}\{\delta\breve{\mathfrak{g}}\cdot(\breve{\mathfrak{s}} - \breve{\mathfrak{s}})\}\,\mathrm{d}\breve{\theta}^3 + \int_{\breve{\mathcal{C}}_0}\Big\{\delta\breve{\mathfrak{k}}\cdot(\breve{\boldsymbol{w}} - \breve{\mathfrak{w}})\Big\}\,\mathrm{d}\breve{\theta}^3 = 0, \tag{5.61}$$

with boundary conditions $\boldsymbol{\varphi} = \overline{\boldsymbol{\varphi}}$ and $\delta\boldsymbol{\varphi} = \boldsymbol{0}$ on $\partial\breve{\Omega}_0^D$, as well as beam endpoint conditions

$$[\breve{\boldsymbol{\varphi}} - \boldsymbol{\varphi}_{\breve{E}}]\!]_{\partial\breve{\Omega}_0^{\breve{E}}}\,|\breve{E}| = 0\,,\quad [\![\breve{\mathfrak{s}}]\!]_{\partial\breve{\Omega}_0^{\breve{E}}} = \overline{\breve{\mathfrak{s}}}_{\breve{E}} + \breve{\boldsymbol{\mu}}_{\breve{E}}|\breve{E}| \quad\text{and}\quad [\![\breve{\mathfrak{w}}]\!]_{\partial\breve{\Omega}_0^{\breve{E}}} = \overline{\breve{\mathfrak{w}}}_{\breve{E}}\,. \tag{5.62}$$

An alternative representation of the third coupling term in eq. (5.60) is given in section 5.A.2.

5.4.2 Constraint projection to the centerline

We employ a projection of the 3D-1D coupling to the beam centerline that is consistent with the regularity of the solid field. In particular, for a displacement $\boldsymbol{\varphi}\in\mathcal{H}^1(\Omega_0)^3$ the point-wise trace on the centerline $\breve{\Omega}_0\subset\Omega_0$, i.e. a codimension-two set, is not available in general causing a direct restriction $[\boldsymbol{\varphi}]\!]_{\breve{\mathcal{C}}_0}$ to be ill-defined. To circumvent this difficulty, we previously introduced cross-sectional circular mean operators $\boldsymbol{\varphi}_c$ and $\boldsymbol{F}_c$, cf. eq. (5.35) - eq. (5.34), as admissible $\mathrm{L}^2(\breve{\Omega}_0)$ line fields, relying on well-posed surface traces followed by averaging.

However, in the following, we assume Galerkin $\mathrm{C}^\epsilon, \epsilon > 1$ conforming approximations, leading to higher regularity of $\boldsymbol{\varphi}$, see section 5.5.1. Hence we are able to express line restrictions $[\boldsymbol{\varphi}]\!]_{\breve{\mathcal{C}}_0}\in\mathrm{L}^2(\breve{\Omega}_0)$ and $[\nabla_{\mathrm{X}}\boldsymbol{\varphi}]\!]_{\breve{\mathcal{C}}_0} = [\boldsymbol{F}]\!]_{\breve{\mathcal{C}}_0}\in\mathrm{L}^2(\breve{\Omega}_0)$ in terms of a Fourier representation of $\boldsymbol{\varphi}$.

With coordinates $\boldsymbol{y} = \breve{\boldsymbol{N}}(\breve{\beta})\breve{r} \in \mathbb{R}^2$ in polar form for the circular cross-section plane, that contains $\breve{C}(\breve{\theta}^3)$ and originates on the centerline, we write using Fourier variable $\boldsymbol{\omega}$ now

$$\begin{aligned}\Big[\boldsymbol{\varphi}\Big(\breve{\theta}^3,\breve{\beta}\Big)\Big]\Big\|_{\breve{C}(\breve{\theta}^3)} &= \int\limits_{\mathbb{R}^2}\Big\{\hat{\boldsymbol{\varphi}}(\breve{\theta}^3,\boldsymbol{\omega})\, e^{\,\mathrm{i}\,\boldsymbol{y}}\Big\}\,\mathrm{d}\boldsymbol{\omega}\\ &= \int\limits_{\mathbb{R}^2}\Big\{\hat{\boldsymbol{\varphi}}(\breve{\theta}^3,\boldsymbol{\omega})\, e^{\,\mathrm{i}\,\breve{\boldsymbol{N}}(\breve{\beta})\breve{r}}\Big\}\,\mathrm{d}\boldsymbol{\omega}\,,\end{aligned} \tag{5.63}$$

where again $\breve{\boldsymbol{N}}(\breve{\beta}) = \breve{\boldsymbol{D}}_1\cos\Big(\breve{\beta}\Big) + \breve{\boldsymbol{D}}_2\sin\Big(\breve{\beta}\Big)$ (see also in context of eq. (5.30)). Averaging according to eq. (5.35) yields

$$\boldsymbol{\varphi}_c = \frac{1}{|\breve{C}|}\int\limits_{\breve{C}(\breve{\theta}^3)}\Big\{\boldsymbol{\varphi}\Big(\breve{\theta}^3,\breve{\beta}\Big)\Big\}\,\mathrm{d}\breve{C} = \int\limits_{\mathbb{R}^2}\Bigg\{\hat{\boldsymbol{\varphi}}(\breve{\theta}^3,\boldsymbol{\omega})\,\frac{1}{|\breve{C}|}\int_{\breve{C}(\breve{\theta}^3)}\Big\{e^{\,\mathrm{i}\,\breve{\boldsymbol{N}}(\breve{\beta})\breve{r}}\Big\}\,\mathrm{d}\breve{C}\Bigg\}\,\mathrm{d}\boldsymbol{\omega} \tag{5.64}$$

Then we conduct a power-series (*Taylor expansion*) for the kernel

$$e^{\,\mathrm{i}\,\breve{\boldsymbol{N}}(\breve{\beta})\breve{r}} = \sum_{k=0}^{\infty}\frac{\Big(\mathrm{i}\,\boldsymbol{\omega}\cdot\breve{\boldsymbol{N}}(\breve{\beta})\,\breve{r}\Big)^k}{k!}\,. \tag{5.65}$$

Insertion lets all terms with odd k vanish due to $\int_{\breve{C}(\breve{\theta}^3)}\Big\{\breve{\boldsymbol{N}}\Big\}\,\mathrm{d}\breve{C} = \boldsymbol{0}$ (see section 5.A.3). Thus leaving parts for $k = 0$, consolidating all remaining parts for even $k \geq 2$ and transforming back eventually leads to

$$\boldsymbol{\varphi}_c = [\boldsymbol{\varphi}]\|_{\breve{\mathcal{C}}_0} + \mathcal{O}\Big(\breve{r}^2\Big)\,. \tag{5.66}$$

Applying the same Fourier representation and subsequently inserting the Taylor series for the circular mean deformation gradient eq. (5.34), we finally obtain

$$\begin{aligned}\boldsymbol{F}_c &= \frac{1}{|\breve{E}|}\int\limits_{\breve{C}(\breve{\theta}^3)}\Bigg\{\Bigg(\int_{\mathbb{R}^2}\Big\{\hat{\boldsymbol{\varphi}}(\breve{\theta}^3,\boldsymbol{\omega})\,\Big(\mathrm{i}\,\breve{\boldsymbol{N}}(\breve{\beta})\breve{r}\Big)\Big\}\,\mathrm{d}\boldsymbol{\omega}\Bigg)\otimes\breve{\boldsymbol{N}}\Bigg\}\,\mathrm{d}\breve{C}\\ &= \frac{1}{|\breve{E}|}\Bigg(\breve{r}\int\limits_{\mathbb{R}^2}\Big\{\hat{\boldsymbol{\varphi}}(\boldsymbol{\omega},\breve{\theta}^3)\otimes(\mathrm{i}\,\boldsymbol{\omega})\Big\}\,\mathrm{d}\boldsymbol{\omega}\int\limits_{\breve{C}(\breve{\theta}^3)}\Big\{\breve{\boldsymbol{N}}\otimes\breve{\boldsymbol{N}}\Big\}\,\mathrm{d}\breve{C} + \mathcal{O}\Big(\breve{r}^0\Big)\Bigg)\\ &= \frac{1}{|\breve{E}|}\pi\,\breve{r}^2\,[\nabla_{\mathrm{X}}\boldsymbol{\varphi}]\|_{\breve{\mathcal{C}}_0}\,\breve{\boldsymbol{D}}_\alpha\otimes\breve{\boldsymbol{D}}_\alpha + \mathcal{O}\Big(\breve{r}^2\Big)\\ &= [\nabla_{\mathrm{X}}\boldsymbol{\varphi}]\|_{\breve{\mathcal{C}}_0}\,\breve{\boldsymbol{D}}_\alpha\otimes\breve{\boldsymbol{D}}_\alpha + \mathcal{O}\Big(\breve{r}^2\Big)\\ &= [\boldsymbol{F}]\|_{\breve{\mathcal{C}}_0}\,\breve{\boldsymbol{D}}_\alpha\otimes\breve{\boldsymbol{D}}_\alpha + \mathcal{O}\Big(\breve{r}^2\Big)\,.\end{aligned} \tag{5.67}$$

Therein, the additional $\otimes\breve{\boldsymbol{N}}$ now lets even terms vanish, such that $k = 1$ remains and all other terms $k \geq 3$ are consolidated (see again section 5.A.3).

5.4.3 Second gradient model

The $\mathcal{O}(\check{r}^2)$-terms in eq. (5.66) - eq. (5.67) induce $\mathcal{O}(\check{r}^3)$- and $\mathcal{O}(\check{r}^4)$-contributions in eq. (5.40). For a sufficiently thin beam, these are presumed comparable to the discretization error and are therefore neglected. Thus, we state $\boldsymbol{\varphi}_c \approx [\![\boldsymbol{\varphi}]\!]_{\check{\mathcal{C}}_0}$ and $\check{\boldsymbol{\Sigma}} : \boldsymbol{F}_c \approx \check{\boldsymbol{\Sigma}} : [\![\boldsymbol{F}]\!]_{\check{\mathcal{C}}_0}$, using $\check{\boldsymbol{\Sigma}}\check{\boldsymbol{D}}_\alpha \otimes \check{\boldsymbol{D}}_\alpha = \check{\boldsymbol{\Sigma}}$. Since the $\check{\boldsymbol{D}}_3$-component of the gradient does not appear in the constraints, in what follows $\boldsymbol{\varphi}_c$ and $\boldsymbol{F}_c$ are directly replaced in the system eq. (5.59) - eq. (5.61). This substitution yields a second-gradient material model, as will be shown next.

Assuming necessary regularity, we can integrate by parts on the centerline $\check{\mathcal{C}}_0$ and eventually write the system for the matrix deformation field

$$\begin{aligned}\int_{\Omega_0}\Big\{\boldsymbol{P} : \nabla_{\mathrm{X}}\delta\boldsymbol{\varphi} \;-\; \overline{\boldsymbol{B}}\cdot\delta\boldsymbol{\varphi}\Big\}\mathrm{d}V - \int_{\partial\Omega_0^N}\Big\{\overline{\boldsymbol{T}}\cdot\delta\boldsymbol{\varphi}\Big\}\mathrm{d}A \\ + \int_{\check{\mathcal{C}}_0}\Big\{\check{\boldsymbol{\mathfrak{P}}} \vdots \nabla_{\mathrm{X}}^2\delta\boldsymbol{\varphi} + \Big(\check{\boldsymbol{P}}^{\check{\mathfrak{s}}} + \check{\boldsymbol{P}}^{\check{\mathfrak{w}}} + \check{\mathbb{Q}}_\alpha\overline{\check{\boldsymbol{\varpi}}}\check{\boldsymbol{D}}_\alpha\,|\check{E}|\Big) : \nabla_{\mathrm{X}}\delta\boldsymbol{\varphi} - \overline{\check{\boldsymbol{s}}}\cdot\delta\boldsymbol{\varphi}\Big\}\,\mathrm{d}\check{\theta}^3 \\ - \Big[\!\Big[\overline{\check{\boldsymbol{s}}}_{\check{E}}\cdot\delta\boldsymbol{\varphi} + \frac{1}{2}\Big(\check{\mathbb{P}}_\alpha\,\overline{\check{\boldsymbol{w}}}_{\check{E}}\otimes\check{\boldsymbol{D}}_\alpha\Big) : \nabla_{\mathrm{X}}\delta\boldsymbol{\varphi}\Big]\!\Big]_0^L = 0, \quad (5.68)\end{aligned}$$

unchanged constitutive mixed terms

$$\int_{\check{\mathcal{C}}_0}\{\delta\check{\mathfrak{g}}\cdot(\check{\boldsymbol{s}}-\check{\mathfrak{s}})\}\,\mathrm{d}\check{\theta}^3 + \int_{\check{\mathcal{C}}_0}\Big\{\delta\check{\mathfrak{k}}\cdot(\check{\boldsymbol{w}}-\check{\mathfrak{w}})\Big\}\,\mathrm{d}\check{\theta}^3 = 0 \quad (5.69)$$

and remaining coupling conditions

$$\begin{aligned}\int_{\check{\mathcal{C}}_0}\Big\{\delta\check{\boldsymbol{\eta}}\cdot(\boldsymbol{\varphi}-\check{\boldsymbol{\varphi}})\,|\check{C}|\Big\}\,\mathrm{d}\check{\theta}^3 + \int_{\check{\mathcal{C}}_0}\Big\{\check{\mathbb{P}}_\alpha^\top\boldsymbol{F}\,\check{\boldsymbol{D}}_\alpha\cdot\delta\check{\boldsymbol{\vartheta}}\,|\check{E}|\Big\}\,\mathrm{d}\check{\theta}^3 \\ + \int_{\check{\mathcal{C}}_0}\Big\{\Big(\check{\mathbb{Q}}_\alpha^\top\Big(\boldsymbol{F}-\check{\boldsymbol{R}}\Big)\check{\boldsymbol{D}}_\alpha\Big)\cdot\delta\overline{\check{\boldsymbol{\varpi}}}|\check{E}|\Big\}\,\mathrm{d}\check{\theta}^3 = 0, \quad (5.70)\end{aligned}$$

with boundary conditions $\boldsymbol{\varphi} = \overline{\boldsymbol{\varphi}}$ and $\delta\boldsymbol{\varphi} = \boldsymbol{0}$ on $\partial\check{\Omega}_0^D$. Therein we made use of corresponding stresses related to beam contributions

$$\check{\boldsymbol{P}}^{\check{\mathfrak{s}}} := \check{\mathfrak{s}}\otimes\check{\boldsymbol{D}}_3, \quad (5.71)$$

$$\check{\boldsymbol{P}}^{\check{\mathfrak{w}}} := \frac{1}{2}\Big(\check{\mathbb{P}}'_\alpha\,\check{\mathfrak{w}} - \check{\mathbb{P}}_\alpha\Big(\check{\boldsymbol{\varphi}}'\times\check{\mathfrak{s}} + \overline{\check{\boldsymbol{w}}}\Big)\Big)\otimes\check{\boldsymbol{D}}_\alpha, \quad (5.72)$$

$$\check{\boldsymbol{\mathfrak{P}}} := \frac{1}{2}\,\check{\mathbb{P}}_\alpha\,\check{\mathfrak{w}}\otimes\check{\boldsymbol{D}}_\alpha\otimes\check{\boldsymbol{D}}_3\,. \quad (5.73)$$

After integration by parts, the end-face terms vanish due to the centerline projection, whereas the beam endpoint constraints $[\![\check{\boldsymbol{\varphi}}-\boldsymbol{\varphi}_{\check{E}}]\!]_{\partial\check{\Omega}_0^{\check{E}}}\,|\check{E}| = 0$ (where $|\check{E}| = 0$ if the face is not embedded), $[\![\check{\mathfrak{s}}]\!]_{\partial\check{\Omega}_0^{\check{E}}} = \overline{\check{\boldsymbol{s}}}_{\check{E}} + \check{\boldsymbol{\mu}}_{\check{E}}|\check{E}|$ and $[\![\check{\mathfrak{w}}]\!]_{\partial\check{\Omega}_0^{\check{E}}} = \overline{\check{\boldsymbol{w}}}_{\check{E}}$ remain.

We point out $\breve{\mathbb{P}}'_\alpha = [\boldsymbol{\kappa}]_\times \breve{\mathbb{P}}_\alpha - \breve{\mathbb{P}}_\alpha [\boldsymbol{\kappa}]_\times$ with $\boldsymbol{\kappa} = \operatorname{axl}(\breve{\boldsymbol{R}}' \breve{\boldsymbol{R}}^\top)$, as obtained by direct differentiation of eq. (5.33). Furthermore, the identity

$$\breve{\mathbb{P}}_\alpha^\top \boldsymbol{F}\, \breve{\boldsymbol{D}}_\alpha = \left[\breve{\boldsymbol{D}}_2 \breve{\boldsymbol{R}}^\top \boldsymbol{F} \breve{\boldsymbol{D}}_1 - \breve{\boldsymbol{D}}_1 \breve{\boldsymbol{R}}^\top \boldsymbol{F} \breve{\boldsymbol{D}}_2\right] \breve{\boldsymbol{d}}_3 - 2\left[\breve{\boldsymbol{D}}_3 \breve{\boldsymbol{R}}^\top \boldsymbol{F} \breve{\boldsymbol{D}}_1\right] \breve{\boldsymbol{d}}_2 + 2\left[\breve{\boldsymbol{D}}_3 \breve{\boldsymbol{R}}^\top \boldsymbol{F} \breve{\boldsymbol{D}}_2\right] \breve{\boldsymbol{d}}_1. \tag{5.74}$$

shows that the constraints related to $\delta\breve{\boldsymbol{\vartheta}}$ correspond to a planar version of the spherical rotational constraint $\operatorname{axl}\left(\breve{\boldsymbol{R}}^\top \boldsymbol{F}\right) = 0$ introduced in Simo et al. [107]. Finally, eq. (5.68) provides an explicit expression for the third-order stress tensor defined in eq. (3.21). This tensor results from condensing the beam moment equation and depends directly on the resultant torque $\breve{\mathfrak{w}}$ (see eq. (5.14)), expressed through the second and polar areal moments. It acts along the fiber centerline $\breve{\mathcal{C}}_0$, typically at the microscale for short fiber-reinforced polymers. For macroscopic gradient formulations, appropriate homogenization techniques are required. Note that additional terms arise if the beam has an initial curvature $\breve{\boldsymbol{D}}'_\alpha \neq 0$.

5.5 Discrete multidimensional coupling model

For the above given framework for beams embedded in a matrix, we approximate the contained fields to derive a discrete system satisfying regularity prerequisites and subsequently show a reduction scheme to decrease computational effort.

5.5.1 Spatial approximation

Concerning the spatial approximation, the isogeometric discretization scheme established in chapter 2 is employed for matrix, beam and the remaining coupling conditions.

Matrix

For matrix contributions we employ a standard approach for the deformation field $\boldsymbol{\varphi}$ and its variation $\delta\boldsymbol{\varphi}$ as introduced in section 3.5 of the form

$$\boldsymbol{\varphi}^{\mathrm{h}} = \sum_{A \in \Lambda_{\mathrm{I}}} \boldsymbol{\varphi}_A \mathcal{R}^A \quad \text{and} \quad \delta\boldsymbol{\varphi}^{\mathrm{h}} = \sum_{A \in \Lambda_{\mathrm{I}}} \delta\boldsymbol{\varphi}_A \mathcal{R}^A, \tag{5.75}$$

using three-dimensional (NURBS-)basis $\mathcal{R}^A : \Omega_0^{\mathrm{h}} \to \mathbb{R}$ of order $\boldsymbol{p}_{\mathrm{I}}$, where $\boldsymbol{\varphi}_A, \delta\boldsymbol{\varphi}_A \in \mathbb{R}^3$ and with index-space $\Lambda_{\mathrm{I}} \coloneqq \{1, \ldots, \mathfrak{O}_{\mathrm{I}}\}$ for the number of control-points $\mathfrak{O}_{\mathrm{I}}$. Due to the regularity demand arising in the centerline projection, we require $\boldsymbol{\varphi}^{\mathrm{h}}, \delta\boldsymbol{\varphi}^{\mathrm{h}} \in \mathcal{H}^{>2}\left(\Omega_0^{\mathrm{h}}\right)$, hence set $p_{\boldsymbol{\varphi}} \geq 3 \;\forall\; p_{\boldsymbol{\varphi}} \in \boldsymbol{p}_{\mathrm{I}}$.

Beam

Beam associated fields are approximated using a one-dimensional (NUR)BS-basis. For the centerline position appearing in the constraints and quaternions $\breve{\mathbf{q}}$ for the parametrization of $\breve{\boldsymbol{R}}$ as in eq. (5.11) we set

$$\breve{\boldsymbol{\varphi}}^{\mathrm{h}} = \sum_{a \in \Lambda_{\breve{\mathrm{I}}}} \breve{\boldsymbol{\varphi}}_a \, \breve{\mathcal{R}}^a \quad \text{and} \quad \breve{\mathbf{q}}^{\mathrm{h}} = \sum_{a \in \Lambda_{\breve{\mathrm{I}}}} \breve{\mathbf{q}}_a \, \breve{\mathcal{R}}^a \,, \tag{5.76}$$

where $\breve{\mathcal{R}}^a : \breve{\mathcal{C}}_0^{\mathrm{h}} \to \mathbb{R}$ of order $p_{\breve{\mathrm{I}}} = \min(\boldsymbol{p}_{\mathrm{I}})$ and index-space $\Lambda_{\breve{\mathrm{I}}} \coloneqq \{1, \ldots, \mathfrak{O}_{\breve{\mathrm{I}}}\}$. For the augmented/mixed stresses we set

$$\breve{\mathfrak{s}}^{\mathrm{h}} = \sum_{a \in \Lambda_{\breve{\mathrm{II}}}} \breve{\mathfrak{s}}_a \, \breve{\mathcal{M}}^a \quad \text{and} \quad \breve{\mathfrak{w}}^{\mathrm{h}} = \sum_{a \in \Lambda_{\breve{\mathrm{II}}}} \breve{\mathfrak{w}}_a \, \breve{\mathcal{M}}^a \tag{5.77}$$

using $\breve{\mathcal{M}}^a : \breve{\mathcal{C}}_0^{\mathrm{h}} \to \mathbb{R}$ with order $p_{\breve{\mathrm{II}}} \leq p_{\breve{\mathrm{I}}}$ for robustness (cf. section 3.6.1) and index-space $\Lambda_{\breve{\mathrm{II}}}$. We further employ the classical Bubnov-Galerkin approach for augmented deformation tensors ($\delta\breve{\mathfrak{g}} \sim \delta\breve{\mathfrak{s}}$, $\delta\breve{\mathfrak{k}} \sim \delta\breve{\mathfrak{w}}$) yielding

$$\delta\breve{\mathfrak{g}}^{\mathrm{h}} = \sum_{a \in \Lambda_{\breve{\mathrm{II}}}} \delta\breve{\mathfrak{g}}_a \, \breve{\mathcal{M}}^a \quad \text{and} \quad \delta\breve{\mathfrak{k}}^{\mathrm{h}} = \sum_{a \in \Lambda_{\breve{\mathrm{II}}}} \delta\breve{\mathfrak{k}}_a \, \breve{\mathcal{M}}^a \,. \tag{5.78}$$

Remark 5.5.1 – Mixed mode and approximation order. Due to the chosen high approximation order $p_{\breve{\mathrm{I}}} \geq 3$, locking phenomena as described in Weeger et al. [119], are generally negligible such that the Hu-Washizu approach section 5.2.2 may be avoided altogether.

Coupling conditions

We discretize the remaining variations of Lagrange multipliers using $\breve{\mathcal{N}}^a : \breve{\mathcal{C}}_0^{\mathrm{h}} \to \mathbb{R}$ with order $p_{\breve{\mathrm{III}}} \leq p_{\breve{\mathrm{I}}}$ and associated index-space $\Lambda_{\breve{\mathrm{III}}}$ as

$$\delta\breve{\boldsymbol{\eta}}^{\mathrm{h}} = \sum_{a \in \Lambda_{\breve{\mathrm{III}}}} \delta\breve{\boldsymbol{\eta}}_a \, \breve{\mathcal{N}}^a \quad \text{and} \quad \delta\breve{\boldsymbol{\vartheta}}^{\mathrm{h}} = \sum_{a \in \Lambda_{\breve{\mathrm{III}}}} \delta\breve{\boldsymbol{\vartheta}}_a \, \breve{\mathcal{N}}^a \,, \tag{5.79}$$

whose counterparts $\breve{\boldsymbol{\eta}}$ and $\breve{\boldsymbol{\vartheta}}$ are already condensed.

Remark 5.5.2 – Variational condensation. With condensation we can relate $\delta\breve{\boldsymbol{\varphi}}$ to coupling of matrix position with $\breve{\boldsymbol{\eta}}$ and rotation $\delta\breve{\mathbf{q}}$ to $\breve{\boldsymbol{\vartheta}}$ and the quaternion unity constraint thus resulting in a Petrov-Galerkin like method.

Next, we introduce suitable approximations for the coupling force and its variation

$$\breve{\boldsymbol{\varpi}}^{\mathrm{h}} = \sum_{a \in \Lambda_{\breve{\mathrm{IV}}}} \breve{\boldsymbol{\varpi}}_a \, \breve{\mathcal{W}}^a \quad \text{and} \quad \delta\breve{\boldsymbol{\varpi}}^{\mathrm{h}} = \sum_{a \in \Lambda_{\breve{\mathrm{IV}}}} \delta\breve{\boldsymbol{\varpi}}_a \, \breve{\mathcal{W}}^a \,, \tag{5.80}$$

employing $\breve{\mathcal{W}}^a : \breve{\mathcal{C}}_0^{\mathrm{h}} \to \mathbb{R}$ with order $p_{\breve{\mathrm{IV}}} \leq p_{\breve{\mathrm{I}}}$ and associated index-space $\Lambda_{\breve{\mathrm{IV}}}$.

5.5.2 Discrete system

The discretized system as proposed in eq. (5.68) consequently reads

$$\begin{aligned}\boldsymbol{R}_{\boldsymbol{\varphi}} \coloneqq & \int_{\Omega_0^{\mathrm{h}}} \left\{ \boldsymbol{P}^{\mathrm{h}} \cdot \nabla_{\mathrm{X}} \mathcal{R}^A - \mathcal{R}^A \, \overline{\boldsymbol{B}}^{\mathrm{h}} \right\} \mathrm{d}V - \int_{\partial\Omega_0^{\mathrm{h}}} \left\{ \mathcal{R}^A \, \overline{\boldsymbol{T}}^{\mathrm{h}} \right\} \mathrm{d}A \\ & + \int_{\breve{\mathcal{C}}_0^{\mathrm{h}}} \left\{ \breve{\boldsymbol{\mathfrak{P}}}^{\mathrm{h}} : \nabla_{\mathrm{X}}^2 \mathcal{R}^A + \left(\breve{\boldsymbol{P}}^{\breve{\mathfrak{s}},\mathrm{h}} + \breve{\boldsymbol{P}}^{\breve{\mathfrak{w}},\mathrm{h}} + \breve{\mathbb{Q}}_\alpha^{\mathrm{h}} \breve{\boldsymbol{\varpi}}^{\mathrm{h}} \breve{\boldsymbol{D}}_\alpha \, |\breve{E}| \right) \cdot \nabla_{\mathrm{X}} \mathcal{R}^A - \mathcal{R}^A \, \overline{\breve{\boldsymbol{s}}}^{\mathrm{h}} \right\} \mathrm{d}\breve{\theta}^3 \\ & - \left[\!\!\left[\mathcal{R}^A \, \overline{\breve{\boldsymbol{s}}}_{\breve{E}}^{\mathrm{h}} + \frac{1}{2} \left(\breve{\mathbb{P}}_\alpha^{\mathrm{h}} \, \overline{\breve{\boldsymbol{w}}}_{\breve{E}}^{\mathrm{h}} \otimes \breve{\boldsymbol{D}}_\alpha \right) \cdot \nabla_{\mathrm{X}} \mathcal{R}^A \right]\!\!\right]_0^L = \boldsymbol{0}, \end{aligned} \tag{5.81}$$

constitutive mixed terms

$$\boldsymbol{R}_{\breve{\mathfrak{s}}} \coloneqq \int_{\breve{\mathcal{C}}_0^{\mathrm{h}}} \left\{ \breve{\mathcal{M}}^a \left(\breve{\boldsymbol{s}}^{\mathrm{h}} - \breve{\boldsymbol{\mathfrak{s}}}^{\mathrm{h}} \right) \right\} \mathrm{d}\breve{\theta}^3 = \boldsymbol{0} \,, \tag{5.82}$$

$$\boldsymbol{R}_{\breve{\mathfrak{t}}} \coloneqq \int_{\breve{\mathcal{C}}_0^{\mathrm{h}}} \left\{ \breve{\mathcal{M}}^a \left(\breve{\boldsymbol{w}}^{\mathrm{h}} - \breve{\mathfrak{w}}^{\mathrm{h}} \right) \right\} \mathrm{d}\breve{\theta}^3 = \boldsymbol{0} \tag{5.83}$$

and remaining coupling conditions

$$\boldsymbol{R}_{\breve{\eta}} \coloneqq \int_{\breve{\mathcal{C}}_0^{\mathrm{h}}} \left\{ \breve{\mathcal{N}}^a \left(\boldsymbol{\varphi}^{\mathrm{h}} - \breve{\boldsymbol{\varphi}}^{\mathrm{h}} \right) |\breve{C}| \right\} \mathrm{d}\breve{\theta}^3 = \boldsymbol{0} \tag{5.84}$$

$$\boldsymbol{R}_{\breve{\vartheta}} \coloneqq \int_{\breve{\mathcal{C}}_0^{\mathrm{h}}} \left\{ \breve{\mathcal{N}}^a \, \breve{\mathbb{P}}_\alpha^{\top,\mathrm{h}} \boldsymbol{F}^{\mathrm{h}} \, \breve{\boldsymbol{D}}_\alpha \, |\breve{E}| \right\} \mathrm{d}\breve{\theta}^3 = \boldsymbol{0} \tag{5.85}$$

$$\boldsymbol{R}_{\breve{\boldsymbol{\varpi}}} \coloneqq \int_{\breve{\mathcal{C}}_0^{\mathrm{h}}} \left\{ \breve{\mathcal{W}}^a \, \breve{\mathbb{Q}}_\alpha^{\top,\mathrm{h}} \left(\boldsymbol{F}^{\mathrm{h}} - \breve{\boldsymbol{R}}^{\mathrm{h}} \right) \breve{\boldsymbol{D}}_\alpha \, |\breve{E}| \right\} \mathrm{d}\breve{\theta}^3 = \boldsymbol{0} \,, \tag{5.86}$$

where for the last line eq. (5.101) was applied.

The use of quaternions gives rise to an additional balance equation as unity constraint $R_{\breve{\mathfrak{q}}} \coloneqq \breve{\mathfrak{q}} \cdot \breve{\mathfrak{q}} - 1 = 0$, eventually preserving orthogonality of the director triad. Using a scalar multiplier and assuming fulfillment within convergence, thus neglecting contributions entering through $\delta\breve{\mathfrak{q}}$, in a weak sense we require

$$\boldsymbol{R}_{\breve{\mathfrak{q}}} \coloneqq \int_{\breve{\mathcal{C}}_0^{\mathrm{h}}} \left\{ \breve{\mathcal{R}}^a \left(\breve{\mathfrak{q}}^{\mathrm{h}} \cdot \breve{\mathfrak{q}}^{\mathrm{h}} - 1 \right) \right\} \mathrm{d}\breve{\theta}^3 = 0 \tag{5.87}$$

using $\breve{\mathcal{R}}^a : \breve{\Omega}_0^{\mathrm{h}} \to \mathbb{R}$. Alternatively, we can apply a point-wise strong condition at the control points acting like a Dirac delta distribution (cf. remark 2.2.1, see also Wasmer and Betsch [118])

$$\boldsymbol{R}_{\breve{\mathfrak{q}}} \coloneqq \breve{\mathfrak{q}}_a \cdot \breve{\mathfrak{q}}_a - 1 = 0 \,. \tag{5.88}$$

Within the Newton-Raphson iteration (cf. section 3.5.2), we have to solve at every step

$$\underbrace{\begin{bmatrix} \boldsymbol{K}_{\boldsymbol{\varphi}\boldsymbol{\varphi}} & \boldsymbol{K}_{\boldsymbol{\varphi}\breve{\boldsymbol{\varphi}}} & \boldsymbol{K}_{\boldsymbol{\varphi}\breve{\mathbf{q}}} & \boldsymbol{K}_{\boldsymbol{\varphi}\breve{\boldsymbol{s}}} & \boldsymbol{K}_{\boldsymbol{\varphi}\breve{\boldsymbol{w}}} & \boldsymbol{K}_{\boldsymbol{\varphi}\breve{\boldsymbol{\varpi}}} \\ 0 & \boldsymbol{K}_{\breve{\mathfrak{g}}\breve{\boldsymbol{\varphi}}} & 0 & \boldsymbol{K}_{\breve{\mathfrak{g}}\breve{\boldsymbol{s}}} & 0 & 0 \\ 0 & 0 & \boldsymbol{K}_{\breve{\mathfrak{k}}\breve{\mathbf{q}}} & 0 & \boldsymbol{K}_{\breve{\mathfrak{k}}\breve{\boldsymbol{w}}} & 0 \\ \boldsymbol{K}_{\breve{\boldsymbol{\eta}}\boldsymbol{\varphi}} & \boldsymbol{K}_{\breve{\boldsymbol{\eta}}\breve{\boldsymbol{\varphi}}} & 0 & 0 & 0 & 0 \\ \boldsymbol{K}_{\breve{\boldsymbol{\vartheta}}\boldsymbol{\varphi}} & 0 & \boldsymbol{K}_{\breve{\boldsymbol{\vartheta}}\breve{\mathbf{q}}} & 0 & 0 & 0 \\ 0 & 0 & \boldsymbol{K}_{\breve{\mathbf{q}}\breve{\mathbf{q}}} & 0 & 0 & 0 \\ \boldsymbol{K}_{\breve{\boldsymbol{\varpi}}\boldsymbol{\varphi}} & 0 & \boldsymbol{K}_{\breve{\boldsymbol{\varpi}}\breve{\mathbf{q}}} & 0 & 0 & 0 \end{bmatrix}}_{:=\boldsymbol{K}} \underbrace{\begin{bmatrix} \Delta\boldsymbol{\varphi} \\ \Delta\breve{\boldsymbol{\varphi}} \\ \Delta\breve{\mathbf{q}} \\ \Delta\breve{\boldsymbol{s}} \\ \Delta\breve{\boldsymbol{w}} \\ \Delta\breve{\boldsymbol{\varpi}} \end{bmatrix}}_{:=\Delta\boldsymbol{q}} = - \underbrace{\begin{bmatrix} \boldsymbol{R}_{\boldsymbol{\varphi}} \\ \boldsymbol{R}_{\breve{\mathfrak{g}}} \\ \boldsymbol{R}_{\breve{\mathfrak{k}}} \\ \boldsymbol{R}_{\breve{\boldsymbol{\eta}}} \\ \boldsymbol{R}_{\breve{\boldsymbol{\vartheta}}} \\ \boldsymbol{R}_{\breve{\mathbf{q}}} \\ \boldsymbol{R}_{\breve{\boldsymbol{\varpi}}} \end{bmatrix}}_{:=\boldsymbol{R}}, \tag{5.89}$$

which is a non-symmetric linear system that owing to the Petrov-Galerkin approach does not necessarily produce a square matrix $\boldsymbol{K}$, which is investigated in remark 5.5.3.

Remark 5.5.3 – Deterministic system and consistent linearization. Regarding all beam contributions, we can determine the size of the linear equation system. Taking the total degrees of freedom for the five sets of fields $\breve{i} \in (\breve{\boldsymbol{\varphi}}, \breve{\mathbf{q}}, \breve{\boldsymbol{s}}, \breve{\boldsymbol{w}}, \breve{\boldsymbol{\varpi}})$ we have

$$\begin{aligned} n_{\breve{q}} &= \sum d_{\breve{i}} \mathfrak{O}_{\breve{i}} \\ &= 3\mathfrak{O}_{\breve{\mathrm{I}}} + 4\mathfrak{O}_{\breve{\mathrm{I}}} + 3\mathfrak{O}_{\breve{\mathrm{II}}} + 3\mathfrak{O}_{\breve{\mathrm{II}}} + 3\mathfrak{O}_{\breve{\mathrm{IV}}} \\ &= 6\mathfrak{O}_{\breve{\mathrm{II}}} + 3\mathfrak{O}_{\breve{\mathrm{IV}}} + 7\mathfrak{O}_{\breve{\mathrm{I}}} \end{aligned} \tag{5.90}$$

and for the variational sets $\breve{j} \in \left(\boldsymbol{\varphi}, \breve{\mathfrak{g}}, \breve{\mathfrak{k}}, \breve{\boldsymbol{\eta}}, \breve{\boldsymbol{\vartheta}}, \breve{\mathbf{q}}, \breve{\boldsymbol{\varpi}}\right)$ of residual equations

$$\begin{aligned} n_{\breve{R}} &= \sum d_{\breve{j}} \mathfrak{O}_{\breve{j}} \\ &= 3\mathfrak{O}_{\breve{\mathrm{II}}} + 3\mathfrak{O}_{\breve{\mathrm{II}}} + 3\mathfrak{O}_{\breve{\mathrm{III}}} + 3\mathfrak{O}_{\breve{\mathrm{III}}} + 1\mathfrak{O}_{\breve{\mathrm{I}}} + 3\mathfrak{O}_{\breve{\mathrm{IV}}} \\ &= 6\mathfrak{O}_{\breve{\mathrm{II}}} + 3\mathfrak{O}_{\breve{\mathrm{IV}}} + 1\mathfrak{O}_{\breve{\mathrm{I}}} + 6\mathfrak{O}_{\breve{\mathrm{III}}}\,, \end{aligned} \tag{5.91}$$

with respective control point size $d_{\breve{i}}$ and $d_{\breve{j}}$. To create a square solvable and deterministic system we then have to account for asymmetries originating in $\mathfrak{O}_{\breve{\mathrm{III}}} < \mathfrak{O}_{\breve{\mathrm{I}}}$ by explicitly setting beam endpoint constraints eq. (5.49) targeting the $3\left(\mathfrak{O}_{\breve{\mathrm{I}}} - \mathfrak{O}_{\breve{\mathrm{III}}}\right)$ missing conditions for each $\breve{\boldsymbol{\varphi}}$ and $\breve{\mathbf{q}}$. For a fully embedded beam we therefore additionally impose

$$\boldsymbol{R}_{\breve{\boldsymbol{\varphi}},\breve{E}} = \left[\!\left[(\breve{\boldsymbol{\varphi}} - \boldsymbol{\varphi})\right]\!\right]_0^L = \mathbf{0} \quad \text{and} \quad \boldsymbol{R}_{\breve{\mathbf{q}},\breve{E}} = \left[\!\left[\breve{\mathbb{P}}_\alpha^\top \boldsymbol{F}\, \breve{\boldsymbol{D}}_\alpha\right]\!\right]_0^L = \mathbf{0} \tag{5.92}$$

from eq. (5.74), each constituting 6 equations. Hence we limit the choice for $\mathfrak{O}_{\breve{\mathrm{III}}} \geq \mathfrak{O}_{\breve{\mathrm{I}}} - 2$ which for the same number of parametric elements implies $p_{\breve{\mathrm{I}}} - 2 \leq p_{\breve{\mathrm{IV}}} \leq p_{\breve{\mathrm{I}}}$. Note that the system becomes overdetermined when imposing $\boldsymbol{R}_{\breve{\boldsymbol{\varphi}},\breve{E}}$ and $\boldsymbol{R}_{\breve{\mathbf{q}},\breve{E}}$ but setting $p > p_{\breve{\mathrm{I}}} - 2$ and a least-square or another minimization technique is applied, e.g. $\boldsymbol{K}^\top \boldsymbol{K}\, \Delta\boldsymbol{q} = \boldsymbol{K}^\top \boldsymbol{R}$.

We note that discrete system reduction techniques can be employed. This holds in particular for discrete condensation (*Null-Space methods*) of the symmetric and mass-matrix like tangent contributions $\boldsymbol{K}_{\check{\mathfrak{g}}\check{s}} = \boldsymbol{K}_{\check{\mathfrak{r}}\check{\mathfrak{q}}} = \int_{\check{\mathcal{C}}_0} \{ \check{\mathcal{M}}^a \, \check{\mathcal{M}}^b \} \, \mathrm{d}\check{\theta}^3$ associated with the mixed modes, if these terms are not omitted altogether (cf. remark 5.5.1). Depending on the choice of $\check{\mathcal{N}}^a$, components regarding the position coupling $\boldsymbol{K}_{\check{\eta}\check{\varphi}}$ may also be considered. Further possible reduction steps are outlined in section 5.A.4.

5.6 Numerical investigation

This section evaluates the accuracy of the proposed formulation through several benchmark problems. First, a reference test is performed to compare the multidimensional coupling against the surface-based coupling between beam and matrix. Subsequently, a torsion test is analyzed to assess the necessity of rotational constraints as opposed to purely positional ones. Finally, the applicability to larger representative volume elements (*RVE*) containing multiple embedded fibers is demonstrated. In order to avoid excessive use of indices, we denote here $x \coloneqq x_1$, $y \coloneqq x_2$ and $z \coloneqq x_3$.

To examine the influence of the approximation order, we define the order vector $\boldsymbol{p}_{\mathrm{sim}} \coloneqq [p_{\boldsymbol{\varphi}}, p_{\check{\boldsymbol{\varphi}}}, p_{\check{\mathfrak{q}}}, p_{\check{s}}, p_{\check{\boldsymbol{w}}}, p_{\check{\eta}}, p_{\check{\vartheta}}, p_{\check{\boldsymbol{\varpi}}}]$, which collects the polynomial orders of all fields introduced in section 5.5.1. Here, we explicitly differentiate between fields, but recall that the matrix is discretized using the same order in all directions $p_x = p_y = p_z = p_{\boldsymbol{\varphi}} = p_{\mathrm{I}}$ and the same order is applied for beam position and quaternions $p_{\check{\boldsymbol{\varphi}}} = p_{\check{\mathfrak{q}}} = p_{\check{\mathrm{I}}} = p_{\mathrm{I}}$. augmented quantities satisfy $p_{\check{s}} = p_{\check{\boldsymbol{w}}} = p_{\check{\mathrm{II}}}$, while the coupling conditions of condensed fields are discretized using $p_{\check{\eta}} = p_{\check{\vartheta}} = p_{\check{\mathrm{III}}}$ and finally for the remaining coupling we have $p_{\check{\boldsymbol{\varpi}}} = p_{\check{\mathrm{IV}}}$.

5.6.1 Bending of a beam

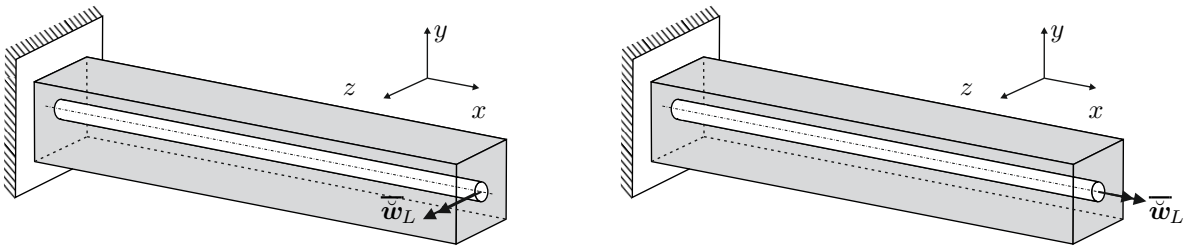


Figure 5.6.1 – Matrix-beam bending test: setup. Reference configuration of the bending test (left) and the torsion test (right).

The first example reproduces a benchmark from Steinbrecher et al. [114], Section 4.2, where a beam of length 5 m and radius $\check{r} = 0.125\,\mathrm{m}$ with Young's modulus $4346\,\mathrm{N/m^2}$ (see eq. (5.15)) is embedded in a $1\,\mathrm{m} \times 1\,\mathrm{m} \times 5\,\mathrm{m}$ matrix block of Saint-Venant-Kirchhoff

material (see eq. (3.77) and remark 3.3.4) with Young's modulus $10\,\mathrm{N/m^2}$. Poisson's ratio is zero for both materials. The parameters are chosen such that the matrix, if treated as a beam, exhibits the same bending stiffness.

Both beam and matrix are clamped at $x = 0\,\mathrm{m}$, and a moment $[\![\breve{\mathfrak{w}}]\!]_L = \overline{\breve{\boldsymbol{w}}}_L = [0,\, 0,\, 0.025]\,\mathrm{Nm}$ is applied at the beam tip ($x = 5\,\mathrm{m}$) as a dead load (figure 5.6.1, left). This test assesses stability, convergence, and model accuracy, since reference data for surface coupling are available in Steinbrecher et al. [114]. The mesh uses n elements in the y- and z-directions, and $5\,n$ in x-direction, yielding uniform elements. The beam employs the same discretization in x, ensuring coinciding control points along the axis.

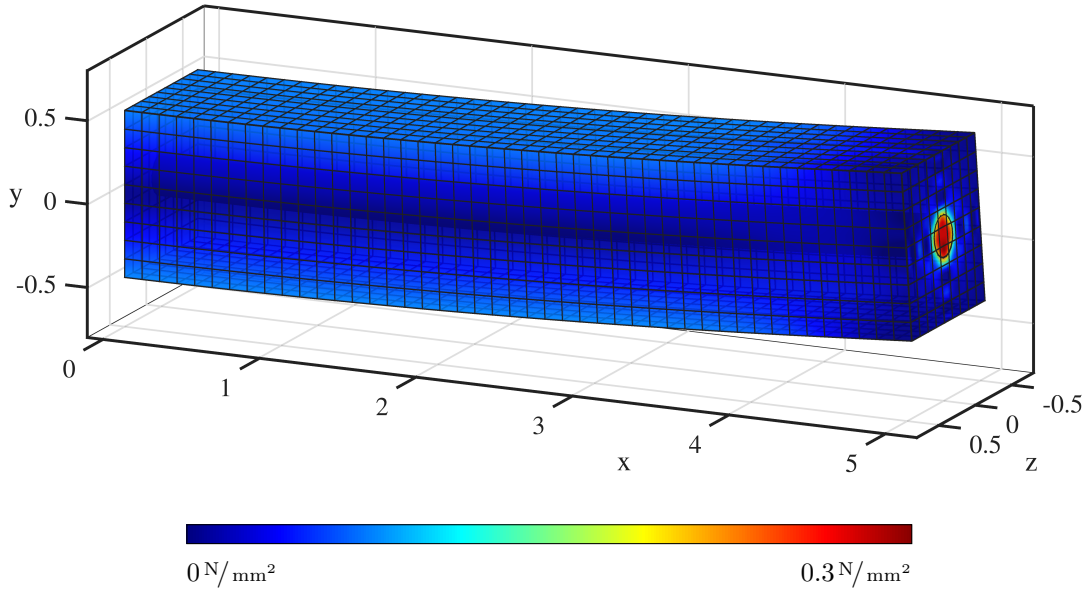


Figure 5.6.2 – **Matrix-beam bending test: results.** Von Mises stress distribution.

The deformation and von Mises stress distribution are shown in figure 5.6.2. As expected, stresses concentrate near the loaded beam end. In figure 5.6.3 we present the tip displacement for second- and fourth-order approximations, where the legend numbers denote the B-spline orders in $\boldsymbol{p}_{\mathrm{sim}}$. Both order combinations converge to the same solution.

Moreover, figure 5.6.4 depicts $\breve{\mathfrak{s}}$, $\breve{\mathfrak{w}}$ and $\breve{\varpi}$ along the beam centerline for various order sets $\boldsymbol{p}_{\mathrm{sim}}$. To prevent spurious oscillations, $\breve{\varpi}$ is fixed to zero at the first node. As expected, $\breve{\mathfrak{s}}_z$, $\breve{\mathfrak{w}}_x$, $\breve{\mathfrak{w}}_y$ and $\breve{\varpi}_z$ are nearly zero. Additionally, explicitly enforcing eq. (5.53) at both beam ends yields results identical to integral enforcement along $\breve{\Omega}_0$.

The deviation of the beam tip displacement between approaches is evaluated via

$$\left| \frac{|(\breve{\boldsymbol{\varphi}}(L) - \breve{\boldsymbol{\varphi}}_0(L)|_a}{|(\breve{\boldsymbol{\varphi}}(L) - \breve{\boldsymbol{\varphi}}_0(L)|_b} - 1 \right| \tag{5.93}$$

expressed as a percentage relative to the reference displacement $0.19078898128\,\mathrm{m}$ (cf. table 5.6.1).

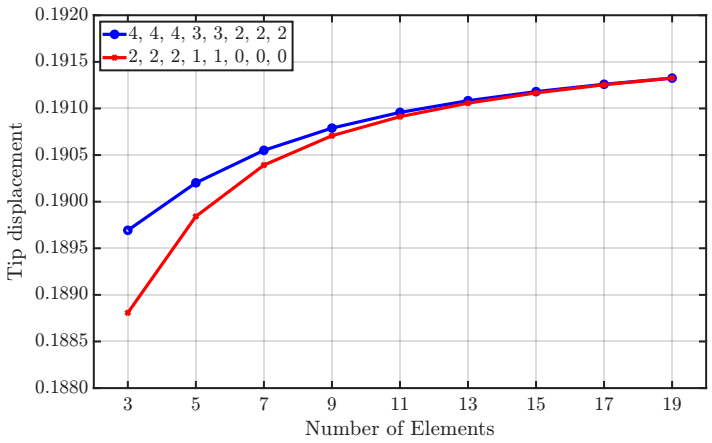


Figure 5.6.3 – Matrix-beam bending test: convergence. Convergence of the tip displacement for different combinations of shape functions.

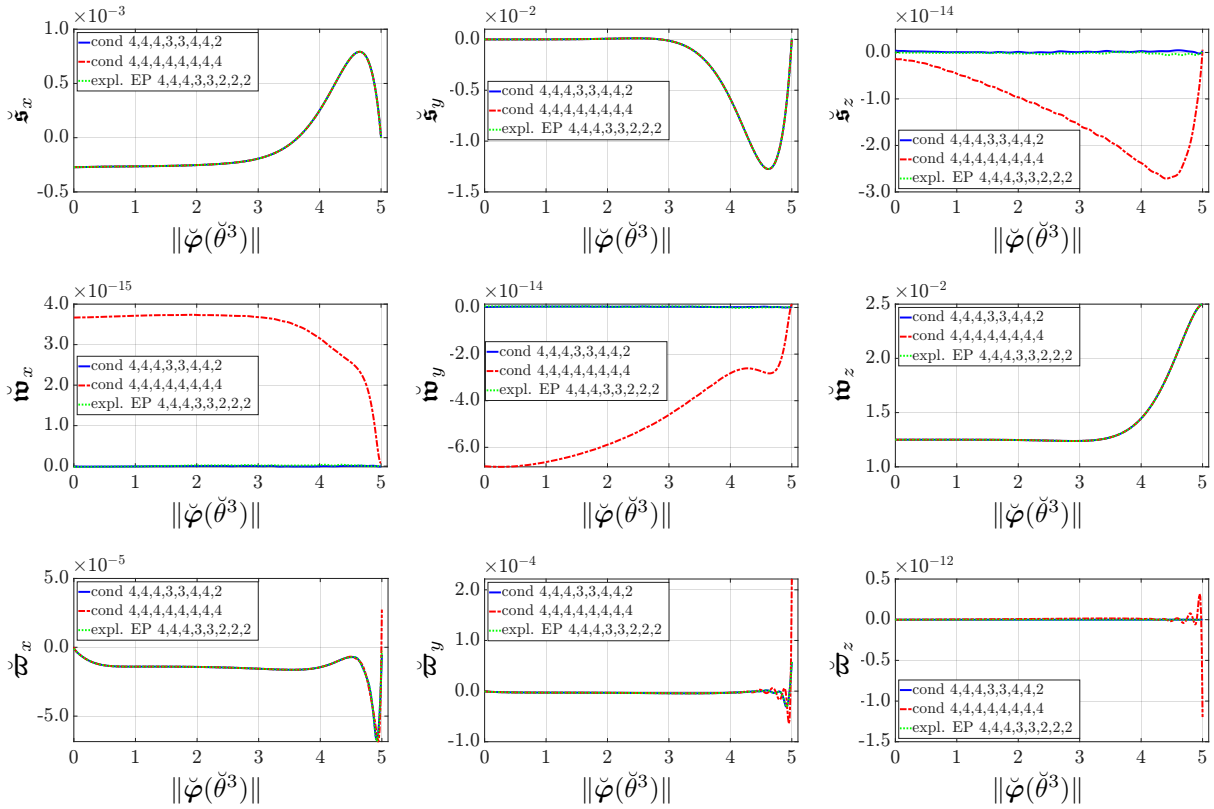


Figure 5.6.4 – Matrix-beam bending test: analysis. From top to bottom: $\breve{\mathfrak{s}}$, $\breve{\mathfrak{w}}$ and $\breve{\mathfrak{w}}$. Left to right: x-, y- and z-components.

Comparisons include explicit endpoint enforcement and alternative treatments of the quaternion unity constraint, either weak using eq. (5.87) or pointwise as in eq. (5.88). The relative deviation between [4, 4, 4, 3, 3, 2, 2, 2] and [4, 4, 4, 4, 4, 3, 3, 3] is in the order of 10^{-5} %, i.e. negligible, though the latter setup is computationally simpler since only two polynomial orders must be evaluated per Gauss point.

Routine	q-unity	orders	expl. EP weak 44433222	expl. EP direct 44433222	expl. EP direct 44444333	expl. EP direct 44444222	cond direct 44433442	cond direct 44433443
expl. EP	weak	44433222		$1.13\cdot10^{-4}$	$1.32\cdot10^{-4}$	$1.13\cdot10^{-4}$	$1.17\cdot10^{-4}$	$1.15\cdot10^{-4}$
expl. EP	direct	44433222	$1.13\cdot10^{-4}$		$1.90\cdot10^{-5}$	$1.00\cdot10^{-7}$	$4.00\cdot10^{-6}$	$2.00\cdot10^{-6}$
expl. EP	direct	44444333	$1.32\cdot10^{-4}$	$1.90\cdot10^{-5}$		$1.90\cdot10^{-5}$	$1.50\cdot10^{-5}$	$1.70\cdot10^{-5}$
expl. EP	direct	44444222	$1.13\cdot10^{-4}$	$1.00\cdot10^{-7}$	$1.90\cdot10^{-5}$		$4.00\cdot10^{-6}$	$2.00\cdot10^{-6}$
cond	direct	44433442	$1.17\cdot10^{-4}$	$4.00\cdot10^{-6}$	$1.50\cdot10^{-5}$	$4.00\cdot10^{-6}$		$2.00\cdot10^{-6}$
cond	direct	44433443	$1.15\cdot10^{-4}$	$2.00\cdot10^{-6}$	$1.70\cdot10^{-5}$	$2.00\cdot10^{-6}$	$2.00\cdot10^{-6}$	

Table 5.6.1 – Matrix-beam bending test: accuracy. Deviation of the beam tip displacement in percent (%) for different orders and approaches for the quaternion unity constraint.

5.6.2 Torsion test

The next study employs the same geometry as in section 5.6.1, but with the Mooney-Rivlin material model eq. (3.70), using $f(J) = 2\,(\alpha + 2\beta)\ln(J) + \frac{2}{3}\,(\alpha+\beta)(J-1)^2$, with $\alpha = 2$ and $\beta = 1$. An external moment $\overline{\breve{\boldsymbol{w}}}_L = [0.9,\, 0,\, 0]\,\mathrm{Nm}$ induces pure torsion (figure 5.6.1, right). Position constraints alone are insufficient here, as they do not restrict beam rotation relative to the matrix. Figure 5.6.5 shows the resulting von Mises stresses on the virtual beam surface inside the matrix. Rotation of the matrix within the beam's virtual volume arises from incorporating geometric data via the second moment of inertia in eq. (5.14). Since only a limited gradient field surrounds the 1D beam, full geometric reconstruction would require higher-order contributions.

Figure 5.6.6 presents $\breve{\mathfrak{s}}$, $\breve{\mathfrak{w}}$ and $\breve{\varpi}$ along the beam centerline for $\boldsymbol{p}_{\mathrm{sim}} = [4,\, 4,\, 4,\, 3,\, 3,\, 2,\, 2,\, 2]$. Components $\breve{\mathfrak{s}}_y$, $\breve{\mathfrak{s}}_z$, $\breve{\mathfrak{w}}_y$ and $\breve{\mathfrak{w}}_z$ remain near numerical zero, consistent with the expected physics. Due to the nonzero Poisson ratio of the Mooney-Rivlin model, a small elongation in x-direction occurs, leading to $\breve{\mathfrak{s}}_x(L) \neq 0$. A comparative simulation with the Saint-Venant-Kirchhoff model yields $\breve{\mathfrak{s}}_x(L) = 0$, confirming this effect. As the torsion produces large deformations, only the Mooney-Rivlin results are retained.

5.6.3 Shear test

The final single-beam test considers simple shear. The lower matrix surface is fixed, while the upper surface is displaced laterally. Figure 5.6.7 shows the von Mises stress distribution with (left) and without (right) hydrostatic and shear constraints (eq. (5.55)).

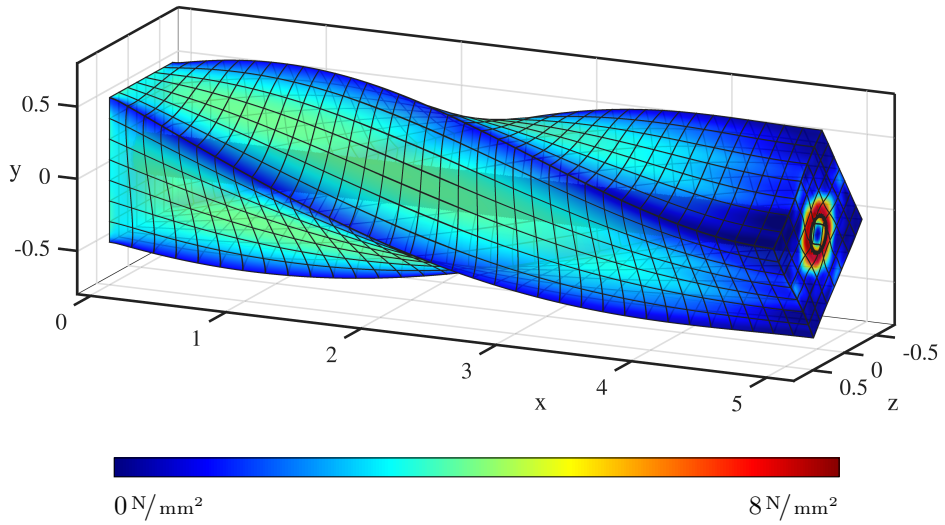


Figure 5.6.5 – Matrix-beam torsion test: results. Von Mises stress distribution.

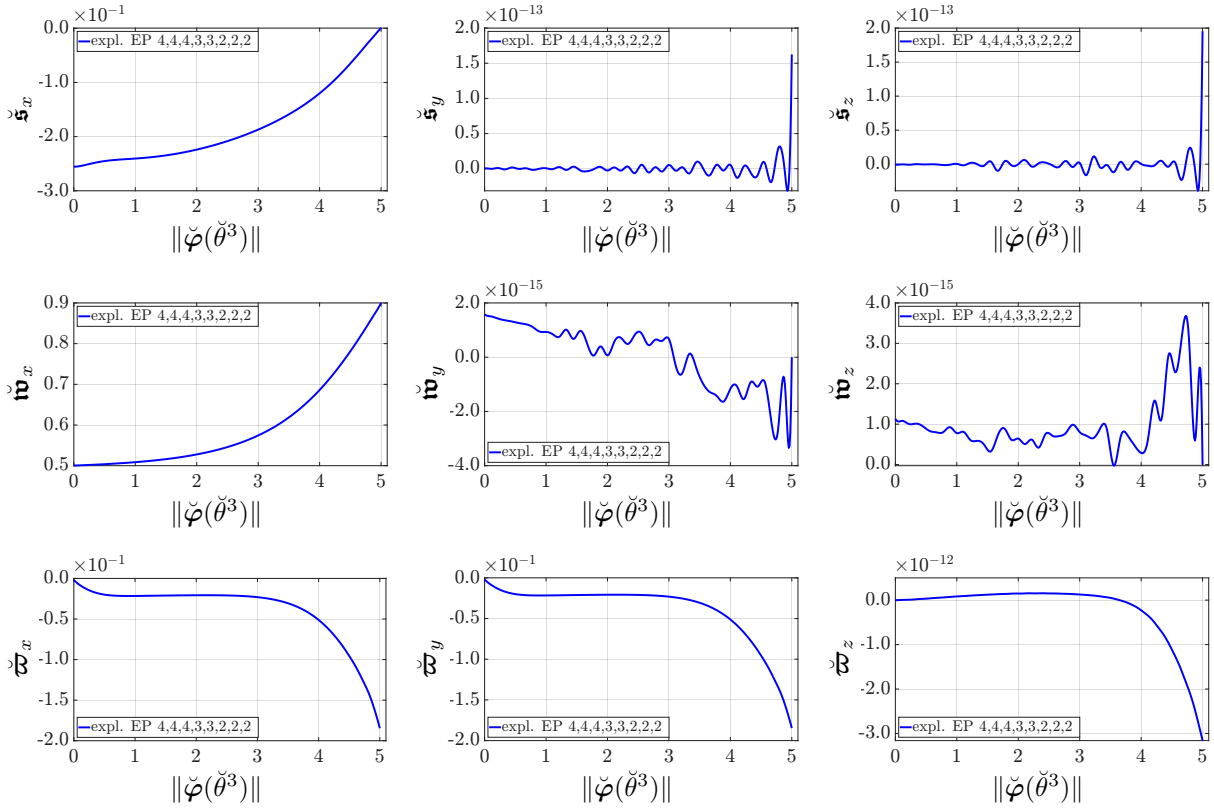


Figure 5.6.6 – Matrix-beam torsion test: analysis. Top to bottom: $\breve{\mathfrak{s}}$, $\breve{\mathfrak{w}}$ and $\breve{\boldsymbol{\varpi}}$. Left to right: x-, y- and z-components.

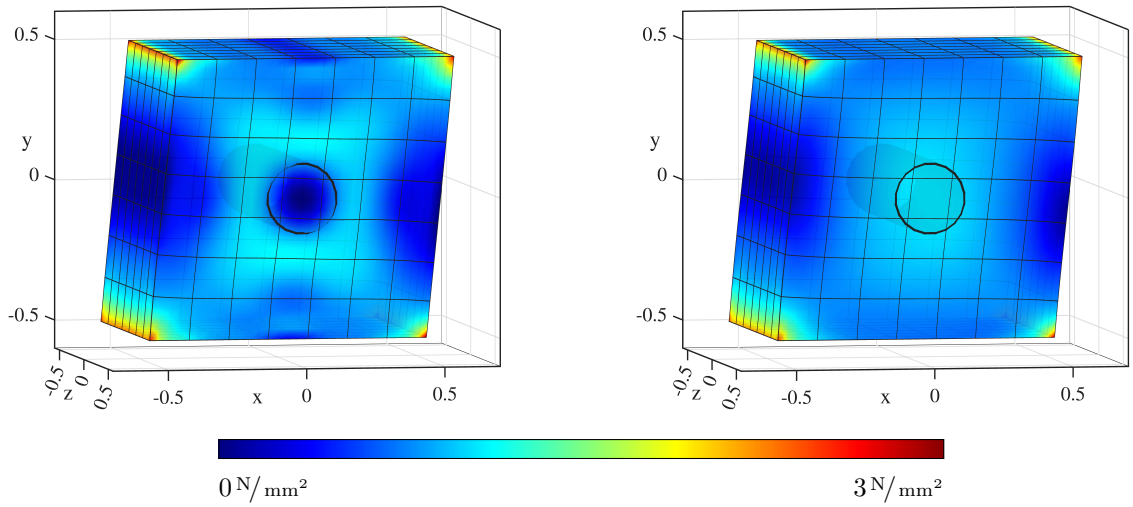


Figure 5.6.7 – Matrix-beam shear test: results. Von Mises stress distribution with (left) and without (right) constraints on hydrostatic pressure and shear.

The shear load does not induce bending or elongation, and the beam rotation remains nearly constant. Without the constraints, the matrix remains largely unaffected by the beam, as evident in figure 5.6.7, right. Enforcing the constraints of eq. (5.55) (or equivalently eq. (5.102)) redistributes the stresses around the virtual beam geometry, as seen in the left plot.

5.6.4 Application of multiple beams

As a proof of concept, the final example investigates a microscopic continuum in the form of a unit cube for fiber-reinforced polymers. The polymer matrix follows the Mooney-Rivlin model from section 5.6.2, with $\alpha = 2000\,\mathrm{N/mm^2}$ and $\beta = 1000\,\mathrm{N/mm^2}$. The fibers have diameter $d = 2\breve{r} = 0.01\,\mathrm{mm}$, approximate length $l = 0.2\,\mathrm{mm}$, Young's modulus $E = 73000\,\mathrm{N/mm^2}$, and Poisson's ratio $\nu = 0.3$.

The cube size is $(-0.5\,\mathrm{mm}, 0.5\,\mathrm{mm})^3$ with 20 elements per direction and order $\boldsymbol{p}_{\mathrm{sim}} = [4, 4, 4, 3, 3, 2, 2, 2]$. Both isotropic and anisotropic configurations include 40 fibers discretized with 2-5 elements each, depending on length. Periodic boundary conditions are applied enforcing equal fluctuations on opposing faces, see section 6.2.1. The prescribed macroscopic deformation gradient

$$\overline{\boldsymbol{F}} = \begin{bmatrix} 0.9985 & 0.0250 & -0.0020 \\ -0.0100 & 1.0005 & -0.0050 \\ -0.0010 & 0.0100 & 0.9985 \end{bmatrix} \tag{5.94}$$

is imposed as a Dirichlet condition at the corners.

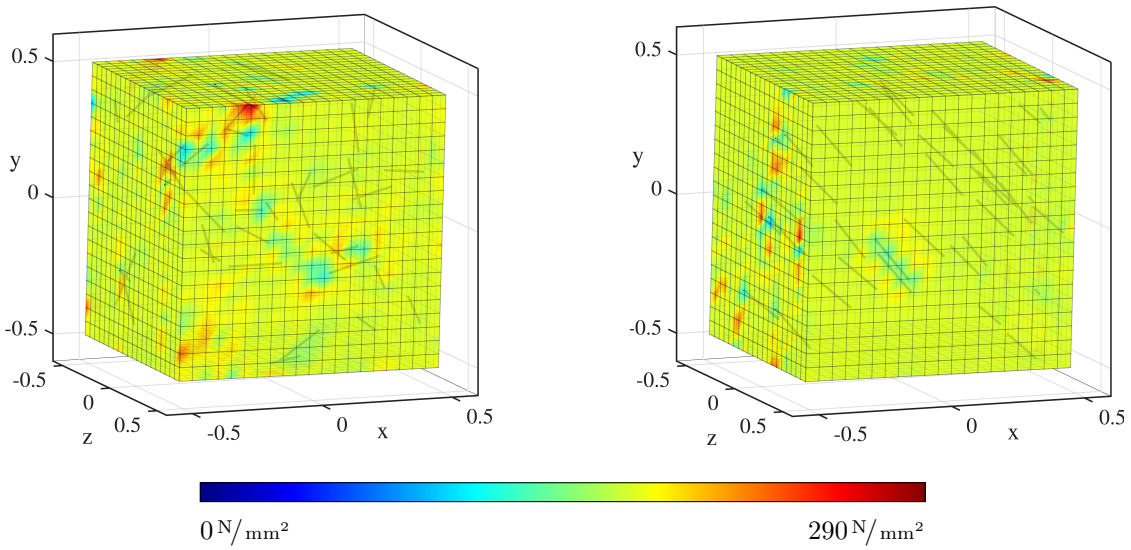


Figure 5.6.8 – Multiple beams: results. Von Mises stress distribution, isotropic (left) and anisotropic (right) case, plotted in the reference configuration.

Finally, figure 5.6.8 illustrates the resulting stress distributions in the matrix. Peak stresses reach approximately $289\,\mathrm{N/mm^2}$ for the isotropic and $266\,\mathrm{N/mm^2}$ for the anisotropic case, compared to mean values of about $170\,\mathrm{N/mm^2}$ in both cases.

5.A Appendix A

5.A.1 Rigid bodies

If instead of the beam a Cosserat point is to be coupled (0D-3D), we have to restrict the whole sphere. Following eq. (5.30), we decompose $\breve{\boldsymbol{\nu}}$ into torque and pressure

$$\breve{\boldsymbol{\nu}}(\breve{\theta}^i) = \breve{\boldsymbol{\vartheta}} \times \left(\breve{\boldsymbol{R}}\,\breve{\boldsymbol{N}}(\breve{\theta}^i)\right) + \breve{\nu}_p\,\breve{\boldsymbol{R}}\,\breve{\boldsymbol{N}}(\breve{\theta}^i). \tag{5.95}$$

Insertion into eq. (5.37) reveals

$$\begin{aligned}\left(\breve{\boldsymbol{\vartheta}} \times \left[\breve{\boldsymbol{R}}\,\breve{\boldsymbol{N}}\right]\right) \cdot \left(\left[\boldsymbol{F}_c - \breve{\boldsymbol{R}}\right] \breve{\theta}^i\,\breve{\boldsymbol{D}}_i\right) &= \left(\breve{\boldsymbol{R}}^\top \breve{\boldsymbol{\vartheta}}\right) \cdot \left[\breve{\boldsymbol{N}} \times \left(\breve{\boldsymbol{R}}^\top \left[\boldsymbol{F}_c - \breve{\boldsymbol{R}}\right]\,\breve{\boldsymbol{N}}\right)\right] \|\breve{\theta}^i\,\breve{\boldsymbol{D}}_i\|\,, \\ &= \left(\breve{\boldsymbol{R}}^\top \breve{\boldsymbol{\vartheta}}\right) \cdot \left[\breve{\boldsymbol{N}} \times \left(\breve{\boldsymbol{R}}^\top \boldsymbol{F}_c\,\breve{\boldsymbol{N}}\right)\right] \|\breve{\theta}^i\,\breve{\boldsymbol{D}}_i\|\,.\end{aligned} \tag{5.96}$$

With the spherical parametrization of the form

$$\breve{\boldsymbol{N}} = \breve{\boldsymbol{D}}_1\,\cos\left(\breve{\beta}\right)\,\sin(\breve{\gamma}) + \breve{\boldsymbol{D}}_2\,\sin\left(\breve{\beta}\right)\,\sin(\breve{\gamma}) + \breve{\boldsymbol{D}}_3\,\cos(\breve{\gamma}), \tag{5.97}$$

we obtain for an arbitrary matrix $\boldsymbol{A}$

$$\begin{aligned}&\int_0^{2\pi}\left\{\int_{-\pi}^{\pi}\left\{\breve{\boldsymbol{N}} \times \left(\boldsymbol{A}\,\breve{\boldsymbol{N}}\right)\right\}\mathrm{d}\breve{\beta}\right\}\mathrm{d}\breve{\beta} \\ &= \int_0^{2\pi}\left\{\int_{-\pi}^{\pi}\left\{\begin{vmatrix} \breve{\boldsymbol{D}}_1 & \breve{\boldsymbol{D}}_2 & \breve{\boldsymbol{D}}_3 \\ \cos\left(\breve{\beta}\right)\,\sin(\breve{\gamma}) & \sin\left(\breve{\beta}\right)\,\sin(\breve{\gamma}) & \cos(\breve{\gamma}) \\ \breve{\boldsymbol{D}}_1{}^\top \boldsymbol{A}\,\breve{\boldsymbol{N}} & \breve{\boldsymbol{D}}_2{}^\top \boldsymbol{A}\,\breve{\boldsymbol{N}} & \breve{\boldsymbol{D}}_3{}^\top \boldsymbol{A}\,\breve{\boldsymbol{N}} \end{vmatrix}\right\}\mathrm{d}\breve{\beta}\right\}\mathrm{d}\breve{\gamma} \\ &= \left[\breve{\boldsymbol{D}}_1, \breve{\boldsymbol{D}}_2, \breve{\boldsymbol{D}}_3\right] \cdot \int_0^{2\pi}\left\{\int_{-\pi}^{\pi}\left\{\begin{bmatrix} \breve{\boldsymbol{D}}_3{}^\top \boldsymbol{A}\,\breve{\boldsymbol{N}} \sin\left(\breve{\beta}\right)\,\sin(\breve{\gamma}) - \breve{\boldsymbol{D}}_2{}^\top \boldsymbol{A}\,\breve{\boldsymbol{N}} \cos(\breve{\gamma}) \\ -\breve{\boldsymbol{D}}_3{}^\top \boldsymbol{A}\,\breve{\boldsymbol{N}} \cos\left(\breve{\beta}\right) \sin(\breve{\gamma}) + \breve{\boldsymbol{D}}_1{}^\top \boldsymbol{A}\,\breve{\boldsymbol{N}} \cos(\breve{\gamma}) \\ \breve{\boldsymbol{D}}_2{}^\top \boldsymbol{A}\,\breve{\boldsymbol{N}} \cos\left(\breve{\beta}\right)\,\sin(\breve{\gamma}) - \breve{\boldsymbol{D}}_1{}^\top \boldsymbol{A}\,\breve{\boldsymbol{N}} \sin\left(\breve{\beta}\right)\,\sin(\breve{\gamma}) \end{bmatrix}\right\}\mathrm{d}\breve{\beta}\right\}\mathrm{d}\breve{\gamma} \\ &= \pi\left[\breve{\boldsymbol{D}}_1, \breve{\boldsymbol{D}}_2, \breve{\boldsymbol{D}}_3\right] \cdot \begin{bmatrix} \breve{\boldsymbol{D}}_3{}^\top \boldsymbol{A}\,\breve{\boldsymbol{D}}_2 - \breve{\boldsymbol{D}}_2{}^\top \boldsymbol{A}\,\breve{\boldsymbol{D}}_3 \\ -\breve{\boldsymbol{D}}_3{}^\top \boldsymbol{A}\,\breve{\boldsymbol{D}}_1 + \breve{\boldsymbol{D}}_1{}^\top \boldsymbol{A}\,\breve{\boldsymbol{D}}_3 \\ \breve{\boldsymbol{D}}_2{}^\top \boldsymbol{A}\,\breve{\boldsymbol{D}}_1 - \breve{\boldsymbol{D}}_1{}^\top \boldsymbol{A}\,\breve{\boldsymbol{D}}_2 \end{bmatrix} \\ &= 2\,\pi\,\left[\breve{\boldsymbol{D}}_1, \breve{\boldsymbol{D}}_2, \breve{\boldsymbol{D}}_3\right] \cdot \mathrm{axl}\left(\left[\breve{\boldsymbol{D}}_1, \breve{\boldsymbol{D}}_2, \breve{\boldsymbol{D}}_3\right]^\top \boldsymbol{A}\,\left[\breve{\boldsymbol{D}}_1, \breve{\boldsymbol{D}}_2, \breve{\boldsymbol{D}}_3\right]\right).\end{aligned} \tag{5.98}$$

Applied to eq. (5.96) in the second-to-last term we get

$$\begin{aligned}&\int_0^{2\pi}\left\{\int_{-\pi}^{\pi}\breve{\boldsymbol{N}} \times \left(\breve{\boldsymbol{R}}^\top \boldsymbol{F}_c\,\breve{\boldsymbol{N}}\right)\mathrm{d}\breve{\beta}\right\}\mathrm{d}\breve{\gamma} \\ &\qquad = 2\,\pi\,\left[\breve{\boldsymbol{D}}_1, \breve{\boldsymbol{D}}_2, \breve{\boldsymbol{D}}_3\right] \cdot \mathrm{axl}\left(\left[\breve{\boldsymbol{D}}_1, \breve{\boldsymbol{D}}_2, \breve{\boldsymbol{D}}_3\right]^\top \breve{\boldsymbol{R}}^\top \boldsymbol{F}_c\,\left[\breve{\boldsymbol{D}}_1, \breve{\boldsymbol{D}}_2, \breve{\boldsymbol{D}}_3\right]\right).\end{aligned} \tag{5.99}$$

Collecting the above identities, we obtain

$$\begin{aligned}\operatorname{skew}\Big(\Big[\breve{\boldsymbol{D}}_1,\breve{\boldsymbol{D}}_2,\breve{\boldsymbol{D}}_3\Big]^\top \breve{\boldsymbol{R}}^\top \boldsymbol{F}_c \Big[\breve{\boldsymbol{D}}_1,\breve{\boldsymbol{D}}_2,\breve{\boldsymbol{D}}_3\Big]\Big)& \\ = \Big[\breve{\boldsymbol{D}}_1,\breve{\boldsymbol{D}}_2,\breve{\boldsymbol{D}}_3\Big]^\top \operatorname{skew}(\breve{\boldsymbol{R}}^\top \boldsymbol{F}_c) \Big[\breve{\boldsymbol{D}}_1,\breve{\boldsymbol{D}}_2,\breve{\boldsymbol{D}}_3\Big]\,.&\end{aligned} \tag{5.100}$$

With regard to the constraint formulation eq. (5.40), we have to enforce $\operatorname{skew}(\breve{\boldsymbol{R}}^\top \boldsymbol{F}_c) = \boldsymbol{0}$, which is equivalent to the formulation shown in Simo et al. [107].

5.A.2 Co-rotational split

We introduce symmetric tensorial representation $[\![(\cdot)]\!]_\circ$, stating for the vector $\breve{\boldsymbol{\varpi}}$ operating in the cross-section

$$\begin{aligned}[\![\breve{\boldsymbol{\varpi}}]\!]_\circ &:= \breve{\boldsymbol{R}}^\top \breve{\mathbb{Q}}_\alpha \breve{\boldsymbol{\varpi}} \otimes \breve{\boldsymbol{D}}_\alpha \\ &= \breve{\varpi}_1 \breve{\boldsymbol{D}}_1 \otimes \breve{\boldsymbol{D}}_1 + \breve{\varpi}_2 \breve{\boldsymbol{D}}_2 \otimes \breve{\boldsymbol{D}}_2 + \breve{\varpi}_3 \left(\breve{\boldsymbol{D}}_1 \otimes \breve{\boldsymbol{D}}_2 + \breve{\boldsymbol{D}}_2 \otimes \breve{\boldsymbol{D}}_1\right) \in \operatorname{Sym}.\end{aligned} \tag{5.101}$$

Following the co-rotational split into co-rotational (rigid) motion and deformation, cf. Felippa and Haugen [40], we decompose the variation of dilatation/shear in eq. (5.55), such that we have $\delta\text{co-rot}\big(\breve{\boldsymbol{R}}\breve{\boldsymbol{R}}^\top\breve{\mathbb{Q}}_\alpha\breve{\boldsymbol{\varpi}}\breve{\boldsymbol{D}}_\alpha\big) = \delta\big(\breve{\boldsymbol{R}}\,[\![\breve{\boldsymbol{\varpi}}]\!]_\circ\big) = \breve{\boldsymbol{R}}\,[\![\delta\breve{\boldsymbol{\varpi}}]\!]_\circ + \boldsymbol{F}_c\,[\![\delta\breve{\boldsymbol{\varpi}}]\!]_\circ + \delta\boldsymbol{F}_c\,[\![\breve{\boldsymbol{\varpi}}]\!]_\circ + \delta\breve{\boldsymbol{R}}\,[\![\breve{\boldsymbol{\varpi}}]\!]_\circ$. Note that the last term vanishes due to symmetry of $[\![\delta\breve{\boldsymbol{\varpi}}]\!]_\circ$ with the definition of rotational variation eq. (5.10). Summing up terms with respect to $\delta\breve{\boldsymbol{\varpi}}$, we have

$$\begin{aligned}\int_{\breve{\mathcal{C}}_0}\Big\{\Big(\breve{\boldsymbol{R}}^\top\Big(\boldsymbol{F}_c-\breve{\boldsymbol{R}}\Big)+\Big(\boldsymbol{F}_c-\breve{\boldsymbol{R}}\Big)^\top\boldsymbol{F}_c\Big) : [\![\delta\breve{\boldsymbol{\varpi}}]\!]_\circ\,|\breve{E}|\Big\}\,\mathrm{d}\breve{\theta}^3& \\ = \int_{\breve{\mathcal{C}}_0}\Big\{\Big(\boldsymbol{F}_c^\top\boldsymbol{F}_c-\boldsymbol{I}\Big) : [\![\delta\breve{\boldsymbol{\varpi}}]\!]_\circ\,|\breve{E}|\Big\}\,\mathrm{d}\breve{\theta}^3 = 0,&\end{aligned} \tag{5.102}$$

given $\boldsymbol{F}_c^\top\boldsymbol{F}_c - \boldsymbol{I} = \breve{\boldsymbol{R}}^\top\Big(\boldsymbol{F}_c-\breve{\boldsymbol{R}}\Big)+\Big(\boldsymbol{F}_c-\breve{\boldsymbol{R}}\Big)^\top\boldsymbol{F}_c$ and eq. (5.101). The associated coupling condition eq. (5.55) can then be rewritten as

$$\int_{\breve{\mathcal{C}}_0}\Big\{\Big(\boldsymbol{F}_c^\top\boldsymbol{F}_c-\boldsymbol{I}\Big) : [\![\delta\breve{\boldsymbol{\varpi}}]\!]_\circ\,|\breve{E}|\Big\}\,\mathrm{d}\breve{\theta}^3 = 0, \tag{5.103}$$

Using eq. (5.101) we get for the variation with respect to $\delta\boldsymbol{F}_c$ accordingly

$$\int_{\breve{\mathcal{C}}_0}\Big\{\breve{\mathbb{Q}}_\alpha\,\breve{\boldsymbol{\varpi}}\otimes\breve{\boldsymbol{D}}_\alpha : \delta\boldsymbol{F}_c|\breve{E}|\,\Big\}\,\mathrm{d}\breve{\theta}^3 = \int_{\breve{\mathcal{C}}_0}\Big\{\boldsymbol{F}_c\,[\![\breve{\boldsymbol{\varpi}}]\!]_\circ : \delta\boldsymbol{F}_c|\breve{E}|\,\Big\}\,\mathrm{d}\breve{\theta}^3\,, \tag{5.104}$$

resulting in

$$\begin{aligned}\breve{\boldsymbol{\Sigma}} : \delta\boldsymbol{F}_c &= \Big(\breve{\mathbb{Q}}_\alpha\,\breve{\boldsymbol{\varpi}}\otimes\breve{\boldsymbol{D}}_\alpha\Big) : \delta\boldsymbol{F}_c + \Big(\breve{\mathbb{P}}_\alpha^\top\breve{\boldsymbol{\vartheta}}\otimes\breve{\boldsymbol{D}}_\alpha\Big)\delta\boldsymbol{F}_c \\ \Leftrightarrow\quad \Big(\breve{\boldsymbol{\Sigma}}-\boldsymbol{F}_c\,[\![\breve{\boldsymbol{\varpi}}]\!]_\circ\Big) : \delta\boldsymbol{F}_c &= \Big(\breve{\mathbb{P}}_\alpha^\top\breve{\boldsymbol{\vartheta}}\otimes\breve{\boldsymbol{D}}_\alpha\Big)\delta\boldsymbol{F}_c\,,\end{aligned} \tag{5.105}$$

transforming the stress component $\breve{\mathbb{Q}}_\alpha\breve{\boldsymbol{\varpi}}\breve{\boldsymbol{D}}_\alpha = \boldsymbol{F}_c\,[\![\breve{\boldsymbol{\varpi}}]\!]_\circ$.

5.A.3 Circular integral

It holds $\int_0^{2\pi}\left\{\breve{\boldsymbol{N}}^{\otimes(2j+1)}\right\}\mathrm{d}\breve{\beta}=\boldsymbol{0}$ for $j\in\mathbb{N}_0$. Setting $\breve{\beta}^*=\breve{\beta}+\pi$, we have $\breve{\boldsymbol{N}}(\breve{\beta}^*-\pi)=-\breve{\boldsymbol{N}}(\breve{\beta})$. Insertion yields

$$\begin{aligned}\int_0^{2\pi}\left\{\breve{\boldsymbol{N}}(\breve{\beta})^{\otimes(2j+1)}\right\}\mathrm{d}\breve{\beta}&=\int_0^{2\pi}\left\{\breve{\boldsymbol{N}}(\breve{\beta}^*-\pi)^{\otimes(2j+1)}\right\}\mathrm{d}\breve{\beta}=\int_0^{2\pi}\left\{\left(-\breve{\boldsymbol{N}}(\breve{\beta}^*)\right)^{\otimes(2j+1)}\right\}\mathrm{d}\breve{\beta}\\&=-\int_0^{2\pi}\left\{\breve{\boldsymbol{N}}(\breve{\beta}^*)^{\otimes(2j+1)}\right\}\mathrm{d}\breve{\beta}=-\int_0^{2\pi}\left\{\breve{\boldsymbol{N}}(\breve{\beta})^{\otimes(2j+1)}\right\}\mathrm{d}\breve{\beta}\,.\end{aligned}\tag{5.106}$$

5.A.4 Continuous reduction

It should be emphasized that the coupling condition in eq. (5.55) explicitly includes the rotation tensor $\breve{\boldsymbol{R}}$. Due to its orthogonality, this condition can equivalently be expressed solely in terms of $\boldsymbol{F}$ (see section 5.A.2). However, in the quaternion-based formulation, an approximation error in the orthogonality of $\breve{\boldsymbol{R}}^{\mathrm{h}}$ arises, as the unit-length constraints introduce numerical inaccuracies. Additionally, the effectively coupling of $\breve{\mathfrak{q}}^{\mathrm{h}}$ and $\boldsymbol{F}^{\mathrm{h}}$ in eq. (5.55) also does not guarantee exact orthogonality at every evaluation point due to further numerical errors. These shortcomings are reduced when the condition is formulated in the alternative form eq. (5.102).

Without proof, it is further noted that the quaternions can be eliminated from the system by using eq. (5.54) in combination with eq. (5.104). Accordingly, the director field is evaluated as $\breve{\boldsymbol{d}}_\alpha=\boldsymbol{F},\breve{\boldsymbol{D}}_\alpha$, with $\breve{\boldsymbol{d}}_3=\breve{\boldsymbol{d}}_1\times\breve{\boldsymbol{d}}_2$ computed at the respective Gauss points along the beam centerline. The rotation tensor then follows as $\breve{\boldsymbol{R}}=\breve{\boldsymbol{d}}_i\otimes\breve{\boldsymbol{D}}_i$. Assuming again straight initial fibers, the derivative $\breve{\boldsymbol{R}}'$ is obtained as $\breve{\boldsymbol{R}}'=\breve{\boldsymbol{d}}_i'\otimes\breve{\boldsymbol{D}}_i$, which directly yields

$$\breve{\boldsymbol{d}}_\alpha'=\nabla_{\mathrm{x}}\boldsymbol{F}:\breve{\boldsymbol{D}}_\alpha\otimes\breve{\boldsymbol{D}}_3,\quad\text{and}\quad\breve{\boldsymbol{d}}_3'=(\nabla_{\mathrm{x}}\boldsymbol{F}:\breve{\boldsymbol{D}}_1\otimes\breve{\boldsymbol{D}}_3)\times\breve{\boldsymbol{d}}_2+\breve{\boldsymbol{d}}_1\times(\nabla_{\mathrm{x}}\boldsymbol{F}:\breve{\boldsymbol{D}}_2\otimes\breve{\boldsymbol{D}}_3).\tag{5.107}$$

This ultimately leads to a system that is solved with respect to the matrix degrees of freedom $\boldsymbol{\varphi}$ and the Lagrange multipliers $\breve{\boldsymbol{\varpi}}$, beside potentially not condensed mixed-fields. If desired, appropriate techniques such as the augmented Lagrange method may be employed to solve the problem exclusively in terms of the matrix unknowns. In the numerical examples presented in the following section, the quaternion formulation is adopted.

6 Dimension expansion: Continuous higher-order multi-scale method

In the previous chapters 4 and 5, the higher-order behavior of fiber-reinforced media was recovered in two complementary ways. First, a continuous approach was pursued by modeling fiber kinematics within a second-order material law. Second, discrete Cosserat beams were embedded into a three-dimensional Cauchy continuum, with subsequent condensation resulting into an effective second-gradient solid. In that setting, the influence of the microstructure is contained in a finite set of higher-order constitutive moduli that are directly related to the geometric and material parameters of the embedded beams. The microstructure therefore enters only implicitly through these condensed parameters, while the macroscopic problem is formulated entirely on the physical domain Ω_0.

In the present chapter we follow a complementary route. Instead of eliminating the micro-degrees of freedom by static condensation, we expand the description to a product domain $\Omega_0 \times \tilde{\Omega}_0$ and retain an explicit microstructural representation on a representative volume element (RVE) as micro-domain, capturing non-local interactions, higher-order effects and other material or geometrical heterogeneity as depicted in figure 6.0.1.

The macroscopic kinematics are approximated by a Taylor expansion in the vicinity of the RVE position and enriched by fluctuation fields that are constrained to have vanishing volume average. An energetic averaging over the micro-domain then yields a consistent macro-micro coupling, from which generalized stresses and the associated micro-scale boundary value problem are obtained in a unified variational framework. Classical first-order FE^2-type schemes are recovered as a special case when only the leading-order terms of this expansion are retained, whereas the full setting naturally leads to a continuous higher-order multi-scale framework. The resulting formulation enables a monolithic treatment of micro- and macro-problems, avoiding iterative scale-separation loops and enhancing numerical robustness.

In the following sections, the theoretical setting of this higher-order multi-scale method is developed, starting from the extended kinematical set, proceeding to variational principles of energetic homogenization and extending them toward second-order continua.

6.1 Macroscopic boundary value problem

As a starting point, we briefly recap the generalized continuum as established in chapter 3, which provides the macroscopic description. Consider a body with macroscopic geometric

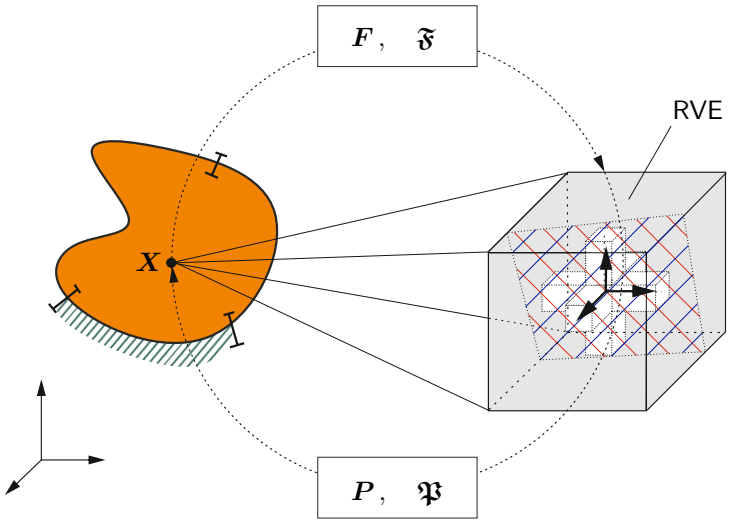


Figure 6.0.1 – Continuous micro-scale expansion scheme. Macro-scale deformation is transitioned to the micro-scale and the stress response is obtained by homogenization.

domain Ω_0 including its boundary $\partial\Omega_0$ in reference configuration and with position vector $\boldsymbol{X} \in \mathbb{R}^d$. Its motion is denoted as $\boldsymbol{\varphi}(\boldsymbol{X}) = \boldsymbol{x}$ from reference to current configuration $\boldsymbol{x}$. Deformation measures are given in the form of the first- and second-order deformation gradients

$$\boldsymbol{F} = \nabla_{\mathrm{x}} \boldsymbol{\varphi} \quad \text{and} \quad \mathfrak{F} = \nabla^2_{\mathrm{x}} \boldsymbol{\varphi}\,, \tag{6.1}$$

respectively. Following the introduction of an internal energy functional $\Psi(\boldsymbol{F}, \mathfrak{F})$, we identify first- and second-order stresses

$$\boldsymbol{P} = \frac{\partial \Psi}{\partial \boldsymbol{F}} \quad \text{and} \quad \mathfrak{P} = \frac{\partial \Psi}{\partial \mathfrak{F}}\,. \tag{6.2}$$

Variation yields the balance equation in weak form

$$\begin{aligned} \int_{\Omega_0} \Big\{ \boldsymbol{P} : \nabla_{\mathrm{x}} \delta\boldsymbol{\varphi} + \mathfrak{P} \vdots \nabla^2_{\mathrm{x}} \delta\boldsymbol{\varphi} \Big\} \mathrm{d}V \\ = \int_{\Omega_0} \Big\{ \delta\boldsymbol{\varphi} \cdot \overline{\boldsymbol{B}} \Big\} \mathrm{d}V + \int_{\partial\Omega_0^T} \Big\{ \delta\boldsymbol{\varphi} \cdot \overline{\boldsymbol{T}} \Big\} \mathrm{d}A + \int_{\partial\Omega_0^M} \Big\{ \nabla_{\mathrm{x}} \delta\boldsymbol{\varphi} : \overline{\boldsymbol{M}} \Big\} \mathrm{d}A\,, \end{aligned} \tag{6.3}$$

with the internal virtual work on the left-hand side and virtual external contributions omitting line forces on the right hand side. For completeness of variational statement 6.3, we specify the admissible space of admissible variations as

$$\mathcal{V}_{\delta\boldsymbol{\varphi}} = \Big\{ \delta\boldsymbol{\varphi} \in \mathcal{H}^2(\Omega_0) \mid \delta\boldsymbol{\varphi} = \boldsymbol{0} \text{ on } \partial\Omega_0^{\boldsymbol{\varphi}}\,, \quad \nabla_{\mathrm{x}} \delta\boldsymbol{\varphi} \boldsymbol{N} = \boldsymbol{0} \text{ on } \partial\Omega_0^{\nabla\boldsymbol{\varphi}} \Big\}\,, \tag{6.4}$$

that reflects the solution space

$$\mathcal{V}_{\boldsymbol{\varphi}} := \Big\{ \boldsymbol{\varphi} \in \mathcal{H}^2(\Omega_0) \mid \boldsymbol{\varphi} = \overline{\boldsymbol{\varphi}} \text{ on } \partial\Omega_0^{\boldsymbol{\varphi}}, \quad \nabla_{\mathrm{x}} \boldsymbol{\varphi} \boldsymbol{N} = \overline{\nabla_{\mathrm{x}} \boldsymbol{\varphi} \boldsymbol{N}} \text{ on } \partial\Omega_0^{\nabla\boldsymbol{\varphi}} \Big\}\,. \tag{6.5}$$

The balance equation is complemented by Neumann boundary conditions

$$(\boldsymbol{P} - \nabla_{\mathrm{X}} \cdot \mathfrak{P})\, \boldsymbol{N} = \overline{\boldsymbol{T}} \quad \text{on } \partial\Omega_0^T \quad \text{and} \quad \mathfrak{P}\, \boldsymbol{N} = \overline{\boldsymbol{M}} \quad \text{on } \partial\Omega_0^M\,, \tag{6.6}$$

where $\partial\Omega_0 = \partial\Omega_0^{\varphi} \cup \partial\Omega_0^T = \partial\Omega_0^{\nabla\varphi} \cup \partial\Omega_0^M$ and $\partial\Omega_0^{\varphi} \cap \partial\Omega_0^T = \partial\Omega_0^{\nabla\varphi} \cap \partial\Omega_0^M = \emptyset$.

6.2 Microscopic continuum

We subsequently derive micro-scale quantities, based on the assumed existence of an underlying microstructure for every macroscopic point $\boldsymbol{X} \in \Omega_0$. The micro-structure takes form of a representative volume element (RVE), that determines the overall behavior of the body and inherits all occurring inhomogeneities. Thus the macroscopic domain is expanded by a microscopic subdomain $\tilde{\Omega}_0(\boldsymbol{X})$ with local position vector $\tilde{\boldsymbol{X}} \in \tilde{\Omega}_0(\boldsymbol{X})$, whose extents are much smaller compared to macroscopic scales. For the local deformation map $\tilde{\boldsymbol{\varphi}}(\boldsymbol{X}, (\cdot))\colon \tilde{\Omega}_0 \to \mathbb{R}^d$ we conduct a Taylor series expansion up to second-order around the center $\tilde{\boldsymbol{X}}_c = \boldsymbol{X}$ of the RVE

$$\begin{aligned}\tilde{\boldsymbol{\varphi}}\big(\boldsymbol{X}, \tilde{\boldsymbol{X}}\big) = \tilde{\boldsymbol{x}}_c + \Big[\nabla_{\mathrm{X}} \tilde{\boldsymbol{\varphi}}\big(\boldsymbol{X}, \tilde{\boldsymbol{X}}\big)\Big]\Big|_{\tilde{\boldsymbol{X}}_c} \big(\tilde{\boldsymbol{X}} - \tilde{\boldsymbol{X}}_c\big) \\ + \frac{1}{2}\Big[\nabla_{\mathrm{X}}^2 \tilde{\boldsymbol{\varphi}}\big(\boldsymbol{X}, \tilde{\boldsymbol{X}}\big)\Big]\Big|_{\tilde{\boldsymbol{X}}_c} : \Big(\big(\tilde{\boldsymbol{X}} - \tilde{\boldsymbol{X}}_c\big) \otimes \big(\tilde{\boldsymbol{X}} - \tilde{\boldsymbol{X}}_c\big)\Big) + \tilde{\boldsymbol{w}}\big(\boldsymbol{X}, \tilde{\boldsymbol{X}}\big)\end{aligned} \tag{6.7}$$

and link quantities evaluated at the center to the macroscopic deformation, i.e.

$$\Big[\nabla_{\mathrm{X}} \tilde{\boldsymbol{\varphi}}\big(\boldsymbol{X}, \tilde{\boldsymbol{X}}\big)\Big]\Big|_{\tilde{\boldsymbol{X}}_c} = \boldsymbol{F}(\boldsymbol{X}) \quad \text{and} \quad \Big[\nabla_{\mathrm{X}}^2 \tilde{\boldsymbol{\varphi}}\big(\boldsymbol{X}, \tilde{\boldsymbol{X}}\big)\Big]\Big|_{\tilde{\boldsymbol{X}}_c} = \mathfrak{F}(\boldsymbol{X})\,. \tag{6.8}$$

Further setting $\tilde{\boldsymbol{X}}_c = \boldsymbol{0}$ in the local coordinate system we arrive at the kinematic micro to macro transition

$$\tilde{\boldsymbol{\varphi}}\big(\boldsymbol{X}, \tilde{\boldsymbol{X}}\big) = \boldsymbol{F}(\boldsymbol{X})\, \tilde{\boldsymbol{X}} + \frac{1}{2}\, \mathfrak{F}(\boldsymbol{X}) : \big(\tilde{\boldsymbol{X}} \otimes \tilde{\boldsymbol{X}}\big) + \tilde{\boldsymbol{w}}\big(\boldsymbol{X}, \tilde{\boldsymbol{X}}\big)\,, \tag{6.9}$$

where we denote the microscopic fluctuation field $\tilde{\boldsymbol{w}}\big(\boldsymbol{X}, \tilde{\boldsymbol{X}}\big)\colon \Omega_0 \times \tilde{\Omega}_0 \to \mathbb{R}^d$. In the following we mark quantities referring to the microscopic scale using $\tilde{(\cdot)}$. Note that second-order terms vanish if the macro-level takes form of a (first order) Cauchy continuum.

6.2.1 Multi-scale kinematic

Given microscopic deformation map, we denote local first- and second-order gradients

$$\tilde{\boldsymbol{F}} \coloneqq \tilde{\boldsymbol{F}}(\boldsymbol{F}, \mathfrak{F}, \nabla_{\mathrm{X}} \tilde{\boldsymbol{w}}) = \nabla_{\mathrm{X}} \tilde{\boldsymbol{\varphi}} = \boldsymbol{F} + \mathfrak{F}\, \tilde{\boldsymbol{X}} + \nabla_{\mathrm{X}} \tilde{\boldsymbol{w}} \tag{6.10}$$

$$\tilde{\mathfrak{F}} \coloneqq \tilde{\mathfrak{F}}\big(\mathfrak{F}, \nabla_{\mathrm{X}}^2 \tilde{\boldsymbol{w}}\big) = \nabla_{\mathrm{X}}^2 \tilde{\boldsymbol{\varphi}} = \mathfrak{F} + \nabla_{\mathrm{X}}^2 \tilde{\boldsymbol{w}}\,. \tag{6.11}$$

For justification of the micro-macro transition eq. (6.8), we relate macroscopic deformation gradients to volumetric averages of microscopic counterparts

$$\boldsymbol{F} = \frac{1}{|\tilde{\Omega}_0|}\int_{\tilde{\Omega}_0}\left\{\tilde{\boldsymbol{F}}\right\}\mathrm{d}\tilde{V} \quad \text{and} \quad \boldsymbol{\mathfrak{F}} = \frac{1}{|\tilde{\Omega}_0|}\int_{\tilde{\Omega}_0}\left\{\tilde{\boldsymbol{\mathfrak{F}}}\right\}\mathrm{d}\tilde{V}\,, \tag{6.12}$$

also known as averaging theorem. For this to hold, we arrive at distinct conditions obtained by insertion of the micro-scale kinematic. Hence using eq. (6.10), the first order gradient can be rewritten as

$$\boldsymbol{F} = \frac{1}{|\tilde{\Omega}_0|}\int_{\tilde{\Omega}_0}\left\{\tilde{\boldsymbol{F}}\right\}\mathrm{d}\tilde{V} = \frac{1}{|\tilde{\Omega}_0|}\int_{\tilde{\Omega}_0}\left\{\boldsymbol{F} + \boldsymbol{\mathfrak{F}}\,\tilde{\boldsymbol{X}} + \nabla_{\tilde{\mathrm{X}}}\tilde{\boldsymbol{w}}\right\}\mathrm{d}\tilde{V} = \boldsymbol{F} + \frac{1}{|\tilde{\Omega}_0|}\int_{\tilde{\Omega}_0}\{\nabla_{\tilde{\mathrm{X}}}\tilde{\boldsymbol{w}}\}\mathrm{d}\tilde{V}\,. \tag{6.13}$$

As mentioned, by design the geometric center coincides with the origin $\tilde{\boldsymbol{X}}_c = \boldsymbol{0}$, such that for a geometrically symmetric RVE, with $-\tilde{\boldsymbol{X}} \in \tilde{\Omega}_0 \forall \tilde{\boldsymbol{X}} \in \tilde{\Omega}_0$, follows $\int_{\tilde{\Omega}_0}\left\{\tilde{\boldsymbol{X}}\right\}\mathrm{d}\tilde{V} = \boldsymbol{0}$ and thus the cancellation of the second-order contribution. The remaining condition then becomes

$$\int_{\tilde{\Omega}_0}\{\nabla_{\tilde{\mathrm{X}}}\tilde{\boldsymbol{w}}\}\mathrm{d}\tilde{V} = \int_{\partial\tilde{\Omega}_0}\left\{\tilde{\boldsymbol{w}}\otimes\tilde{\boldsymbol{N}}\right\}\mathrm{d}\tilde{A} = \boldsymbol{0} \tag{6.14}$$

which intuitively demands vanishing volumetric average fluctuations. Alternatively, after application of the divergence theorem, all fluctuations on the boundary must cancel. For the second gradient, eq. $(6.12)_2$ reads with insertion of eq. (6.11) now

$$\boldsymbol{\mathfrak{F}} = \frac{1}{|\tilde{\Omega}_0|}\int_{\tilde{\Omega}_0}\left\{\tilde{\boldsymbol{\mathfrak{F}}}\right\}\mathrm{d}\tilde{V} = \frac{1}{|\tilde{\Omega}_0|}\int_{\tilde{\Omega}_0}\left\{\boldsymbol{\mathfrak{F}} + \nabla^2_{\tilde{\mathrm{X}}}\tilde{\boldsymbol{w}}\right\}\mathrm{d}\tilde{V} = \boldsymbol{\mathfrak{F}} + \frac{1}{|\tilde{\Omega}_0|}\int_{\tilde{\Omega}_0}\left\{\nabla^2_{\tilde{\mathrm{X}}}\tilde{\boldsymbol{w}}\right\}\mathrm{d}\tilde{V} \tag{6.15}$$

with emerging second-order requirement

$$\int_{\tilde{\Omega}_0}\left\{\nabla^2_{\tilde{\mathrm{X}}}\tilde{\boldsymbol{w}}\right\}\mathrm{d}\tilde{V} = \int_{\partial\tilde{\Omega}_0}\left\{\nabla_{\tilde{\mathrm{X}}}\tilde{\boldsymbol{w}}\,\tilde{\boldsymbol{N}}\right\}\mathrm{d}\tilde{A} = \boldsymbol{0}\,. \tag{6.16}$$

Fulfillment for equations (6.14) and (6.16) leaves mainly three choices of constraints, cf. Miehe et al. [84]:

(I) **Voigt.** Firstly, we can restrict all fluctuations to vanish

$$\tilde{\boldsymbol{w}} = \boldsymbol{0} \quad \text{in } \tilde{\Omega}_0\,, \tag{6.17}$$

from which inherently follows $\nabla_{\tilde{\mathrm{X}}}\tilde{\boldsymbol{w}} = \boldsymbol{0}$in $\tilde{\Omega}_0$ and thus prescribing the total deformation of the RVE. We refer to this setting as either *Taylor-Hypothesis*, as the Taylor assumption eq. (6.8) is extended to the whole domain, or as Voigt-type condition (see Taylor [115]), since the macroscopic stresses then emerge as volumetric weighted average micro-stresses (cf. section 6.2.2).

(II) **Dirichlet.** Making use of the divergence theorem, we can alternatively restrict fluctuations only on the boundary. For the *Dirichlet* set we eliminate all fluctuations on the boundary

$$\tilde{\boldsymbol{w}} = \boldsymbol{0}\,, \quad \nabla_{\tilde{\mathrm{X}}}\tilde{\boldsymbol{w}}\tilde{\boldsymbol{N}} = \boldsymbol{0} \quad \text{on } \partial\tilde{\Omega}_0\,, \tag{6.18}$$

for which we conveniently define Dirichlet boundaries $\partial\Omega_0^{\tilde{w}} = \partial\tilde{\Omega}_0$ and $\partial\Omega_0^{\nabla\tilde{w}} = \partial\tilde{\Omega}_0$ for first- and second-order restrictions.

(III) **Periodic.** For the third setting, we define pairs of opposing surfaces on the RVE, where for boundary point $\tilde{\boldsymbol{X}}^+ \in \partial\tilde{\Omega}_0$ there is an opposing point $\tilde{\boldsymbol{X}}^- := -\tilde{\boldsymbol{X}}^+ \in \partial\tilde{\Omega}_0$, whose outward normals satisfy $\tilde{\boldsymbol{N}}\left(\tilde{\boldsymbol{X}}^-\right) = -\tilde{\boldsymbol{N}}(\tilde{\boldsymbol{X}}^+)$.

$$[\![\tilde{\boldsymbol{w}}]\!]_{\tilde{\boldsymbol{X}}^-} = [\![\tilde{\boldsymbol{w}}]\!]_{\tilde{\boldsymbol{X}}^+}\,, \quad \left[\nabla_{\tilde{\mathrm{X}}}\tilde{\boldsymbol{w}}\tilde{\boldsymbol{N}}\right]\Big|_{\tilde{\boldsymbol{X}}^-} = -\left[\nabla_{\tilde{\mathrm{X}}}\tilde{\boldsymbol{w}}\tilde{\boldsymbol{N}}\right]\Big|_{\tilde{\boldsymbol{X}}^+} \quad \text{on } \partial\tilde{\Omega}_0. \tag{6.19}$$

Note that $\tilde{\boldsymbol{w}}^+ = \tilde{\boldsymbol{w}}^-$ on $\partial\tilde{\Omega}_0$ inherently restricts the tangential gradient, such that we alternatively write

$$\tilde{\boldsymbol{w}}\left(\tilde{\boldsymbol{X}}^-\right) = \tilde{\boldsymbol{w}}\left(\tilde{\boldsymbol{X}}^+\right), \quad \nabla_{\tilde{\mathrm{X}}}\tilde{\boldsymbol{w}}\left(\tilde{\boldsymbol{X}}^-\right) = \nabla_{\tilde{\mathrm{X}}}\tilde{\boldsymbol{w}}\left(\tilde{\boldsymbol{X}}^+\right) \quad \text{on } \partial\tilde{\Omega}_0 \tag{6.20}$$

for the *Periodic* constraints, see also the illustration in figure 6.2.1.

In the following two remarks we address firstly implications of the unknown $\tilde{\boldsymbol{x}}_c$ in remark 6.2.1 and secondly comment on specifics about setting up an RVE in remark 6.2.2.

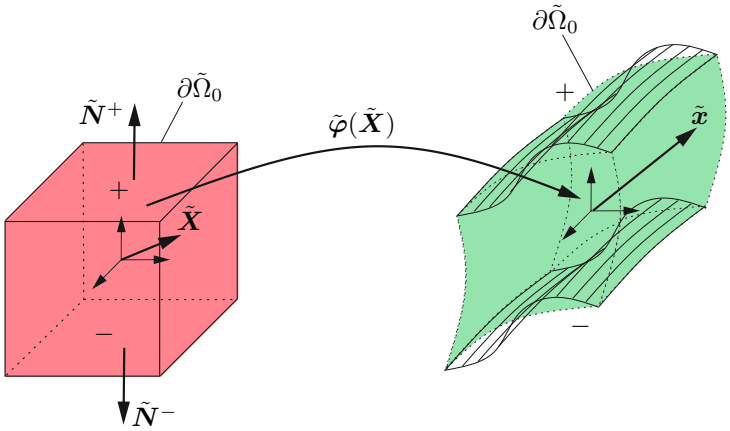


Figure 6.2.1 – Micro-scale BVP: periodicity. Microscopic boundary value problem, periodic boundary constraints on $\partial\tilde{\Omega}_0$, here only displayed for top and bottom for better understanding.

Remark 6.2.1 – Center position and rigid body movement. We point out that, in case of vanishing fluctuations (i.e. constraint (I), eq. (6.17)), the current center position $\tilde{\boldsymbol{x}}_c$ can directly be calculated $\tilde{\boldsymbol{x}}_c = \tilde{\boldsymbol{X}}_c = \boldsymbol{0}$, whereas for Dirichlet (II) and Periodic (III) constraints the center position acts as a translation ("offset"), that with given translational invariance (see section 3.3.1) does not influence the system. Hence

to restrict rigid body translation we set without loss of generality likewise $\tilde{\boldsymbol{x}}_c = \boldsymbol{0}$. Alternatively one may choose any corner position (cf. Kouznetsova [66]). Rigid body rotation is then automatically avoided by choosing Dirichlet constraints (II), whereas for periodicity (III) we additionally restrict fluctuations to vanish at the corners of the RVE

$$\tilde{\boldsymbol{w}}\Big(\Big[\tilde{\boldsymbol{X}}\Big]\Big|_{\text{corner}}\Big) = \boldsymbol{0}\,, \quad \partial\Omega_0^{\tilde{w}} = \partial\Omega_0^{\nabla\tilde{w}} = \bigcup\Big\{\Big[\tilde{\boldsymbol{X}}\Big]\Big|_{\text{corner}}\Big\} \subset \partial\tilde{\Omega}_0\,, \tag{6.21}$$

making enforcement necessary for a single corner due to periodicity.

Remark 6.2.2 – Choice of RVE. The construction of a representative volume element is a constitutive component, as its geometry, orientation, size, and boundary conditions may directly influence the recovered macroscopic response (see Schröder [101], Kouznetsova et al. [69] and Bargmann et al. [11] among others).

For periodic microstructures, the natural choice is a unit cell reflecting the inherent material symmetry. Such a unit cell can be stacked into a single RVE comprising an integer number of repetitions in every spatial direction to reduce boundary induced effects, as long as the microstructural length scale remains small compared to macroscopic variations. Non-periodic microstructures, e.g. as in section 5.6.4, the influence of geometric choices increases due to localization (cf. Glüge [48]), and generally different shapes can be used (e.g. spheres in Glüge et al. [47]). For further reading we also point to Ostoja-Starzewski [90], Kanit et al. [63].

Moreover another influence lies in the choice of energetic consistency constraint (I), (II) or (III). In Schröder [101] and Glüge [48] it is further shown, that constraint (I) as higher order equivalent of a uniform displacement tends to produce an upper bound on stiffness, whereas traction boundaries, i.e. prescribing surface tractions instead of deformation, produces a lower bound. We point out, that periodicity (III) in general is the most flexible, as less actual fluctuation degrees of freedom are restricted. This is addressed in some simulations in section 6.6.1.

6.2.2 Energetic micro-macro transition

Besides kinematic averaging, we further assume energetically consistent the volumetric average of the micro-scale Helmholtz-energy $\tilde{\Psi}$ to be equal to the macro-scale potential

$$\Psi = \frac{1}{|\tilde{\Omega}_0|}\int_{\tilde{\Omega}_0}\big\{\tilde{\Psi}\big\}\mathrm{d}\tilde{V}\,, \tag{6.22}$$

such that macroscopic stresses now yield

$$\boldsymbol{P} = \frac{1}{|\tilde{\Omega}_0|}\int_{\tilde{\Omega}_0}\left\{\frac{\partial\tilde{\Psi}}{\partial\boldsymbol{F}}\right\}\mathrm{d}\tilde{V} \quad \text{and} \quad \mathfrak{P} = \frac{1}{|\tilde{\Omega}_0|}\int_{\tilde{\Omega}_0}\left\{\frac{\partial\tilde{\Psi}}{\partial\mathfrak{F}}\right\}\mathrm{d}\tilde{V}\,. \tag{6.23}$$

Before investigating these further, we define micro-scale first- and second-order stresses as

$$\tilde{\boldsymbol{P}} = \frac{\partial \tilde{\Psi}}{\partial \tilde{\boldsymbol{F}}} \quad \text{and} \quad \tilde{\mathfrak{P}} = \frac{\partial \tilde{\Psi}}{\partial \tilde{\mathfrak{F}}} \,. \tag{6.24}$$

Applying chain rule and inserting eq. (6.10), the first order macro-stress reads

$$\boldsymbol{P} = \frac{1}{|\tilde{\Omega}_0|} \int_{\tilde{\Omega}_0} \left\{ \frac{\partial \tilde{\Psi}}{\partial \boldsymbol{F}} \right\} \mathrm{d}\tilde{V} = \frac{1}{|\tilde{\Omega}_0|} \int_{\tilde{\Omega}_0} \left\{ \frac{\partial \tilde{\Psi}}{\partial \tilde{\boldsymbol{F}}} : \frac{\partial \tilde{\boldsymbol{F}}}{\partial \boldsymbol{F}} \right\} \mathrm{d}\tilde{V} = \frac{1}{|\tilde{\Omega}_0|} \int_{\tilde{\Omega}_0} \left\{ \tilde{\boldsymbol{P}} \right\} \mathrm{d}\tilde{V} \,, \tag{6.25}$$

which ends up as volumetric average of the first order micro-scale stress. We analogously obtain for the second-order

$$\mathfrak{P} = \frac{1}{|\tilde{\Omega}_0|} \int_{\tilde{\Omega}_0} \left\{ \frac{\partial \tilde{\Psi}}{\partial \mathfrak{F}} \right\} \mathrm{d}\tilde{V} = \frac{1}{|\tilde{\Omega}_0|} \int_{\tilde{\Omega}_0} \left\{ \frac{\partial \tilde{\Psi}}{\partial \tilde{\boldsymbol{F}}} : \frac{\partial \tilde{\boldsymbol{F}}}{\partial \mathfrak{F}} + \frac{\partial \tilde{\Psi}}{\partial \tilde{\mathfrak{F}}} \vdots \frac{\partial \tilde{\mathfrak{F}}}{\partial \mathfrak{F}} \right\} \mathrm{d}\tilde{V} = \frac{1}{|\tilde{\Omega}_0|} \int_{\tilde{\Omega}_0} \left\{ \tilde{\boldsymbol{P}} \otimes \tilde{\boldsymbol{X}} + \tilde{\mathfrak{P}} \right\} \mathrm{d}\tilde{V} \,, \tag{6.26}$$

containing the second-order contribution $\tilde{\mathfrak{P}}$ in combination with the micro-scale (leveraged) first order stress-moment $\tilde{\boldsymbol{P}} \otimes \tilde{\boldsymbol{X}}$. For reference, $^{\partial \tilde{\boldsymbol{F}}}/_{\partial \boldsymbol{F}}$ and $^{\partial \tilde{\mathfrak{F}}}/_{\partial \mathfrak{F}}$ represent the second- and third-order identity tensors, respectively.

6.3 Variational formulation

For the derivation of balance equation and the weak total system, we adapt the macroscopic boundary value problem presented in section 6.1 towards the energy formulation eq. (6.22), leading to the internal energy as double integral over macro- and micro-domain

$$\Pi^{\mathrm{int}}(\boldsymbol{\varphi}, \tilde{\boldsymbol{w}}) \coloneqq \int_{\Omega_0} \{\Psi(\boldsymbol{\varphi}, \tilde{\boldsymbol{w}})\} \mathrm{d}V = \int_{\Omega_0} \left\{ \frac{1}{|\tilde{\Omega}_0|} \int_{\tilde{\Omega}_0} \left\{ \tilde{\Psi}\left(\tilde{\boldsymbol{F}}(\boldsymbol{\varphi}, \tilde{\boldsymbol{w}}), \tilde{\mathfrak{F}}(\boldsymbol{\varphi}, \tilde{\boldsymbol{w}}) \right) \right\} \mathrm{d}\tilde{V} \right\} \mathrm{d}V \,. \tag{6.27}$$

We assume external contributions nonetheless being restricted to the macro-domain

$$\Pi^{\mathrm{ext}}(\boldsymbol{\varphi}) \coloneqq \int_{\Omega_0} \left\{ \boldsymbol{\varphi} \cdot \overline{\boldsymbol{B}} \right\} \mathrm{d}V + \int_{\partial \Omega_0^T} \left\{ \boldsymbol{\varphi} \cdot \overline{\boldsymbol{T}} \right\} \mathrm{d}A + \int_{\partial \Omega_0^M} \left\{ \nabla_{\mathrm{X}} \boldsymbol{\varphi} : \overline{\boldsymbol{M}} \right\} \mathrm{d}A \,, \tag{6.28}$$

as the microstructure is not directly exposed to external loads, especially regarding scale-differences. Furthermore, this maintains energetic consistency, see remark 6.3.4, as internal loads would increase micro-scale energy. Without loss of generality we neglect volumetric forces, hence set $\overline{\boldsymbol{B}} = \boldsymbol{0}$.

Stationarity of the energy balance with respect to the paired primary fields $(\boldsymbol{\varphi}, \tilde{\boldsymbol{w}})$ accordingly gives the minimization problem

$$\{\boldsymbol{\varphi}^*, \tilde{\boldsymbol{w}}^*\} = \arg \left\{ \inf_{(\boldsymbol{\varphi}, \tilde{\boldsymbol{w}}) \in \mathcal{V}_{\boldsymbol{\varphi}} \times \mathcal{V}_{\tilde{\boldsymbol{w}}}} \Pi^{\mathrm{int}}(\boldsymbol{\varphi}, \tilde{\boldsymbol{w}}) - \Pi^{\mathrm{ext}}(\boldsymbol{\varphi}) \right\} \tag{6.29}$$

for the solution $\{\boldsymbol{\varphi}^*, \tilde{\boldsymbol{w}}^*\}$ of suitable spaces $\mathcal{V}_{\boldsymbol{\varphi}}$ and $\mathcal{V}_{\tilde{\boldsymbol{w}}}$ as energetic minimizers of the multi-scale formulation. Assuming non-vanishing micro-scale fluctuations, i.e. employing constraints (II) or (III), variation requires the introduction of the micro-scale fluctuation trial space

$$\mathcal{V}_{\delta\tilde{\boldsymbol{w}}} = \left\{ \delta\tilde{\boldsymbol{w}} \in \mathrm{L}^2\Big(\Omega_0; \mathcal{H}^2\Big(\tilde{\Omega}_0\Big)\Big) \mid \delta\tilde{\boldsymbol{w}} = \boldsymbol{0} \text{ on } \partial\Omega_0^{\tilde{w}} \,, \quad \nabla_{\!\mathrm{X}}\, \delta\tilde{\boldsymbol{w}} \tilde{\boldsymbol{N}} = \boldsymbol{0} \text{ on } \partial\Omega_0^{\nabla\tilde{w}} \right\}. \tag{6.30}$$

Remark 6.3.1 – Fluctuation function space. Note that for completeness, the solution space coincides with the trial space, as the Dirichlet constraints contained in (II) or (III) also set $\delta\tilde{\boldsymbol{w}} = \boldsymbol{0}$ on $\partial\Omega_0^{\tilde{w}}$ and $\nabla_{\!\mathrm{X}}\, \delta\tilde{\boldsymbol{w}} \tilde{\boldsymbol{N}} = \boldsymbol{0}$ on $\partial\Omega_0^{\nabla\tilde{w}}$. If periodicity (III) is chosen, constraint eq. (6.20) is also valid for the variation of fluctuations, i.e. $\tilde{\boldsymbol{w}}\big(\tilde{\boldsymbol{X}}^-\big) = \tilde{\boldsymbol{w}}\big(\tilde{\boldsymbol{X}}^+\big)$ and $\nabla_{\!\mathrm{X}}\, \tilde{\boldsymbol{w}}\big(\tilde{\boldsymbol{X}}^-\big) = \nabla_{\!\mathrm{X}}\, \tilde{\boldsymbol{w}}\big(\tilde{\boldsymbol{X}}^+\big)$ on $\partial\tilde{\Omega}_0$.

We further point out $\delta\boldsymbol{\varphi} \in \mathcal{H}^1(\Omega_0)$ and $\delta\tilde{\boldsymbol{w}} \in \mathrm{L}^2\Big(\Omega_0; \mathcal{H}^1\Big(\tilde{\Omega}_0\Big)\Big)$ is sufficient in case of vanishing second-order contributions on both scales, thus leaving multi-scale first order continua.

Applying variational calculus, the internal energy yields

$$\begin{aligned}
\delta\Pi^{\mathrm{int}} &= \int_{\Omega_0} \left\{ \frac{1}{|\tilde{\Omega}_0|} \int_{\tilde{\Omega}_0} \Big\{ \delta\tilde{\Psi}\Big(\tilde{\boldsymbol{F}}(\boldsymbol{F}, \tilde{\boldsymbol{\mathfrak{F}}}, \nabla_{\!\mathrm{X}}\, \tilde{\boldsymbol{w}}), \tilde{\tilde{\boldsymbol{\mathfrak{F}}}}\Big(\tilde{\boldsymbol{\mathfrak{F}}}, \nabla^2_{\!\mathrm{X}}\, \tilde{\boldsymbol{w}}\Big)\Big)\Big\} \mathrm{d}\tilde{V} \right\} \mathrm{d}V \\
&= \int_{\Omega_0} \left\{ \frac{1}{|\tilde{\Omega}_0|} \int_{\tilde{\Omega}_0} \Big\{ \frac{\partial\tilde{\Psi}}{\partial\tilde{\boldsymbol{F}}} : \delta\tilde{\boldsymbol{F}} + \frac{\partial\tilde{\Psi}}{\partial\tilde{\boldsymbol{\mathfrak{F}}}} \vdots \delta\tilde{\boldsymbol{\mathfrak{F}}} \Big\} \mathrm{d}\tilde{V} \right\} \mathrm{d}V \\
&= \int_{\Omega_0} \left\{ \frac{1}{|\tilde{\Omega}_0|} \int_{\tilde{\Omega}_0} \Big\{ \tilde{\boldsymbol{P}} : \Big(\nabla_{\!\mathrm{X}}\, \delta\boldsymbol{\varphi} + \nabla^2_{\!\mathrm{X}}\, \delta\boldsymbol{\varphi}\, \tilde{\boldsymbol{X}} + \nabla_{\!\mathrm{X}}\, \delta\tilde{\boldsymbol{w}} \Big) + \tilde{\boldsymbol{\mathfrak{P}}} \vdots \Big(\nabla^2_{\!\mathrm{X}}\, \delta\boldsymbol{\varphi} + \nabla^2_{\!\mathrm{X}}\, \delta\tilde{\boldsymbol{w}} \Big) \Big\} \mathrm{d}\tilde{V} \right\} \mathrm{d}V \\
&= \int_{\Omega_0} \left\{ \frac{1}{|\tilde{\Omega}_0|} \int_{\tilde{\Omega}_0} \Big\{ \tilde{\boldsymbol{P}} : \nabla_{\!\mathrm{X}}\, \delta\boldsymbol{\varphi} + \Big(\tilde{\boldsymbol{P}} \otimes \tilde{\boldsymbol{X}} + \tilde{\boldsymbol{\mathfrak{P}}} \Big) \vdots \nabla^2_{\!\mathrm{X}}\, \delta\boldsymbol{\varphi} + \tilde{\boldsymbol{P}} : \nabla_{\!\mathrm{X}}\, \delta\tilde{\boldsymbol{w}} + \tilde{\boldsymbol{\mathfrak{P}}} \vdots \nabla^2_{\!\mathrm{X}}\, \delta\tilde{\boldsymbol{w}} \Big\} \mathrm{d}\tilde{V} \right\} \mathrm{d}V \\
&= \int_{\Omega_0} \Big\{ \boldsymbol{P} : \nabla_{\!\mathrm{X}}\, \delta\boldsymbol{\varphi} + \boldsymbol{\mathfrak{P}} \vdots \nabla^2_{\!\mathrm{X}}\, \delta\boldsymbol{\varphi} \Big\} \mathrm{d}V + \int_{\Omega_0} \left\{ \frac{1}{|\tilde{\Omega}_0|} \int_{\tilde{\Omega}_0} \Big\{ \tilde{\boldsymbol{P}} : \nabla_{\!\mathrm{X}}\, \delta\tilde{\boldsymbol{w}} + \tilde{\boldsymbol{\mathfrak{P}}} \vdots \nabla^2_{\!\mathrm{X}}\, \delta\tilde{\boldsymbol{w}} \Big\} \mathrm{d}\tilde{V} \right\} \mathrm{d}V \,,
\end{aligned} \tag{6.31}$$

where for the last line we inserted eq. (6.25)-(6.26) and used $\int_{\tilde{\Omega}_0}\{A\} = A\,|\tilde{\Omega}_0|\,, A \notin \tilde{\Omega}_0$.

Remark 6.3.2 – Stress symmetry. Note that due to the symmetry of $\nabla^2_{\!\mathrm{X}}\, \tilde{\boldsymbol{w}}$, we may be alternatively write

$$\boldsymbol{\mathfrak{P}} = \frac{1}{2\,|\tilde{\Omega}_0|} \int_{\tilde{\Omega}_0} \Big\{ \tilde{\boldsymbol{P}} \otimes \tilde{\boldsymbol{X}} + \tilde{\boldsymbol{\mathfrak{P}}} + \Big(\tilde{\boldsymbol{P}} \otimes \tilde{\boldsymbol{X}} + \tilde{\boldsymbol{\mathfrak{P}}} \Big)^{\top 23} \Big\} \mathrm{d}\tilde{V} \,. \tag{6.32}$$

With variation of external contributions in eq. (6.28), stationarity $\delta\Pi^{\text{int}} = \delta\Pi^{\text{ext}}$ results in

$$\int_{\Omega_0}\Big\{\boldsymbol{P} : \nabla_{\mathrm{X}}\delta\boldsymbol{\varphi} + \boldsymbol{\mathfrak{P}} \vdots \nabla^2_{\mathrm{X}}\delta\boldsymbol{\varphi}\Big\}\mathrm{d}V + \int_{\Omega_0}\Bigg\{\frac{1}{|\tilde{\Omega}_0|}\int_{\tilde{\Omega}_0}\Big\{\tilde{\boldsymbol{P}} : \nabla_{\mathrm{X}}\delta\tilde{\boldsymbol{w}} + \tilde{\boldsymbol{\mathfrak{P}}} \vdots \nabla^2_{\mathrm{X}}\delta\tilde{\boldsymbol{w}}\Big\}\mathrm{d}\tilde{V}\Bigg\}\mathrm{d}V$$
$$= \int_{\partial\Omega_0^T}\Big\{\delta\boldsymbol{\varphi}\cdot\overline{\boldsymbol{T}}\Big\}\mathrm{d}A + \int_{\partial\Omega_0^M}\Big\{\nabla_{\mathrm{X}}\delta\boldsymbol{\varphi} : \overline{\boldsymbol{M}}\Big\}\mathrm{d}A \quad \forall(\delta\boldsymbol{\varphi},\delta\tilde{\boldsymbol{w}}) \in \mathcal{V}_{\delta\boldsymbol{\varphi}}\times\mathcal{V}_{\delta\tilde{\boldsymbol{w}}}\,, \quad (6.33)$$

which we equivalently write as

$$R_{\boldsymbol{\varphi}} \coloneqq \int_{\Omega_0}\Big\{\boldsymbol{P} : \nabla_{\mathrm{X}}\delta\boldsymbol{\varphi} + \boldsymbol{\mathfrak{P}} \vdots \nabla^2_{\mathrm{X}}\delta\boldsymbol{\varphi}\Big\}\mathrm{d}V$$
$$- \int_{\partial\Omega_0^T}\Big\{\delta\boldsymbol{\varphi}\cdot\overline{\boldsymbol{T}}\Big\}\mathrm{d}A - \int_{\partial\Omega_0^M}\Big\{\nabla_{\mathrm{X}}\delta\boldsymbol{\varphi} : \overline{\boldsymbol{M}}\Big\}\mathrm{d}A = 0 \qquad \forall\delta\boldsymbol{\varphi}\in\mathcal{V}_{\delta\boldsymbol{\varphi}}\,, \quad (6.34)$$

$$R_{\tilde{\boldsymbol{w}}} \coloneqq \int_{\Omega_0}\Bigg\{\frac{1}{|\tilde{\Omega}_0|}\int_{\tilde{\Omega}_0}\Big\{\tilde{\boldsymbol{P}} : \nabla_{\mathrm{X}}\delta\tilde{\boldsymbol{w}} + \tilde{\boldsymbol{\mathfrak{P}}} \vdots \nabla^2_{\mathrm{X}}\delta\tilde{\boldsymbol{w}}\Big\}\mathrm{d}\tilde{V}\Bigg\}\mathrm{d}V = 0 \qquad \forall\delta\tilde{\boldsymbol{w}}\in\mathcal{V}_{\delta\tilde{\boldsymbol{w}}}\,. \quad (6.35)$$

Note that above equilibrium equations are possibly subjected to the periodicity constraint eq. (6.20). Within the multi-scale framework eq. (6.34) hereby recasts the well-known weak formulation for the macro-scale second-order continuum, whose material relations are henceforth obtained by homogenization of micro-domain stresses. The second equation (6.35) represents the micro-scale equilibrium which will be investigated in the following two remarks.

Remark 6.3.3 – Micro-scale equilibrium. Applying the divergence theorem on the inner integral in eq. (6.35), we obtain analogously to eq. (3.26) now for the micro-scale

$$\int_{\tilde{\Omega}_0}\Big\{\delta\tilde{\boldsymbol{w}}\cdot\Big(\nabla_{\mathrm{X}}\cdot\Big(\nabla_{\mathrm{X}}\cdot\tilde{\boldsymbol{\mathfrak{P}}} - \tilde{\boldsymbol{P}}\Big)\Big)\Big\}\mathrm{d}\tilde{V}$$
$$+ \int_{\partial\tilde{\Omega}_0}\Big\{\delta\tilde{\boldsymbol{w}}\cdot\Big(\Big(\tilde{\boldsymbol{P}} - \nabla_{\mathrm{X}}\cdot\tilde{\boldsymbol{\mathfrak{P}}}\Big)\tilde{\boldsymbol{N}}\Big) + \nabla_{\mathrm{X}}\delta\tilde{\boldsymbol{w}} : \Big(\tilde{\boldsymbol{\mathfrak{P}}}\,\tilde{\boldsymbol{N}}\Big)\Big\}\mathrm{d}\tilde{A}. \quad (6.36)$$

Inserting the previously established boundary conditions for fluctuations, i.e. either eq. (6.17) (Voigt) or (6.18) (Dirichlet), cancel out surface terms and for arbitrary variations we arrive at the micro-scale static equilibrium

$$\nabla_{\mathrm{X}}\cdot\Big(\tilde{\boldsymbol{P}} - \nabla_{\mathrm{X}}\cdot\tilde{\boldsymbol{\mathfrak{P}}}\Big) = \boldsymbol{0} \quad \text{in} \quad \tilde{\Omega}_0\,. \quad (6.37)$$

We point out, that for conformity the periodic boundary conditions eq. (6.20) have to be complemented by antiperiodic traction relations

$$\overline{\tilde{\boldsymbol{M}}}\big(\tilde{\boldsymbol{X}}^+\big) = -\,\overline{\tilde{\boldsymbol{M}}}\big(\tilde{\boldsymbol{X}}^-\big) \quad \text{and} \quad \overline{\tilde{\boldsymbol{T}}}\big(\tilde{\boldsymbol{X}}^+\big) = -\,\overline{\tilde{\boldsymbol{T}}}\big(\tilde{\boldsymbol{X}}^-\big)\,, \quad (6.38)$$

which along with $\mathrm{d}\tilde{A}^- = \mathrm{d}\tilde{A}^+$ and $\tilde{\boldsymbol{N}}^- = -\tilde{\boldsymbol{N}}^+$ result for the surface terms in cancellation

$$\begin{aligned}
&\int_{\partial\tilde{\Omega}_0} \left\{\delta\tilde{\boldsymbol{w}} \cdot \left(\left(\tilde{\boldsymbol{P}} - \nabla_{\tilde{\mathrm{X}}} \cdot \tilde{\boldsymbol{\mathfrak{P}}}\right)\tilde{\boldsymbol{N}}\right) + \nabla_{\tilde{\mathrm{X}}}\delta\tilde{\boldsymbol{w}} : \left(\tilde{\boldsymbol{\mathfrak{P}}}\,\tilde{\boldsymbol{N}}\right)\right\}\mathrm{d}\tilde{A} \\
&= \int_{\partial\tilde{\Omega}_0^+} \left\{\delta\tilde{\boldsymbol{w}}^+ \cdot \left(\left(\tilde{\boldsymbol{P}} - \nabla_{\tilde{\mathrm{X}}} \cdot \tilde{\boldsymbol{\mathfrak{P}}}\right)\tilde{\boldsymbol{N}}\right)^+ + \nabla_{\tilde{\mathrm{X}}}\delta\tilde{\boldsymbol{w}}^+ : \left(\tilde{\boldsymbol{\mathfrak{P}}}\,\tilde{\boldsymbol{N}}\right)^+\right\}\mathrm{d}\tilde{A}^+ \\
&\qquad + \int_{\partial\tilde{\Omega}_0^-} \left\{\delta\tilde{\boldsymbol{w}}^- \cdot \left(\left(\tilde{\boldsymbol{P}} - \nabla_{\tilde{\mathrm{X}}} \cdot \tilde{\boldsymbol{\mathfrak{P}}}\right)\tilde{\boldsymbol{N}}\right)^- + \nabla_{\tilde{\mathrm{X}}}\delta\tilde{\boldsymbol{w}}^- : \left(\tilde{\boldsymbol{\mathfrak{P}}}\,\tilde{\boldsymbol{N}}\right)^-\right\}\mathrm{d}\tilde{A}^- \\
&= \int_{\partial\tilde{\Omega}_0^+} \left\{\delta\tilde{\boldsymbol{w}}^+ \cdot \left(\overline{\tilde{\boldsymbol{T}}}^+ + \overline{\tilde{\boldsymbol{T}}}^-\right) + \nabla_{\tilde{\mathrm{X}}}\delta\tilde{\boldsymbol{w}}^+ : \left(\overline{\tilde{\boldsymbol{M}}}^+ + \overline{\tilde{\boldsymbol{M}}}^-\right)\right\}\mathrm{d}\tilde{A}^+ = \boldsymbol{0}\,,
\end{aligned} \tag{6.39}$$

or in this case are the consequence of static equilibrium with applied kinematic periodicity.

Remark 6.3.4 – Hill-Mandel criterion. Above weak fluctuation equilibrium $R_{\tilde{\boldsymbol{w}}}$ along with the introduced boundary conditions eq. (6.17), (6.18) and (6.20), satisfies the well known *Hill-Mandel criterion*, stating the virtual energy on micro-scale with respect to the micro-motion is equivalent to the virtual macro-scale energy with respect to the macro-motion

$$\frac{1}{|\tilde{\Omega}_0|}\int_{\tilde{\Omega}_0}\left\{\tilde{\boldsymbol{P}} : \nabla_{\tilde{\mathrm{X}}}\delta\tilde{\boldsymbol{\varphi}} + \tilde{\boldsymbol{\mathfrak{P}}} : \nabla^2_{\tilde{\mathrm{X}}}\delta\tilde{\boldsymbol{\varphi}}\right\}\mathrm{d}\tilde{V} = \boldsymbol{P} : \nabla_{\mathrm{X}}\delta\boldsymbol{\varphi} + \boldsymbol{\mathfrak{P}} : \nabla^2_{\mathrm{X}}\delta\boldsymbol{\varphi}\,. \tag{6.40}$$

Therein, the variation of the micro-scale motion $\tilde{\boldsymbol{\varphi}}$ (cf. eq. (6.41)) is done with respect to macro-motion $\boldsymbol{\varphi}$ and micro-fluctuations $\tilde{\boldsymbol{w}}$, reading

$$\delta\tilde{\boldsymbol{\varphi}} = \nabla_{\mathrm{X}}\delta\boldsymbol{\varphi}\,\tilde{\boldsymbol{X}} + \frac{1}{2}\nabla^2_{\mathrm{X}}\delta\boldsymbol{\varphi} : \left(\tilde{\boldsymbol{X}} \otimes \tilde{\boldsymbol{X}}\right) + \nabla_{\tilde{\mathrm{X}}}\delta\tilde{\boldsymbol{w}}\,. \tag{6.41}$$

The left-hand side of eq. (6.40) can be rewritten after insertion as

$$\begin{aligned}
&\frac{1}{|\tilde{\Omega}_0|}\int_{\tilde{\Omega}_0}\left\{\tilde{\boldsymbol{P}} : \left(\nabla_{\mathrm{X}}\delta\boldsymbol{\varphi} + \nabla^2_{\mathrm{X}}\delta\boldsymbol{\varphi}\,\tilde{\boldsymbol{X}} + \nabla_{\tilde{\mathrm{X}}}\delta\tilde{\boldsymbol{w}}\right) + \tilde{\boldsymbol{\mathfrak{P}}} : \left(\nabla^2_{\mathrm{X}}\delta\boldsymbol{\varphi} + \nabla^2_{\tilde{\mathrm{X}}}\delta\tilde{\boldsymbol{w}}\right)\right\}\mathrm{d}\tilde{V} \\
&= \frac{1}{|\tilde{\Omega}_0|}\int_{\tilde{\Omega}_0}\left\{\tilde{\boldsymbol{P}} : \nabla_{\mathrm{X}}\delta\boldsymbol{\varphi} + \left(\tilde{\boldsymbol{P}} \otimes \tilde{\boldsymbol{X}} + \tilde{\boldsymbol{\mathfrak{P}}}\right) : \nabla^2_{\mathrm{X}}\delta\boldsymbol{\varphi} + \tilde{\boldsymbol{P}} : \nabla_{\tilde{\mathrm{X}}}\delta\tilde{\boldsymbol{w}} + \tilde{\boldsymbol{\mathfrak{P}}} : \nabla^2_{\tilde{\mathrm{X}}}\delta\tilde{\boldsymbol{w}}\right\}\mathrm{d}\tilde{V} \\
&= \boldsymbol{P} : \nabla_{\mathrm{X}}\delta\boldsymbol{\varphi} + \boldsymbol{\mathfrak{P}} : \nabla^2_{\mathrm{X}}\delta\boldsymbol{\varphi} + \frac{1}{|\tilde{\Omega}_0|}\underbrace{\int_{\tilde{\Omega}_0}\left\{\tilde{\boldsymbol{P}} : \nabla_{\tilde{\mathrm{X}}}\delta\tilde{\boldsymbol{w}} + \tilde{\boldsymbol{\mathfrak{P}}} : \nabla^2_{\tilde{\mathrm{X}}}\delta\tilde{\boldsymbol{w}}\right\}\mathrm{d}\tilde{V}}_{=0\,,\text{ cf. eq. (6.35) and remark 6.3.3}} \\
&= \boldsymbol{P} : \nabla_{\mathrm{X}}\delta\boldsymbol{\varphi} + \boldsymbol{\mathfrak{P}} : \nabla^2_{\mathrm{X}}\delta\boldsymbol{\varphi}\,,
\end{aligned} \tag{6.42}$$

which is identical to the right hand side in eq. (6.40) and thereby proves the statement.

6.4 Discrete setting

To solve the weak formulation, we adopt the discretization strategy introduced in chapter 2. For approximation (throughout denoted using $(\cdot)^{\mathrm{h}}$), we first employ the same procedure previously for the macro-scale and then cover the micro-scale afterwards.

6.4.1 Macro-scale

Following section 3.5.1, approximation for the macro-fields takes the form

$$\boldsymbol{\varphi}^{\mathrm{h}}(\boldsymbol{X}) = \sum_{A\in\Lambda_\varphi} \boldsymbol{\varphi}_A \mathcal{R}^A(\boldsymbol{X}) \quad \text{and} \quad \delta\boldsymbol{\varphi}^{\mathrm{h}}(\boldsymbol{X}) = \sum_{A\in\Lambda_\varphi} \delta\boldsymbol{\varphi}_A \mathcal{R}^A(\boldsymbol{X})\,, \tag{6.43}$$

using three-dimensional (NURBS-)basis $\mathcal{R}^A : \Omega_0^{\mathrm{h}} \to \mathbb{R}$ of order $\boldsymbol{p}_\varphi$, where $\boldsymbol{X} \in \Omega_0^{\mathrm{h}}$, $\boldsymbol{\varphi}_A, \delta\boldsymbol{\varphi}_A \in \mathbb{R}^3$ and with index-space $\Lambda_\varphi \coloneqq \{1, \dots, \mathfrak{O}_\varphi\}$ for the number of control-points $\mathfrak{O}_\varphi$, together with the corresponding discrete function spaces

$$\begin{aligned}
\mathcal{V}_\varphi^{\mathrm{h}} &\coloneqq \Big\{\boldsymbol{\varphi}^{\mathrm{h}} \in \mathcal{H}^2\big(\Omega_0^{\mathrm{h}}\big) \mid \boldsymbol{\varphi}^{\mathrm{h}} = \overline{\boldsymbol{\varphi}}^{\mathrm{h}} \text{ on } \partial\Omega_0^{\varphi}, \quad \nabla_{\mathrm{X}}\boldsymbol{\varphi}^{\mathrm{h}}\boldsymbol{N} = \overline{\nabla_{\mathrm{X}}\boldsymbol{\varphi}\boldsymbol{N}}^{\mathrm{h}} \text{ on } \partial\Omega_0^{\nabla\varphi}\Big\} \quad \text{and} \\
\mathcal{V}_{\delta\varphi}^{\mathrm{h}} &\coloneqq \Big\{\delta\boldsymbol{\varphi}^{\mathrm{h}} \in \mathcal{H}^2\big(\Omega_0^{\mathrm{h}}\big) \mid \delta\boldsymbol{\varphi}^{\mathrm{h}} = \boldsymbol{0} \text{ on } \partial\Omega_0^{\varphi}, \quad \nabla_{\mathrm{X}}\delta\boldsymbol{\varphi}^{\mathrm{h}}\boldsymbol{N} = \boldsymbol{0} \text{ on } \partial\Omega_0^{\nabla\varphi}\Big\}\,.
\end{aligned} \tag{6.44}$$

With discretization, the macro-balance eq. (6.34) transforms into

$$\begin{aligned}
\delta\boldsymbol{\varphi}_A \cdot \int_{\Omega_0^{\mathrm{h}}} \Big\{\boldsymbol{P}^{\mathrm{h}} \cdot \nabla_{\mathrm{X}}\mathcal{R}^A + \boldsymbol{\mathfrak{P}}^{\mathrm{h}} : \nabla_{\mathrm{X}}^2\mathcal{R}^A\Big\}\mathrm{d}V \\
= \delta\boldsymbol{\varphi}_A \cdot \left(\int_{\partial\Omega_0^{T,\mathrm{h}}} \Big\{\mathcal{R}^A\ \overline{\boldsymbol{T}}^{\mathrm{h}}\Big\}\mathrm{d}A - \int_{\partial\Omega_0^{M,\mathrm{h}}} \Big\{\nabla_{\mathrm{X}\perp}\mathcal{R}^A \cdot \overline{\boldsymbol{M}}^{\mathrm{h}}\Big\}\mathrm{d}A \right) \quad \forall\delta\boldsymbol{\varphi}_A \in \mathbb{R}^3
\end{aligned} \tag{6.45}$$

Applying a suitable quadrature formula (cf. section 2.2.2), transforms integral evaluation into a summation over the functions evaluated at Gauss points $\boldsymbol{X}_{\mathrm{G}}$ multiplied with associated weights w_{G}, where $\mathrm{G} = 1, \dots, n_{\mathrm{gp}}$, yielding

$$\boldsymbol{R}_{\boldsymbol{\varphi}}^A = \sum_{\mathrm{G}=1}^{n_{\mathrm{gp}}} \mathrm{w}_{\mathrm{G}}\Big\{\boldsymbol{P}^{\mathrm{h}}\Big(\boldsymbol{X}_{\mathrm{G}}, \tilde{\boldsymbol{X}}\Big) \cdot \nabla_{\mathrm{X}}\mathcal{R}^A(\boldsymbol{X}_{\mathrm{G}}) + \boldsymbol{\mathfrak{P}}^{\mathrm{h}}\Big(\boldsymbol{X}_{\mathrm{G}}, \tilde{\boldsymbol{X}}\Big) : \nabla_{\mathrm{X}}^2\mathcal{R}^A(\boldsymbol{X}_{\mathrm{G}})\Big\} - \overline{\mathbf{F}}_{\mathrm{Q}}^A = \boldsymbol{0}\,, \tag{6.46}$$

where we collected evaluated external contributions into the nodal vector

$$\overline{\mathbf{F}}_{\mathrm{Q}}^A \coloneqq \sum_{\mathrm{H}=1}^{n_{\mathrm{gp}}(T)} \mathrm{w}_{\mathrm{H}}\Big\{\mathcal{R}^A(\boldsymbol{X}_{\mathrm{H}})\ \overline{\boldsymbol{T}}^{\mathrm{h}}\Big\} + \sum_{\mathrm{I}=1}^{n_{\mathrm{gp}}(M)} \mathrm{w}_{\mathrm{I}}\Big\{\nabla_{\mathrm{X}\perp}\mathcal{R}^A(\boldsymbol{X}_{\mathrm{I}}) \cdot \overline{\boldsymbol{M}}^{\mathrm{h}}\Big\}\,. \tag{6.47}$$

Recalling homogenization eq. (6.25)-(6.26), the discrete values for the macroscopic stresses are obtained from the micro-scale for which a similar integration scheme is used, eventually

leading to

$$\begin{aligned}\boldsymbol{P}^{\mathrm{h}}\big(\boldsymbol{X}_{\mathrm{G}},\tilde{\boldsymbol{X}}_{\tilde{\mathrm{K}}}\big) &= \frac{1}{|\tilde{\Omega}_0^{\mathrm{h}}|}\sum_{\tilde{\mathrm{K}}=1}^{\tilde{n}_{\mathrm{gp}}}\tilde{\mathrm{w}}_{\tilde{\mathrm{K}}}\Big\{\tilde{\boldsymbol{P}}^{\mathrm{h}}\big(\boldsymbol{X}_{\mathrm{G}},\tilde{\boldsymbol{X}}_{\tilde{\mathrm{K}}}\big)\Big\} \quad \text{and}\\ \boldsymbol{\mathfrak{P}}^{\mathrm{h}}\big(\boldsymbol{X}_{\mathrm{G}},\tilde{\boldsymbol{X}}_{\tilde{\mathrm{K}}}\big) &= \frac{1}{|\tilde{\Omega}_0^{\mathrm{h}}|}\sum_{\tilde{\mathrm{K}}=1}^{\tilde{n}_{\mathrm{gp}}}\tilde{\mathrm{w}}_{\tilde{\mathrm{K}}}\Big\{\tilde{\boldsymbol{P}}^{\mathrm{h}}\big(\boldsymbol{X}_{\mathrm{G}},\tilde{\boldsymbol{X}}_{\tilde{\mathrm{K}}}\big)\otimes\tilde{\boldsymbol{X}}_{\tilde{\mathrm{K}}}+\tilde{\boldsymbol{\mathfrak{P}}}^{\mathrm{h}}\big(\boldsymbol{X}_{\mathrm{G}},\tilde{\boldsymbol{X}}_{\tilde{\mathrm{K}}}\big)\Big\}.\end{aligned} \tag{6.48}$$

6.4.2 Micro-scale

Regarding the micro-scale, we aim at a suitable approximation of the fluctuations defined in the expanded domain $\Omega_0\times\tilde{\Omega}_0$ and therefore introduce the tensor product of macro- and micro-scale shape functions

$$\begin{aligned}\tilde{\boldsymbol{w}}^{\mathrm{h}}\big(\boldsymbol{X},\tilde{\boldsymbol{X}}\big) &= \sum_{C\in\Lambda_{\bar{\varphi}}}\sum_{B\in\Lambda_{\tilde{w}}}\tilde{\boldsymbol{w}}_{C,B}\,\mathcal{M}^{C}(\boldsymbol{X})\,\tilde{\mathcal{N}}^{B}\big(\tilde{\boldsymbol{X}}\big)\\ \delta\tilde{\boldsymbol{w}}^{\mathrm{h}}\big(\boldsymbol{X},\tilde{\boldsymbol{X}}\big) &= \sum_{C\in\Lambda_{\bar{\varphi}}}\sum_{B\in\Lambda_{\tilde{w}}}\delta\tilde{\boldsymbol{w}}_{C,B}\,\mathcal{W}^{C}(\boldsymbol{X})\,\tilde{\mathcal{N}}^{B}\big(\tilde{\boldsymbol{X}}\big),\end{aligned} \tag{6.49}$$

with $\tilde{\boldsymbol{w}}_{C,B}\,,\ \delta\tilde{\boldsymbol{w}}_{C,B}\in\mathbb{R}^3$. Therein for the micro-scale we have $\tilde{\boldsymbol{X}}\in\tilde{\Omega}_0^{\mathrm{h}}$, $\tilde{\mathcal{N}}^{B}:\tilde{\Omega}_0^{\mathrm{h}}\to\mathbb{R}$ with index-space $\Lambda_{\tilde{w}}:=\{1,\ldots,\mathfrak{O}_{\tilde{w}}\}$ for the number of micro control-points $\mathfrak{O}_{\tilde{w}}$. Correspondingly the macro domain part features $\boldsymbol{X}\in\Omega_0^{\mathrm{h}}$ and shape-functions $\mathcal{M}^{C}$, $\mathcal{W}^{C}:\Omega_0^{\mathrm{h}}\to\mathbb{R}$ for the solution and variational parts, respectively, with index-space $\Lambda_{\bar{\varphi}}:=\{1,\ldots,\mathfrak{O}_{\bar{\varphi}}\}$ for the number of macro points $\mathfrak{O}_{\bar{\varphi}}$. Note that the nature of both macro-domain functions being in L^2 allows for different treatments as will be investigated next.

Concerning the micro-scale weak boundary value problem (6.35), insertion of the approximations provides

$$\begin{aligned}0 &= \int_{\Omega_0}\Bigg\{\frac{1}{|\tilde{\Omega}_0|}\int_{\tilde{\Omega}_0}\Bigg\{\tilde{\boldsymbol{P}}^{\mathrm{h}}\big(\boldsymbol{X},\tilde{\boldsymbol{X}}\big):\Big(\delta\tilde{\boldsymbol{w}}_{C,B}\otimes\nabla_{\tilde{\mathrm{X}}}\Big(\mathcal{M}^{C}(\boldsymbol{X})\,\tilde{\mathcal{N}}^{B}\big(\tilde{\boldsymbol{X}}\big)\Big)\Big)\\ &\qquad\qquad+\tilde{\boldsymbol{\mathfrak{P}}}^{\mathrm{h}}\big(\boldsymbol{X},\tilde{\boldsymbol{X}}\big)\vdots\Big(\delta\tilde{\boldsymbol{w}}_{C,B}\otimes\nabla^2_{\tilde{\mathrm{X}}}\Big(\mathcal{M}^{C}(\boldsymbol{X})\,\tilde{\mathcal{N}}^{B}\big(\tilde{\boldsymbol{X}}\big)\Big)\Big)\Bigg\}\mathrm{d}\tilde{A}\Bigg\}\mathrm{d}V\\ &= \int_{\Omega_0}\Bigg\{\mathcal{M}^{C}(\boldsymbol{X})\,\delta\tilde{\boldsymbol{w}}_{C,B}\cdot\frac{1}{|\tilde{\Omega}_0|}\int_{\tilde{\Omega}_0}\Bigg\{\tilde{\boldsymbol{P}}^{\mathrm{h}}\big(\boldsymbol{X},\tilde{\boldsymbol{X}}\big)\cdot\nabla_{\tilde{\mathrm{X}}}\tilde{\mathcal{N}}^{B}\big(\tilde{\boldsymbol{X}}\big)\\ &\qquad\qquad+\tilde{\boldsymbol{\mathfrak{P}}}^{\mathrm{h}}\big(\boldsymbol{X},\tilde{\boldsymbol{X}}\big):\nabla^2_{\tilde{\mathrm{X}}}\tilde{\mathcal{N}}^{B}\big(\tilde{\boldsymbol{X}}\big)\Bigg\}\mathrm{d}\tilde{V}\Bigg\}\mathrm{d}V\qquad\forall\delta\tilde{\boldsymbol{w}}_{C,B}\in\mathbb{R}^3\end{aligned} \tag{6.50}$$

6.4.3 Choice of Ansatz-functions

To reduce computational effort and to directly link the homogenization procedure to the micro-scale balance equation, we use a Dirac-Delta distribution (cf. remark 2.2.1 and eq. (2.26)) for the macro-domain based shape-functions for virtual fluctuations $\mathcal{W}^C(\boldsymbol{X}) = \delta\big(\boldsymbol{X} - \boldsymbol{X}^C\big)$ to turn the integral into a point-wise evaluation. Setting further all points to be the macro-domain quadrature points $\boldsymbol{X}^C = \boldsymbol{X}_{\mathrm{G}}$, consequently $\mathfrak{O}_{\bar{\varphi}} = n_{\mathrm{gp}}$ and $\Lambda_{\bar{\varphi}} \coloneqq \{1, \ldots, n_{\mathrm{gp}}\}$, yields

$$\delta\tilde{\boldsymbol{w}}^{\mathrm{h}}\big(\boldsymbol{X}, \tilde{\boldsymbol{X}}\big) = \sum_{\mathrm{G}\in\Lambda_{\bar{\varphi}}} \sum_{B\in\Lambda_{\tilde{w}}} \delta(\boldsymbol{X} - \boldsymbol{X}_{\mathrm{G}})\, \tilde{\mathcal{N}}^B\big(\tilde{\boldsymbol{X}}\big)\, \delta\tilde{\boldsymbol{w}}_{\mathrm{G},B} \tag{6.51}$$

Insertion into eq. (6.50) gives

$$\begin{aligned} 0 = \frac{1}{|\tilde{\Omega}_0|}\delta\tilde{\boldsymbol{w}}_{\mathrm{G},B} \cdot \int_{\tilde{\Omega}_0} \Big\{ & \tilde{\boldsymbol{P}}^{\mathrm{h}}\big(\boldsymbol{X}_{\mathrm{G}}, \tilde{\boldsymbol{X}}\big) \cdot \nabla_{\tilde{\mathrm{x}}} \tilde{\mathcal{N}}^B\big(\tilde{\boldsymbol{X}}\big) \\ & + \tilde{\mathfrak{P}}^{\mathrm{h}}\big(\boldsymbol{X}_{\mathrm{G}}, \tilde{\boldsymbol{X}}\big) : \nabla^2_{\tilde{\mathrm{x}}} \tilde{\mathcal{N}}^B\big(\tilde{\boldsymbol{X}}\big) \Big\} \mathrm{d}\tilde{V} \qquad \forall \delta\tilde{\boldsymbol{w}}_{\mathrm{G},B} \in \mathbb{R}^3\,, \end{aligned} \tag{6.52}$$

from which we for arbitrary (scaled) variations $^1/_{|\tilde{\Omega}_0|}\,\delta\tilde{\boldsymbol{w}}_{\mathrm{G},B}$ obtain the micro-scale balance equation for every integration point $\boldsymbol{X}_{\mathrm{G}}$ on the macro-scale

$$\begin{aligned} \boldsymbol{R}^{\mathrm{G},B}_{\tilde{\boldsymbol{w}}} &\coloneqq \int_{\tilde{\Omega}_0} \Big\{ \tilde{\boldsymbol{P}}^{\mathrm{h}}\big(\boldsymbol{X}_{\mathrm{G}}, \tilde{\boldsymbol{X}}\big) \cdot \nabla_{\tilde{\mathrm{x}}} \tilde{\mathcal{N}}^B\big(\tilde{\boldsymbol{X}}\big) + \tilde{\mathfrak{P}}^{\mathrm{h}}\big(\boldsymbol{X}_{\mathrm{G}}, \tilde{\boldsymbol{X}}\big) : \nabla^2_{\tilde{\mathrm{x}}} \tilde{\mathcal{N}}^B\big(\tilde{\boldsymbol{X}}\big) \Big\} \mathrm{d}\tilde{V} \\ &= \sum_{\tilde{\mathrm{K}}=1}^{\tilde{n}_{\mathrm{gp}}} \tilde{\mathrm{w}}_{\tilde{\mathrm{K}}} \Big\{ \tilde{\boldsymbol{P}}^{\mathrm{h}}\big(\boldsymbol{X}_{\mathrm{G}}, \tilde{\boldsymbol{X}}_{\tilde{\mathrm{K}}}\big) \cdot \nabla_{\tilde{\mathrm{x}}} \tilde{\mathcal{N}}^B\big(\tilde{\boldsymbol{X}}_{\tilde{\mathrm{K}}}\big) + \tilde{\mathfrak{P}}^{\mathrm{h}}\big(\boldsymbol{X}_{\mathrm{G}}, \tilde{\boldsymbol{X}}_{\tilde{\mathrm{K}}}\big) : \nabla^2_{\tilde{\mathrm{x}}} \tilde{\mathcal{N}}^B\big(\tilde{\boldsymbol{X}}_{\tilde{\mathrm{K}}}\big) \Big\} = \boldsymbol{0}\,. \end{aligned} \tag{6.53}$$

For further separation of macro- and micro-domain, making homogenization eq. (6.48) computationally simpler, we use Kronecker Delta functions for the macro-scale anchored contributions in the solution $\tilde{\boldsymbol{w}}\big(\boldsymbol{X}, \tilde{\boldsymbol{X}}\big)$ as analogous to the Dirac-Delta distribution for fluctuation variations

$$\mathcal{M}^{\mathrm{G}}(\boldsymbol{X}) = \delta'(\boldsymbol{X} - \boldsymbol{X}_{\mathrm{G}})\,, \quad \text{where} \quad \delta'(\boldsymbol{A}) = \begin{cases} 1, & \text{if } \boldsymbol{A} = 0 \\ 0, & \text{otherwise} \end{cases}. \tag{6.54}$$

Consequently the discrete fluctuations and their gradients only exist (i.e. differ from 0) at the macro-integration points $\boldsymbol{X}_{\mathrm{G}}$ therefore reading

$$\begin{aligned} \tilde{\boldsymbol{w}}\big(\boldsymbol{X}_{\mathrm{G}}, \tilde{\boldsymbol{X}}\big) &= \tilde{\boldsymbol{w}}_{\mathrm{G},B}\, \tilde{\mathcal{N}}^B\big(\tilde{\boldsymbol{X}}\big)\,, \\ \nabla_{\tilde{\mathrm{x}}} \tilde{\boldsymbol{w}}\big(\boldsymbol{X}_{\mathrm{G}}, \tilde{\boldsymbol{X}}\big) &= \tilde{\boldsymbol{w}}_{\mathrm{G},B} \otimes \nabla_{\tilde{\mathrm{x}}} \tilde{\mathcal{N}}^B\big(\tilde{\boldsymbol{X}}\big)\,, \\ \nabla^2_{\tilde{\mathrm{x}}} \tilde{\boldsymbol{w}}\big(\boldsymbol{X}_{\mathrm{G}}, \tilde{\boldsymbol{X}}\big) &= \tilde{\boldsymbol{w}}_{\mathrm{G},B} \otimes \nabla^2_{\tilde{\mathrm{x}}} \tilde{\mathcal{N}}^B\big(\tilde{\boldsymbol{X}}\big)\,. \end{aligned} \tag{6.55}$$

Insertion into the motion, we then can isolate macro- and micro-scale contributions

$$\tilde{\boldsymbol{\varphi}}\Big(\boldsymbol{X}_{\mathrm{G}}, \tilde{\boldsymbol{X}}\Big) = \boldsymbol{F}(\boldsymbol{X}_{\mathrm{G}})\, \tilde{\boldsymbol{X}} + \frac{1}{2}\, \boldsymbol{\mathfrak{F}}(\boldsymbol{X}_{\mathrm{G}}) : \Big(\tilde{\boldsymbol{X}} \otimes \tilde{\boldsymbol{X}}\Big) + \tilde{\boldsymbol{w}}\Big(\tilde{\boldsymbol{X}}\Big)\,, \tag{6.56}$$

revealing the only transfer from the macro- to micro-scale lying in forwarding discrete evaluated deformation tensors $\boldsymbol{F}(\boldsymbol{X}_{\mathrm{G}})$ and $\boldsymbol{\mathfrak{F}}(\boldsymbol{X}_{\mathrm{G}})$. Together with the point-wise micro-scale equilibrium eq. (6.53), the choice of paired Dirac-Delta functions ultimately recasts the classical FE^2 or generalized IGA^2 formalism (e.g. Schröder [101] and Schmidt et al. [100] among others).

6.4.4 Discrete multi-scale framework

In combination, the full discrete multi-scale framework choosing Dirac-Delta reads

$$\begin{aligned}
\boldsymbol{R}^A_{\boldsymbol{\varphi}} &= \sum_{\mathrm{G}=1}^{n_{\mathrm{gp}}} \mathrm{w}_{\mathrm{G}} \Bigg\{ \frac{1}{|\tilde{\Omega}^{\mathrm{h}}_0|} \sum_{\tilde{\mathrm{K}}=1}^{\tilde{n}_{\mathrm{gp}}} \tilde{\mathrm{w}}_{\tilde{\mathrm{K}}} \Big\{ \tilde{\boldsymbol{P}}^{\mathrm{h}}\Big(\boldsymbol{X}_{\mathrm{G}}, \tilde{\boldsymbol{X}}_{\tilde{\mathrm{K}}}\Big) \cdot \nabla_{\mathrm{x}} \mathcal{R}^A(\boldsymbol{X}_{\mathrm{G}}) \Big\} \\
&\qquad + \frac{1}{|\tilde{\Omega}^{\mathrm{h}}_0|} \sum_{\tilde{\mathrm{K}}=1}^{\tilde{n}_{\mathrm{gp}}} \tilde{\mathrm{w}}_{\tilde{\mathrm{K}}} \Big\{ \Big(\tilde{\boldsymbol{P}}^{\mathrm{h}}\Big(\boldsymbol{X}_{\mathrm{G}}, \tilde{\boldsymbol{X}}_{\tilde{\mathrm{K}}}\Big) \otimes \tilde{\boldsymbol{X}}_{\tilde{\mathrm{K}}} + \tilde{\boldsymbol{\mathfrak{P}}}^{\mathrm{h}}\Big(\boldsymbol{X}_{\mathrm{G}}, \tilde{\boldsymbol{X}}_{\tilde{\mathrm{K}}}\Big) \Big) : \nabla^2_{\mathrm{x}} \mathcal{R}^A(\boldsymbol{X}_{\mathrm{G}}) \Big\} \Bigg\} - \overline{\mathbf{F}}^A_{\mathrm{Q}} = \mathbf{0}\,, \\
\boldsymbol{R}^B_{\tilde{\boldsymbol{w}}} &= \sum_{\mathrm{G}=1}^{n_{\mathrm{gp}}} \Big\{ \boldsymbol{R}^{\mathrm{G},B}_{\tilde{\boldsymbol{w}}} \Big\} \\
&= \sum_{\mathrm{G}=1}^{n_{\mathrm{gp}}} \Bigg\{ \sum_{\tilde{\mathrm{K}}=1}^{\tilde{n}_{\mathrm{gp}}} \tilde{\mathrm{w}}_{\tilde{\mathrm{K}}} \Big\{ \tilde{\boldsymbol{P}}^{\mathrm{h}}\Big(\boldsymbol{X}_{\mathrm{G}}, \tilde{\boldsymbol{X}}_{\tilde{\mathrm{K}}}\Big) \cdot \nabla_{\tilde{\mathrm{x}}} \tilde{\mathcal{N}}^B\Big(\tilde{\boldsymbol{X}}_{\tilde{\mathrm{K}}}\Big) + \tilde{\boldsymbol{\mathfrak{P}}}^{\mathrm{h}}\Big(\boldsymbol{X}_{\mathrm{G}}, \tilde{\boldsymbol{X}}_{\tilde{\mathrm{K}}}\Big) : \nabla^2_{\tilde{\mathrm{x}}} \tilde{\mathcal{N}}^B\Big(\tilde{\boldsymbol{X}}_{\tilde{\mathrm{K}}}\Big) \Big\} \Bigg\} = \mathbf{0}\,.
\end{aligned} \tag{6.57}$$

accompanied by discrete macro-scale boundary conditions

$$\begin{aligned}
\boldsymbol{\varphi}^{\mathrm{h}} = \overline{\boldsymbol{\varphi}}^{\mathrm{h}} \text{ on } \partial\Omega_0^{\varphi,\mathrm{h}}\,, \quad \nabla_{\mathrm{x}} \boldsymbol{\varphi}^{\mathrm{h}} \boldsymbol{N}^{\mathrm{h}} = \overline{\nabla_{\mathrm{x}} \boldsymbol{\varphi} \boldsymbol{N}}^{\mathrm{h}} \text{ on } \partial\Omega_0^{\nabla\varphi,\mathrm{h}}\,, \\
\big(\boldsymbol{P} - \nabla_{\mathrm{x}} \cdot \boldsymbol{\mathfrak{P}}\big)^{\mathrm{h}} \boldsymbol{N}^{\mathrm{h}} = \overline{\boldsymbol{T}}^{\mathrm{h}} \text{ on } \partial\Omega_0^{T,\mathrm{h}}\,, \quad \boldsymbol{\mathfrak{P}}^{\mathrm{h}} \boldsymbol{N}^{\mathrm{h}} = \overline{\boldsymbol{M}}^{\mathrm{h}} \text{ on } \partial\Omega_0^{M,\mathrm{h}}\,.
\end{aligned} \tag{6.58}$$

We point out that explicitly writing out the homogenization procedure without equivalent transformations to include macro quantities like w_{G}, allow for an easier implementation and, in combination with the Dirac-Delta setting, to separate macro- from micro-processes as detailed in algorithm 6.4.1.

Depending on the choice of fluctuation restriction (I) to (III), discrete counterparts have to be enforced. Since the paired Dirac-Delta functions separate the micro-scale fluctuations from macro-scale influence on the shape-functions, we can write the micro-scale boundary conditions independently and therefore omit any integration point index $(\cdot)_{\mathrm{G}}$.

(Id) **Voigt.** For vanishing fluctuations over the whole micro-domain we set $\tilde{\boldsymbol{w}}_B = \mathbf{0} \quad \forall \tilde{\boldsymbol{w}}_B \in \mathbb{R}^3$.

(IId) **Dirichlet.** Constraint eq. (6.18) may be written in a simple approach using a set of evaluation points $\boldsymbol{P}_i \in \partial\tilde{\Omega}_0^{\mathrm{h}}$, $i \in \mathcal{I} \coloneqq \{1, \dots, \mathfrak{O}_D\}$ along the boundary for which we require

$$\left| \begin{matrix} \sum_{B\in\Lambda_{\tilde{w}}} \tilde{\mathcal{N}}^B(\boldsymbol{P}_i)\, \tilde{\boldsymbol{w}}_B & = \boldsymbol{0} \\ \sum_{B\in\Lambda_{\tilde{w}}} \nabla_{\bar{\mathrm{x}}} \tilde{\mathcal{N}}^B(\boldsymbol{P}_i)\, \tilde{\boldsymbol{w}}_B & = \boldsymbol{0} \end{matrix} \right| \quad \forall \boldsymbol{P}_i \in \partial\tilde{\Omega}_0^{\mathrm{h}}\,, \tag{6.59}$$

providing $d = 3$ scalar equations for the first order constraint and additionally d^2 scalar equations if a second-order domain is assumed. Denoting $\tilde{\boldsymbol{q}} = \{\tilde{\boldsymbol{w}}_B\} = \{\tilde{w}_b\}$, with $b \in \Lambda_{\tilde{\boldsymbol{q}}} \coloneqq \{1, \dots, d\,\mathfrak{O}_{\tilde{w}}\}$ as set of total scalar degrees of freedom for the discrete fluctuations, the point-wise constraint can be written as linear equation system $\boldsymbol{A}\,\tilde{\boldsymbol{q}} = \boldsymbol{0}$, where $\boldsymbol{A} \in \mathbb{R}^{n_{\mathrm{cd}} \times d\,\mathfrak{O}_{\tilde{w}}}$ with the number of total scalar Dirichlet constraints $n_{\mathrm{cd}} = (d + d^2)\,\mathfrak{O}_D$. As in general only boundary associated degrees of freedom are affected, we introduce the active index set $\Lambda_A \subseteq \Lambda_{\tilde{\boldsymbol{q}}}$, collecting indices of corresponding nonzero columns of $\boldsymbol{A}$. With the restriction operator $\mathbf{R}_A \in \{0,1\}^{|\Lambda_A| \times |\Lambda_{\tilde{\boldsymbol{q}}}|}$ we can now identify active parts for the degrees of freedom $\hat{\tilde{\boldsymbol{q}}} \coloneqq \mathbf{R}_A \tilde{\boldsymbol{q}}$ and the constraint matrix $\widehat{\boldsymbol{A}} \coloneqq \boldsymbol{A}\mathbf{R}^\top{}_A$. Ultimately setting

$$\hat{\tilde{\boldsymbol{q}}}_A = \boldsymbol{0} \tag{6.60}$$

we subsequently fulfill $\widehat{\boldsymbol{A}}\,\hat{\tilde{\boldsymbol{q}}}_A = \boldsymbol{0}$ and thereby eq. (6.59).

(IIId) **Periodic.** Analogous to the periodicity constraint, we introduce sets of opposing evaluation points $\left\{\boldsymbol{P}_j^+, \boldsymbol{P}_j^-\right\} \in \partial\tilde{\Omega}_0^{\mathrm{h}}$, $j \in \mathcal{J} \coloneqq \{1, \dots, \mathfrak{O}_P\}$, such that eq. (6.20) is formulated as

$$\left| \begin{matrix} \sum_{B\in\Lambda_{\tilde{w}}} \left(\tilde{\mathcal{N}}^B\left(\boldsymbol{P}_j^+\right) - \tilde{\mathcal{N}}^B\left(\boldsymbol{P}_j^-\right)\right) \tilde{\boldsymbol{w}}_B & = \boldsymbol{0} \\ \sum_{B\in\Lambda_{\tilde{w}}} \left(\nabla_{\bar{\mathrm{x}}}\tilde{\mathcal{N}}^B\left(\boldsymbol{P}_j^+\right) - \nabla_{\bar{\mathrm{x}}}\tilde{\mathcal{N}}^B\left(\boldsymbol{P}_j^-\right)\right) \tilde{\boldsymbol{w}}_B & = \boldsymbol{0} \end{matrix} \right| \quad \forall \left\{\boldsymbol{P}_j^+, \boldsymbol{P}_j^-\right\} \in \partial\tilde{\Omega}_0\,, \tag{6.61}$$

which again can be rewritten as a linear equation system $\boldsymbol{B}\,\tilde{\boldsymbol{q}} = \boldsymbol{0}$ with $\boldsymbol{B} \in \mathbb{R}^{n_{\mathrm{cp}} \times d\,\mathfrak{O}_{\tilde{w}}}$, where $n_{\mathrm{cp}} = (d + d^2)\,\mathfrak{O}_P$ is the number of total scalar periodicity constraints. With corresponding active index set $\Lambda_B \subseteq \Lambda_{\tilde{\boldsymbol{q}}}$ and restriction operator $\mathbf{R}_B \in \{0,1\}^{|\Lambda_B| \times |\Lambda_{\tilde{\boldsymbol{q}}}|}$ we can now collect involved degrees of freedom $\hat{\tilde{\boldsymbol{q}}} \coloneqq \mathbf{R}_B \tilde{\boldsymbol{q}}$ and create the active constraint matrix $\widehat{\boldsymbol{B}} \coloneqq \boldsymbol{B}\mathbf{R}^\top{}_B$. The discrete periodicity condition can then be written equivalently as $\widehat{\boldsymbol{B}}\,\hat{\tilde{\boldsymbol{q}}}_B = \boldsymbol{0}$.

Following Dittmann et al. [34] we now assume, that the active index set can be partitioned into two disjoint subsets $\Lambda_B = \Lambda_{B1} \cup \Lambda_{B2}$, where $\Lambda_{B1} \cap \Lambda_{B2} = \emptyset$, such that we decompose restricted constrained matrix and vector $\hat{\tilde{\boldsymbol{q}}}_B = \left(\hat{\tilde{\boldsymbol{q}}}_1\,,\ \hat{\tilde{\boldsymbol{q}}}_2\right)^\top$ and $\widehat{\boldsymbol{B}} = \left(\widehat{\boldsymbol{B}}_1\,,\ \widehat{\boldsymbol{B}}_2\right)$, where $\hat{\tilde{\boldsymbol{q}}}_1 \in \mathbb{R}^{|\Lambda_{B1}|}$ and $\hat{\tilde{\boldsymbol{q}}}_2 \in \mathbb{R}^{|\Lambda_{B2}|}$. Condition eq. (6.61) then takes the form

$$\widehat{\boldsymbol{B}}_1\,\hat{\tilde{\boldsymbol{q}}}_1 + \widehat{\boldsymbol{B}}_2\,\hat{\tilde{\boldsymbol{q}}}_2 = \boldsymbol{0}\,. \tag{6.62}$$

With oversampling boundary points $\left\{\boldsymbol{P}_j^+, \boldsymbol{P}_j^-\right\}$, above system reads in a least-square sense the optimization problem

$$\min_{\hat{\tilde{\boldsymbol{q}}}_1} \left\| \widehat{\boldsymbol{B}}_1\,\hat{\tilde{\boldsymbol{q}}}_1 + \widehat{\boldsymbol{B}}_2\,\hat{\tilde{\boldsymbol{q}}}_2 \right\|_2^2\,, \tag{6.63}$$

for which the associated normal equation reads $\widehat{\boldsymbol{B}}_1{}^{\top}\widehat{\boldsymbol{B}}_1\,\hat{\tilde{\boldsymbol{q}}}_1 + \widehat{\boldsymbol{B}}_1{}^{\top}\widehat{\boldsymbol{B}}_2\,\hat{\tilde{\boldsymbol{q}}}_2 = \boldsymbol{0}$. Provided $\widehat{\boldsymbol{B}}_1{}^{\top}\widehat{\boldsymbol{B}}_1$ is nonsingular, this yields the relation for degrees of freedom

$$\hat{\tilde{\boldsymbol{q}}}_1\big(\hat{\tilde{\boldsymbol{q}}}_2\big) = \mathfrak{M}\,\hat{\tilde{\boldsymbol{q}}}_2\,, \tag{6.64}$$

with constant linear periodicity matrix $\mathfrak{M} \coloneqq -\big(\widehat{\boldsymbol{B}}_1{}^{\top}\widehat{\boldsymbol{B}}_1\big)^{-1}\widehat{\boldsymbol{B}}_1{}^{\top}\widehat{\boldsymbol{B}}_2$, solely composed of discrete shape functions. With this so called "basis modification" we are able to condense $\hat{\tilde{\boldsymbol{q}}}_1\big(\hat{\tilde{\boldsymbol{q}}}_2\big) = \mathfrak{M}\,\hat{\tilde{\boldsymbol{q}}}_2$ and correspondingly $\delta\hat{\tilde{\boldsymbol{q}}}_1\big(\delta\hat{\tilde{\boldsymbol{q}}}_2\big) = \mathfrak{M}\,\delta\hat{\tilde{\boldsymbol{q}}}_2$ into the system (6.57_1).

Note that structured meshes may allow to easily identify sets Λ_{B1} and Λ_{B2} a priori by assigning primary-secondary nodal pairs from opposing surfaces while carefully treating edges and corners. For a first order continuum, an equidistant Lagrange mesh allows nodal coupling.

All proposed discrete conditions imply restricting involved degrees of freedom, in case of periodicity additionally calculating the basis modification matrix, and therefore are inherent to the RVE-mesh and determined upon initialization. We remark here, that the combination of both periodicity subsets is equal to the Dirichlet subset $\Lambda_{B1} \cup \Lambda_{B2} = \Lambda_A$, such that the procedure for discrete constraint (IIId) may also be used for (IId). Beside introduced strong enforcement of fluctuation constraints, other options include the use of Lagrange multipliers or penalty methods.

6.5 Solution of the multi-scale problem

In this section, we address the solution of the nonlinear multi-scale problem. The procedure is based on the Newton-Raphson scheme introduced in section 3.5.2, which requires the linearization of the residuals on both scales with respect to the discrete primary fields $\boldsymbol{\varphi}_A$ and $\tilde{\boldsymbol{w}}_{\mathrm{G},B}$. The generalized formulation proposed herein enhances robustness and reduces computational cost, while still containing the classical solution strategy employed by Schröder and Keip [102], Kouznetsova et al. [67], and others as a special case. To this end, we go into greater detail on the linearized contributions and the resulting two-field tangent operator.

We exploit the independence of both fields in the external contributions. For brevity, the discretization indicator $(\cdot)^{\mathrm{h}}$ is omitted, and the integral notation is reinstated on the micro-scale. Moreover, we employ index notation (cf. section 0.1.2), in which the nodal or control-point indices $(\cdot)_A$ and $(\cdot)_{\mathrm{G},B}$ are written as superscripts. The linearized residuals

Pre-processing (offline phase)

Set up RVE with boundary conditions. Calculate $|\tilde{\Omega}_0|$ and $\mathfrak{M}$

Determine number of Gauss points n_{gp} in the macro domain and prepare load distribution

do

Localization phase (macro level)

for $\mathrm{G} = 1 : n_{\text{gp}}$ **do** ▷ n_{gp}: Gauss points

Collect macroscopic deformation gradients at Gauss point $\boldsymbol{X}_{\mathrm{G}}$: $\boldsymbol{F}_{\mathrm{G}}$ and $\mathfrak{F}_{\mathrm{G}}$

end for

RVE**-phase (micro level)**

for $\mathrm{G} = 1 : n_{\text{gp}}$ **do** ▷ each G independent, parallelizable

Provide specific deformation $\boldsymbol{F}_{\mathrm{G}}$ and $\mathfrak{F}_{\mathrm{G}}$

Assemble micro residual $\boldsymbol{R}^{\mathrm{G}}_{\tilde{\boldsymbol{w}}}$:

for $\tilde{\mathrm{K}} = 1 : \tilde{n}_{\text{gp}}$ **do**

Calculate contribution $\boldsymbol{R}^{\mathrm{G},B}_{\tilde{\boldsymbol{w}},\tilde{\mathrm{K}}}$

end for

Optional: solve RVE boundary value problem $\boldsymbol{R}^{\mathrm{G},B}_{\tilde{\boldsymbol{w}}} = \boldsymbol{0}$ (cf. section 6.5)

Compute homogenized stresses

$$\boldsymbol{P}_{\mathrm{G}} = \frac{1}{|\tilde{\Omega}_0|}\int_{\tilde{\Omega}_0}\left\{\tilde{\boldsymbol{P}}\right\}\mathrm{d}\tilde{V} \quad \text{and} \quad \mathfrak{P}_{\mathrm{G}} = \frac{1}{|\tilde{\Omega}_0|}\int_{\tilde{\Omega}_0}\left\{\tilde{\boldsymbol{P}}\otimes\tilde{\boldsymbol{X}} + \tilde{\mathfrak{P}}\right\}\mathrm{d}\tilde{V}$$

for $\tilde{\mathrm{K}} = 1 : \tilde{n}_{\text{gp}}$ **do**

Calculate contributions $\tilde{\boldsymbol{P}}_{\mathrm{G},\tilde{\mathrm{K}}}$, $\tilde{\boldsymbol{P}}_{\mathrm{G},\tilde{\mathrm{K}}}\otimes\tilde{\boldsymbol{X}}_{\mathrm{G},\tilde{\mathrm{K}}}$, $\tilde{\mathfrak{P}}_{\mathrm{G},\tilde{\mathrm{K}}}$

end for

end for

Global residual assembly (macro level)

for $\mathrm{G} = 1 : n_{\text{gp}}$ **do**

Collect homogenized stresses $\boldsymbol{P}_{\mathrm{G}}$ and $\mathfrak{P}_{\mathrm{G}}$ and assemble macro residual $\boldsymbol{R}_{\boldsymbol{\varphi}}$

end for

while $\|\boldsymbol{R}_{\boldsymbol{\varphi}}\| > \varepsilon_{\boldsymbol{\varphi}}$

Algorithm 6.4.1 – Computational multi-scale algorithm. Offline-online scheme for FE^2/IGA^2.

then take the form

$$\begin{aligned}\left[\Delta\boldsymbol{R}_{\boldsymbol{\varphi}}\right]_{i}^{A} = \sum_{\mathrm{G}=1}^{n_{\mathrm{gp}}} \mathrm{w}_{\mathrm{G}} \Bigg\{ \left[\nabla_{\mathrm{X}}\mathcal{R}\right]_{J}^{A} \frac{1}{|\tilde{\Omega}_0^{\mathrm{h}}|} \int_{\tilde{\Omega}_0} \left\{ \left[\Delta\tilde{\boldsymbol{P}}\right]_{iJ}^{\mathrm{G}} \right\} \mathrm{d}\tilde{V} \\ + \left[\nabla_{\mathrm{X}}^2\mathcal{R}\right]_{JK}^{A} \frac{1}{|\tilde{\Omega}_0^{\mathrm{h}}|} \int_{\tilde{\Omega}_0} \left\{ \left[\Delta\tilde{\boldsymbol{P}}\right]_{iJ}^{\mathrm{G}} \left[\tilde{\boldsymbol{X}}\right]_{K} + \left[\Delta\tilde{\mathfrak{P}}\right]_{iJK}^{\mathrm{G}} \right\} \mathrm{d}\tilde{V} \Bigg\} \end{aligned} \tag{6.65}$$

$$\left[\Delta\boldsymbol{R}_{\tilde{\boldsymbol{w}}}\right]_{i}^{\mathrm{G},B} = \sum_{\mathrm{G}=1}^{n_{\mathrm{gp}}} \left\{ \int_{\tilde{\Omega}_0} \left\{ \left[\Delta\tilde{\boldsymbol{P}}\right]_{iJ}^{\mathrm{G}} \left[\nabla_{\tilde{\mathrm{X}}}\tilde{\mathcal{N}}\right]_{J}^{B} + \left[\Delta\tilde{\mathfrak{P}}\right]_{iJK}^{\mathrm{G}} \left[\nabla_{\tilde{\mathrm{X}}}^2\tilde{\mathcal{N}}\right]_{JK}^{B} \right\} \mathrm{d}\tilde{V} \right\}.$$

As the only direct dependency on the solution fields lie in the discrete values of the stresses evaluated at the macro-quadrature points, we conduct the overall linearization with respect to the primary fields using the linearized stresses. Applying the chain rule, the linearized stress tensors read in index-notation

$$\begin{aligned} \left[\Delta\tilde{\boldsymbol{P}}\right]_{iJ} &= \left[\tilde{\mathbb{C}}\right]_{iJsT} \left[\Delta\tilde{\boldsymbol{F}}\right]_{sT} + \left[\tilde{\mathbb{D}}\right]_{iJsTU} \left[\Delta\tilde{\mathfrak{F}}\right]_{sTU} \quad \text{and} \\ \left[\Delta\tilde{\mathfrak{P}}\right]_{iJK} &= \left[\tilde{\mathbb{M}}\right]_{iJKsT} \left[\Delta\tilde{\boldsymbol{F}}\right]_{sT} + \left[\tilde{\mathbb{N}}\right]_{iJKsTU} \left[\Delta\tilde{\mathfrak{F}}\right]_{sTU} \end{aligned} \tag{6.66}$$

for which we introduced material stress derivatives

$$\tilde{\mathbb{C}} \coloneqq \frac{\partial\tilde{\boldsymbol{P}}}{\partial\tilde{\boldsymbol{F}}}, \quad \tilde{\mathbb{D}} \coloneqq \frac{\partial\tilde{\boldsymbol{P}}}{\partial\tilde{\mathfrak{F}}}, \quad \tilde{\mathbb{M}} \coloneqq \frac{\partial\tilde{\mathfrak{P}}}{\partial\tilde{\boldsymbol{F}}} \quad \text{and} \quad \tilde{\mathbb{N}} \coloneqq \frac{\partial\tilde{\mathfrak{P}}}{\partial\tilde{\mathfrak{F}}}. \tag{6.67}$$

Note that here $\left[\tilde{\mathbb{M}}\right]_{(iJK)(sT)}^{\top(123)(45)} = \left[\tilde{\mathbb{D}}\right]_{(sT)(iJK)}$. The linearization of micro-scale deformation gradients yields

$$\left[\Delta\tilde{\boldsymbol{F}}\right]_{sT}^{\mathrm{G}} = \left[\nabla_{\mathrm{X}}\mathcal{R}\right]_{T}^{C} \left[\Delta\boldsymbol{\varphi}\right]_{s}^{C} + \left[\tilde{\boldsymbol{X}}\right]_{U} \left[\nabla_{\mathrm{X}}^2\mathcal{R}\right]_{TU}^{C} \left[\Delta\boldsymbol{\varphi}\right]_{s}^{C} + \left[\nabla_{\tilde{\mathrm{X}}}\tilde{\mathcal{N}}\right]_{T}^{D} \left[\Delta\tilde{\boldsymbol{w}}\right]_{s}^{\mathrm{G},D} \tag{6.68}$$

for the first and analogously for the second gradient

$$\left[\Delta\tilde{\mathfrak{F}}\right]_{sTU}^{\mathrm{G}} = \left[\nabla_{\mathrm{X}}^2\mathcal{R}\right]_{TU}^{C} \left[\Delta\boldsymbol{\varphi}\right]_{s}^{C} + \left[\nabla_{\tilde{\mathrm{X}}}^2\tilde{\mathcal{N}}\right]_{TU}^{D} \left[\Delta\tilde{\boldsymbol{w}}\right]_{s}^{\mathrm{G},D}. \tag{6.69}$$

After insertion into eq. (6.65) (see also section 6.A.2), the tangent parts can be separated and we get

$$\begin{aligned}\left[\boldsymbol{K}_{\boldsymbol{\varphi}\boldsymbol{\varphi}}\right]_{is}^{AC} = \sum_{\mathrm{G}=1}^{n_{\mathrm{gp}}} \mathrm{w}_{\mathrm{G}} \Big\{ \left[\nabla_{\mathrm{X}}\mathcal{R}\right]_{J}^{A} \left[\mathsf{C}\right]_{iJsT} \left[\nabla_{\mathrm{X}}\mathcal{R}\right]_{T}^{C} + \left[\nabla_{\mathrm{X}}\mathcal{R}\right]_{J}^{A} \left[\mathsf{D}\right]_{iJsTU} \left[\nabla_{\mathrm{X}}^2\mathcal{R}\right]_{TU}^{C} \\ + \left[\nabla_{\mathrm{X}}^2\mathcal{R}\right]_{JK}^{A} \left[\mathsf{M}\right]_{iJKsT} \left[\nabla_{\mathrm{X}}\mathcal{R}\right]_{T}^{C} + \left[\nabla_{\mathrm{X}}^2\mathcal{R}\right]_{JK}^{A} \left[\mathsf{N}\right]_{iJKsTU} \left[\nabla_{\mathrm{X}}^2\mathcal{R}\right]_{TU}^{C} \Big\} \end{aligned} \tag{6.70}$$

with

$$\begin{aligned}\big[\mathsf{C}\big]_{iJsT} &:= \frac{1}{|\tilde{\Omega}_0^{\mathrm{h}}|}\int_{\tilde{\Omega}_0}\Big\{\big[\tilde{\mathbb{C}}\big]_{iJsT}\Big\}\mathrm{d}\tilde{V}\,, \quad \big[\mathsf{D}\big]_{iJsTU} := \frac{1}{|\tilde{\Omega}_0^{\mathrm{h}}|}\int_{\tilde{\Omega}_0}\Big\{\big[\tilde{\mathbb{C}}\big]_{iJsT}\big[\tilde{\boldsymbol{X}}\big]_U + \big[\tilde{\mathbb{D}}\big]_{iJsTU}\Big\}\mathrm{d}\tilde{V}\,,\\ \big[\mathsf{M}\big]_{iJKsT} &:= \frac{1}{|\tilde{\Omega}_0^{\mathrm{h}}|}\int_{\tilde{\Omega}_0}\Big\{\big[\tilde{\boldsymbol{X}}\big]_K\big[\tilde{\mathbb{C}}\big]_{iJsT} + \big[\tilde{\mathbb{M}}\big]_{iJKsT}\Big\}\mathrm{d}\tilde{V} \quad \text{and}\\ \big[\mathsf{N}\big]_{iJKsTU} &:= \frac{1}{|\tilde{\Omega}_0^{\mathrm{h}}|}\int_{\tilde{\Omega}_0}\Big\{\big[\tilde{\boldsymbol{X}}\big]_K\big[\tilde{\mathbb{C}}\big]_{iJsT}\big[\tilde{\boldsymbol{X}}\big]_U + \big[\tilde{\boldsymbol{X}}\big]_K\big[\tilde{\mathbb{D}}\big]_{iJsTU} + \big[\tilde{\mathbb{M}}\big]_{iJKsT}\big[\tilde{\boldsymbol{X}}\big]_U + \big[\tilde{\mathbb{N}}\big]_{iJKsTU}\Big\}\mathrm{d}\tilde{V}\end{aligned} \tag{6.71}$$

as the macro-macro tangent. As can be seen, in absence of fluctuations this is equivalent to volumetric stiffness averaging in context of the Voigt-type homogenization Equation 6.17. Proceeding with the micro-micro tangent, we arrive at

$$\begin{aligned}\big[\boldsymbol{K}_{\tilde{\boldsymbol{w}}\tilde{\boldsymbol{w}}}\big]_{is}^{(\mathrm{G},B)(\mathrm{G},D)} = \int_{\tilde{\Omega}_0}\Big\{&\big[\nabla_{\tilde{\mathrm{X}}}\tilde{\mathcal{N}}\big]_J^B\big[\tilde{\mathbb{C}}\big]_{iJsT}\big[\nabla_{\tilde{\mathrm{X}}}\tilde{\mathcal{N}}\big]_T^D + \big[\nabla_{\tilde{\mathrm{X}}}\tilde{\mathcal{N}}\big]_J^B\big[\tilde{\mathbb{D}}\big]_{iJsTU}\big[\nabla^2_{\tilde{\mathrm{X}}}\tilde{\mathcal{N}}\big]_{TU}^D\\ &+ \big[\nabla^2_{\tilde{\mathrm{X}}}\tilde{\mathcal{N}}\big]_{JK}^B\big[\tilde{\mathbb{M}}\big]_{iJKsT}\big[\nabla_{\tilde{\mathrm{X}}}\tilde{\mathcal{N}}\big]_T^D + \big[\nabla^2_{\tilde{\mathrm{X}}}\tilde{\mathcal{N}}\big]_{JK}^B\big[\tilde{\mathbb{N}}\big]_{iJKsTU}\big[\nabla^2_{\tilde{\mathrm{X}}}\tilde{\mathcal{N}}\big]_{TU}^D\Big\}\mathrm{d}\tilde{V}\,,\end{aligned} \tag{6.72}$$

and eventually the micro-macro tangent reads

$$\begin{aligned}\big[\boldsymbol{K}_{\tilde{\boldsymbol{w}}\boldsymbol{\varphi}}\big]_i^{(\mathrm{G},B)C} &= \int_{\tilde{\Omega}_0}\Big\{\big[\nabla_{\tilde{\mathrm{X}}}\tilde{\mathcal{N}}\big]_J^B\big[\tilde{\mathbb{C}}\big]_{iJsT} + \big[\nabla^2_{\tilde{\mathrm{X}}}\tilde{\mathcal{N}}\big]_{JK}^B\big[\tilde{\mathbb{M}}\big]_{iJKsT}\Big\}\mathrm{d}\tilde{V}\big[\nabla_{\mathrm{X}}\mathcal{R}\big]_T^C\\ &+\int_{\tilde{\Omega}_0}\Big\{\big[\nabla_{\tilde{\mathrm{X}}}\tilde{\mathcal{N}}\big]_J^B\Big(\big[\tilde{\mathbb{C}}\big]_{iJsT}\big[\tilde{\boldsymbol{X}}\big]_U + \big[\tilde{\mathbb{D}}\big]_{iJsTU}\Big) + \big[\nabla^2_{\tilde{\mathrm{X}}}\tilde{\mathcal{N}}\big]_{JK}^B\Big(\big[\tilde{\mathbb{M}}\big]_{iJKsT}\big[\tilde{\boldsymbol{X}}\big]_U + \big[\tilde{\mathbb{N}}\big]_{iJKsTU}\Big)\Big\}\mathrm{d}\tilde{V}\big[\nabla^2_{\mathrm{X}}\mathcal{R}\big]_{TU}^C.\end{aligned} \tag{6.73}$$

Therein, the first integral in linked to the change of the micro-scale with $\boldsymbol{F}$ whereas the second integral is the reaction on $\mathfrak{F}$. This can be useful for transferring data between the scales. Note that both mixed tangents are connected $\boldsymbol{K}_{\boldsymbol{\varphi}\tilde{\boldsymbol{w}}}{}^{\top} = |\tilde{\Omega}_0^{\mathrm{h}}|\boldsymbol{K}_{\tilde{\boldsymbol{w}}\boldsymbol{\varphi}}$.

6.5.1 Linearized System

In particular, we solve

$$\begin{bmatrix}\delta\boldsymbol{\varphi}_A\\ \delta\tilde{\boldsymbol{w}}_{\mathrm{G},B}\end{bmatrix}^{\top}\cdot\begin{bmatrix}\boldsymbol{K}_{\boldsymbol{\varphi}\boldsymbol{\varphi}}^{AC} & \boldsymbol{K}_{\boldsymbol{\varphi}\tilde{\boldsymbol{w}}}^{A(\mathrm{G},D)}\\ \boldsymbol{K}_{\tilde{\boldsymbol{w}}\boldsymbol{\varphi}}^{(\mathrm{G},B)C} & \boldsymbol{K}_{\tilde{\boldsymbol{w}}\tilde{\boldsymbol{w}}}^{(\mathrm{G},B)(\mathrm{G},D)}\end{bmatrix}\begin{bmatrix}\Delta\boldsymbol{\varphi}_C\\ \Delta\tilde{\boldsymbol{w}}_{\mathrm{G},D}\end{bmatrix} = -\begin{bmatrix}\delta\boldsymbol{\varphi}_A\\ \delta\tilde{\boldsymbol{w}}_{\mathrm{G},B}\end{bmatrix}^{\top}\cdot\begin{bmatrix}\boldsymbol{R}_{\boldsymbol{\varphi}}^{A}\\ \boldsymbol{R}_{\tilde{\boldsymbol{w}}}^{\mathrm{G},B}\end{bmatrix}, \tag{6.74}$$

where each Gauss-point G creates an own residual-tangent pair in the total system. We now show a version for numbered Gauss-points to illustrate how the Dirac-Delta choice of

shape-functions enables fast solving

$$\begin{bmatrix} \boldsymbol{K}_{\varphi\varphi} & \boldsymbol{K}^1_{\varphi\tilde{\boldsymbol{w}}} & \boldsymbol{K}^2_{\varphi\tilde{\boldsymbol{w}}} & \boldsymbol{K}^3_{\varphi\tilde{\boldsymbol{w}}} & \cdots \\ \boldsymbol{K}^1_{\tilde{\boldsymbol{w}}\varphi} & \boldsymbol{K}^1_{\tilde{\boldsymbol{w}}\tilde{\boldsymbol{w}}} & & & \\ \boldsymbol{K}^2_{\tilde{\boldsymbol{w}}\varphi} & & \boldsymbol{K}^2_{\tilde{\boldsymbol{w}}\tilde{\boldsymbol{w}}} & & \\ \boldsymbol{K}^3_{\tilde{\boldsymbol{w}}\varphi} & & & \boldsymbol{K}^3_{\tilde{\boldsymbol{w}}\tilde{\boldsymbol{w}}} & \\ \vdots & & & & \ddots \end{bmatrix} \begin{bmatrix} \Delta\boldsymbol{\varphi} \\ \Delta\tilde{\boldsymbol{w}}_1 \\ \Delta\tilde{\boldsymbol{w}}_2 \\ \Delta\tilde{\boldsymbol{w}}_3 \\ \vdots \end{bmatrix} = - \begin{bmatrix} \boldsymbol{R}_{\varphi} \\ \boldsymbol{R}^1_{\tilde{\boldsymbol{w}}} \\ \boldsymbol{R}^2_{\tilde{\boldsymbol{w}}} \\ \boldsymbol{R}^3_{\tilde{\boldsymbol{w}}} \\ \vdots \end{bmatrix} . \tag{6.75}$$

The block-diagonal structure and the parametric separation from each micro-scale residual now enables condensation and allows to utilize the online-offline scheme (cf. algorithm 6.4.1). Since the structure of the tangent is clear, we omit the Gauss-point indication in the following with natural schemes $E \coloneqq E(\mathrm{G}, B) = B + (\mathrm{G}-1)\,\mathfrak{O}_{\tilde{\boldsymbol{w}}}$ and $F \coloneqq F(\mathrm{G}, D) = D + (\mathrm{G}-1)\,\mathfrak{O}_{\tilde{\boldsymbol{w}}}$, giving

$$\begin{bmatrix} \boldsymbol{K}^{AC}_{\varphi\varphi} & \boldsymbol{K}^{AF}_{\varphi\tilde{\boldsymbol{w}}} \\ \boldsymbol{K}^{EC}_{\tilde{\boldsymbol{w}}\varphi} & \boldsymbol{K}^{EF}_{\tilde{\boldsymbol{w}}\tilde{\boldsymbol{w}}} \end{bmatrix} \begin{bmatrix} \Delta\boldsymbol{\varphi}_C \\ \Delta\tilde{\boldsymbol{w}}_F \end{bmatrix} = - \begin{bmatrix} \boldsymbol{R}^A_{\varphi} \\ \boldsymbol{R}^E_{\tilde{\boldsymbol{w}}} \end{bmatrix} , \tag{6.76}$$

Analogously, $\tilde{\boldsymbol{w}}_F \in \mathbb{R}^{3\,n_{\mathrm{gp}}\,\mathfrak{O}_{\tilde{\boldsymbol{w}}}}$ summarizes all fluctuation degrees of freedom and respectively $\boldsymbol{R}^E_{\tilde{\boldsymbol{w}}} \in \mathbb{R}^{3\,n_{\mathrm{gp}}\,\mathfrak{O}_{\tilde{\boldsymbol{w}}}}$ aggregates all micro-residuals.

6.5.2 Classical solution strategy

In conventional FE^2 frameworks (cf. Schröder and Keip [102]; Kouznetsova et al. [67]), the solution process is commonly staggered. Firstly focusing on the second line of eq. (6.76)

$$\boldsymbol{K}^{EC}_{\tilde{\boldsymbol{w}}\varphi}\,\Delta\boldsymbol{\varphi}_C + \boldsymbol{K}^{EF}_{\tilde{\boldsymbol{w}}\tilde{\boldsymbol{w}}}\,\Delta\tilde{\boldsymbol{w}}_F = -\boldsymbol{R}^E_{\tilde{\boldsymbol{w}}} , \tag{6.77}$$

in the first stage the macroscopic degrees of freedom $\boldsymbol{\varphi}_C$ are held fixed, implying $\Delta\boldsymbol{\varphi}_C = \boldsymbol{0}$ and thus

$$\boldsymbol{K}^{EF}_{\tilde{\boldsymbol{w}}\tilde{\boldsymbol{w}}}\,\Delta\tilde{\boldsymbol{w}}_F = -\boldsymbol{R}^E_{\tilde{\boldsymbol{w}}} . \tag{6.78}$$

Above now de-coupled micro-scale system is then block-wise independently per macro-Gauss-point resolved solely with respect to the micro-fluctuation field $\tilde{\boldsymbol{w}}_F$. Thereby criterion $\|\boldsymbol{R}^E_{\tilde{\boldsymbol{w}}}\| < \varepsilon_{\tilde{w}}$ is enforced. Assuming further $\boldsymbol{R}^E_{\tilde{\boldsymbol{w}}} = \boldsymbol{0}$, re-inserting into the second line of eq. (6.77) yields

$$\begin{aligned} & \boldsymbol{K}^{EC}_{\tilde{\boldsymbol{w}}\varphi}\,\Delta\boldsymbol{\varphi}_C + \boldsymbol{K}^{EF}_{\tilde{\boldsymbol{w}}\tilde{\boldsymbol{w}}}\,\Delta\tilde{\boldsymbol{w}}_F = \boldsymbol{0} \\ \Leftrightarrow \quad & \Delta\tilde{\boldsymbol{w}}_F = -\Big(\boldsymbol{K}^{EF}_{\tilde{\boldsymbol{w}}\tilde{\boldsymbol{w}}}\Big)^{-1} \boldsymbol{K}^{EC}_{\tilde{\boldsymbol{w}}\varphi}\,\Delta\boldsymbol{\varphi}_C . \end{aligned} \tag{6.79}$$

Condensing into the macro-scale equilibrium in the fist line of eq. (6.76) allows now to solve a single macro-scale Newton step

$$\begin{aligned} & \boldsymbol{K}^{AC}_{\varphi\varphi}\,\Delta\boldsymbol{\varphi}_C + \boldsymbol{K}^{AF}_{\varphi\tilde{\boldsymbol{w}}}\,\Delta\tilde{\boldsymbol{w}}_F = -\boldsymbol{R}^A_{\varphi} \\ \Leftrightarrow \quad & \Big(\boldsymbol{K}^{AC}_{\varphi\varphi} - \boldsymbol{K}^{AF}_{\varphi\tilde{\boldsymbol{w}}} \Big(\boldsymbol{K}^{EF}_{\tilde{\boldsymbol{w}}\tilde{\boldsymbol{w}}}\Big)^{-1} \boldsymbol{K}^{EC}_{\tilde{\boldsymbol{w}}\varphi}\Big)\,\Delta\boldsymbol{\varphi}_C = -\boldsymbol{R}^A_{\varphi} \end{aligned} \tag{6.80}$$

We emphasize here, that this strategy requires re-enforcing the assumed condition $\boldsymbol{R}^E_{\tilde{\boldsymbol{w}}} = \boldsymbol{0}$, whenever $\boldsymbol{\varphi}_C$ is updated. Consequently, each macro-iteration necessitates a complete re-solution of all representative volume elements.

6.5.3 Generalization of the solution strategy

To generalize the solution strategy we apply a standard condensation by pre-multiplication of eq. (6.76) with the rectangular null-space matrix

$$\boldsymbol{P}^{A(CE)} = \left[\mathbf{I}^{AC}, \quad -\boldsymbol{K}^{AF}_{\boldsymbol{\varphi}\tilde{\boldsymbol{w}}} \left(\boldsymbol{K}^{EF}_{\tilde{\boldsymbol{w}}\tilde{\boldsymbol{w}}}\right)^{-1}\right]^{\top}, \tag{6.81}$$

where $\mathbf{I}^{AC} = \mathrm{id} \in \{0,1\}^{\mathfrak{D}_{\boldsymbol{\varphi}} \times \mathfrak{D}_{\boldsymbol{\varphi}}}$ is the identity matrix for the macro-field. Multiplication on both sides of the linear multi-scale system eq. (6.76)

$$\left(\boldsymbol{P}^{A(CE)}\right)^{\top} \cdot \begin{bmatrix} \boldsymbol{K}^{AC}_{\boldsymbol{\varphi}\boldsymbol{\varphi}} & \boldsymbol{K}^{AF}_{\boldsymbol{\varphi}\tilde{\boldsymbol{w}}} \\ \boldsymbol{K}^{EC}_{\tilde{\boldsymbol{w}}\boldsymbol{\varphi}} & \boldsymbol{K}^{EF}_{\tilde{\boldsymbol{w}}\tilde{\boldsymbol{w}}} \end{bmatrix} \begin{bmatrix} \Delta\boldsymbol{\varphi}_C \\ \Delta\tilde{\boldsymbol{w}}_F \end{bmatrix} = -\left(\boldsymbol{P}^{A(CE)}\right)^{\top} \cdot \begin{bmatrix} \boldsymbol{R}^A_{\boldsymbol{\varphi}} \\ \boldsymbol{R}^E_{\tilde{\boldsymbol{w}}} \end{bmatrix} \tag{6.82}$$

yields for the macro-Newton iteration

$$\left(\boldsymbol{K}^{AC}_{\boldsymbol{\varphi}\boldsymbol{\varphi}} - \boldsymbol{K}^{AF}_{\boldsymbol{\varphi}\tilde{\boldsymbol{w}}} \left(\boldsymbol{K}^{EF}_{\tilde{\boldsymbol{w}}\tilde{\boldsymbol{w}}}\right)^{-1} \boldsymbol{K}^{EC}_{\tilde{\boldsymbol{w}}\boldsymbol{\varphi}}\right) \Delta\boldsymbol{\varphi}_C = -\boldsymbol{R}^A_{\boldsymbol{\varphi}} + \boldsymbol{K}^{AF}_{\boldsymbol{\varphi}\tilde{\boldsymbol{w}}} \left(\boldsymbol{K}^{EF}_{\tilde{\boldsymbol{w}}\tilde{\boldsymbol{w}}}\right)^{-1} \boldsymbol{R}^E_{\tilde{\boldsymbol{w}}} \tag{6.83}$$

The micro-update is then performed using

$$\Delta\tilde{\boldsymbol{w}}_F = -\left(\boldsymbol{K}^{EF}_{\tilde{\boldsymbol{w}}\tilde{\boldsymbol{w}}}\right)^{-1} \left(\boldsymbol{K}^{EC}_{\tilde{\boldsymbol{w}}\boldsymbol{\varphi}}\, \Delta\boldsymbol{\varphi}_C + \boldsymbol{R}^E_{\tilde{\boldsymbol{w}}}\right). \tag{6.84}$$

The essential distinction lies in forwarding the micro-scale residual to the global level, which permits a simultaneous update of both primary fields and thereby reduces the number of micro-scale iterations. As long as the macro-problem has not reached equilibrium, there is, in fact, no meaningful physical interpretation of a micro-scale state that is numerically converged with respect to its own balance.

The generalized framework can still be operated in a staggered manner. However convergence of the micro-problem in each macro-iteration it no longer required, since any non-vanishing micro-residual $\boldsymbol{R}^E_{\tilde{\boldsymbol{w}}}$ is consistently transferred to the global iteration. In contrast, enforcing $\boldsymbol{R}^E_{\tilde{\boldsymbol{w}}} = \boldsymbol{0}$ in the classical strategy is a purely numerical condition but the micro-residual typically does not vanish exactly. This, in turn, deteriorates the quadratic convergence of the overall Newton scheme. Hence, the proposed formulation is generally more advantageous.

6.6 Numerical experiments

In this section we investigate the performance and accuracy of proposed multi-scale framework. We firstly investigate the RVE itself in a series of simulations focusing

on higher-order contributions, homogenization and the influential choice of micro-scale fluctuation constraints. In the second part we address the continuous macro-micro domain and the generalized solution approach. Eventually a large scale higher-order multi-scale example is presented.

In the absence of further specification, subsequent length specifications are given in millimeters (mm). For a consistent comparison of material parameters, a unit thickness of 1 mm is assumed in each omitted spatial direction. First and second-order stresses are given in $^{\mathrm{N}}/_{\mathrm{mm}^2}$ and $^{\mathrm{N\,mm}}/_{\mathrm{mm}^2}$, respectively.

In order to numerically verify the approach, we introduce a normed error measure $\mathrm{err}_{\boldsymbol{A}}^{c}(\boldsymbol{B})$ for the difference between tensors $\boldsymbol{B}$ and $\boldsymbol{A}$ with respect to $\boldsymbol{A}$ and where c specifies the type of error, i.e.

$$\mathrm{err}_{\boldsymbol{A}}^{\mathrm{L}^2(\Omega_0)}(\boldsymbol{B}) \coloneqq \frac{\|\boldsymbol{B}-\boldsymbol{A}\|_{L_2(\Omega_0)}}{\|\boldsymbol{A}\|_{L_2(\Omega_0)}}, \quad \mathrm{err}_{\boldsymbol{A}}^{\mathrm{L}^2(\Omega_0\times\tilde{\Omega}_0)}(\boldsymbol{B}) \coloneqq \frac{\|\boldsymbol{B}-\boldsymbol{A}\|_{L_2(\Omega_0\times\tilde{\Omega}_0)}}{\|\boldsymbol{A}\|_{L_2(\Omega_0\times\tilde{\Omega}_0)}},$$
$$\mathrm{err}_{\boldsymbol{A}}^{\max}(\boldsymbol{B}) \coloneqq \frac{\max(|\boldsymbol{B}-\boldsymbol{A}|)}{\|\boldsymbol{A}\|} \quad \text{and} \quad \mathrm{err}_{\boldsymbol{A}}^{2}(\boldsymbol{B}) \coloneqq \frac{\|\boldsymbol{B}-\boldsymbol{A}\|}{\|\boldsymbol{A}\|}. \tag{6.85}$$

Therein, the first and second measures are denoted as *relative* L^2 error, whereas the third and last are referred to as *relative maximum* and *relative norm* error.

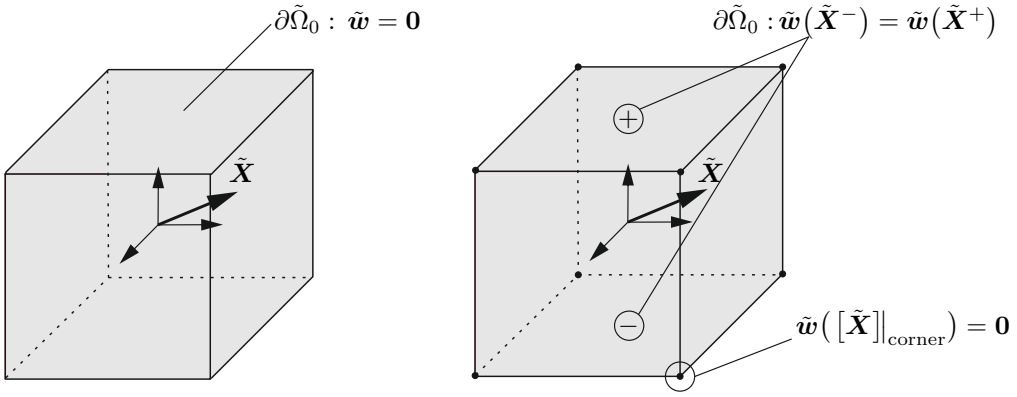


Figure 6.6.1 – First-order homogeneous RVE: setup. Left to right: Dirichlet (II) and periodic (III) boundaries.

6.6.1 RVE investigation

We start with a homogeneous first-order benchmark test highlighting certain aspects of homogenization. Then we investigate the influence of higher-order contributions and then additionally show inhomogeneities. All following tests are performed on the same RVE representing a cube $\tilde{\Omega}_0$ with edge length 0.1 and coordinate system is fixed in the center. The microscopic boundary value problem is set up with different fluctuation restrictions, either $\tilde{\boldsymbol{w}} = \boldsymbol{0}$ (I), $\tilde{\boldsymbol{w}} = \boldsymbol{0}$ on $\partial\tilde{\Omega}_0$ (II) or $\tilde{\boldsymbol{w}}\big(\tilde{\boldsymbol{X}}^-\big) = \tilde{\boldsymbol{w}}\big(\tilde{\boldsymbol{X}}^+\big)$ on $\partial\tilde{\Omega}_0$ (III) (see section 6.2.1 and figure 6.6.1).

The prescribed macroscopic fields $\overline{\boldsymbol{F}}$ and $\overline{\mathfrak{F}}$ are

$$\begin{aligned}
\overline{\boldsymbol{F}} &\coloneqq \begin{bmatrix} 0.897 & 0.500 & -0.400 \\ -0.070 & 1.001 & -0.100 \\ 0.082 & 0.020 & 0.997 \end{bmatrix}, \quad \overline{\mathfrak{F}}(1,:,:) \coloneqq \begin{bmatrix} -0.033 & 0.015 & -0.020 \\ 0.015 & 0.013 & 0.043 \\ -0.020 & 0.043 & 0.029 \end{bmatrix}, \\
\overline{\mathfrak{F}}(2,:,:) &\coloneqq \begin{bmatrix} 0.015 & -0.005 & 0.024 \\ -0.005 & 0.028 & 0.028 \\ 0.024 & 0.028 & 0.014 \end{bmatrix}, \quad \overline{\mathfrak{F}}(3,:,:) \coloneqq \begin{bmatrix} 0.023 & 0.005 & -0.031 \\ 0.005 & -0.042 & -0.001 \\ -0.031 & -0.001 & -0.012 \end{bmatrix},
\end{aligned} \tag{6.86}$$

with $\overline{\mathfrak{F}}$ chosen symmetric in accordance with eq. (3.10). In all following RVE benchmarks, the micro-scale BVP is solved up to numerical limits. Unless stated otherwise, quadratic B-spline basis functions per direction are employed.

RVE benchmark: Homogeneous first-order

As a first proof of concept, we assume a first-order continuum, hence here $\mathfrak{F} = \mathbf{0}$, and investigate the RVE using a homogeneous Mooney-Rivlin material (cf. section 3.3.4). The first-order constitutive relation $\tilde{\Psi}\left(\tilde{\boldsymbol{F}}\right)$ is taken from eq. (3.70), where we set $\alpha = 2000\,{}^{\mathrm{N}}/_{\mathrm{mm}^2}$, $\beta = 1000\,{}^{\mathrm{N}}/_{\mathrm{mm}^2}$ and $\gamma = {}^{\alpha+\beta}/_{3}$.

Remark 6.6.1 – Homogeneous first-order: trivial setting. Note that in case of vanishing fluctuations, the micro-scale is per construction always in equilibrium. Moreover, for a homogeneous material distribution, $\tilde{\Psi}$ is independent on the micro-scale quantities as well as on discretization. Derived stresses and tangents follow analogously, hence

$$\Psi_{(\mathrm{I})} = \frac{1}{|\tilde{\Omega}_0|} \int_{\tilde{\Omega}_0} \left\{\tilde{\Psi}\right\} \mathrm{d}\tilde{V}_{(\mathrm{I})} = \tilde{\Psi}\,, \quad \boldsymbol{P}_{(\mathrm{I})} = \tilde{\boldsymbol{P}} \quad \text{and} \quad \mathsf{C}_{(\mathrm{I})} = \partial_{\boldsymbol{F}} \boldsymbol{P}_{(\mathrm{I})} = \tilde{\mathbb{C}}\,. \tag{6.87}$$

For present higher-order contributions, there is no homogenization-free relation, since a direct dependency on the location is given (see also eq. (6.71)). Note that this dependency may be computed a priori by extracting geometric quantities, cf. Kouznetsova et al. [68].

The corresponding errors in homogenized energy, stress, and tangent moduli are reported in table 6.6.1 for both fluctuation boundary conditions, using the trivial configuration as reference (cf. eq. (6.87)). Both the normed maximum and relative errors remain in the range of 10^{-16} to 10^{-14}, indicating that deviations are bound by numerical accuracy of the underlying discretization.

On account of the first-order Mooney-Rivlin material model and the linear boundary constraints, the resulting stress field is spatially uniform and corresponding representation can be found in 6.A.3.

Elements	$4 \times 4 \times 4$		$8 \times 8 \times 8$		$16 \times 16 \times 16$	
Boundary $*$	(II)	(III)	(II)	(III)	(II)	(III)
$\mathrm{err}^{\max}_{\Psi_{(\mathrm{I})}}(\Psi_*)$	$1.24 \cdot 10^{-16}$	$1.24 \cdot 10^{-16}$	$2.11 \cdot 10^{-15}$	$2.11 \cdot 10^{-15}$	$1.11 \cdot 10^{-14}$	$1.11 \cdot 10^{-14}$
$\mathrm{err}^{\max}_{\boldsymbol{P}_{(\mathrm{I})}}(\boldsymbol{P}_*)$	$7.00 \cdot 10^{-16}$	$7.00 \cdot 10^{-16}$	$7.13 \cdot 10^{-15}$	$7.13 \cdot 10^{-15}$	$1.05 \cdot 10^{-14}$	$1.05 \cdot 10^{-14}$
$\mathrm{err}^{2}_{\boldsymbol{P}_{(\mathrm{I})}}(\boldsymbol{P}_*)$	$1.06 \cdot 10^{-16}$	$1.06 \cdot 10^{-15}$	$8.64 \cdot 10^{-15}$	$8.64 \cdot 10^{-15}$	$2.11 \cdot 10^{-14}$	$2.11 \cdot 10^{-14}$

Table 6.6.1 – First-order homogeneous RVE: accuracy. Rows top to bottom: relative maximum error of the energies and relative maximum/normed error of homogenized stresses for an RVE with 4, 8 and 16 elements per direction with Dirichlet (II) or periodic boundaries (III).

RVE benchmark: Homogeneous second-order

This benchmark addresses a setting dominated by second-order effects. To that end, we again consider a homogeneous medium, now governed by the continuous fiber model introduced in chapter 4. The objective is to quantify the hyper-stress field induced by prescribed second-order macroscopic deformation. Consequently, the micro-scale boundary conditions (II)-(III) must additionally constrain the boundary fluctuation gradient.

The composite consists of a matrix following the Mooney-Rivlin law and uniformly woven fibers with two orientations as defined in eq. (4.16). Material parameters follow typical ranges for woven fiber-reinforced polymers reported in Asmanoglo and Menzel [5] and Dittmann et al. [33].

In the first step, Dirichlet conditions (II) are imposed such that $\tilde{\boldsymbol{w}} = \boldsymbol{0}$ and $\nabla_{\mathbb{X}} \tilde{\boldsymbol{w}} = \boldsymbol{0}$. In the second step, periodic conditions (III) are enforced, i.e. $\tilde{\boldsymbol{w}}(\tilde{\boldsymbol{X}}^-) = \tilde{\boldsymbol{w}}(\tilde{\boldsymbol{X}}^+)$ and $\nabla_{\mathbb{X}} \tilde{\boldsymbol{w}}(\tilde{\boldsymbol{X}}^-) = \nabla_{\mathbb{X}} \tilde{\boldsymbol{w}}(\tilde{\boldsymbol{X}}^+)$, supplemented by vanishing corner fluctuations. Figure 6.6.2 displays the von Mises stress and the norm of the hyper-stress $\tilde{\mathfrak{P}}$ for a discretization with 16 quadratic B-spline elements in each direction. The two enforcement strategies for the energetic condition lead to visibly distinct stress distributions, in particular regarding the second-order contributions.

To quantify the accuracy of the formulation, we next consider a setting approximating a pure second-gradient material. Because the anisotropic second-gradient law is singular in the absence of first-gradient terms, a stabilization is required. The first-gradient stiffness is therefore successively scaled by a factor down to 10^{-8}. For all cases, 16 elements and quadratic B-splines per direction are employed and we apply either Dirichlet (II) or periodic conditions (III).

Table 6.6.3 compares firstly the prescribed deformation with the homogenized kinematic and shows the maximum error of the resultant second-order stress with respect to the

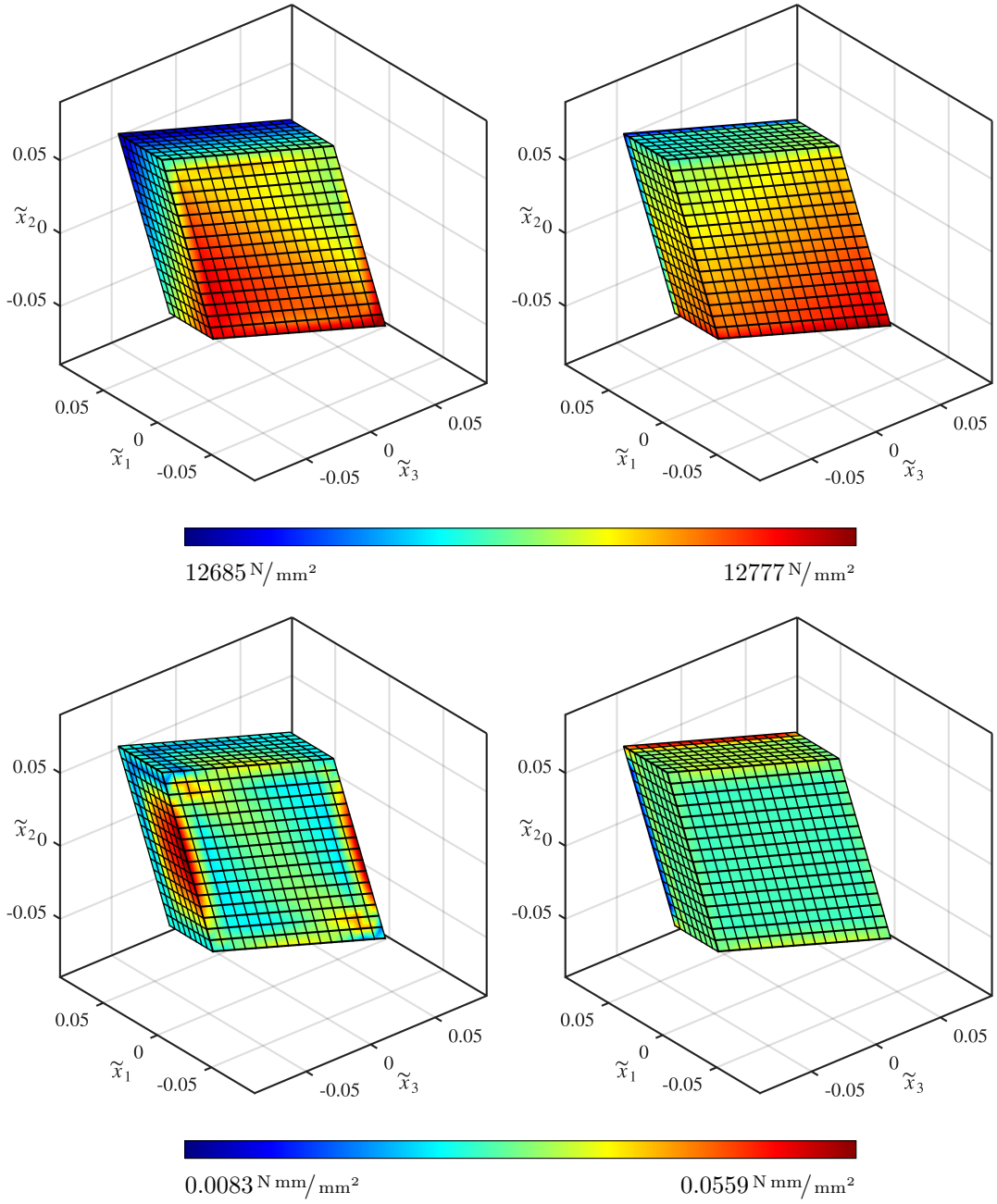


Figure 6.6.2 – Second-order homogeneous RVE: results. Stresses for RVE with 16 elements in each direction. Left to right: Dirichlet and periodic boundaries. Top to bottom: $\|\tilde{\boldsymbol{P}}\|$ and $\|\tilde{\mathfrak{P}}\|$.

Matrix			
Parameter	α	2000	N/mm^2
Parameter	β	1000	N/mm^2
Parameter	γ	$\alpha+\beta/3$	
Volume fraction	ζ^{m}	0.5	–
Fiber			
Shear parameter	b	150000	N/mm^2
Stretch parameter	a	3000	N/mm^2
Scalar curvature parameter	c	1.25	N
Orientation of fiber 1	$\boldsymbol{L}^1$	$1/\sqrt{4.25}$ [-1; -1; 1.5]	–
Orientation of fiber 2	$\boldsymbol{L}^2$	$1/\sqrt{4.25}$ [-1; -1; -1.5]	–

Table 6.6.2 – Second-order homogeneous RVE: Material. Parameter setting of the fiber-reinforced polymer according to eq. (4.16).

analytical macro-scale evaluation of the same material law, i.e.

$$\mathfrak{P}_{(\mathrm{A})} = \frac{\partial \tilde{\Psi}\left(\overline{\mathfrak{F}}\right)}{\partial \overline{\mathfrak{F}}} \,. \tag{6.88}$$

Secondly, to assess the magnitude of stress moments induced by inhomogeneities, we introduce following measures

$$\mathfrak{P}^{\tilde{P}} := \frac{1}{|\tilde{\Omega}_0|}\int_{\tilde{\Omega}_0}\left\{\frac{1}{2}\left(\tilde{\boldsymbol{P}}\otimes\tilde{\boldsymbol{X}}+\left(\tilde{\boldsymbol{P}}\otimes\tilde{\boldsymbol{X}}\right)^{\top 32}\right)\right\}\mathrm{d}\tilde{V} \quad \text{and} \quad \mathfrak{P}^{\tilde{\mathfrak{P}}} := \frac{1}{|\tilde{\Omega}_0|}\int_{\tilde{\Omega}_0}\left\{\tilde{\mathfrak{P}}\right\}\mathrm{d}\tilde{V}\,, \tag{6.89}$$

whose norms and the ratio of $\mathfrak{P}^{\tilde{\boldsymbol{P}}}$ are also listed. The normed deviation of the averaged second-order stress with respect to the analytical value $\mathrm{err}^{\max}_{\mathfrak{P}_{(\mathrm{A})}}\left(\mathfrak{P}_{(\mathrm{II})}\right)$ decreases in direct proportion to the diminishing first-gradient stiffness and the remaining second-gradient response converges as expected to the analytical value for constant deformation.

RVE benchmark: Inhomogeneous second-order

We now apply the previously examined second-gradient formulation to a geometrically inhomogeneous RVE containing a centered three-dimensional cross-shaped void. Such configurations are representative of lightweight lattice-like structures often encountered in additive manufacturing.

In the present setting, the void is modeled by reducing the constitutive parameters in the cross region to negligibly small values, as setting them exactly to zero tends to cause numerical instabilities. Both Dirichlet and periodic micro-scale boundary conditions are

Scaling	10^{-0}		10^{-4}		10^{-8}	
Boundary $*$	(II)	(III)	(II)	(III)	(II)	(III)
$\mathrm{err}^{\max}_{\overline{\boldsymbol{F}}}(\boldsymbol{F}_*)$	$1.77\cdot10^{-15}$	$1.18\cdot10^{-15}$	$8.44\cdot10^{-16}$	$1.01\cdot10^{-15}$	$1.60\cdot10^{-15}$	$1.35\cdot10^{-15}$
$\mathrm{err}^{\max}_{\overline{\mathfrak{F}}}(\mathfrak{F}_*)$	$8.37\cdot10^{-16}$	$6.85\cdot10^{-16}$	$7.61\cdot10^{-16}$	$9.13\cdot10^{-16}$	$7.61\cdot10^{-16}$	$8.37\cdot10^{-16}$
$\mathrm{err}^{\max}_{\mathfrak{P}_{(\mathrm{A})}}(\mathfrak{P}_*)$	$1.41\cdot10^{+01}$	$1.12\cdot10^{+01}$	$1.82\cdot10^{-03}$	$1.79\cdot10^{-03}$	$1.53\cdot10^{-05}$	$2.35\cdot10^{-05}$
$\lVert\mathfrak{P}^{\tilde{\mathfrak{P}}}\rVert$	$2.70\cdot10^{-02}$	$2.70\cdot10^{-02}$	$2.70\cdot10^{-02}$	$2.70\cdot10^{-02}$	$2.70\cdot10^{-02}$	$2.70\cdot10^{-02}$
$\lVert\mathfrak{P}^{\tilde{P}}\rVert$	$1.05\cdot10^{+00}$	$8.13\cdot10^{-01}$	$1.18\cdot10^{-04}$	$1.17\cdot10^{-04}$	$4.96\cdot10^{-07}$	$8.17\cdot10^{-07}$
$\lVert\mathfrak{P}^{\tilde{P}}\rVert/\lVert\mathfrak{P}\rVert$	99.5%	99.3%	0.44%	0.43%	0.0018%	0.0030%

Table 6.6.3 – Second-order homogeneous RVE: higher-order contributions. Relative absolute maximum error of $\boldsymbol{F}$, $\mathfrak{F}$ and $\mathfrak{P}$, norm of averaged second-order stress contributions $\mathfrak{P}^{\tilde{\mathfrak{P}}}$ and $\mathfrak{P}^{\tilde{P}}$ along with the ratio $\mathfrak{P}^{\tilde{P}}$ over $\mathfrak{P}$.

imposed on the RVE, which retains the same edge length and origin as in the homogeneous benchmark. The 3D cross consists of intersecting arms with edge lengths $l/6$ (short) and $l/4$ (long), cf. figure 6.6.3. Within the cross-domain, parameters of matrix- and fiber-material (α, β, γ, a, b, c) are reduced by the factor 10^{-6} in order to mimic a structural void while maintaining numerical stability due to non-vanishing stiffness in corresponding elements.

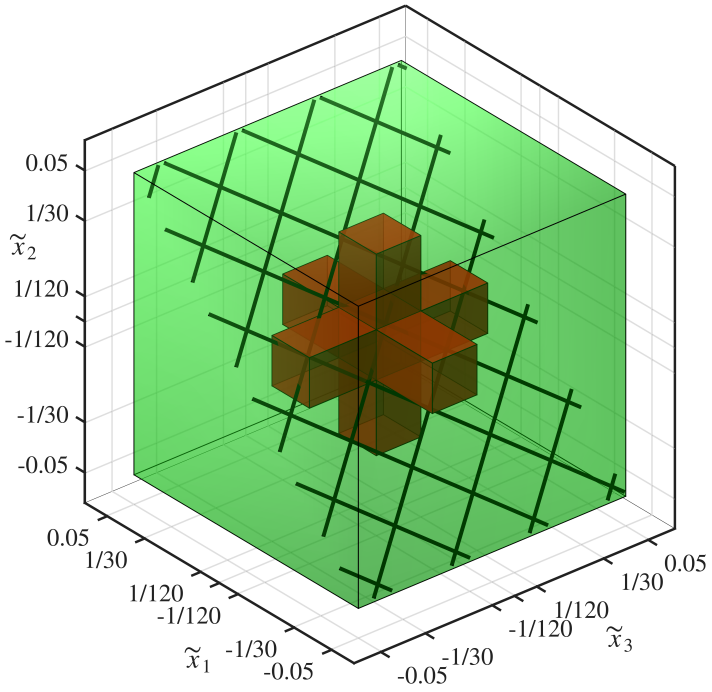


Figure 6.6.3 – Inhomogeneous second-order RVE: setup. RVE with a 3D void and illustrated fiber structure.

Figure 6.6.4 shows the stresses of matrix and fibers, displayed on a mid-plane cut of the domain. The discretization employs 24 quadratic B-spline elements per spatial direction. As expected, the inhomogeneity induces a pronounced anisotropic stress response governed by the oriented fiber architecture and the second-gradient contributions. The hyper-stress magnitude $\|\tilde{\mathfrak{P}}\|$ illustrates the localized higher-order effects around the void and across the fiber-aligned directions.

In contrast to the previous case, higher-order effects intensify due to increased stress localization, enhanced directionality and strong spatial gradients in $\tilde{\mathfrak{P}}$, solely generated by the void. The resulting deviations from the homogeneous case illustrate that second-gradient theories capture not only constitutive size effects but also geometric micro-structuring, with the void acting as a source of internal length-scale activation. Consequently, the inhomogeneous RVE develops nontrivial hyper-stress patterns that are absent in the homogeneous configuration, demonstrating the sensitivity of second-order continua to both material and geometric microstructure.

Elements	$12 \times 12 \times 12$		$24 \times 24 \times 24$	
Boundary $*$	(II)	(III)	(II)	(III)
$\|\boldsymbol{P}\|$	$1.13 \cdot 10^{+04}$	$1.11 \cdot 10^{+04}$	$1.11 \cdot 10^{+04}$	$1.08 \cdot 10^{+04}$
$\|\mathfrak{P}^{\tilde{\mathfrak{P}}}\|$	$2.54 \cdot 10^{-02}$	$2.45 \cdot 10^{-02}$	$2.52 \cdot 10^{-02}$	$2.42 \cdot 10^{-02}$
$\|\mathfrak{P}^{\tilde{P}}\|$	$1.02 \cdot 10^{+00}$	$7.90 \cdot 10^{-01}$	$1.00 \cdot 10^{+00}$	$7.70 \cdot 10^{-01}$
$\|\mathfrak{P}^{\tilde{P}}\|/\|\mathfrak{P}\|$	99.50%	99.15%	99.47%	99.09%

Table 6.6.4 – Second-order homogeneous RVE: higher-order contributions. Relative absolute maximum error of $\boldsymbol{F}$, $\mathfrak{F}$ and $\mathfrak{P}$, norm of averaged second-order stress contributions $\mathfrak{P}^{\tilde{\mathfrak{P}}}$ and $\mathfrak{P}^{\tilde{P}}$ along with the ratio of $\mathfrak{P}^{\tilde{P}}$ over $\mathfrak{P}$.

The effect of the boundary conditions can be quantified more directly. In line with the previous tests, table 6.6.4 compares the homogenized stress measures and additionally includes results obtained on a coarser discretization. The previously observed trend is confirmed. The Dirichlet setting yields larger stresses due to the kinematic rigidity of the constrained boundary, whereas periodic boundary conditions permit a comparatively compliant response. This discrepancy is particularly pronounced for the second-order stresses, since the Dirichlet constraints promote both elevated local stress concentrations and larger second-order moments along the constrained boundary.

Figure 6.6.5 further isolates the contributions of the fiber phase. Although the fibers are modeled within a continuum setting, we illustrate the underlying woven-mesh assumption by selecting line sets in the plane spanned by the out-of-plane normal (cf. eq. (4.18)) and passing through the RVE center. These material lines, aligned with the two prescribed fiber orientations, are advected with the deformation of the RVE under periodic boundary conditions, and the associated stress response is evaluated along their trajectories.

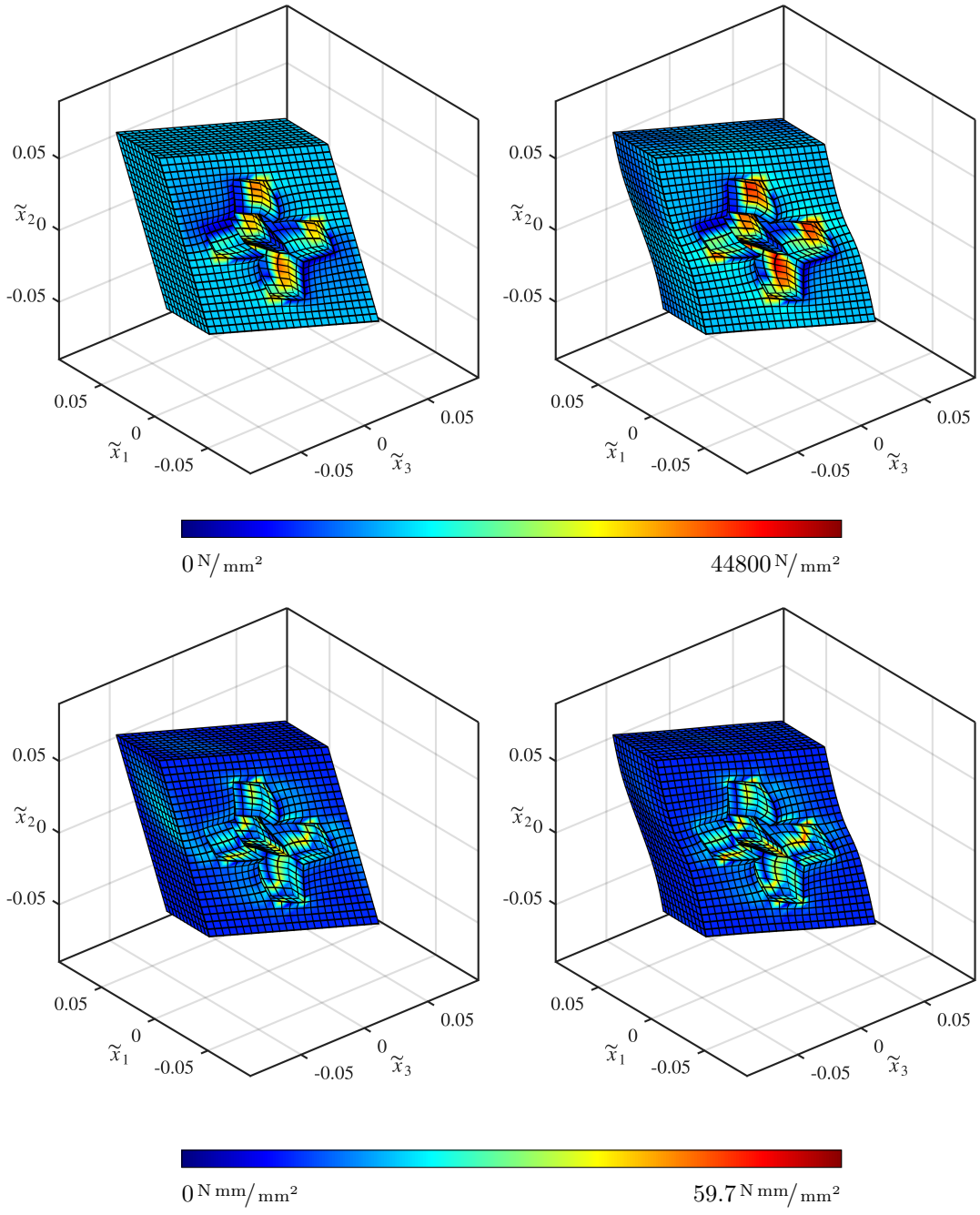


Figure 6.6.4 – Inhomogeneous second-order RVE: results. Stresses shown for the RVE with 24 elements in each direction, sliced to show x-elements 13 to 24 and with void-elements excluded from plot. Top to bottom: $\|\tilde{\boldsymbol{P}}\|$ and $\|\tilde{\mathfrak{P}}\|$. Left to right: Dirichlet and periodic conditions.

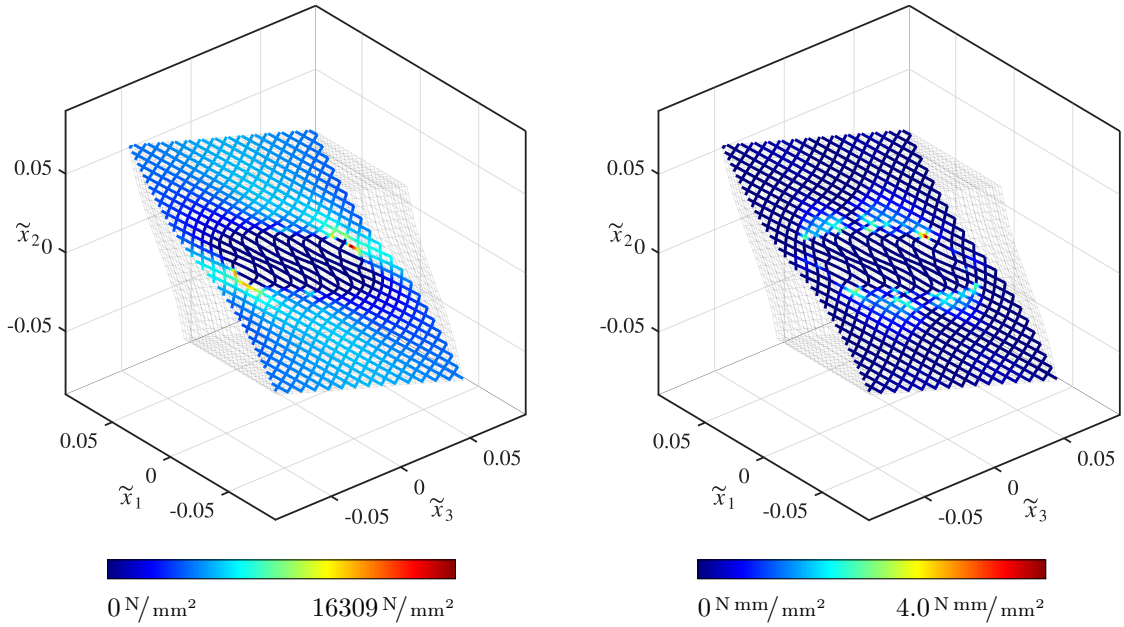


Figure 6.6.5 – Inhomogeneous second-order RVE: fiber deformation. Exemplary depiction of the underlying fiber structure. Left to right: $\|\boldsymbol{P}\|$ and $\|\mathfrak{P}\|$.

RVE benchmark: Unit cell

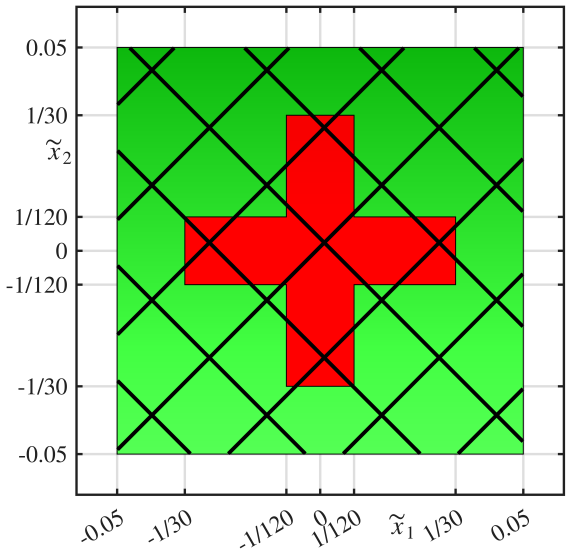


Figure 6.6.6 – Inhomogeneous second-order RVE: 2D setup. reviewUnit cell with a 2D void and schematic fiber structure.

Next, we examine the sensitivity with respect to the selected RVE size. To this end, we construct a two-dimensional counterpart of the previous geometry, shown in figure 6.6.6,

and refer to it as a unit cell because it contains all microstructural features within the smallest admissible geometric domain.

In the two-dimensional setting, the matrix and fiber material parameters (α, β, γ, a, b, c) are scaled by a factor of 10^{-2}. The fiber orientations are set to $\boldsymbol{L}^1 = {}^1/\sqrt{2}\,[1;\,1]$ and $\boldsymbol{L}^2 = {}^1/\sqrt{2}\,[1;\,-1]$. For the macroscopic deformation, we retain only the $\boldsymbol{e}_1$ and $\boldsymbol{e}_2$ components of the previously introduced tensors (see also eq. (3.68)), yielding

$$\overline{\boldsymbol{F}}_{2\mathrm{D}} \coloneqq \begin{bmatrix} 0.897 & 0.500 \\ -0.070 & 1.001 \end{bmatrix} \quad \text{and}$$

$$\overline{\mathfrak{F}}_{2\mathrm{D}}(1,:,:) \coloneqq \begin{bmatrix} -0.033 & 0.015 \\ 0.015 & 0.013 \end{bmatrix}, \quad \overline{\mathfrak{F}}_{2\mathrm{D}}(2,:,:) \coloneqq \begin{bmatrix} 0.015 & -0.005 \\ -0.005 & 0.028 \end{bmatrix}. \tag{6.90}$$

The objective is to assess the impact of different micro-scale geometry choices discussed in 6.2.2. We therefore compare RVEs obtained by stacking this unit cell to form domains containing 1, 2, 4 and 8 unit cells per direction. Each unit cell is discretized with 24×24 bi-quadratic B-spline elements, and neighboring cells are coupled with C^1 continuity. Figure 6.6.7 shows the stress measures for the 2×2 unit cell and indicates a repeating deformation and stress pattern.

Figure 6.6.8 plots the normed first- and second-order stresses versus the number of unit cells. The rigid Dirichlet condition again increases the first-order stress, although this influence diminishes as more unit cells are assembled into the RVE and the response approaches the periodic case. At the same time, the increasing domain size in combination with anisotropy and inhomogeneity amplifies the stress moments $\boldsymbol{P} \times \boldsymbol{X}$, which leads to larger second-order stresses.

6.6.2 Multi-scale benchmarks

In the following, we examine several numerical studies that demonstrate the behavior of the continuous multi-domain formulation and assess the convergence characteristics of the generalized solution strategy introduced in section 6.5.3.

Analytical micro-scale

As an initial validation and to quantify the influence of different approximation spaces, we consider a one-dimensional first-gradient benchmark for which the coupled macro-micro problem admits a closed-form analytical solution. The macro-domain and micro-domain are given by $\Omega_0 = (0, 1000)\,\mathrm{mm}$ and $\tilde{\Omega}_0 = (0, 1)\,\mathrm{mm}$, respectively. Note that in this and the following example all geometric measures are given in mm.

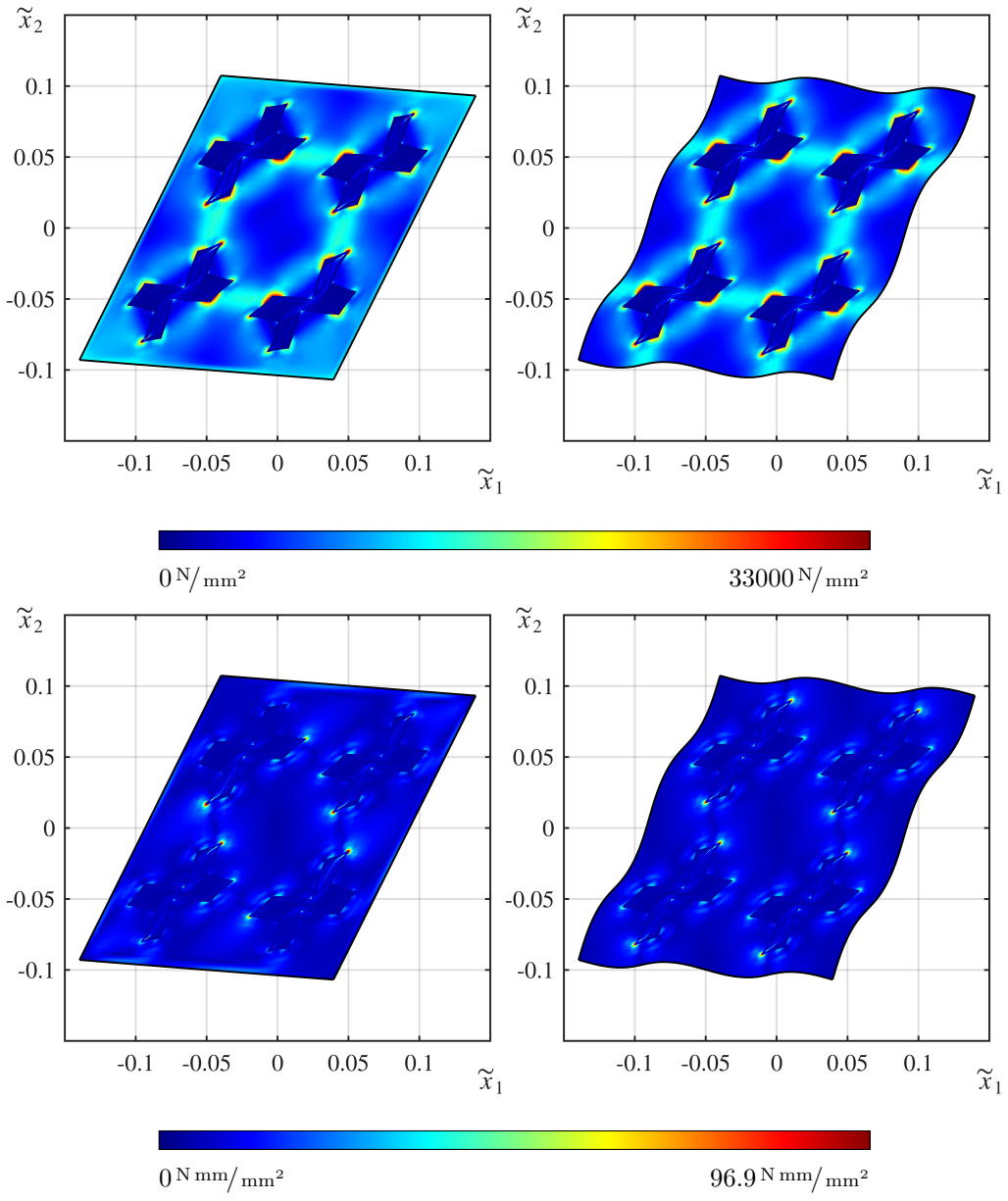


Figure 6.6.7 – Unit cell comparison: results. Stresses shown for the RVE with 48 elements in each direction, consisting of 2×2 unit cells. Top to bottom: $\|\tilde{\boldsymbol{P}}\|$ and $\|\tilde{\mathfrak{P}}\|$. Left to right: Dirichlet and periodic conditions.

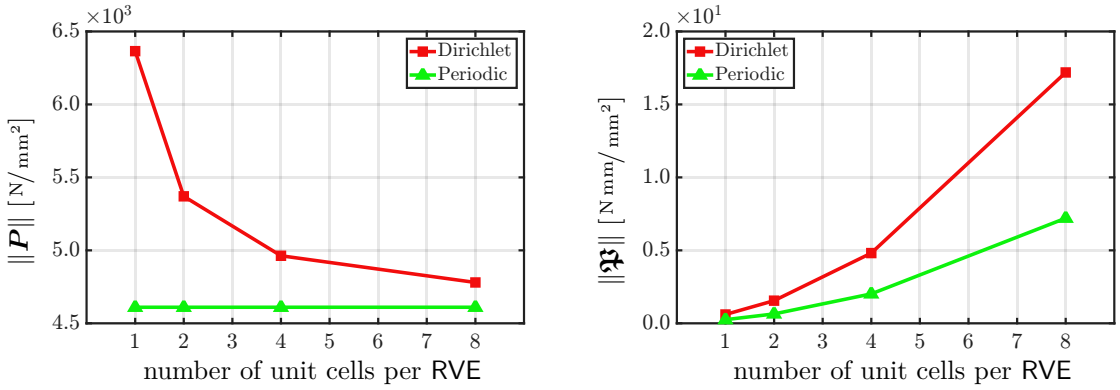


Figure 6.6.8 – Unit cell comparison: homogenization. Stress curves for $\|\boldsymbol{P}\|$ and $\|\mathfrak{P}\|$ over the number of unit cells per direction.

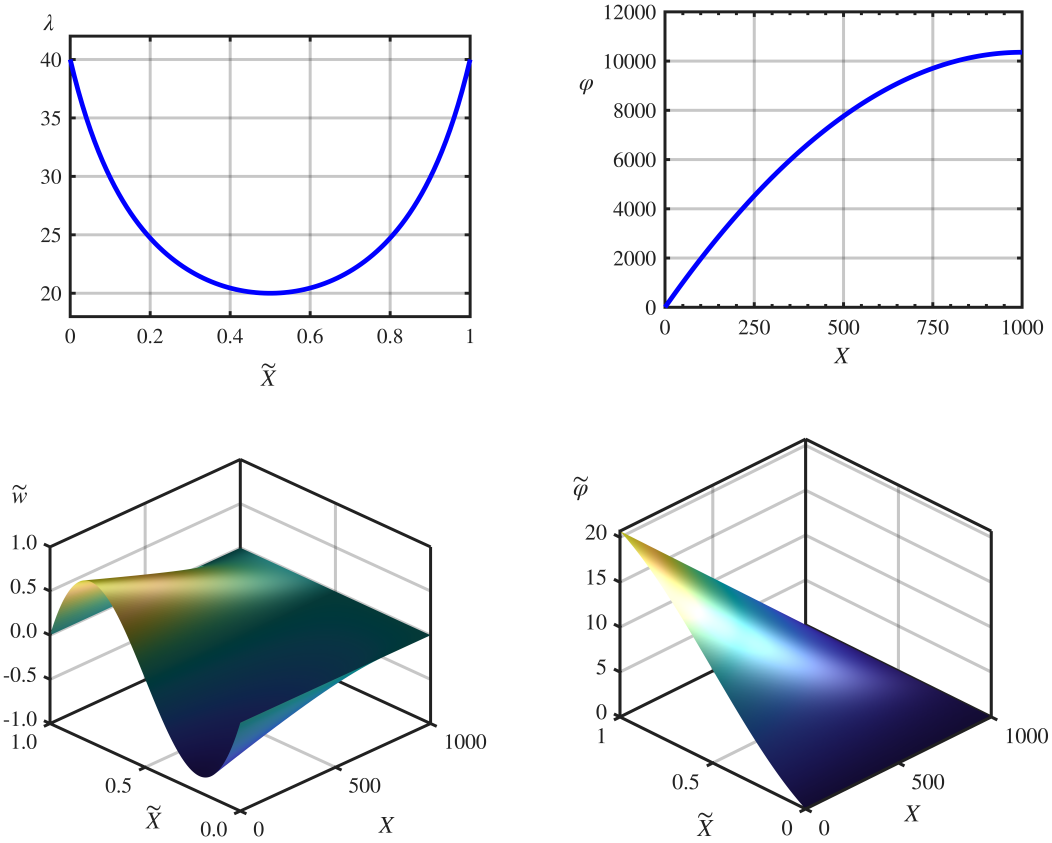


Figure 6.6.9 – Continuous 1D multi-scale test: setup. Top left to right: material parameter $\lambda\left(\tilde{X}\right)$ and macro-deformation φ. Bottom left to right: micro-fluctuation $\tilde{w}$ and micro-deformation $\tilde{\varphi}$.

The material response is defined through the strain-energy density

$$\tilde{\Psi}\big(\tilde{F},\tilde{X}\big) = \lambda\big(\tilde{X}\big)(\tilde{F}^2-1)\,, \quad \lambda\big(\tilde{X}\big) = 20\left[\cos\Big(\frac{2\,\pi}{3}\tilde{X}-\frac{\pi}{3}\Big)\right]^{-1} \,\mathrm{N}/\mathrm{mm}^2, \tag{6.91}$$

where $\lambda\big(\tilde{X}\big)$ varies periodically along the micro-coordinate, see figure 6.6.9. The spatial variation induces residual stresses, so the reference configuration is not stress-free (cf. section 3.3.4). With the body load and boundary conditions

$$B = 1\,\mathrm{N}/\mathrm{mm}^3\,, \quad \varphi(0)=0 \quad \text{and} \quad \varphi(1000) = \frac{37575\,\sqrt{3}}{2\,\pi} \tag{6.92}$$

and the micro-fluctuation Dirichlet condition (II), an analytical solution $\varphi_{(\mathrm{A})}\colon \Omega_0 \to \mathbb{R}$ and $\tilde{w}_{(\mathrm{A})}\colon \Omega_0 \times \tilde{\Omega}_0 \to \mathbb{R}$ of the coupled boundary value problems eq. (6.34)-(6.35) is obtained as

$$\varphi_{(\mathrm{A})}(X) = -\frac{3\,\sqrt{3}}{160\,\pi}\,X^2 + \frac{3003\,\sqrt{3}}{80\,\pi}\,X, \tag{6.93}$$

$$\tilde{w}_{(\mathrm{A})}(X,\tilde{X}) = \tilde{F}_{(\mathrm{A})}(X)\left[\frac{1}{\sqrt{3}}\sin\Big(\frac{2\,\pi}{3}\,\tilde{X}-\frac{\pi}{3}\Big) - \tilde{X} + \frac{1}{2}\right], \tag{6.94}$$

where $\tilde{\boldsymbol{F}}_{(\mathrm{A})} = \partial_X \varphi_{(\mathrm{A})}$, see figure 6.6.9 for illustration. The weak forms governing φ and $\tilde{w}$ reduce in this one-dimensional setting to

$$\int_0^{1000}\left\{\int_0^1\Big\{\lambda\,(\partial_X\varphi + \partial_{\tilde{X}}\tilde{w})\,\partial_X\delta\varphi\Big\}\,\mathrm{d}\tilde{X}\right\}\mathrm{d}X = \frac{1}{2}\int_0^{1000}\{\delta\varphi\}\,\mathrm{d}X\,, \quad \forall\,\delta\varphi\in\mathcal{V}^{\delta\varphi}\,, \tag{6.95}$$

$$\int_0^{1000}\left\{\int_0^1\Big\{\lambda\,(\partial_X\varphi + \partial_{\tilde{X}}\tilde{w})\,\partial_{\tilde{X}}\delta\tilde{w}\Big\}\,\mathrm{d}\tilde{X}\right\}\mathrm{d}X = 0, \quad \forall\,\delta\tilde{w}\in\mathcal{V}^{\delta\tilde{w}}\,, \tag{6.96}$$

which serve as the basis for the subsequent approximation studies.

Nine discretization variants are examined, each differing in the choice or order of the macro and micro approximation spaces $\boldsymbol{p} = \big[p_\varphi,\, p_{\tilde{w}(X)},\, p_{\tilde{w}(\tilde{X})}\big]$. Specifically, combine three orders $p = 1, 2, 4$, i.e. linear, quadratic and quartic, with three schemes. First, the Dirac-based micro-ansatz functions introduced in section 6.4.3 is employed $\boldsymbol{p} = [p, \delta, p]$, second a mixed scheme $\boldsymbol{p} = [p, 0, p]$ with $\tilde{w}$ taken piecewise constant in X and third, a continuous scheme $\boldsymbol{p} = [p, p, p]$. For corresponding results obtained with Lagrangian shape functions, we refer to Hesch et al. [57].

In the convergence study, we employ meshes with 2^k macro-elements and $2^k \times 2^k$ elements on $\Omega_0 \times \tilde{\Omega}_0$ ($k = 4, \ldots, 9$) are employed. The relative L^2 errors $\mathrm{err}^{\mathrm{L}^2(\Omega_0)}_{\varphi_{(\mathrm{A})}}(\varphi)$ and $\mathrm{err}^{\mathrm{L}^2(\Omega_0\times\tilde{\Omega}_0)}_{\tilde{w}_{(\mathrm{A})}}(\tilde{w})$ are reported in figure 6.6.10.

For the macro field φ, the linear and piecewise-constant settings $\{[2,0,2],\,[4,0,4]\}$ reveal second-order convergence. Both quadratic non-constant choices $\{[2,\delta,2],\,[2,2,2]\}$ achieve fourth-order convergence, whereas the quartic non-constant variants $\{[4,\delta,4],\,[4,4,4]\}$

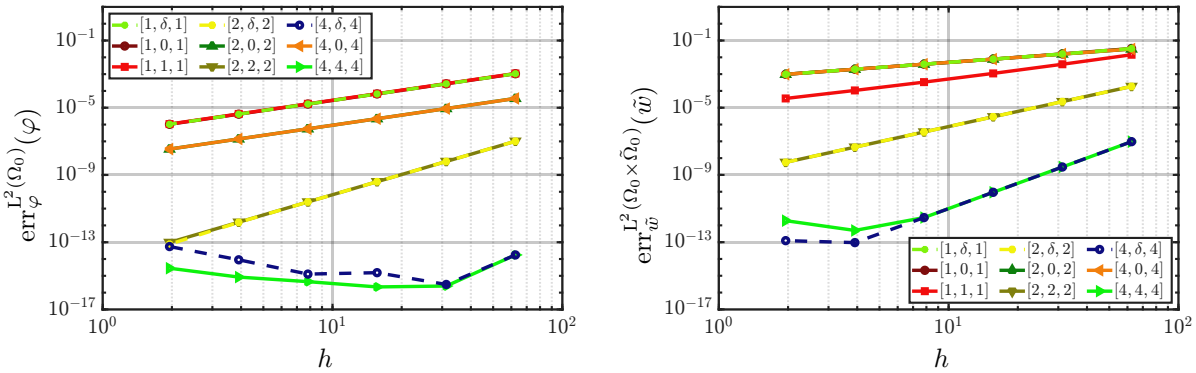


Figure 6.6.10 – Continuous 1D multi-scale test: accuracy. Errors as functions of the mesh-size h. Left: $\mathrm{err}_{\varphi_{(\mathrm{A})}}^{\mathrm{L}^2(\Omega_0)}(\varphi)$, where curves $\{[1,\delta,1],\,[1,0,1],\,[1,1,1]\}$, $\{[2,\delta,2],\,[2,2,2]\}$ and $\{[2,0,2],\,[4,0,4]\}$ coincide. Right: $\mathrm{err}_{\tilde{w}_{(\mathrm{A})}}^{\mathrm{L}^2(\Omega_0\times\tilde{\Omega}_0)}(\tilde{w})$, where curves $\{[1,\delta,1],\,[1,0,1],\,[2,0,2],\,[4,0,4]\}$ and $\{[2,\delta,2],\,[2,2,2]\}$ coincide.

remain in the pre-asymptotic regime over the considered mesh range. The error behavior for the fluctuation field $\tilde{w}$ is shown in the right panel of figure 6.6.10. All piecewise constant approximations achieve convergence with rate 1. The linear approximation $[1,1,1]$ converges roughly at order 1.8, while the quadratic and Dirac/quadratic variants, $[2,\delta,2]$ and $[2,2,2]$, attain third-order convergence. The quartic and Dirac/quartic settings $\{[4,\delta,4],\,[4,4,4]\}$ reach fifth-order convergence before saturating due to numerical limits.

Overall, this benchmark illustrates that macro-scale accuracy is inherited from the micro-scale representation and that consistent approximation across scales is essential for achieving the expected convergence behavior in fully nonlinear multi-scale analyses.

Generalized solution scheme: convergence

We next assess the performance of the classical and generalized solution strategies introduced in section 6.5.2 and section 6.5.3 using the two-dimensional Cook's membrane benchmark. The reference configuration of the macro-continuum is defined by corner points $\boldsymbol{P}^1 = (0,0)^\top$, $\boldsymbol{P}^2 = (480,440)^\top$, $\boldsymbol{P}^3 = (480,600)^\top$, and $\boldsymbol{P}^4 = (0,440)^\top$, corresponding to the lower left, lower right, upper right, and upper left corners, respectively. The computational domain is therefore given by

$$\Omega_0 = \left\{ \boldsymbol{X} = (X_1, X_2) \in \mathbb{R}^2 \,|\, X_1 \in (0,480),\ \frac{11}{12} X_1 < X_2 < \frac{1}{3} X_1 + 440 \right\} . \tag{6.97}$$

The left boundary $\partial\Omega_0^\varphi = \{\boldsymbol{X} \in \mathbb{R}^2 \,|\, X_1 = 0,\ 0 < X_2 < 440\}$ of the membrane is fixed, while on the remaining boundary $\partial\Omega_0^T = \partial\Omega_0 \backslash \partial\Omega_0^\varphi$ we prescribe the surface traction

$$\overline{\boldsymbol{T}}:\ \partial\Omega_0^T \to \mathbb{R}^2\,, \quad \overline{\boldsymbol{T}}(\boldsymbol{X}) = \begin{cases} (-250,500)^\top\ \mathrm{N/mm^2} & \text{if } X_1 = 480,\ 440 < X_2 < 600 \\ (0,0)^\top\ \mathrm{N/mm^2} & \text{otherwise,} \end{cases} \tag{6.98}$$

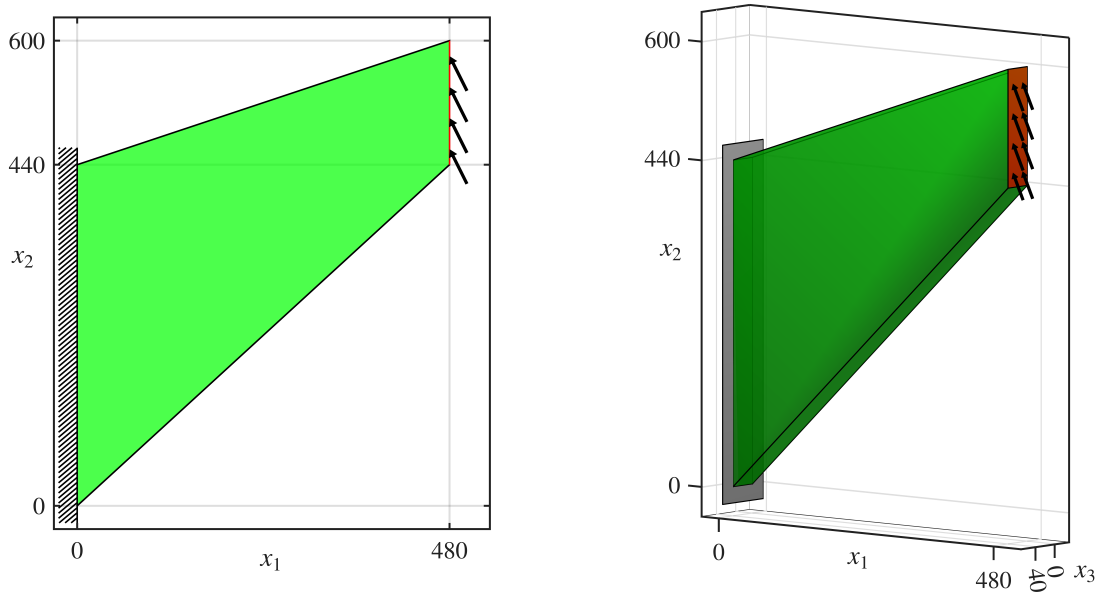


Figure 6.6.11 – Multi-scale test: Cook's Membrane. Reference configuration for the two and three-dimensional multi-scale problems with indicated surface loads (cf. eq. (6.98) and (6.102)).

as shown in figure 6.6.11, left. Body forces are neglected, $\overline{\boldsymbol{B}} = \mathbf{0}$.

The associated micro-domain is taken from the unit cell tests in section 6.6.1, with the same inclusion-parameter scaling of 10^{-2}. The RVE consists of a single unit cell equipped with periodic boundary conditions. For the micro-fluctuations, we employ the Dirac-Delta approach (cf. eq. (6.52) and (6.54)). The Cook's membrane is discretized with 12×12 bi-quadratic B-Spline elements on the macro-scale and the RVE consists of 24×24 bi-quadratic B-Spline elements. Macro-scale integration uses 3 Gauss-points per direction, resulting in 9 quadrature points per element and thus in total $n_{\text{gp}} = (12 \times 12) \cdot 9 = 1296$ RVEs. Each RVE is integrated using the same quadrature rule giving $\tilde{n}_{\text{gp}} = (24 \times 24) \cdot 9 = 5184$ Gauss points.

The load is applied incrementally using n_l load steps. The converged solution of step k serves as the initial configuration for step $(k+1)$, improving robustness of the Newton iterations. The resulting macro-scale response with fully applied load is shown in figure 6.6.12.

We compare two strategies. First, the classical staggered FE^2 procedure of section 6.5.2 is employed with micro- and macro-termination tolerances $\varepsilon_{\tilde{w}} = 10^{-7}$ and $\varepsilon_{\varphi} = 10^{-7}$. Second, the generalized monolithic strategy of section 6.5.3 is applied with a unified tolerance $\varepsilon_{\varphi,\tilde{w}} = 10^{-7}$. Table 6.6.5 summarizes both approaches, where $\min(n_l)$ denotes the minimal required step count in order to reach the prescribed tolerance. Failure is declared if either the macro- or micro-residual norm exceeds 10^{10} or if convergence is not achieved within 15 iterations. Computational effort is quantified by the average number of global newton iterations per step $\langle n_{\text{it}} \rangle$ and the average number of micro-scale iterations $\langle n_{\tilde{\text{it}}} \rangle$ per

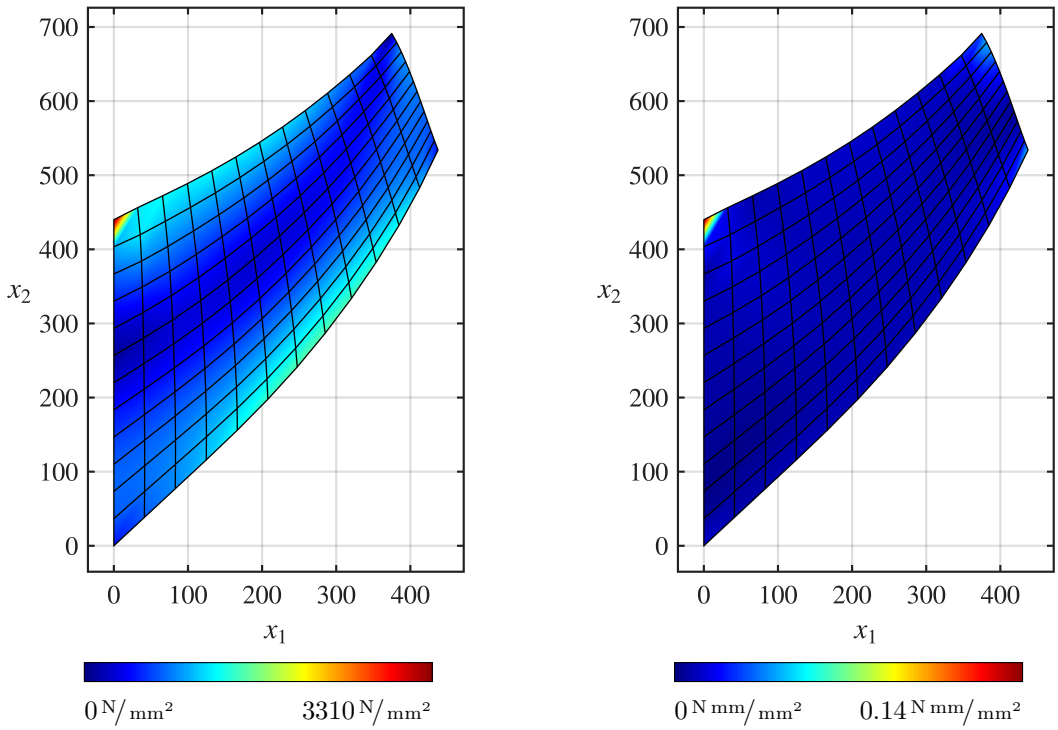


Figure 6.6.12 – 2D multi-scale test: stress. Stress measures for the 2D cooks membrane after fully applied load. Left to right: $\|\boldsymbol{P}\|$ and $\|\mathfrak{P}\|$.

increment, as well as the total number of micro-scale homogenization solves $n_{\tilde{\Omega}_0}$.

Strategy	$\min(n_l)$	$\langle n_{\mathrm{it}} \rangle$	$\langle n_{\tilde{\mathrm{it}}} \rangle$	$n_{\tilde{\Omega}_0}$
Generalized	5	6.6	–	$4.3 \cdot 10^{+04}$
FE^2	8	4.1	2.9	$4.3 \cdot 10^{+04}$

Table 6.6.5 – Continuous 2D multi-scale test: performance. Strategy comparison in terms of minimum of required load steps, associated average macro- and micro-scale newton iterations and total number of micro-scale homogenization solves.

The classical FE^2 scheme converges for $n_l = 8$, whereas in the generalized approach produces a robust solution already for $n_l = 5$. To compare computational cost, we count Gauss-points evaluations. For each Newton iteration k within the generalized solution scheme, in total

$$\Sigma_{\mathrm{ev}}^k = n_{\mathrm{gp}}(1 + \tilde{n}_{\mathrm{gp}}) = 1296 \cdot (1 + 5184) \approx 6.7 \cdot 10^{+06} \tag{6.99}$$

evaluations are performed across all multi-scale quadrature points. For the classical staggered method, assuming an average number of local Newton iterations $\tilde{l}_k = 2.9$, the

corresponding cost per macro-iteration k becomes

$$\Sigma_{\text{ev}}^{k} = n_{\text{gp}}\Big(1 + \tilde{n}_{\text{gp}}\tilde{l}_{k}\Big) \approx 19.5 \cdot 10^{+06} \,. \tag{6.100}$$

Thus, for a comparable number of global iterations, the generalized monolithic strategy requires a substantially reduced computational effort, since the classical approach effectively multiplies the micro-scale work by the local re-equilibration iterations required for every macro step. In addition, the generalized scheme attains convergence with fewer load increments in the present example. Table 6.6.6 shows the convergence behavior if both schemes are run with the same n_l. Although the generalized scheme then requires more global increments, the overall reduction in per-iteration cost together with its improved robustness remains evident.

k	Generalized	FE^2	
		Macro	RVE
1	$3.11 \cdot 10^{+03}$	$3.11 \cdot 10^{+03}$	$1.13 \cdot 10^{-08}$
2	$4.26 \cdot 10^{+03}$	$4.26 \cdot 10^{+03}$	$4.53 \cdot 10^{+00}$
			$2.26 \cdot 10^{-02}$
			$5.50 \cdot 10^{-07}$
			$2.40 \cdot 10^{-13}$
3	$2.36 \cdot 10^{+01}$	$1.01 \cdot 10^{+01}$	$2.12 \cdot 10^{+00}$
			$4.07 \cdot 10^{-03}$
			$4.80 \cdot 10^{-08}$
4	$1.39 \cdot 10^{-01}$	$9.85 \cdot 10^{-03}$	$2.12 \cdot 10^{+00}$
			$4.07 \cdot 10^{-03}$
			$4.80 \cdot 10^{-08}$
5	$1.20 \cdot 10^{-05}$	$7.97 \cdot 10^{-09}$	$2.12 \cdot 10^{+00}$
			$4.07 \cdot 10^{-03}$
			$4.80 \cdot 10^{-08}$
6	$9.65 \cdot 10^{-09}$		
Σ_{ev}	$2.62 \cdot 10^{+08}$	$8.65 \cdot 10^{+08}$ (+230%)	

Table 6.6.6 – Continuous 2D multi-scale test: convergence. Newton convergence in last load step and approximate total number of evaluations Σ_{ev}. The chosen RVE is at the 1296^{th} Gauss-point.

3D second-order multi-scale simulation

As a final example, we consider a fully three-dimensional macro problem governed by the second-gradient formulation. The RVE is the void-inclusion configuration introduced in

section 6.6.1, with material parameters summarized in table 6.6.2. Here, we impose the Dirichlet set (II) for micro-scale fluctuation boundary. The macro-geometry is obtained by extruding the two-dimensional Cook's membrane by 40 mm in the out-of-plane direction,

$$\Omega_0 = \left\{ \boldsymbol{X} = (X_1, X_2, X_3) \in \mathbb{R}^3 \,|\, X_1 \in (0, 480),\, \frac{11}{12} X_1 < X_2 < \frac{1}{3} X_1 + 440,\, X_3 \in (0, 40) \right\}. \tag{6.101}$$

The clamped boundary is again $\partial\Omega_0^{\varphi} = \{\boldsymbol{X} \in \mathbb{R}^3 \,|\, X_1 = 0,\, 0 < X_2 < 440,\, X_3 \in (0, 40)\}$ and the remaining boundary $\partial\Omega_0^T = \partial\Omega_0 \backslash \partial\Omega_0^{\varphi}$ is loaded by $\overline{\boldsymbol{T}}\colon\ \partial\Omega_0^T \to \mathbb{R}^3$,

$$\overline{\boldsymbol{T}}(\boldsymbol{X}) = \begin{cases} (-100, 200, 0)^{\top}\,{}^{\mathrm{N}}/_{\mathrm{mm}^2} & \text{if } X_1 = 480,\ 440 < X_2 < 600,\ X_3 \in (0, 40) \\ (0, 0)^{\top}\,{}^{\mathrm{N}}/_{\mathrm{mm}^2} & \text{otherwise} \end{cases} \tag{6.102}$$

as illustrated in figure 6.6.11, right.

As required for second-order continua, tri-quadratic B-splines are used on both scales. To mitigate the computational effort, we employ the multigrid-solution strategy based on knot insertion described in section 2.3.2. Three macro-scale meshes are considered,

$$\mathcal{M}^0 = (4 \times 4 \times 1)\,, \quad \mathcal{M}^1 = (8 \times 8 \times 2) \quad \text{and} \quad \mathcal{M}^2 = (16 \times 16 \times 4)\,, \tag{6.103}$$

each obtained by a refinement factor of two. The full multi-scale solution is first computed on the coarsest level using an incremental scheme with $n_l = 5$ steps. The solution is then transferred to the finer levels, where only corrector steps ($n_l = 1$) are performed. The approach is further complemented by two micro meshes $\tilde{\mathcal{M}}^0 = (12 \times 12 \times 12)$ and $\tilde{\mathcal{M}}^1 = (24 \times 24 \times 24)$, enabling increased micro-scale resolution. For the present problem, we solve

$$\underbrace{\left\{\mathcal{M}^0 | \tilde{\mathcal{M}}^0\right\}}_{\text{level 1}} \xrightarrow{\mathbb{T}^{1,0}} \underbrace{\left\{\mathcal{M}^1 | \tilde{\mathcal{M}}^0\right\}}_{\text{level 2}} \xrightarrow{\tilde{\mathbb{T}}^{1,0}} \underbrace{\left\{\mathcal{M}^1 | \tilde{\mathcal{M}}^1\right\}}_{\text{level 3}} \xrightarrow{\mathbb{T}^{2,1}} \underbrace{\left\{\mathcal{M}^2 | \tilde{\mathcal{M}}^1\right\}}_{\text{level 4}}. \tag{6.104}$$

Figure 6.6.13 shows the stress fields obtained at each level. The second-gradient stress localizes near the clamped boundary and exhibits the expected boundary-layer behavior associated with second-gradient elasticity. Finally, table 6.6.7 summarizes the convergence history across the multigrid levels, demonstrating both the computational savings and the overall multi-scale convergence achieved with the generalized solution scheme.

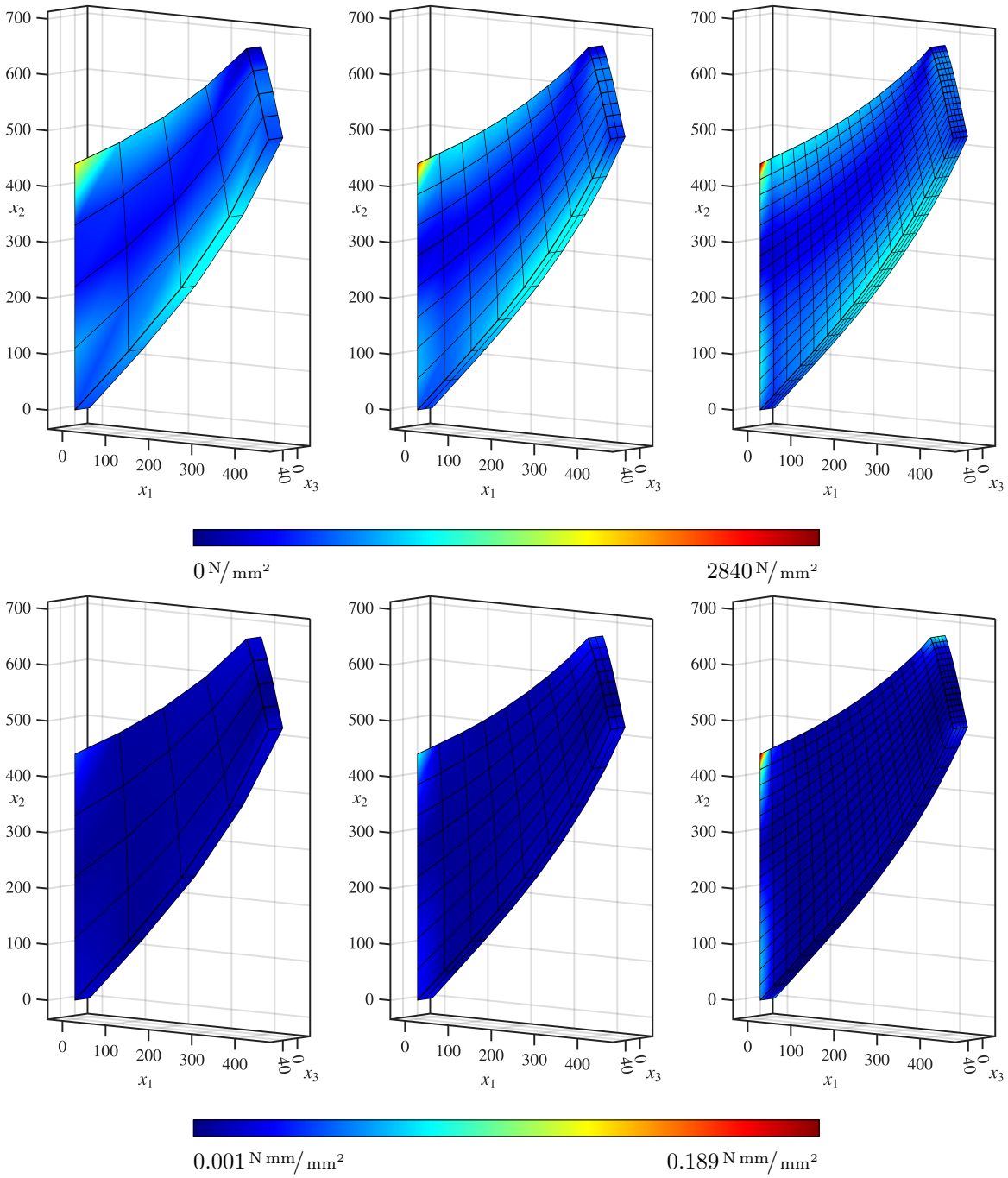


Figure 6.6.13 – 3D higher-order multi-scale: results. Left to right: Level one, three and four according to table 6.6.7. Rows (top to bottom) $\|\boldsymbol{P}\|$ and $\|\mathfrak{P}\|$.

Level	1			2	3	4
Macro res.	$4 \times 4 \times 1$			$8 \times 8 \times 2$	$8 \times 8 \times 2$	$16 \times 16 \times 4$
Micro res.	$12 \times 12 \times 12$			$12 \times 12 \times 12$	$24 \times 24 \times 24$	$24 \times 24 \times 24$
Step	1/5	$\cdots$	5/5	1/1	1/1	1/1
NR-Iterations	$7.29 \cdot 10^{+04}$		$7.45 \cdot 10^{+04}$	$7.26 \cdot 10^{+05}$	$9.76 \cdot 10^{+04}$	$3.70 \cdot 10^{+05}$
	$6.44 \cdot 10^{+05}$		$5.42 \cdot 10^{+05}$	$9.21 \cdot 10^{+03}$	$3.50 \cdot 10^{+02}$	$4.47 \cdot 10^{+03}$
	$1.75 \cdot 10^{+02}$	$\cdots$	$3.20 \cdot 10^{+02}$	$4.89 \cdot 10^{+00}$	$1.86 \cdot 10^{-03}$	$4.23 \cdot 10^{+00}$
	$1.98 \cdot 10^{-01}$		$1.06 \cdot 10^{+00}$	$1.27 \cdot 10^{-04}$	$5.66 \cdot 10^{-07}$	$2.62 \cdot 10^{-04}$
	$4.93 \cdot 10^{-07}$		$5.58 \cdot 10^{-07}$	$6.19 \cdot 10^{-07}$		$5.82 \cdot 10^{-07}$
ΣRVE			9072	17280	13824	138240

Table 6.6.7 – 3D higher-order multi-scale: performance. Newton convergence utilizing the multi-grid and generalized solution scheme with total number of calculated RVE for all steps per level.

6.A Appendix A

6.A.1 Global shape functions

Introducing a multi-scale index-scheme $D(C,B) = C + (B-1)\,\mathfrak{O}_{\tilde{w}}$, we can use global numbering with product index space $\Lambda_{\tilde{\varphi}} \coloneqq \{1, \dots, \mathfrak{O}_{\tilde{\varphi}}\}$, where $\mathfrak{O}_{\tilde{\varphi}} = \mathfrak{O}_{\bar{\varphi}}\mathfrak{O}_{\tilde{w}}$. Denoting $\tilde{\mathcal{R}}^D\big(\boldsymbol{X},\tilde{\boldsymbol{X}}\big) \coloneqq \mathcal{M}^C(\boldsymbol{X})\,\tilde{\mathcal{N}}^B\big(\tilde{\boldsymbol{X}}\big)$, we write

$$\begin{aligned}
\tilde{\boldsymbol{w}}^{\mathrm{h}}\big(\boldsymbol{X},\tilde{\boldsymbol{X}}\big) &= \sum_{D\in\Lambda_{\tilde{\varphi}}} \tilde{\boldsymbol{w}}_D\,\tilde{\mathcal{R}}^D\big(\boldsymbol{X},\tilde{\boldsymbol{X}}\big)\,,\\
\nabla_{\mathrm{X}}\tilde{\boldsymbol{w}}\big(\boldsymbol{X},\tilde{\boldsymbol{X}}\big) &= \sum_{D\in\Lambda_{\tilde{\varphi}}} \tilde{\boldsymbol{w}}_D\otimes\nabla_{\mathrm{X}}\tilde{\mathcal{R}}^D\big(\boldsymbol{X},\tilde{\boldsymbol{X}}\big)\,,\\
\nabla^2_{\mathrm{X}}\tilde{\boldsymbol{w}}\big(\boldsymbol{X},\tilde{\boldsymbol{X}}\big) &= \sum_{D\in\Lambda_{\tilde{\varphi}}} \tilde{\boldsymbol{w}}_D\otimes\nabla^2_{\mathrm{X}}\tilde{\mathcal{R}}^D\big(\boldsymbol{X},\tilde{\boldsymbol{X}}\big)\,.
\end{aligned} \tag{6.105}$$

The variation of fluctuations follows analogously as we use the same global shape functions. Given $d_\Omega = d_{\tilde{\Omega}} = d$-dimensional macro- and micro-domains, the tensor product requires a $d_{\widehat{\Omega}} = 2\,d$-dimensional parametric domain for $\tilde{\mathcal{R}}^D$. Integration is then performed using standard Gaussian quadrature on the multi-domain $\Omega_0 \times \tilde{\Omega}_0$.

6.A.2 Linearized stresses

Inserting eq. (6.68) and (6.5) into (6.66) yields

$$\begin{aligned}
\big[\Delta\tilde{\boldsymbol{P}}\big]^{\mathrm{G}}_{iJ} &= \Big(\big[\tilde{\mathbb{C}}\big]_{iJsT}\big[\nabla_{\mathrm{X}}\mathcal{R}\big]^C_T + \Big(\big[\tilde{\mathbb{C}}\big]_{iJsT}\big[\tilde{\boldsymbol{X}}\big]_U + \big[\tilde{\mathbb{D}}\big]_{iJsTU}\Big)\big[\nabla^2_{\mathrm{X}}\mathcal{R}\big]^C_{TU}\Big)\big[\Delta\boldsymbol{\varphi}\big]^C_s\\
&\qquad + \Big(\big[\tilde{\mathbb{C}}\big]_{iJsT}\big[\nabla_{\mathrm{X}}\tilde{\mathcal{N}}\big]^D_T + \big[\tilde{\mathbb{D}}\big]_{iJsTU}\big[\nabla^2_{\mathrm{X}}\tilde{\mathcal{N}}\big]^D_{TU}\Big)\big[\Delta\tilde{\boldsymbol{w}}\big]^{\mathrm{G},D}_s\\
\big[\Delta\tilde{\mathfrak{P}}\big]^{\mathrm{G}}_{iJK} &= \Big(\big[\tilde{\mathbb{M}}\big]_{iJKsT}\big[\nabla_{\mathrm{X}}\mathcal{R}\big]^C_T + \Big(\big[\tilde{\mathbb{M}}\big]_{iJKsT}\big[\tilde{\boldsymbol{X}}\big]_U + \big[\tilde{\mathbb{N}}\big]_{iJKsTU}\Big)\big[\nabla^2_{\mathrm{X}}\mathcal{R}\big]^C_{TU}\Big)\big[\Delta\boldsymbol{\varphi}\big]^C_s\\
&\qquad + \Big(\big[\tilde{\mathbb{M}}\big]_{iJKsT}\big[\nabla_{\mathrm{X}}\tilde{\mathcal{N}}\big]^D_T + \big[\tilde{\mathbb{N}}\big]_{iJKsTU}\big[\nabla^2_{\mathrm{X}}\tilde{\mathcal{N}}\big]^D_{TU}\Big)\big[\Delta\tilde{\boldsymbol{w}}\big]^{\mathrm{G},D}_s
\end{aligned} \tag{6.106}$$

for the discrete first- and second-order stress, respectively.

6.A.3 RVE benchmark: homogeneous first order - stress evaluation

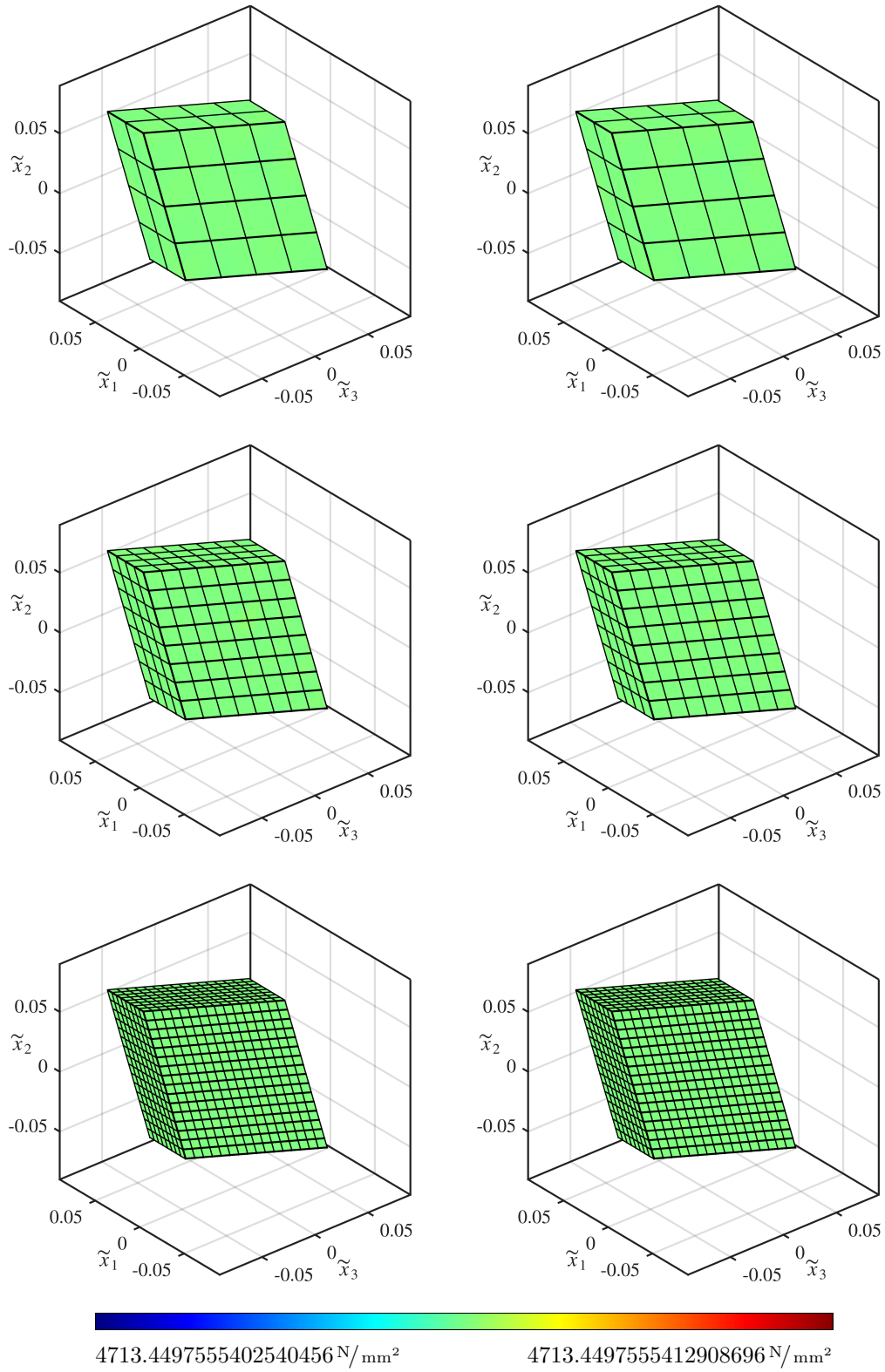


Figure 6.A.1 – First order homogeneous RVE: results. First order stress distribution ($\|\tilde{\boldsymbol{P}}\|$). Left to right: $\tilde{\Omega}_0$ with Dirichlet and periodic boundaries. Top to bottom: 4, 8 and 16 elements per direction.

7 Summary and outlook

7.1 Summary of the work

The present thesis has addressed the modeling and numerical simulation of materials and structures with distinct microstructural features, such as fiber-reinforced composites and engineered media. The work is motivated by the observation that explicitly resolving the microstructure in a fully three-dimensional setting is prohibitively expensive for realistic component sizes, while classical first-gradient Cauchy continua are often unable to represent bending- and torsion-dominated mechanisms, size effects, and non-local interactions that are relevant for such materials.

To bridge this gap, two complementary lines of development have been pursued. The first line is based on higher-order continua and dimension reduction. Starting from three-dimensional second-order continuum mechanics, continuous embedded fiber models and discrete embedded beam formulations including systematic reduction have been derived as effective second-gradient descriptions. The second line is based on dimension expansion in a continuous higher-order multi-scale framework. Therein, macroscopic fields are enriched by micro-fluctuation fields defined on representative volume elements (RVEs) from which in turn governing equations are obtained from an energetic macro-micro coupling.

Both lines are implemented in an isogeometric analysis (IGA) setting. Smooth NURBS-based approximation spaces are employed to represent geometry and solution fields on both the macro- and micro-scale, which is essential for a consistent discretization of second-order deformation gradients and higher-order stresses. The thesis thus combines advanced continuum modeling, consistent variational formulations and tailored numerical solution strategies into a coherent framework for the analysis of higher-order and multi-scale problems.

7.1.1 Higher-order continua and dimension reduction

After notation, introduction and covering the basics on IGA, the first main part of the thesis focuses on higher-order continua arising from embedded slender structures and their systematic reduction to effective second-gradient models.

Starting from the fundamentals of generalized continuum mechanics, a large-strain second-order model is formulated, including the associated balance laws, boundary conditions and weak form. This model provides the continuum-mechanical foundation for all subsequent

developments and clarifies the role of second gradients and higher-order tractions in a three-dimensional setting.

On this basis, a continuous embedded fiber formulation is introduced. Direction fields are used to represent families of rod-like reinforcements within a three-dimensional matrix. The energetic contribution of these fibers is expressed in terms of curvature and torsion measures that are consistently related to the second deformation gradient of motion. In this way, bending and twisting stiffness of the embedded structures are incorporated at the continuum level without explicitly meshing each fiber. Numerical examples demonstrate that the resulting second-gradient model can capture fiber-induced stiffness contributions and associated size effects that are inaccessible to classical Cauchy continua.

An alternative approach is then developed based on dimension reduction and discrete embedding. Finite-strain beam formulations including rotational degrees of freedom and curvature-based measures are embedded into a three-dimensional Cauchy continuum. The coupling between matrix and beams is enforced through suitable constraint formulations for coupling deformation and transferring acting forces and moments. A key result of reformulation and interpretation of arising constraint fields is a systematic static condensation procedure. By eliminating beam and coupling fields, an equivalent second-gradient continuum model is obtained that is applicable to solids reinforced by an arbitrary number of embedded beams with general orientations. The multidimensional coupling framework thereby comprises complex beam networks while still admitting a consistent condensation to a second-gradient formulation. The resulting condensed model makes the higher-order character of the effective medium explicit and provides a direct link between the parameters of the underlying beam formulation and the second-gradient moduli of the resulting continuum.

The discrete formulation mirrors this structure and additional reduction of degrees of freedom can be employed to eliminate explicit beam unknowns. Numerical investigations, including bending and torsion tests of matrix-beam systems, confirm that the condensed second-gradient model reproduces the response of the fully resolved beam-matrix system with good accuracy at significantly reduced computational cost. Moreover, the studies illustrate how the order of the underlying IGA basis functions and the choice of constraint enforcement influence accuracy and robustness, while the multi-beam applications indicate a route toward modeling discrete second-order microstructures for generic fiber-reinforced polymers.

In summary, this part of the thesis shows that higher-order continua derived from embedded slender structures provide a powerful and physically interpretable means to capture bending and torsion effects, non-local interactions and size-dependent behavior in fiber-reinforced materials, while retaining the computational advantages of continuum models.

7.1.2 Continuous higher-order multi-scale framework

The second main part of the thesis is devoted to a continuous higher-order multi-scale framework based on dimension expansion. In contrast to the dimension-reduction approach

above, the micro-scale is here retained explicitly in the form of a micro-kinematical extension of the macroscopic motion. A Taylor series expansion on the latter then provides the leading-order contribution and its gradients, while additional fluctuation fields are introduced on the micro-scale to represent the local heterogeneity.

Based on an energetic averaging assumption and vanishing mean fluctuations, a unified variational form provides a coupled macro-micro system including appropriate boundary conditions for the RVE. From this variational principle, the macro-scale equilibrium equations and the micro-scale fluctuation problem are derived simultaneously. The macroscopic first and higher order stresses emerge naturally from the energetic averages over the RVE, underlining the influence of micro-stress heterogeneity and the presence of second gradients at the macro-scale. Therefore, the formulation yields a higher-order generalization of classical homogenization concepts, presenting in detail dependencies of the macroscopic response not only on the average deformation but also on its gradients, directly related to the geometry and material behavior of the microstructure.

Special ansatz functions may be introduced exclusively for the macro-anchored fluctuation part, whereas all remaining parts and fields are discretized directly by the isogeometric formulation. When employed, these ansatz functions enable recovery of classical formulations by replacing the continuous macro-micro coupling with a reduced point-wise association, which in turn gives rise to a characteristic block structure allowing the optional separation of macroscopic and microscopic degrees of freedom. The smoothness of the NURBS basis functions is again exploited to approximate second-order fields and to enforce micro-scale boundary conditions efficiently.

A central contribution of this part is the analysis and exploitation of this block structure for efficient nonlinear solution strategies. The generalized scheme proposed here performs a null-space reduction of the micro-scale degrees of freedom such that the fluctuation fields are condensed at the RVE level. This induces a clear algorithmic separation in which the macroscopic problem is solved first and the micro-scale is updated afterward. Importantly, this reduction does not require the micro-scale equilibrium to be enforced within every macro-scale iteration. Instead, different schemes, including monolithic and fully nested FE^2-type or partially staggered procedures can all be interpreted as special cases of this unified framework.

Numerical experiments show that the proposed multi-scale formulation reproduces reference solutions for benchmark problems with high accuracy. In particular, the RVE studies confirm the expected behavior under different boundary conditions and highlight the role of second-order contributions for capturing non-local effects. Moreover, the problem solution simultaneously on both scales within a unified global scheme leads to a substantial reduction of overall computational cost compared to classical staggered approaches, while remaining compatible with additional acceleration techniques such as multigrid algorithms.

Taken together, these findings demonstrate that the continuous higher-order multi-scale framework developed in this thesis, based on dimension expansion, energetic averaging and unique IGA treatment provides a versatile and efficient tool for the analysis of heterogeneous materials.

7.2 Outlook

The contributions of this thesis open several directions for further research. On the modeling side, the present work has focused primarily on elastic responses. Extending the higher-order continuum formulations and the continuous multi-scale framework to inelastic behavior, such as plasticity, viscoelasticity and damage, is a natural next step. In particular, combining second-gradient effects with phase-field or other regularized damage models appears promising for the simulation of failure in fiber-reinforced composites and architectured materials.

Extensions of the embedded fiber and beam frameworks towards more complex microstructures can be made, like spherical point-wise inclusions, formulations for woven or braided textiles and three-dimensional lattice or truss-like architectures. The static condensation procedure derived here provides a systematic way to translate such discrete micro-architectures into effective higher-order continuum descriptions, but additional work is needed to calibrate and validate these models for realistic industrial configurations.

On the numerical side, adaptive strategies and model reduction techniques merit further investigation. Error estimators tailored to higher-order continua and multi-scale problems could guide local refinement on the macro- and micro-scale and reduce computational effort where the microstructure has a weak influence. Reduced-order or surrogate models for the RVE problems, possibly combined with machine learning techniques, could further accelerate the evaluation of the effective response in large-scale simulations.

The integration of the proposed methods into engineering design workflows remains an open task. This especially includes inverse problems for designing and optimizing microstructures or topology in general based on macro-scale loading conditions. This is particularly attractive in the context of additive manufacturing and the design of mechanical meta-materials.

Finally, a systematic validation of the proposed models against experimental data is essential to assess their predictive capabilities and to identify their limitations. Although the numerical investigations in this thesis indicate that the higher-order and multi-scale formulations behave as expected in a range of benchmark scenarios, their application to real materials and structures will inevitably reveal additional challenges, such as parameter identification, variability of microstructures and the interaction of multiple physical fields.

In conclusion, the thesis has shown that higher-order continuum models derived from embedded slender structures and continuous higher-order multi-scale formulations based on dimension expansion form a coherent and effective toolbox for the analysis of microstructured materials. The combination with IGA provides the necessary numerical machinery to realize these concepts in practice. The results obtained here provide a solid basis for future extensions towards more complex material behavior, richer microstructures and large-scale engineering applications.

Bibliography

[1] E. K. Agiasofitou and M. Lazar. "Conservation and balance laws in linear elasticity of grade three". In: *J. Elast.* 94.1 (Jan. 2009), pp. 69–85.

[2] H. Altenbach and V. A. Eremeyev. "Cosserat Media". In: *Generalized Continua from the Theory to Engineering Applications*. Ed. by Holm Altenbach and Victor A. Eremeyev. CISM International Centre for Mechanical Sciences. Vienna: Springer, 2013, pp. 65–130.

[3] H. Altenbach, G. A. Maugin, and V. Erofeev. *Mechanics of generalized continua*. Vol. 7. Springer, 2011.

[4] S. S. Antman. *Nonlinear problems of elasticity*. Springer, 1995.

[5] T. Asmanoglo and A. Menzel. "A finite deformation continuum modelling framework for curvature effects in fibre-reinforced nanocomposites". In: *Journal of the Mechanics and Physics of Solids* 107 (2017), pp. 411–432.

[6] T. Asmanoglo and A. Menzel. "A multi-field finite element approach for the modelling of fibre-reinforced composites with fibre-bending stiffness". In: *Computer Methods in Applied Mechanics and Engineering* 317 (2017), pp. 1037–1067.

[7] T. Asmanoglo and A. Menzel. "Fibre-reinforced composites with fibre-bending stiffness under azimuthal shear – Comparison of simulation results with analytical solutions". In: *International Journal of Non-Linear Mechanics* 91 (May 2017), pp. 128–139.

[8] F. Auricchio, P. Carotenuto, and A. Reali. "On the geometrically exact beam model: A consistent, effective and simple derivation from three-dimensional finite-elasticity". In: *International Journal of Solids and Structures* 45.17 (Aug. 2008), pp. 4766–4781.

[9] J. M. Ball. "Convexity conditions and existence theorems in nonlinear elasticity". In: *Arch. Ration. Mech. Anal.* 63.4 (Dec. 1976), pp. 337–403.

[10] J. M. Ball, J. C. Currie, and P. J. Olver. "Null Lagrangians, weak continuity, and variational problems of arbitrary order". In: *Journal of Functional Analysis* 41.2 (1981), pp. 135–174.

[11] Swantje Bargmann, Benjamin Klusemann, Jürgen Markmann, Jan Eike Schnabel, Konrad Schneider, Celal Soyarslan, and Jana Wilmers. "Generation of 3D representative volume elements for heterogeneous materials: A review". In: *Progress in Materials Science* 96 (July 2018), pp. 322–384.

[12] A. Bertram. "Finite gradient elasticity and plasticity: a constitutive mechanical framework". In: *Contin. Mech. Thermodyn.* 27.6 (Nov. 2015), pp. 1039–1058.

[13] A. Bertram and S. Forest. *Mechanics of strain gradient materials*. Centro Internazionale di Scienze Meccaniche. Springer, 2020.

[14] P. Betsch, A. Janz, and C. Hesch. "A mixed variational framework for the design of energy–momentum schemes inspired by the structure of polyconvex stored energy functions". In: *Computer Methods in Applied Mechanics and Engineering* 335 (2018), pp. 660–696.

[15] P. Betsch and R. Siebert. "Rigid body dynamics in terms of quaternions: Hamiltonian formulation and conserving numerical integration". In: *International Journal for Numerical Methods in Engineering* 79 (2009), pp. 444–473.

[16] P. Betsch and P. Steinmann. "Conservation Properties of a Time FE Method. Part III: Mechanical systems with holonomic constraints". In: *International Journal for Numerical Methods in Engineering* 53 (2002), pp. 2271–2304.

[17] P. Betsch and P. Steinmann. "Constrained dynamics of geometrically exactbeams". In: *Computational Mechanics* 31 (2003), pp. 49–59.

[18] J. Bonet, A. J. Gil, and R. Ortigosa. "A computational framework for polyconvex large strain elasticity". In: *Computer Methods in Applied Mechanics and Engineering* 283 (2015), pp. 1061–1094.

[19] J. Bonet, A. J. Gil, and R. Ortigosa. "On a tensor cross product based formulation of large strain solid mechanics". In: *International Journal of Solids and Structures* 84 (May 2016), pp. 49–63.

[20] J. Bonet and R. D. Wood. *Nonlinear Continuum Mechanics for Finite Element Analysis*. 2nd ed. Cambridge University Press, Mar. 13, 2008.

[21] A.-L. Cauchy. "Recherches sur l'équilibre et le mouvement intérieur des corps solides ou fluides, élastiques ou non élastiques". In: *Bulletin de la Société philomatique* (1823).

[22] A.-L. Cauchy. "Mecanique moleculaire - Note sur l'équilibre et les mouvements vibratoires des corps solides". In: *C. R., T. XXXII* (1851), pp. 341–346.

[23] D. Chapelle and K. J. Bathe. "The inf-sup test". In: *Computers & Structures* 47.4-5 (June 1993), pp. 537–545.

[24] P. G. Ciarlet and J. Nečas. "Injectivity and self-contact in nonlinear elasticity". In: *Arch. Ration. Mech. Anal.* 97.3 (Sept. 1987), pp. 171–188.

[25] E. Cosserat and F. Cosserat. *Theorie des corps deformables*. A. Hermann et fils, 1909.

[26] J. A. Cottrell, T. J. R. Hughes, and Y. Bazilevs. *Isogeometric Analysis: Toward Integration of CAD and FEA*. Wiley, 2009.

[27] C. De Boor. "On calculating with B-splines". In: *Journal of Approximation Theory* 6.1 (July 1972), pp. 50–62.

[28] F. Dell'Isola. *The complete works of Gabrio Piola: Volume I: Commented English Translation*. Advanced Structured Materials 38. Cham: Springer, 2014.

[29] F. dell'Isola, P. Seppecher, M. Spagnuolo, E. Barchiesi, F. Hild, T. Lekszycki, I. Giorgio, L. Placidi, U. Andreaus, M. Cuomo, S. R. Eugster, A. Pfaff, K. Hoschke, R. Langkemper, E. Turco, R. Sarikaya, A. Misra, M. De Angelo, F. D'Annibale, A. Bouterf, X. Pinelli, A. Misra, B. Desmorat, M. Pawlikowski, C. Dupuy, D. Scerrato, P. Peyre, M. Laudato, L. Manzari, P. Göransson, C. Hesch, S. Hesch, P. Franciosi, J. Dirrenberger, F. Maurin, Z. Vangelatos, C. Grigoropoulos, V. Melissinaki, M. Farsari, W. Muller, B. E. Abali, C. Liebold, G. Ganzosch, P. Harrison, R. Drobnicki, L. Igumnov, F. Alzahrani, and T. Hayat. "Advances in pantographic structures: design, manufacturing, models, experiments and image analyses". In: *Continuum Mechanics and Thermodynamics* 31 (2019), pp. 1231–1282.

[30] F. dell'Isola, A. D. Corte, and I. Giorgio. "Higher-gradient continua: The legacy of Piola, Mindlin, Sedov and Toupin and some future research perspectives". In: *Mathematics and Mechanics of Solids* 22.4 (Apr. 2017), pp. 852–872.

[31] F. dell'Isola, I. Giorgio, M. Pawlikowski, and N. L. Rizzi. "Large deformations of planar extensible beams and pantographic lattices: heuristic homogenization, experimental and numerical examples of equilibrium". In: *Proceedings of the Royal Society of London A: Mathematical, Physical and Engineering Sciences* 472.2185 (2016).

[32] M. Dittmann. "Isogeometric analysis and hierarchical refinement for multi-field contact problems". PhD thesis. University of Siegen, 2017.

[33] M. Dittmann, J. Schulte, F. Schmidt, and C. Hesch. "A strain-gradient formulation for fiber reinforced polymers: hybrid phase-field model for porous-ductile fracture". In: *Computational Mechanics* 67.6 (June 2021), pp. 1747–1768.

[34] M. Dittmann, S. Schuß, B. Wohlmuth, and C. Hesch. "Weak C^n coupling for multi-patch isogeometric analysis in solid mechanics". In: *International Journal for Numerical Methods in Engineering* 118 (2019), pp. 678–699.

[35] T. X. Duong, V. N. Khiem, M. Itskov, and R. A. Sauer. "A general theory for anisotropic Kirchhoff-Love shells with embedded fibers and in-plane bending". In: *Materials Science* (2020), submitted, arXiv:2101.03122.

[36] A. C. Eringen. *Microcontinuum Field Theories I: Foundations and Solids*. Springer, 1999.

[37] S. R. Eugster, C. Hesch, P. Betsch, and C. Glocker. "Director-based beam finite elements relying on the geometrically exact beam theory formulated in skew coordinates". In: *International Journal for Numerical Methods in Engineering* 97 (2014), pp. 111–129.

[38] L. Euler. "Principes généraux de l'état d'équilibre d'un fluide". In: *Mémoires de l'académie des sciences de Berlin* 11 (1757), pp. 274–315.

[39] R. Fedele. "Approach à la Piola for the equilibrium problem of bodies with second gradient energies. Part II: Variational derivation of second gradient equations and their transport". In: *Contin. Mech. Thermodyn.* 34.5 (Sept. 2022), pp. 1087–1111.

[40] C. A. Felippa and B. Haugen. "A unified formulation of small-strain corotational finite elements: I. Theory". In: *Computer Methods in Applied Mechanics and Engineering* 194.21-24 (June 2005), pp. 2285–2335.

[41] F. Feyel and J.-L. Chaboche. "FE2 multiscale approach for modelling the elasto-viscoplastic behaviour of long fibre SiC/Ti composite materials". In: *Computer methods in applied mechanics and engineering* 183.3-4 (2000), pp. 309–330.

[42] S. Forest and D. K. Trinh. "Generalized continua and non-homogeneous boundary conditions in homogenisation methods". In: *ZAMM-Journal of Applied Mathematics and Mechanics/Zeitschrift für Angewandte Mathematik und Mechanik* 91.2 (2011), pp. 90–109.

[43] U. Frisch. *Translation of Leonhard Euler's: General Principles of the Motion of Fluids*. 2008.

[44] Marc G. D. Geers, Varvara G. Kouznetsova, Karel Matouš, and Julien Yvonnet. "Homogenization Methods and Multiscale Modeling: Nonlinear Problems". In: *Encyclopedia of Computational Mechanics Second Edition*. Ed. by Erwin Stein, René Borst, and Thomas J R Hughes. 1st ed. Wiley, Dec. 2017, pp. 1–34.

[45] P. Germain. "The Method of Virtual Power in Continuum Mechanics. Part 2: Microstructure". In: *SIAM Journal on Applied Mathematics* 25.3 (Nov. 1973), pp. 556–575.

[46] I. Giorgio. "Numerical identification procedure between a micro-Cauchy model and a macro-second gradient model for planar pantographic structures." In: *Zeitschrift für angewandte Mathematik und Physik* 67:95 (2016), pp. 1–17.

[47] R. Glüge, M. Weber, and A. Bertram. "Comparison of spherical and cubical statistical volume elements with respect to convergence, anisotropy, and localization behavior". In: *Computational Materials Science* 63 (Oct. 2012), pp. 91–104.

[48] Rainer Glüge. "Generalized boundary conditions on representative volume elements and their use in determining the effective material properties". In: *Computational Materials Science* 79 (Nov. 2013), pp. 408–416.

[49] M. E. Gurtin. "Thermodynamics and the possibility of spatial interaction in elastic materials". In: *Archive for Rational Mechanics and Analysis* 19.5 (Jan. 1965), pp. 339–352.

[50] M. E. Gurtin. *An Introduction to Continuum Mechanics*. Vol. 158. Mathematics in Science and Engineering. Academic Press, 1981.

[51] Stefan Hartmann and Patrizio Neff. "Polyconvexity of generalized polynomial-type hyperelastic strain energy functions for near-incompressibility". In: *International Journal of Solids and Structures* 40.11 (June 2003), pp. 2767–2791.

[52] Z. Hashin and S. Shtrikman. "A variational approach to the theory of the elastic behaviour of multiphase materials". In: *Journal of the Mechanics and Physics of Solids* 11.2 (1963), pp. 127–140.

[53] T. J. Healey and S. Krömer. “Injective weak solutions in second-gradient nonlinear elasticity”. In: *ESAIM: Control, Optimisation and Calculus of Variations* 15.4 (July 2008), pp. 863–871.

[54] E. Hellinger. “Die Allgemeinen Ansätze der Mechanik der Kontinua”. In: *Mechanik*. Ed. by F. Klein and . Müller. Wiesbaden: Vieweg & Teubner Verlag, 1914, pp. 601–694.

[55] C. Hesch, A. J. Gil, A. Arranz Carreño, and J. Bonet. “On continuum immersed strategies for Fluid–Structure Interaction”. In: *Computer Methods in Applied Mechanics and Engineering* 247-248 (2012), pp. 51–64.

[56] C. Hesch, A. J. Gil, A. Arranz Carreno, J. Bonet, and P. Betsch. “A Mortar approach for Fluid-Structure Interaction problems: Immersed strategies for deformable and rigid bodies”. In: *Computer Methods in Applied Mechanics and Engineering* 278 (2014), pp. 853–882.

[57] C. Hesch, F. Schmidt, and S. Schuß. “Variational formulation and monolithic solution of computational homogenization methods”. In: *International Journal for Numerical Methods in Engineering* 125.20 (Oct. 30, 2024).

[58] R. Hill. “The elastic behaviour of a crystalline aggregate”. In: *Proceedings of the Physical Society. Section A* 65.5 (1952), p. 349.

[59] R. Hill. “A self-consistent mechanics of composite materials”. In: *Journal of the Mechanics and Physics of Solids* 13.4 (1965), pp. 213–222.

[60] G. A. Holzapfel. *Nonlinear solid mechanics: a continuum approach for engineering*. Chichester ; New York: Wiley, 2000.

[61] T. J. R. Hughes, J. A. Cottrell, and Y. Bazilevs. “Isogeometric analysis: CAD, finite elements, NURBS, exact geometry and mesh refinement”. In: *Computer Methods in Applied Mechanics and Engineering* 194.39–41 (2005), pp. 4135–4195.

[62] A. Javili, F. dell’Isola, and P. Steinmann. “Geometrically nonlinear higher-gradient elasticity with energetic boundaries”. In: *Journal of the Mechanics and Physics of Solids* 61.12 (2013), pp. 2381–2401.

[63] T. Kanit, S. Forest, I. Galliet, V. Mounoury, and D. Jeulin. “Determination of the size of the representative volume element for random composites: statistical and numerical approach”. In: *International Journal of Solids and Structures* 40.13-14 (June 2003), pp. 3647–3679.

[64] U. Khristenko, S. Schuß, M. Krüger, F. Schmidt, B. Wohlmuth, and C. Hesch. “Multidimensional coupling: A variationally consistent approach to fiber-reinforced materials”. In: *Computer Methods in Applied Mechanics and Engineering* 382 (Aug. 2021), p. 113869.

[65] T. Köppl, E. Vidotto, B. Wohlmuth, and P. Zunino. “Mathematical modeling, analysis and numerical approximation of second-order elliptic problems with inclusions”. In: *Mathematical Models and Methods in Applied Sciences* 28.05 (2018), pp. 953–978.

[66] V. G. Kouznetsova. *Computational homogenization for the multi-scale analysis of multi-phase materials*. PhD thesis. Technische Universiteit Eindhoven, 2002.

[67] V. G. Kouznetsova, W. A. M. Brekelmans, and F. P. T. Baaijens. "An approach to micro-macro modeling of heterogeneous materials". In: *Computational mechanics* 27.1 (2001), pp. 37–48.

[68] V. G. Kouznetsova, M. G. D. Geers, and W. A. M. Brekelmans. "Multi-scale constitutive modelling of heterogeneous materials with a gradient-enhanced computational homogenization scheme". In: *International Journal for Numerical Methods in Engineering* 54 (2002), pp. 1235–1260.

[69] V. G. Kouznetsova, M. G. D. Geers, and W. A. M. Brekelmans. "Multi-scale second-order computational homogenization of multi-phase materials: a nested finite element solution strategy". In: *Computer Methods in Applied Mechanics and Engineering*. Advances in Computational Plasticity 193.48 (Dec. 2004), pp. 5525–5550.

[70] A. Krischok and C. Linder. "A generalized inf–sup test for multi-field mixed-variational methods". In: *Computer Methods in Applied Mechanics and Engineering* 357 (Dec. 2019), p. 112497.

[71] J. L. Lagrange, W. T. Kelvin, and W. Howie. *Méchanique analitique*. A Paris: Chez la veuve Desaint, 1788.

[72] Y.-L Lai, J. S.-S. Wu, J.-P. Hung, and J.-H. Chen. "Degree reduction of NURBS curves". In: *The International Journal of Advanced Manufacturing Technology* 27.11 (Feb. 2006), pp. 1124–1131.

[73] S. Lang. *Introduction to Linear Algebra*. Springer New York, 1986.

[74] Nils Lange, Geralf Hütter, and Björn Kiefer. "An efficient monolithic solution scheme for FE^2 problems". In: *Computer Methods in Applied Mechanics and Engineering* 382 (2021), p. 113886.

[75] Pierre Simon Laplace, Hugh Gordon, John Gordon, and Burndy Library. *Traité de mécanique céleste*. A Paris: De L'Imprimerie de Crapelet : Chez J. B. M. Duprat, 1798.

[76] W. K. Liu, D. W. Kim, and S. Tang. "Mathematical foundations of the immersed finite element method". In: *Computational Mechanics* 39 (2007), pp. 211–222.

[77] A. Madeo, I. D. Ghiba, P. Neff, and I. Münch. "A new view on boundary conditions in the Grioli–Koiter–Mindlin–Toupin indeterminate couple stress model." In: *European Journal of Mechanics - A/Solids* 59 (2016), pp. 294–322.

[78] J. E. Marsden and T. J. R. Hughes. *Mathematical Foundations of Elasticity*. Prentice -Hall, Inc., Englewood Cliffs, N.J., 1983.

[79] J. E. Marsden and T. S. Ratiu. *Introduction to Mechanics and Symmetry*. Springer, 2003.

[80] K. Matouš, M. G. D. Geers, V. G. Kouznetsova, and A. Gillman. "A review of predictive nonlinear theories for multiscale modeling of heterogeneous materials". In: *Journal of Computational Physics* 330 (2017), pp. 192–220.

[81] G. A. Maugin and A. V. Metrikine. *Mechanics of generalized continua*. One Hundred Years After the Cosserats. Springer, 2010.

[82] F. A. McRobie and J. Lasenby. "Simo–Vu Quoc rods using Clifford algebra". In: *International Journal for Numerical Methods in Engineering* 45 (1999), pp. 377–398.

[83] C. Meier, A. Popp, and W. A. Wall. "Geometrically exact finite element formulations for slender beams: Kirchhoff–Love theory versus Simo–Reissner theory". In: *Archives of Computational Methods in Engineering* 26.1 (2019), pp. 163–243.

[84] C. Miehe, J. Schröder, and J. Schotte. "Computational homogenization analysis in finite plasticity simulation of texture development in polycrystalline materials". In: *Computer methods in applied mechanics and engineering* 171.3-4 (1999), pp. 387–418.

[85] R. D. Mindlin. "Micro-structure in linear elasticity". In: *Archive for Rational Mechanics and Analysis* 16.1 (1964), pp. 51–78.

[86] R. D. Mindlin. "On the equations of elastic materials with microstructure". In: *International Journal of Solids and Structures* 1 (1965), pp. 73–78.

[87] R. D. Mindlin. "Second gradient of strain and surface-tension in linear elasticity". In: *International Journal of Solids and Structures* 1.4 (1965), pp. 417–438.

[88] T. Mori and K. Tanaka. "Average stress in matrix and average elastic energy of materials with misfitting inclusions". In: *Acta metallurgica* 21.5 (1973), pp. 571–574.

[89] R. Ortigosa, A. J. Gil, J. Bonet, and C. Hesch. "A computational framework for polyconvex large strain elasticity for geometrically exact beam theory". In: *Computational Mechanics* 57.2 (2016), pp. 277–303.

[90] Martin Ostoja-Starzewski. "Material spatial randomness: From statistical to representative volume element". In: *Probabilistic Engineering Mechanics* 21.2 (Apr. 2006), pp. 112–132.

[91] A. Z. Palmer and T. J. Healey. "Injectivity and self-contact in second-gradient nonlinear elasticity". In: *Calc. Var. Partial Differ. Equ.* 56.4 (Aug. 2017).

[92] L. Piegl and W. Tiller. *The NURBS Book*. 2nd. Springer, 2010.

[93] G. Piola. *Intorno alle equazioni fondamentali del movimento di corpi qualsivogliono, considerati secondo la naturale loro formae costituzione.* Vol. 24. Memorie della Società Italiana delle Scienze residente en Modena. Modena: Società Italiana delle Scienze residente en Modena, 1848.

[94] A. Reali and T. J. R. Hughes. "An Introduction to Isogeometric Collocation Methods". In: *Isogeometric Methods for Numerical Simulation*. Ed. by Gernot Beer and Stéphane Bordas. Vienna: Springer Vienna, 2015, pp. 173–204.

[95] E. Reissner. "On finite deformations of space-curved beams." In: *Zeitschrift für angewandte Mathematik und Physik* 32 (1981), pp. 734–744.

[96] I. Romero and F. Armero. "An objective finite element approximation of the kinematics of geometrically exact rods and its use in the formulation of an energy-momentum conserving scheme in dynamics". In: *International Journal for Numerical Methods in Engineering* 54 (2002), pp. 1683–1716.

[97] M. B. Rubin. *Cosserat Theories: Shells, Rods and Points*. Kluwer Academic Publishers, 2000.

[98] C. Sansour. "On the physical assumptions underlying the volumetric-isochoric split and the case of anisotropy". In: *European Journal of Mechanics - A/Solids* 27.1 (Jan. 2008), pp. 28–39.

[99] F. Schmidt, M. Krüger, and C. Hesch. "Numerical Homogenisation of Gradient Materials". In: *Advanced Structured Materials*. Cham: Springer International Publishing, 2022, pp. 487–503.

[100] F. Schmidt, M. Krüger, M.-A. Keip, and C. Hesch. "Computational homogenization of higher-order continua". In: *International Journal for Numerical Methods in Engineering* 123.11 (June 15, 2022), pp. 2499–2529.

[101] J. Schröder. "A numerical two-scale homogenization scheme: the FE^2-method." In: *Plasticity and Beyond: Microstructures, Crystal-Plasticity and Phase Transitions*. Springer Vienna, 2014, pp. 1–64.

[102] J. Schröder and M.-A. Keip. "Two-scale homogenization of electromechanically coupled boundary value problems". In: *Computational Mechanics* 50 (2012), pp. 229–244.

[103] J. Schulte, M. Dittmann, S. R. Eugster, S. Hesch, T. Reinicke, F. Dell'Isola, and C. Hesch. "Isogeometric analysis of fiber reinforced composites using Kirchhoff–Love shell elements". In: *Computer Methods in Applied Mechanics and Engineering* 362 (2020), p. 112845.

[104] S. Schuß. "Cn-continuous mortar method for Isogeometric Analysis". Doctoral Thesis. Siegen, Germany: University of Siegen, 2024.

[105] S. Schuß, S. Glas, and C. Hesch. "Non-linear space-time elasticity". In: *International Journal for Numerical Methods in Engineering* 124.9 (2023), pp. 1965–1990.

[106] J. C. Simo. "A finite strain beam formulation. The three-dimensional dynamic problem. Part I". In: *Computer Methods in Applied Mechanics and Engineering* 49.1 (1985), pp. 55–70.

[107] J. C. Simo, D. D. Fox, and T. J. R. Hughes. "Formulations of finite elasticity with independent rotations". In: *Computer Methods in Applied Mechanics and Engineering* 95 (1992), pp. 277–288.

[108] J. C. Simo and L. Vu-Quoc. "A three-dimensional finite-strain rod model. Part II: Computational aspects". In: *Computer Methods in Applied Mechanics and Engineering* 58 (1986), pp. 79–116.

[109] R. J. M. Smit, W. A. M. Brekelmans, and H. E. H. Meijer. "Prediction of the mechanical behavior of nonlinear heterogeneous systems by multi-level finite element modeling". In: *Computer methods in applied mechanics and engineering* 155.1-2 (1998), pp. 181–192.

[110] K. P. Soldatos. "Second-gradient plane deformations of ideal fibre-reinforced materials: implications of hyper-elasticity theory". In: *J. Eng. Math.* 68 (2010), pp. 99–127.

[111] K. P. Soldatos. "Foundation of Polar Linear Elasticity for Fibre-Reinforced Materials II: Advanced Anisotropy". In: *Journal of Elasticity* 118.2 (Feb. 2015), pp. 223–242.

[112] A. J. M. Spencer and K. P. Soldatos. "Finite deformations of fibre-reinforced elastic solids with fibre bending stiffness". In: *International Journal of Non-Linear Mechanics* 42 (2007), pp. 355–368.

[113] D. J. Steigmann. "Equilibrium of elastic lattice shells". In: *J. Eng. Math.* 109 (2018), pp. 47–61.

[114] I. Steinbrecher, M. Mayr, M. J. Grill, J. Kremheller, C. Meier, and A. Popp. "A mortar-type finite element approach for embedding 1D beams into 3D solid volumes". In: *Computational Mechanics* 66 (2020), pp. 1377–1398.

[115] G. I. Taylor. "Plastic strain in metals". In: *Plastic Strain in Metals* (1938), pp. 307–324.

[116] R. A. Toupin. "Elastic materials with couple-stresses". In: *Archive for Rational Mechanics and Analysis* 11 (1962), pp. 385–414.

[117] R. A. Toupin. "Theories of elasticity with couple-stress". In: *Archive for Rational Mechanics and Analysis* 17.2 (1964), pp. 85–112.

[118] Paul Wasmer and Peter Betsch. "A projection-based quaternion discretization of the geometrically exact beam model". In: *International Journal for Numerical Methods in Engineering* 125.20 (Oct. 2024).

[119] O. Weeger, S. K. Yeung, and M. L. Dunn. "Isogeometric collocation methods for Cosserat rods and rod structures". In: *Computer Methods in Applied Mechanics and Engineering* 316 (2017), pp. 100–122.

[120] J. R. Willis. "Bounds and self-consistent estimates for the overall properties of anisotropic composites". In: *Journal of the Mechanics and Physics of Solids* 25 (1977), pp. 185–202.

Vol. 2

Publication series of the Chair of Computational Mechanics

Editor: Prof. Dr. habil. Christian Hesch

Abstract

Microstructured and fiber-reinforced materials exhibit mechanical behavior that cannot always be captured by classical continuum models. Bending-dominated mechanisms, size effects and non-local interactions require formulations that go beyond first-gradient Cauchy continua, while fully resolved three-dimensional simulations of the underlying microstructure are often computationally extensive.

This work develops higher-order modeling and simulation frameworks that bridge this gap. Embedded slender reinforcements are described either by continuous second-gradient fiber models or by geometrically exact Cosserat beams coupled to a surrounding threedimensional matrix. Through consistent kinematic coupling and static condensation, these descriptions lead to effective higher-order continua capable of representing fiberinduced stiffness and curvature effects efficiently.

In addition, a continuous higher-order multi-scale formulation based on dimension expansion is proposed. By combining macroscopic Taylor expansions with microscopic fluctuation fields and energetically consistent averaging, the framework derives generalized macroscopic stresses directly from the microstructure and includes the classical FE^2 method as a special case. The resulting approaches provide a coherent computational framework for investigating micro-structured materials within an isogeometric analysis setting.

ISBN 978-3-96182-240-9